

JOINT TRANSPORTATION RESEARCH PROGRAM

INDIANA DEPARTMENT OF TRANSPORTATION
AND PURDUE UNIVERSITY



FIBER REINFORCED POLYMER BRIDGE DECKS

Judy Liu

Professor of Civil Engineering
Purdue University
Corresponding Author

Elisa D. Sotelino

Professor of Civil Engineering
Purdue University

Rita E. Rodriguez-Vera

Graduate Research Assistant
School of Civil Engineering
Purdue University

Nicolas J. Lombardi

Graduate Research Assistant
School of Civil Engineering
Purdue University

Marcelo A. S. Machado

Graduate Research Assistant
School of Civil Engineering
Purdue University

SPR-2943

Report Number: FHWA/IN/JTRP-2011/04

DOI: 10.5703/1288284314242

This page intentionally left blank.

RECOMMENDED CITATION

Rodriguez-Vera, R. E., N. J. Lombardi, M. A. Machado, J. Liu, and E. D. Sotelino. *Fiber Reinforced Polymer Bridge Decks*. Publication FHWA/IN/JTRP-2011/04. Joint Transportation Research Program, Indiana Department of Transportation and Purdue University, West Lafayette, Indiana, 2011. doi: 10.5703/1288284314242.

CORRESPONDING AUTHORS

Professor Judy Liu
School of Civil Engineering
Purdue University
(765)494-2254
jliu@purdue.edu

JOINT TRANSPORTATION RESEARCH PROGRAM

The Joint Transportation Research Program serves as a vehicle for INDOT collaboration with higher education institutions and industry in Indiana to facilitate innovation that results in continuous improvement in the planning, design, construction, operation, management and economic efficiency of the Indiana transportation infrastructure.
https://engineering.purdue.edu/JTRP/index_html

Published reports of the Joint Transportation Research Program are available at: <http://docs.lib.purdue.edu/jtrp/>

NOTICE

The contents of this report reflect the views of the authors, who are responsible for the facts and the accuracy of the data presented herein. The contents do not necessarily reflect the official views and policies of the Indiana Department of Transportation or the Federal Highway Administration. The report does not constitute a standard, specification or regulation.

This page intentionally left blank.

| | | | |
|--|------------------------------------|--|--|
| 1. Report No. FHWA/IN/JTRP-2011/04 | 2. Government Accession No. | 3. Recipient's Catalog No. | |
| 4. Title and Subtitle Fiber Reinforced Polymer Bridge Decks | | 5. Report Date 2011 | |
| 7. Author(s) Rita E. Rodriguez-Vera, Nicolas J. Lombardi, Marcelo A.S. Machado, Judy Liu, Elisa D. Sotelino | | 6. Performing Organization Code | |
| 9. Performing Organization Name and Address Joint Transportation Research Program Purdue University 550 Stadium Mall Drive West Lafayette, IN 47907-2051 | | 8. Performing Organization Report No. FHWA/IN/JTRP-2011/04 | |
| 12. Sponsoring Agency Name and Address Indiana Department of Transportation State Office Building 100 North Senate Avenue Indianapolis, IN 46204 | | 10. Work Unit No. | |
| 15. Supplementary Notes Prepared in cooperation with the Indiana Department of Transportation and Federal Highway Administration. | | 11. Contract or Grant No. SPR-2943 | |
| 16. Abstract <p>The overarching goal of this study was to perform a comprehensive evaluation of various issues related to the strength and serviceability of the FRP deck panels that are available in the industry. Specific objectives were to establish critical limit states to be considered in the design of FRP deck panel, to provide performance specifications to designers, and to develop evaluation techniques for the deck panels in service.</p> <p>Two different FRP panels were studied during the research project: a sandwich panel and a pultruded panel. The sandwich panel was initially selected for the rehabilitation case study bridge. However, for a variety of reasons outside of the scope of this study, both the sandwich panel and the initial case study bridge were dropped from consideration. A new case study bridge was selected, and new proposals from FRP deck manufacturers were solicited. At that time, the pultruded deck was selected. Analysis and experimental results related to both FRP deck panels are included in this report, as information from both decks is relevant to the overarching goal of this study.</p> <p>In November 2009, Sugar Creek Bridge became the first bridge in Indiana to be rehabilitated with an FRP bridge deck. An extensive study, including literature review, analysis, and load tests, suggest that the installed deck should perform well, with web buckling as the ultimate failure mode at a factor of safety of 5. Deflection limits, generally an issue with FRP decks, are satisfied with the installed deck. Meanwhile, some combination of acoustic emission methods, infrared thermography and a newly developed traveling truck deflection method show promise for non-destructive evaluation of the deck in-situ and identification of damage such as delamination of the wearing surface or web buckling. However, such methods have shown variability and could be prohibitively labor-intensive. Therefore, further evaluation is needed if such methods are to be pursued.</p> | | 13. Type of Report and Period Covered <p style="text-align: center;">Final Report</p> | |
| 17. Key Words Bridge Decks, Fiber-reinforced Polymer, Non-destructive Evaluation | | 14. Sponsoring Agency Code | |
| 19. Security Classif. (of this report) <p style="text-align: center;">Unclassified</p> | | 13. Type of Report and Period Covered Final Report | |
| 20. Security Classif. (of this page) <p style="text-align: center;">Unclassified</p> | | 16. Abstract <p>The overarching goal of this study was to perform a comprehensive evaluation of various issues related to the strength and serviceability of the FRP deck panels that are available in the industry. Specific objectives were to establish critical limit states to be considered in the design of FRP deck panel, to provide performance specifications to designers, and to develop evaluation techniques for the deck panels in service.</p> <p>Two different FRP panels were studied during the research project: a sandwich panel and a pultruded panel. The sandwich panel was initially selected for the rehabilitation case study bridge. However, for a variety of reasons outside of the scope of this study, both the sandwich panel and the initial case study bridge were dropped from consideration. A new case study bridge was selected, and new proposals from FRP deck manufacturers were solicited. At that time, the pultruded deck was selected. Analysis and experimental results related to both FRP deck panels are included in this report, as information from both decks is relevant to the overarching goal of this study.</p> <p>In November 2009, Sugar Creek Bridge became the first bridge in Indiana to be rehabilitated with an FRP bridge deck. An extensive study, including literature review, analysis, and load tests, suggest that the installed deck should perform well, with web buckling as the ultimate failure mode at a factor of safety of 5. Deflection limits, generally an issue with FRP decks, are satisfied with the installed deck. Meanwhile, some combination of acoustic emission methods, infrared thermography and a newly developed traveling truck deflection method show promise for non-destructive evaluation of the deck in-situ and identification of damage such as delamination of the wearing surface or web buckling. However, such methods have shown variability and could be prohibitively labor-intensive. Therefore, further evaluation is needed if such methods are to be pursued.</p> | |
| 18. Distribution Statement No restrictions. This document is available to the public through the National Technical Information Service, Springfield, VA 22161 | | 22. Price | |
| 21. No. of Pages | | 22. Price | |

This page intentionally left blank.

CONTENTS

| | |
|---|-----|
| LIST OF TABLES | iii |
| LIST OF FIGURES | iv |
| EXECUTIVE SUMMARY | 1 |
| CHAPTER 1. INTRODUCTION | 2 |
| 1.1 Background & Motivation | 2 |
| 1.2 Objectives & Scope | 2 |
| 1.3 Methodology | 2 |
| 1.4 Organization | 2 |
| CHAPTER 2. FIBER REINFORCED POLYMER DECKS | 2 |
| 2.1 General | 2 |
| 2.2 Manufacturing Techniques | 3 |
| 2.3 Key Issues for Implementation of Fiber Reinforced Polymer Decks | 3 |
| 2.4 FRP Decks in Study | 15 |
| 2.5 Conclusions | 16 |
| CHAPTER 3. SERVICEABILITY CRITERIA FOR FRP BRIDGE DECKS | 18 |
| 3.1 Background and Motivation | 18 |
| 3.2 Current Specifications | 18 |
| 3.3 Numerical Models for Predicting Deflections | 20 |
| 3.4 Alternative Vibration Control Serviceability Criteria | 21 |
| 3.5 Hybrid Beam Concept | 27 |
| 3.6 Conclusions | 35 |
| CHAPTER 4. CASE STUDY BRIDGE: WILDCAT CREEK BRIDGE | 35 |
| 4.1 General | 35 |
| 4.2 Case Study Bridge: WildCat Creek Bridge | 36 |
| 4.3 Simple Overhang Serviceability Parametric Study for KSCI Panels | 36 |
| 4.4 Experimental Work | 36 |
| 4.5 Conclusions | 48 |
| CHAPTER 5. CASE STUDY BRIDGE: SUGAR CREEK BRIDGE | 50 |
| 5.1 General | 50 |
| 5.2 Case Study Bridge: Sugar Creek Bridge | 50 |
| 5.3 Experimental Work | 51 |
| 5.4 Sugar Creek Bridge Deck Installation | 74 |
| 5.5 Conclusions | 79 |
| CHAPTER 6. NON DESTRUCTIVE EVALUATION | 79 |
| 6.1 Introduction | 79 |
| 6.2 Non Destructive Evaluation Techniques | 79 |
| 6.3 Acoustic Emission | 79 |
| 6.4 Previous Studies – Literature Review | 80 |
| 6.5 Acoustic Emission Experimental Results | 83 |
| 6.6 NCHRP ZellComp Specimen Thermographic Imaging | 89 |
| 6.7 Acousto-Ultrasonics and Airborne UT Sensor | 89 |
| 6.8 Traveling Truck Deflection Measurements | 91 |
| 6.9 Conclusions | 95 |
| CHAPTER 7. CONCLUSIONS AND FUTURE WORK | 97 |
| 7.1 General | 97 |
| 7.2 FRP Bridge Decks | 97 |
| 7.3 Serviceability Criteria | 97 |
| 7.4 Wildcat Creek Bridge and KSCI Deck | 97 |
| 7.5 Sugar Creek Bridge and ZellComp Deck | 97 |

| | |
|---|----|
| 7.6 Non-destructive Evaluation Methods. | 98 |
| 7.7 Implementation Plan | 98 |
| 7.8 Conclusions | 98 |
| REFERENCES | 98 |

LIST OF TABLES

| | |
|--|----|
| Table 3-1: Comparisons of Deflection Models | 21 |
| Table 3-2: Matrix of Selected Design Parameters | 23 |
| Table 3-3: Peak acceleration limits for human response to vertical vibrations (Wright and Walker 1971) | 23 |
| Table 3-4: Results of parametric study | 24 |
| Table 3-5: Hybrid GFRP-steel study progression matrix | 27 |
| Table 3-6: L and W direction beam equivalent flexural modulus summary | 34 |
| Table 3-7: L and W direction beam equivalent shear modulus summary | 35 |
| Table 4-1: Overhang Deflections | 37 |
| Table 5-1: Flexogrid / PolyCarb Specification Comparison | 69 |
| Table 5-2: Flexolith / TAMMS Specification Comparison | 70 |
| Table 5-3: T-48 / Transpo Specification Comparison | 70 |
| Table 5-4: Flexogrid Specification Comparison | 71 |
| Table 5-5: Pull-off Test Results | 74 |
| Table 6-1: Tension Coupon Test Results | 84 |

LIST OF FIGURES

| | |
|--|----|
| Figure 2.1: Pultrusion Process (http://www.afp fiberglass.com/images/pultrusionProcess.jpg) | 3 |
| Figure 2.2: VARTM process | 3 |
| Figure 2.3: Hand Lay-Up Process | 3 |
| Figure 2.4: FRP Deck Manufacturers and Types (adapted from Telang, et al., 2006) | 5 |
| Figure 2.5: FRP Threaded Shear Stud with Clamp Connection (Righman, et al., 2004) | 6 |
| Figure 2.6: Grouted Shear Stud Connection (Zellcomp, Inc., 2006) | 7 |
| Figure 2.7: Stud Connection with Expanding Foam (Composite Advantage, 2006) | 7 |
| Figure 2.8: J-Bolt Connection (Strongwell, 2006) | 7 |
| Figure 2.9: Possible Clip Connections (Zellcomp, Inc., 2006) | 8 |
| Figure 2.10: Typical Shear Stud Deformation after Test (Righman, et al., 2004) | 8 |
| Figure 2.11: Types of Panel-to-Panel Connections (Telang, et al., 2006) | 9 |
| Figure 2.12: Mechanical Fasteners for Panel to Panel Connections and Top Plate Connection (Zhao, 2006) | 9 |
| Figure 2.13: Test of Concrete Barrier (left) and Steel Rail (right) (Toillion, 2001) | 11 |
| Figure 2.14: Guide rail and Connection to Deck (Nystrom, et al., 2002) | 12 |
| Figure 2.15: Failure of FRP Face at Loading Plate (Camata and Shing, 2004) | 12 |
| Figure 2.16: Simulated Tire Patch (Cousins and Lesko, 2004) | 12 |
| Figure 2.17: Punching Shear due to Steel Plate (left) and Surface Cracking for Simulated Tire Patch (Cousins and Lesko, 2004) | 13 |
| Figure 2.18: Delamination (a) and Buckling of Core (b) for honeycomb sandwich panel (Nystrom, et al., 2002) | 13 |
| Figure 2.19: Plan View of Test Set-up for O'Fallon Park Bridge (Camata and Shing, 2004) | 14 |
| Figure 2.20: Loading for O'Fallon Park Bridge (Camata and Shing, 2004) | 14 |
| Figure 2.21: Test Specimen for Plate and Tube FRP deck (Cousins and Lesko, 2004) | 14 |
| Figure 2.22: Delamination of Bottom Flange (left) and Web Failure (right) for Zellcomp Deck (Zhao, 2006) | 15 |
| Figure 2.23 KSCI Deck Cross-Section (Righman, 2004) | 16 |
| Figure 2.24: Tongue and Groove Connection | 16 |
| Figure 2.25: Direction of KSCI Panels with Respect to Bridge Girders | 16 |
| Figure 2.26: Sketch of Panel to Girder Connection | 16 |
| Figure 2.27: Picture of Panel to Girder Connection | 17 |
| Figure 2.28: Resin Infused Mechanical Fasteners | 17 |
| Figure 2.29: ZellComp Deck Cross-Section | 17 |
| Figure 2.30: Grouted-in-Place Stud Connection | 17 |
| Figure 2.31: Fiber Properties for the ZellComp Deck | 18 |
| Figure 3.1: Serviceability Criterion | 18 |
| Figure 3.2: Service Deflection criteria per Ontario code (Ministry 1992) | 19 |
| Figure 3.3 Criteria for human response to acceleration (Ministry 1995) | 19 |
| Figure 3.4: Elevation View of Bridge Deck Model + Loading | 20 |
| Figure 3.5: FRP deck-on-steel girder bridge cross-sections of models 1,2,3, and 4 | 22 |
| Figure 3.6: FRP deck-on-steel girder bridge cross-sections of models 5,6,7, and 8 | 22 |
| Figure 3.7: FRP deck-on-steel girder bridge cross-sections of models 9,10,11, and 12 | 22 |
| Figure 3.8: Schematic of the applied moving load model | 24 |
| Figure 3.9: Acceleration history and frequency response between girders of model 2 | 24 |

| | |
|--|----|
| Figure 3.10: Experimental over numerical peak acceleration ratios | 25 |
| Figure 3.11: Steel tube FE model: 36 inch overhang/48 inch tube spacing | 28 |
| Figure 3.12: Steel plate and steel tube summary: 36 inch overhang | 29 |
| Figure 3.13: KSCI cross section (left) and plan view (right) | 29 |
| Figure 3.14: Face sheet stiffness/honeycomb core stiffness study results | 30 |
| Figure 3.15: Steel deck core FE model comparison | 31 |
| Figure 3.16: Vulcraft 1.5A hexagonal honeycomb core unit cell | 31 |
| Figure 3.17: W-direction hybrid beam honeycomb core (plan view) | 32 |
| Figure 3.18: Typical beam test setup and components (drawings and photo) | 33 |
| Figure 3.19: L-direction beam core shear stress vs. strain summary | 34 |
| Figure 3.20: W-direction beam core shear stress vs. strain summary | 35 |
| Figure 4.1: Wild Cat Creek Bridge Existing and Proposed Cross-Sections | 37 |
| Figure 4.2: KSCI Sample Panel #1 | 38 |
| Figure 4.3: KSCI Panel 2 Setup | 39 |
| Figure 4.4: Picture of Retrofitted Connection for KSCI #P2 | 39 |
| Figure 4.5: Schematic of KSCI #P3 Test Setup | 39 |
| Figure 4.6: Picture of KSCI #P1a Test Setup | 40 |
| Figure 4.7: Picture of KSCI #P1b Test Setup During Loading | 40 |
| Figure 4.8: Picture of KSCI Panel 3 (KSCI #P3) Test Setup | 41 |
| Figure 4.9: Schematic of Instrumentation for KSCI Panel 1 – KSCI #P1a Test | 42 |
| Figure 4.10: Schematic of Instrumentation for KSCI Panel 1 – KSCI #P1b Test | 43 |
| Figure 4.11: Schematic of Instrumentation for KSCI Panel 2 – KSCI #P2 Test | 44 |
| Figure 4.12: Total Load vs. Overhang Deflection near Joint (LVDT 4O) – KSCI #P1a Test | 45 |
| Figure 4.13: Total Load vs. Top Panel Longitudinal Strains – KSCI #P1a Test | 45 |
| Figure 4.14: Longitudinal Joint Damage at Overhang at 50-kips Total Load – KSCI #P1a Test | 46 |
| Figure 4.15: View of Longitudinal Joint Damage at Overhang – KSCI #P1a Test | 46 |
| Figure 4.16: View of Longitudinal Joint; Top Plate Removed – KSCI #P1a Test | 47 |
| Figure 4.17: View of Longitudinal Joint; Side Removed, Showing Voids – KSCI #P1a Test | 47 |
| Figure 4.18: Bottom Panel Longitudinal Strains – KSCI #P1b Test | 48 |
| Figure 4.19: KSCI #P1b Test Specimen Damage at Longitudinal Joint Under Loading Beam | 48 |
| Figure 4.20: KSCI #P1b Test Specimen at Maximum Applied Load | 49 |
| Figure 4.21: KSCI #P2 Test Specimen Total Load-Deflection Plot | 49 |
| Figure 4.22: East side of the panel: $1 \frac{3}{8}$ " (total gap) – $\frac{1}{2}$ " (neoprene thickness) = $\frac{7}{8}$ " | 49 |
| Figure 4.23: Opening at West Side of FRP Panel: $1 \frac{1}{4}$ " (total gap) – $\frac{1}{2}$ " (neoprene thickness) = $\frac{3}{4}$ " | 50 |
| Figure 4.24: Experimental Load-Horizontal Translation of Deck-to-Girder Connection (Machado, 2006) | 50 |
| Figure 4.25: Detail of the Stud Connector After Test | 50 |
| Figure 4.26: Initial Portion of Experimental Load-Horizontal Translation Deck-to-Girder Connection (Machado, 2006) | 50 |
| Figure 5.1: Existing Sugar Creek Bridge Cross Section | 51 |
| Figure 5.2: Rehabilitated Sugar Creek Bridge Cross Section | 51 |
| Figure 5.3: Section View at Grouted Haunch | 52 |
| Figure 5.4: Section View Showing Shear Studs in Grout Pockets | 52 |

| | |
|---|----|
| Figure 5.5: Section View at Crown Connection | 53 |
| Figure 5.6: Bridge Cross Section | 53 |
| Figure 5.7: Cut at Center of Bottom Section | 53 |
| Figure 5.8: Kerf-cut at Center Top Plate (Test #1) | 53 |
| Figure 5.9: (a) & (b) Views of the Panel to Panel Connection; (c) Panel to Panel Connection with Screws | 54 |
| Figure 5.10: Epoxy-infused Screws | 54 |
| Figure 5.11: Layout of Top Plates | 54 |
| Figure 5.12: Deck to Girder Connectors (embedded in non-shrink epoxy grout) | 55 |
| Figure 5.13: Epoxy-infused Screws Connecting Top Plate to Bottom Section | 55 |
| Figure 5.14: ZellComp Specimen with Braced Spreader Beam | 55 |
| Figure 5.15: Instrumentation Plan | 56 |
| Figure 5.16: Instrumentation (view in the mirror placed on the floor) | 56 |
| Figure 5.17: TS Load 1 & TS Load 2 vs Total Load | 57 |
| Figure 5.18: TS-CL & TN-CL vs Total Load | 58 |
| Figure 5.19: T-CL 1 & T-CL 2 vs Total Load | 58 |
| Figure 5.20: BN Load 1,2,3,4 & BS Load 1,2,3,4 vs Total Load | 59 |
| Figure 5.21: TS Load 1,2 & BS Load 1,2 vs Total Load | 60 |
| Figure 5.22: SAP 2000 Inflection Point Analysis | 60 |
| Figure 5.23: Zones Utilized to Calculate the Inflection Point | 61 |
| Figure 5.24: Strain vs. Length (Section 3a) | 61 |
| Figure 5.25: Strain vs. Length (Section 4a) | 62 |
| Figure 5.26: Strain vs. Length (Section 3b) | 62 |
| Figure 5.27: Strain vs. Distance (Section 4b) | 63 |
| Figure 5.28: Deflection vs. Total Load | 63 |
| Figure 5.29: TS Load 1 & TS Load 2 vs Total Load | 64 |
| Figure 5.30: T-CL 1, T-CL 2 & T-CL 3 vs Total Load | 64 |
| Figure 5.31: TS-CL & TN-CL vs Total Load | 65 |
| Figure 5.32: BN Load 1,2,3,4 & BS Load 1,2,3,4 vs Total Load | 66 |
| Figure 5.33: TS Load 1, 2 & BS Load 1, 2 vs Total Load | 66 |
| Figure 5.34: Rosette S. Load - E. Web vs Total Load | 67 |
| Figure 5.35: N. Load - W. Web vs Total Load | 67 |
| Figure 5.36: Deflection vs. Total Load | 68 |
| Figure 5.37: Loading for Wearing Surface Test | 71 |
| Figure 5.38: Placement of Top Plates in Wearing Surface Specimen | 72 |
| Figure 5.39: Wearing Surface Specimen in Loading Frame | 72 |
| Figure 5.40: Instrumentation of Wearing Surface Specimen | 72 |
| Figure 5.41: Reference String Lines on Both Sides of Wearing Surface Specimen | 73 |
| Figure 5.42: Crown Connection Crack in Wearing Surface | 73 |
| Figure 5.43: Dishing Deformation at the Load Patch | 73 |
| Figure 5.44: Schematic of Web Buckling | 73 |
| Figure 5.45: Damage to Deck Webs Under Load Patch | 74 |

| | |
|--|----|
| Figure 5.46: Failure of Steel Disk to Wearing Surface in Test Specimen #4 | 74 |
| Figure 5.47: Failure of Steel Disk to Wearing Surface in Test Specimen #5 | 74 |
| Figure 5.48: Failure of Steel Disk to Wearing Surface in Test Specimen #6 | 75 |
| Figure 5.49: Plan View of FRP Deck Layout | 75 |
| Figure 5.50: View of Bottom Deck Sections | 76 |
| Figure 5.51: View of Girders Prepared with Angles for Grouted Haunches | 76 |
| Figure 5.52: Placement of an FRP Deck Panel on Girders | 76 |
| Figure 5.53: Placement of an FRP Deck Panel on Girders | 76 |
| Figure 5.54: Bottom FRP Deck Sections at Crown Connection with Holes for Shear Studs | 76 |
| Figure 5.55: Splice Plates at the Crown Connection (Abutment Reinforcement in Foreground) | 76 |
| Figure 5.56: Reinforcement and Shear Studs at Guardrail Location | 77 |
| Figure 5.57: Shear Studs and Foam Dams for Grout Pockets | 77 |
| Figure 5.58: Tube to Allow Water to Flow Through Pocket After Grouted | 77 |
| Figure 5.59: Foam Dams in Place at Girder Lines and Guardrail Connection Locations | 77 |
| Figure 5.60: Placement of Grout in Shear Stud Grout Pocket | 77 |
| Figure 5.61: Grout Pockets After Grout Placed | 77 |
| Figure 5.62: Placement of FRP Top Plate | 78 |
| Figure 5.63: Protective Tarp on Deck Without Wearing Surface; Work on Approach Spans | 78 |
| Figure 5.64: Finished Bridge with Wearing Surface and Guardrails | 78 |
| Figure 5.65: Steel Angle Protecting End of Deck from Vehicle Impact Off of Approach Span | 78 |
| Figure 5.66: Guardrail and Sugar Creek | 78 |
| Figure 6.1: Acoustic Emission Sensors on FRP Sandwich Beam for Pencil Test | 80 |
| Figure 6.2: Top Plate and Longitudinal Joint on ZellComp Deck Specimen | 81 |
| Figure 6.3: Acoustic Emission Sensor Positions for Passive Tests on Damaged Zellcomp Deck | 81 |
| Figure 6.4: Acoustic Emission Data for Passive Tests on Damaged Zellcomp Deck, Flanges | 82 |
| Figure 6.5: Acoustic Emission Data for Passive Tests on Damaged Zellcomp Deck, Webs | 82 |
| Figure 6.6: Acoustic Emission Test on Tension Coupon | 83 |
| Figure 6.7: Acoustic Emission Sensor Locations (Circles) on Tension Coupon | 83 |
| Figure 6.8: Tension Coupon (Fibers Longitudinal) After Test | 83 |
| Figure 6.9: Tension Coupon (Fibers Transverse) After Test | 84 |
| Figure 6.10: Acoustic Emission Duration vs. Amplitude Results for Tension Coupon | 84 |
| Figure 6.11: Acoustic Emission Output for Tension Coupon | 84 |
| Figure 6.12: Acoustic Emission Output for Tension Coupon | 85 |
| Figure 6.13: Acoustic Emission Sensors on NCHRP Wearing Surface Specimens | 85 |
| Figure 6.14: NCHRP Wearing Surface Specimen Load Cycle | 86 |
| Figure 6.15: NCHRP Wearing Surface Specimen With Acoustic Emission Sensors | 86 |
| Figure 6.16: NCHRP Wearing Surface Specimen With Acoustic Emission Sensor Locations and Pencil Break Locations | 86 |
| Figure 6.17: NCHRP Wearing Surface Specimen Acoustic Emission Amplitudes After 12 Load Cycles | 87 |
| Figure 6.18: NCHRP Wearing Surface Specimen Acoustic Emission Amplitudes After 23 Load Cycles | 88 |
| Figure 6.19: Heating Specimen (Left) and Taking Image with Thermographic Camera (Right) | 89 |
| Figure 6.20: "Hot Spot" at Delamination Captured by Thermographic Camera | 90 |

| | |
|---|----|
| Figure 6.21: Delamination Between Wearing Surface and FRP Plate | 90 |
| Figure 6.22: Pocket Acousto-Ultrasonic Device | 90 |
| Figure 6.23: Sample Acousto-Ultrasonic Output (a) and (b) | 91 |
| Figure 6.24: Graphic of Acoustic-Ultrasonic Wave Reflected in a Composite | 91 |
| Figure 6.25: Acoustic-Ultrasonic Pulser and Receiver Set-Up To Test Detection of Hole in Top of Flange of ZellComp Deck Section | 91 |
| Figure 6.26: Acoustic-Ultrasonic Pulser and Receiver Set-Up To Test Detection of Simulated Delamination in Flange of ZellComp Deck Section | 92 |
| Figure 6.27: Acoustic-Ultrasonic Pulser and Receiver Set-Up To Test Detection of Simulated Delamination in Flange of ZellComp Deck Section | 92 |
| Figure 6.28: ABAQUS Analysis of FRP Top Plate Deflections Longitudinal and Transverse to Truck Travel Direction | 92 |
| Figure 6.29: ABAQUS Results of FRP Top Plate Deflections Longitudinal to Truck Travel Direction for Reductions in Web Stiffness | 93 |
| Figure 6.30: Summary of ABAQUS Results of FRP Top Plate Deflections Longitudinal and Transverse to Truck Travel Direction for Reductions in Web Stiffness | 93 |
| Figure 6.31: Truck with Part of Frame Attached at Rear Wheel | 94 |
| Figure 6.32: Truck with Deflection Frame Attached at Rear Wheel, Stopped at End of Bridge | 94 |
| Figure 6.33: Truck with Deflection Frame Attached at Rear Wheel, at End of Path | 94 |
| Figure 6.34: Layout of LVDTs for Deflection Frame | 95 |
| Figure 6.35: Plan View of Bridge Deck with Grouted Sections Shaded | 95 |
| Figure 6.36: Deflection vs. Position on Bridge, Pots 1,6 and 11 | 96 |
| Figure 6.37: Deflection vs. Position on Bridge, Pots 4,9 and 14 | 96 |

EXECUTIVE SUMMARY

FIBER REINFORCED POLYMER BRIDGE DECKS

Introduction

A number of researchers have addressed the use of Fiber Reinforced Polymer (FRP) deck as a replacement solution for deteriorated bridge decks made of traditional materials. The use of new, advanced materials such as FRP is advantageous when the bridge is load-rated and much of the weight of the superstructure can be reduced with installation of a new deck without replacing the beams thus providing a quick and economical solution. Studies have shown that the use of fiberglass decks can reduce the life cycle cost of a bridge from 10% to 30% over the design life of the bridge, due to less traffic impact during construction and reduction in maintenance (e.g., corrosion resistance). These advantages were a motivation for this study of the use of FRP as a possible solution for the replacement of deteriorated bridge decks.

The overarching goal of this study was to perform a comprehensive evaluation of various issues related to the strength and serviceability of FRP deck panels. Specific objectives were to establish critical limit states to be considered in the design of FRP deck panel, to provide performance specifications to designers, and to develop evaluation techniques for the FRP bridge deck panels in service. Results of the study were applied to rehabilitation of a Tippecanoe County bridge with an FRP deck.

Findings

- Serviceability criteria, or deflection limits, govern the design of FRP decks. However, the limits typically used for bridge decks may not be applicable to FRP decks because of their relative light weight, low stiffness, and resulting difference in vibration response. A couple of side studies were conducted on this issue of deflection limits, as well as a small literature review. One side study investigated the development of an alternative criterion based on the dynamic response of the FRP decks. Another investigated a hybrid GFRP-steel solution, providing a deck with much higher shear stiffness in the core. Meanwhile, one suggestion made later in the project for the actual case study bridge was a deflection limit between girders of span/500, based on expected strains in the deck and wearing surface and an attempt to minimize cracking of the wearing surface in the negative moment region over girders.
- The case study bridge, CR 900 E. over Sugar Creek, was studied for use of a fiber reinforced polymer (FRP) deck for bridge rehabilitation and deck widening. The 2% cross slope on the deck was to be built into the FRP deck installation;

the crown connection was one of a number of concerns that were studied experimentally. The FRP deck was installed on the Sugar Creek Bridge in November 2009.

- The FRP deck was subjected to a number of tests, primarily to evaluate any issues with the crown connection. Test results demonstrated that a special joint would be needed at the crown to prevent moisture ingress. Results also demonstrated that the deck design was adequate. The ultimate failure mode, at a factor of safety of approximately 5, was web buckling.
- A number of non-destructive evaluation methods were considered for monitoring of the FRP deck in service. Of the various technologies, acoustic emission appeared to be the most promising. Passive tests on damaged specimens, acoustic emission tests on FRP deck specimens as they were loaded, and acoustic emission tests on FRP coupons as they were loaded showed different frequencies, amplitudes and durations for different failure modes and proximity to damaged locations. However, some limitations to acoustic emission include the inability of the acoustic waves to traverse joints between FRP deck panel sections, as well as the connection between the top plate and bottom section of the FRP deck. Therefore, use of acoustic emission would be labor intensive, requiring measurements at regular and frequent intervals along the deck, between deck joints.
- Infrared thermography also appeared to be promising for identifying delamination between the wearing surface and the FRP top plate. However, use of the infrared thermographic camera would also be labor intensive, requiring heating of small sections of deck at a time and then quickly taking the thermographic image. Furthermore, results would show variability with amount of heating and cooling before the image is acquired.
- Meanwhile, a traveling truck deflection measurement method was developed. This procedure was tested on the FRP deck after installed on the Sugar Creek Bridge. This method showed some promise, but also showed variability and sensitivity to small variations in the surface of the deck. It is believed that this method would be successful at locating severe damage of the webs, as deflection measurements would show marked increases local to the damage. However, further validation and baseline measurements on the FRP bridge deck with the wearing surface are required if this method is to be pursued.

Implementation

Items to be implemented include design procedures as related to deflection limits, crown connection details, and guardrail details. Inspection and monitoring procedures may also be implemented.

INDOT design and inspection personnel are recommended to be involved in the implementation of the findings of this study.

CHAPTER 1. INTRODUCTION

1.1 Background & Motivation

A number of researchers have addressed the use of Fiber Reinforced Polymer (FRP) deck as a replacement solution for deteriorated bridge decks made of traditional materials. The use of new advanced materials such as FRP is advantageous when the bridge is load-rated and much of the weight of the superstructure can be reduced with installation of a new deck without replacing the beams thus providing a quick and economical solution. The ability to make a quick installation reduces the inconvenience that detours will bring to people in the area. Studies have shown that the use of fiberglass decks can reduce the life cycle cost of a bridge from 10% to 30% over the design life of the bridge, due to less traffic impact during construction and reduction in maintenance (e.g., corrosion resistance) (Cassidy, 2000). These advantages were a motivation for this study of the use of FRP as a possible solution for the replacement of deteriorated bridge decks.

1.2 Objectives & Scope

The overarching goal of this study was to perform a comprehensive evaluation of various issues related to the strength and serviceability of the FRP deck panels that are available in the industry. Specific objectives were to establish critical limit states to be considered in the design of FRP deck panel, to provide performance specifications to designers, and to develop evaluation techniques for the deck panels in service.

Two different FRP panels were studied during the research project: a sandwich panel manufactured by Kansas Structural Composites, Inc. (KSCI) and a pultruded panel manufactured by ZellComp, Inc. The KSCI panel was initially selected for the rehabilitation case study bridge. However, for a variety of reasons outside of the scope of this study, both the KSCI panel and the initial case study bridge were dropped from consideration. A new case study bridge was selected, and new proposals from FRP deck manufacturers were solicited. At this time, the ZellComp deck was selected. Analysis and experimental results related to both FRP deck panels are included in this report, as information from both decks is relevant to the overarching goal of this study.

1.3 Methodology

The studies performed, which will be described in this report, included analytical studies as well as experimental work. Before any test was conducted, a comprehensive literature review of the FRP panels and their studied performance was conducted. After the literature review was completed, two different panels were evaluated; one of those panels was selected to replace a concrete deck of a bridge in Tippecanoe County. Evaluations included finite element analysis

and parametric studies to establish guidelines related to serviceability limits for FRP decks, load tests on critical components of the FRP decks, and small-scale tests to determine viable non-destructive evaluation techniques for the FRP decks. Additional in-situ experiments were conducted on the selected FRP deck panel after installation on the bridge. The various analyses and experiments will be described in detail in the following chapters.

1.4 Organization

Chapter 1 provides an introduction of the study as well as background information and the motivation for the research. It also offers a brief description of the methodology.

Chapter 2 presents a brief description of FRP panels in general, as well as the different manufacturing techniques. It also describes in more detail the two different FRP panels studied in depth for this research.

Chapter 3 provides answers to one of the biggest concerns with FRP deck designs: serviceability issues. This chapter provides a brief description of the serviceability design criteria currently used and how they can be implemented for FRP decks. It also shows numerical analyses and parametric studies conducted, as well as experimental work on a concept that could be used to modify an FRP panel in order to make it stiffer.

Chapter 4 presents one of two case study bridges that were considered during this project for rehabilitation with FRP panels. For this bridge, over WildCat Creek in Tippecanoe County, the KSCI panel was considered. Chapter 4 presents all of the analytical and experimental work conducted for this case study bridge using the KSCI panel.

Chapter 5 presents the second case study bridge that was considered for rehabilitation with an FRP deck. This bridge runs over Sugar Creek in Tippecanoe County. Chapter 5 illustrates all of the analytical and experimental work conducted for this case study using the ZellComp, Inc. panel. Also included in Chapter 5 is a summary of the installation of the FRP deck on the Sugar Creek Bridge.

Chapter 6 provides an overview of different non-destructive monitoring techniques that were considered for evaluation of the performance of the FRP panels once in service and provides guidelines on how to monitor the FRP deck once in place. A description of in-situ tests on the Sugar Creek Bridge is also included.

Chapter 7 provides a summary and highlights the most important conclusions of the study.

CHAPTER 2. FIBER REINFORCED POLYMER DECKS

2.1 General

A number of FRP panels have been in the bridge deck market. Each one of them has its unique characteristics. This chapter shows a brief description of the different manufacturing techniques most commonly used and

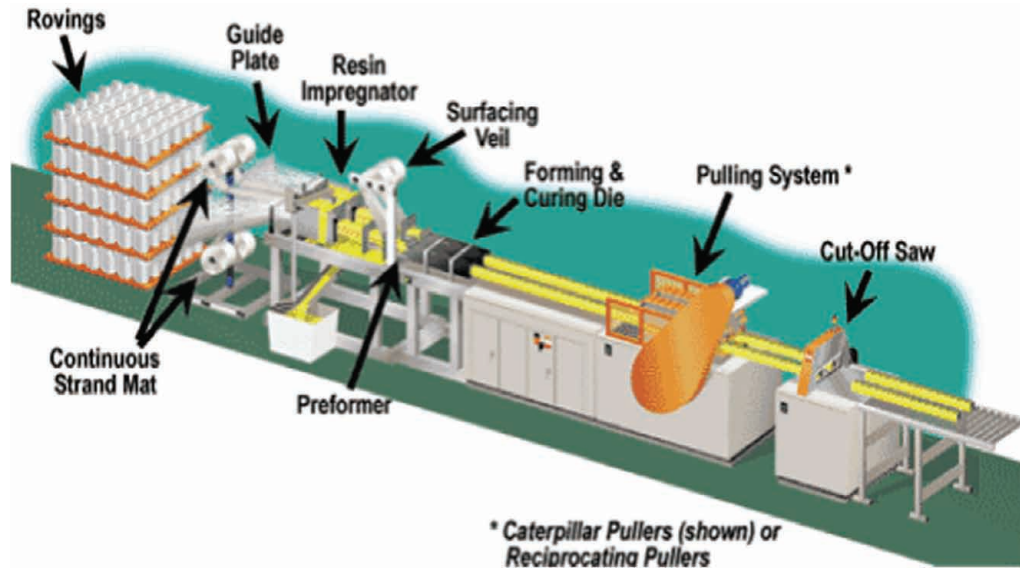


Figure 2.1: Pultrusion Process (<http://www.afpiberglass.com/images/pultrusionProcess.jpg>)

describes in more detail the two panels studied. Meanwhile, various issues have been observed with installed FRP decks, such as leakage of joints, delamination of wearing surface and FRP, inadequate stiffness, and lack of methods for identifying damage in service. These observations have motivated some of the objectives of this study.

2.2 Manufacturing Techniques

Fiber reinforced polymer bridge decks can be manufactured by various processes which include pultrusion, vacuum assisted resin transfer molding (VARTM) and hand lay-up. The pultrusion process consists of pulling resin impregnated reinforcement fibers through a machine to create a structural member (Figure 2.1). The pultrusion process can be used to produce channels, I-shaped and other such sections. The VARTM method consists of using pressure to introduce resin into a sealed mold which has the fiber reinforcement inside (Figure 2.2). VARTM is more typically seen for molded shapes such as boat hulls. The hand lay-up technique consists of layering of fiber mats

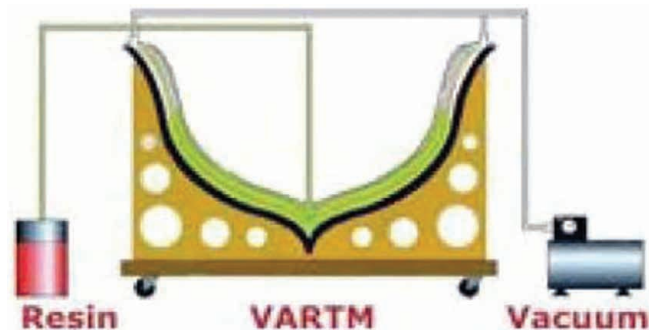


Figure 2.2: VARTM process (http://www.precisioneering.com/images/laminating_methods/vartm.jpg)

and resin by hand; this method is typically used to fabricate sandwich panels which consist of face skins and a center core (Figure 2.3).

For this study, an FRP sandwich panel manufactured by the hand lay-up technique and an FRP deck produced by pultrusion were studied. The panels used were from Kansas Structural Composites Inc. and ZellComp, Inc. Although specimens from these specific manufacturers were investigated, the basic principles used could also form the basis of evaluation of other FRP panels.

2.3 Key Issues for Implementation of Fiber Reinforced Polymer Decks

In NCHRP Report 503, “Application of Fiber Reinforced Polymer Composites to the Highway Infrastructure,” the state-of-the-art is evaluated, with the objective of developing a strategic plan for “guiding the implementation of FRP composite materials in the highway infrastructure.” Mertz et al. (2003) cite the benefits of high strength-to-weight ratio, corrosion resistance, and excellent fatigue resistance. The authors believe that increased use of FRP could make the



Figure 2.3: Hand Lay-Up Process

material competitive with traditional construction materials. However, Mertz et al. (2003) also identify the need for development of design specifications, as well as development of documentation and training for engineers, fabricators, and contractors. They cite the lack of prescriptive bridge design provisions as a barrier to implementation of FRP.

The major advantages for use of FRP bridge decks are noted as reduced weight, environmental durability, and speed of installation. Reduced deck dead load provides the potential for an increased load rating for a bridge. FRP is corrosion resistant, and FRP decks “should not be affected by road salts and chlorides from seawater (Mertz et al., 2003).” Therefore, reduced life-cycle costs should be realized. Finally, the light weight and pre-fabricated nature of FRP bridge decks means that the FRP decks can be installed in considerably less time than for a traditional bridge deck.

Meanwhile, among the disadvantages listed are problems with durability of the wearing surface and serviceability issues related to the deck joints. The authors note cases in which significant reflective cracking of the wearing surface was observed. They believe the cracking to be due to local flexibility of the FRP decks. For problems with the deck joints, the authors point towards the Salem Avenue Bridge which used four different deck types. Further discussion of wearing surface and serviceability issues and joints are discussed in sections to follow.

As mentioned previously, codes and specifications for FRP bridge decks are lacking. Mertz et al. (2003) note that most of the field applications to date have been designed using project-specific research, and have often relied upon manufacturer data or guidelines. Further discussion of specifications brings up one of the supposed benefits of FRP composites: the ability to tailor the fibers, fiber architecture, and resins to suit any need. However, this creates difficulty in development of standard guidelines and specifications. Furthermore, FRP decks are typically based on patented technologies, and the proprietary nature of these decks is a hindrance. “The interchangeability of manufacturers’ products is not apparent, and this seems to be intentional (Mertz et al., 2003).” This last statement was referring to the fibers and resins, but is applicable to deck sections as well. In NCHRP Report 564, “Field Inspection of In-Service FRP Bridge Decks,” the authors noted that there were six major deck types in service at the time of their survey. “Each of these deck types has unique cross-sectional geometry, material characteristics, manufacturing processes, and behavior. The deck designs are typically proprietary, and each type of deck is manufactured using specialized material and fabrication methods (Telang, et al., 2006).”

Telang et al. (2006) elaborated further on the key issues related to the variety of FRP deck types, including difficulty in establishing a uniform quality and performance standard, variability in types and locations of critical details, and inadequate testing and performance assessment. Materials, subcomponents,

and manufacturing methods lead to variations in quality. Connections between subcomponents vary greatly, as well. Variations in types and locations of critical details result in different limit states and considerations for each type of deck. Furthermore, without standards, any detail can be easily changed, further hampering proper, rigorous testing and evaluation procedures.

For various reasons as stated, “applying FRP composites to the bridge infrastructure in individual demonstration projects has resulted in a quite fragmented effort, with little overlap or interaction between projects. Aside from scholarly journal articles, which typically appear long after project completion, and conference presentations, in which details are sketchy, the sharing of findings is virtually nonexistent. The projects have no continuity or common goal (Mertz et al., 2003).”

Mertz et al. (2003) also comment about the use of performance-related specifications (PRS) instead of prescriptive specifications. “The technical and cultural issues associated with PRSs make it improbable that such a large change in engineering design will become commonly practiced in the foreseeable future. However, using PRSs would require a different level of knowledge about materials among bridge owners. This might relieve concerns about working with newer materials, such as FRP, with which the bridge community is relatively inexperienced.”

2.3.1 Existing FRP decks

A survey of FRP deck manufacturers reveals nine producers. However, to the authors’ knowledge, there remain only four still looking towards new bridge deck projects. These are Zellcomp, Inc., Composite Advantage, Strongwell, and Kansas Structural Composites, Inc. (KSCI).

Figure 2.4, based on Telang et al. (2006), summarizes these manufacturers and deck types.

2.3.2 Condition of FRP Bridge Decks in Service

In NCHRP Report 564, Telang et al. (2006) note that much of the construction of FRP vehicular bridge decks has taken place between 1999 to 2001. There were 83 FRP decks at the time of the survey. The average age of these FRP decks was less than 5 years. However, bridge owners have noted a number of concerns and problems, including the joints between FRP deck panels, wearing surfaces, haunch supports, curbs and parapets, approach joints, deck-to-stringer connectors, delamination of deck components, and moisture ingress.

Joints between panels are a concern because of leakage observed between deck panels, resulting in corrosion of steel girders underneath. It was implied that joints with FRP or other strips adhered to the tops of the joints were not immune to this problem. For the wearing surfaces, delamination and debonding of thin



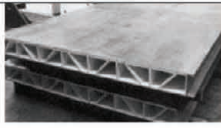

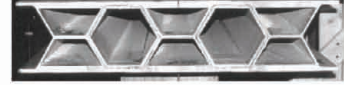
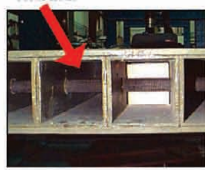



| Manufacturer | Deck Description | Number of Bridges | Deck Cross Section |
|---|--|---|---|
| Kansas Structural Composites, Inc. (KSCI) | Sandwich deck with honeycomb core; hand lay-up | 12 installations, first in 1996, most recent in 2003 |  |
| Infrastructure Composites, Inc. (ICI) | Sandwich deck with honeycomb core | 1 installation in U.S., also in Europe |  |
| Martin Marietta Composites, Inc. (MMC) | Duraspan deck system with trapezoidal cross section; pultruded | 27 installations, first in 1996, most recent in 2004 |  |
| Hardcore Composites | Sandwich deck with foam box core (VARTM) | 26 installations, first in 1997, most recent in 2002 |  |
| Creative Pultrusions, Inc. | Superdeck with pultruded hexagonal sections | 9 installations; first in 1997, most recent in 2002 |  |
| Strongwell | Pultruded tube and plate configuration with steel rods through tubes. | Estimated 3 installations, earliest in 1995, latest in progress |  |
| Zellcomp, Inc. | Pultruded two-part open system, bottom portion with separate top plate, all mechanical fastening | 2 - 3 in progress as of 2007 |  |
| Bedford Reinforced Plastics | Prodeck pultruded deck section | At least 1 installation |  |
| Composite Advantage | TYCOR sandwich with foam core (resin infusion molded) deck. | Estimated 2 installations as of 2006; Wright-Patterson AFB. & bridge in Summit Co., OH. |  |

Figure 2.4: FRP Deck Manufacturers and Types (adapted from Telang, et al., 2006)

epoxy overlays had also been observed. Uneven seating of FRP decks on haunch supports is a concern because of the potential for impact between the deck and haunch due to vehicular traffic. Connections of curbs and parapets to FRP decks and, in particular, effects on the decks from impact and damage to curbs and parapets, are also a concern. Approach joints and proper transitioning from the FRP deck to the approach slabs are problem areas, as well. The deck edge must be stiffened at this location, sometimes by filling a portion of the deck across the width of the bridge. Meanwhile, deck-to-stringer connectors ranging

from clip connections to shear studs have been used. Understanding of the behavior of these connections is limited. Delamination of skin sheets from the deck core has been noted in some cases. Finally, moisture ingress is a concern for FRP, not because of the material resistance, but because freeze-thaw could possibly result in mechanical damage.

2.3.3 Stiffness / Deflections

Stiffness is a significant design issue for FRP bridge decks. Due to the relatively low modulus of the FRP,

deflections govern the design of FRP decks. Furthermore, vibration characteristics of FRP decks have been shown to be drastically different than those of conventional reinforced concrete bridge decks, necessitating a reevaluation of deflection criteria.

Hayes et al. (2000) conducted tests on a tube and plate fiberglass composite bridge deck. This deck was to be a replacement deck for the existing steel grate deck on the Schuyler Heim lift span bridge in Long Beach, California. A 1.22 m × 4.27 m × 121-mm thick prototype deck section, supported on steel beams, was tested. The measured deflections were on the order of the span length divided by 300, nearly three times the criteria for bridge decks. Clearly, deflections would control the design of the deck. Furthermore, the transverse strains were almost as large as the longitudinal strains.

Similar problems were observed on the Stelzer Road bridge replacement in Ohio (Wolfe et al., 2003). One span of a 4-lane, 6-span bridge was replaced with post-tensioned, concrete filled FRP tube deck, the other, conventional reinforced concrete deck. The fiber reinforced system (FRS) deck was designed for an HS20 truck. The maximum allowable dead load strain was limited to 10% of the ultimate strain. Loads included 60 psf of future wearing surface overlays. Factored loads were predicted to reach less than 50% of the ultimate load capacity for the FRS for flexure, and less than 45% of the ultimate capacity in shear.

Tests on the coefficient of thermal expansion were conducted on FRP samples in environmental chambers. The coefficient of thermal expansion was found to be four times higher than that of concrete (and the target value). These tests suggested problems with the bond and interaction between the FRP and concrete, as well as the FRP and wearing surface. Meanwhile, the polyester resin used experiences a loss in stiffness of 19% over the temperature range from 77 to 122°F (25 to 50°C). Three-point bend tests on the small scale FRP tubes under loading also showed that the stiffness of the tube decreased 23% over the temperature range from 71 to 130°F.

Meanwhile, in field tests, the FRP deck deflected 57% more than the concrete deck. Under normal traffic conditions, deflections were on average 56% more for the FRP deck. When the outdoor temperature reached above 50°F the bridge deflected an average of 91% more than its concrete counterpart. With temp at 38°F or less the FRP still exhibited deflections more than 15% higher than in the concrete (Wolfe, et al., 2003). It should be noted that the post-tensioned, concrete-filled FRP tube configuration may have also contributed to the higher deflections.

There remains a lack of rational live-load deflection criteria for FRP bridge decks. Because of the relatively low modulus of elasticity of glass FRP (GFRP), which is the most common because of its also relatively low cost compared to carbon fibers, for example, deflections govern the design of FRP bridge deck applications. However, this results in deck sections much larger

than those required for strength. Certainly, “better economy could be achieved if the criteria could be liberalized (Mertz et al., 2003).”

A number of authors have suggested alternative serviceability criteria to the AASHTO LRFD interim 2005 (2005) static deflection criteria (Wright and Walker, 1971; DeWolf, Kou, and Rose 1986; Demitz et al. 2003). These studies are mainly concerned with controlling undesirable vibrations of bridges, including concrete slab-on-girder bridges and self-supported FRP deck bridges. Some authors have established new limits for static deflections, while others have proposed empirical formulations for calculating maximum acceleration response as a function of the first bending modal frequency of the bridges. Machado (2006) proposed an alternative serviceability criterion based on the bridge vertical acceleration response to traffic and human tolerance to vibrations, while considering torsional modes. Numerical analyses conducted by Machado (2006) confirmed that a non-composite FRP deck-on-steel girder bridge has different vibration characteristics than a composite RC deck-on-steel girder bridge of similar geometry. More detail on the Machado (2006) study will be presented in Chapter 3. The same conclusion has been stated by Cai et al. (2006), who studied the difference in vibration response between a self-supported FRP deck bridge and a simply-supported RC deck bridge. On a related topic, one deck system for the Salem Avenue Bridge project had experimentally obtained impact factors which were found to exceed specified AASHTO limits. (Reising et al., 2004).

2.3.4 Deck to Girder Connections

As mentioned previously, the types of connections vary widely, from clip-type connections to grouted shear stud connections to threaded stud-clamp connections. Some details of these connections are shown in Figure 2.5 to Figure 2.9. In some cases (Figure 2.7), the grout might be replaced with expanding foam (Composite Advantage, 2006).

A number of tests have been conducted on the deck-to-girder connections. However, these tests have provided information mostly on the ultimate capacity,

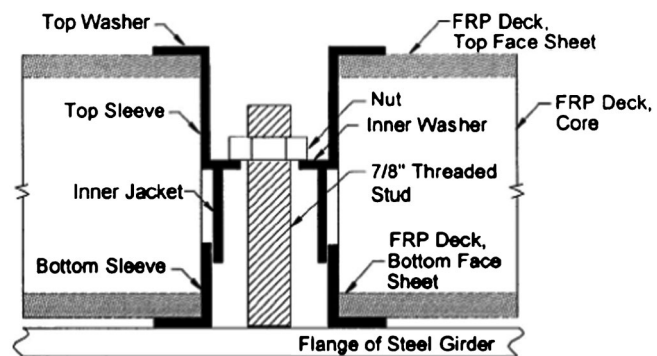


Figure 2.5: FRP Threaded Shear Stud with Clamp Connection (Righman, et al., 2004)

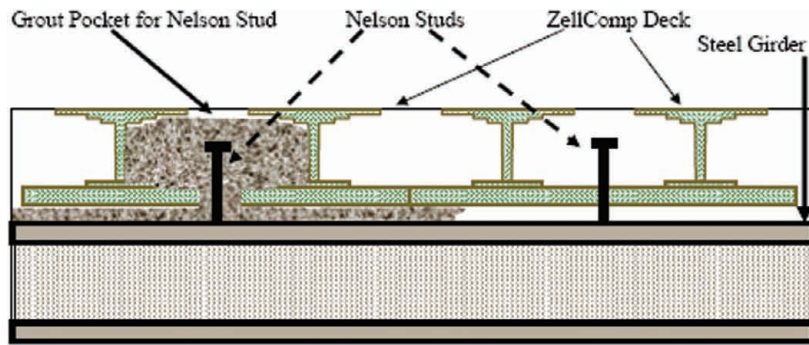


Figure 2.6: Grouted Shear Stud Connection (Zellcomp, Inc., 2006)

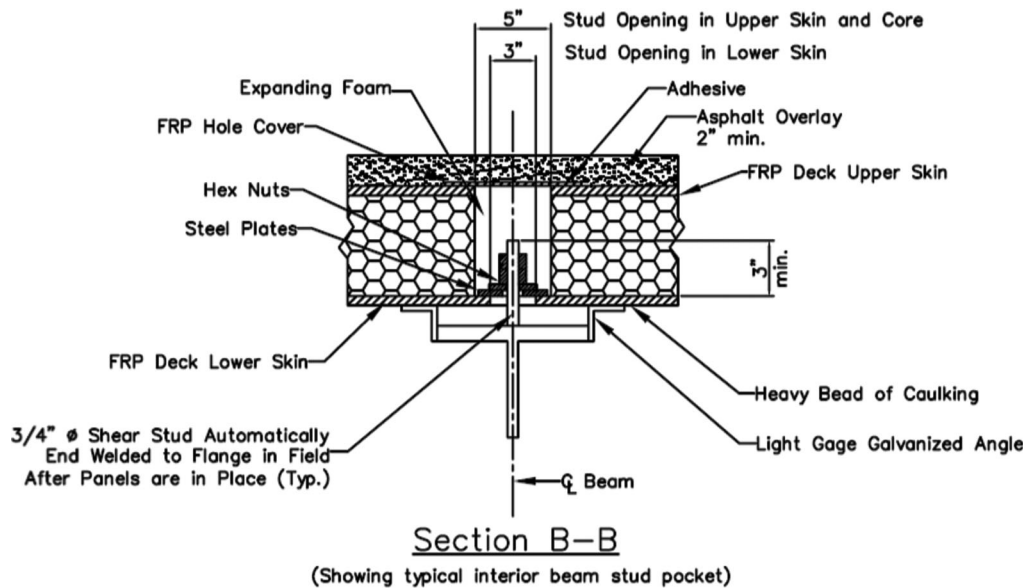


Figure 2.7: Stud Connection with Expanding Foam (Composite Advantage, 2006)

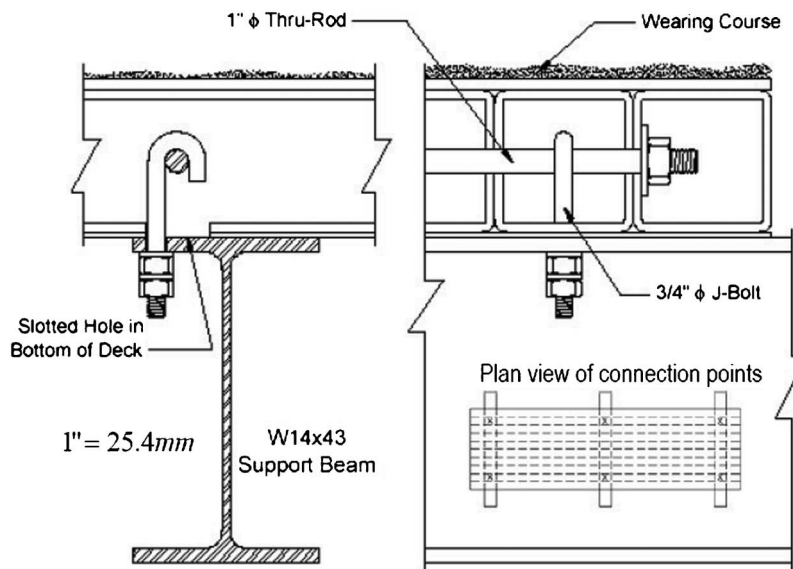


Figure 2.8: J-Bolt Connection (Strongwell, 2006)

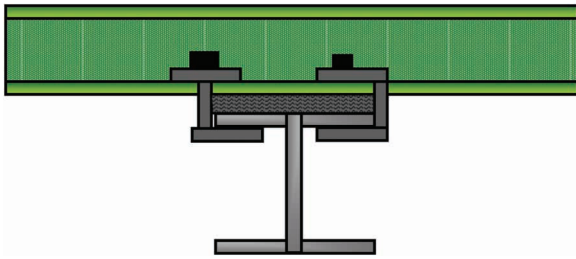


Figure 2.9: Possible Clip Connections (Zellcomp, Inc., 2006)

with reports and observations of the studs at extreme deformed positions (Figure 2.10) (Righman, et al., 2004). Some have made an effort to evaluate the initial stiffness provided by these connections, and their effects on the vibration characteristics of the FRP deck panels in service (Machado, 2006). A review of the literature has revealed no studies in which connections were dynamically or experimentally evaluated for the connections' resistance to vibrations or impact.

2.3.5 Panel to Panel Connections

Panel-to-panel connections also vary with FRP deck type. Some examples of panel-to-panel connections are shown in Figure 2.11. These connections include shear keys, tongue and groove (T&G) connections, and glued butt joints with FRP splice strips. Not shown in Figure 2.11 are the joints with mechanical fasteners for the Zellcomp deck (Figure 2.12). In many cases, the top of the joint is sealed with an FRP strip applied in the field.

Testing of panel-to-panel connections is typically conducted as part of a larger static or fatigue test, as in the Camata and Shing (2004) study and others. The test specimen will include one or two panel-to-panel joints. However, the connection itself is not explicitly loaded and tested to failure.

2.3.6 Fatigue

Procedures for fatigue testing of FRP bridge decks have varied from study to study. Number of cycles is

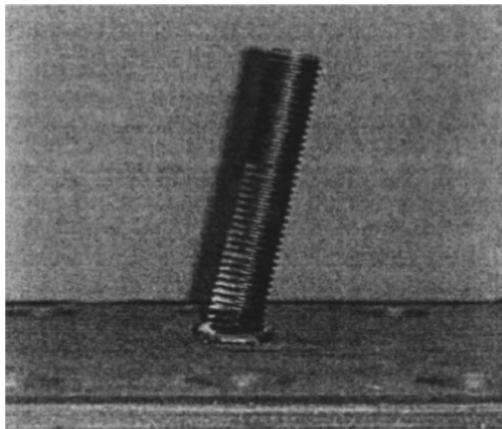


Figure 2.10: Typical Shear Stud Deformation after Test (Righman, et al., 2004)

typically 3,000,000. Some have gone to a higher number of cycles, such as 10,000,000 for a laboratory test, or 7,000,000 for a field test. Some have stopped at 2,000,000 cycles, even without observing any damage (Zhao, 2006). In some cases, the number of cycles was reportedly related to the expected demands on the deck in service for a particular case-study bridge; in other cases, such information was not reported.

In the test by Hayes et al. (2000) on a tube and plate deck on steel beams, no loss of stiffness or strength was found after 3,000,000 cycles of a fatigue load above the design wheel load. No adverse contribution was found from the deck-to-girder connections. The number of cycles was chosen based on 1 year of heavy truck traffic on the bridge for which the FRP deck would be a replacement deck.

Camata and Shing (2004) tested FRP bridge deck panels in fatigue. Three different loading phases were used, one for which the loads in the two actuators were 180 degrees off-phases with a peak load of 40 kips. Another phase had only one actuator with a peak load of 22 kips, and then a final phase with only one actuator with a peak load of 31 kips. In the first phase, the investigators noted possible delamination of the upper face from the core, but no visible damage. No damage was noted in the second phase or third phase up to 1,500,000 cycles, when load-deformation curves and observations indicated delamination, and the test was stopped.

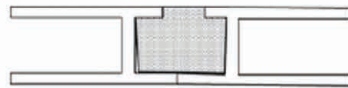
Cousins and Lesko (2004) conducted laboratory and field tests on a tube and plate deck system. The panel was loaded with load patches at the middle of each span, simulating a truck axle load. Laboratory tests showed no strength or stiffness degradation after 4,000,000 cycles of loading. Field measurements on the deck installed at a weigh station showed no significant stiffness loss after 7,000,000 cycles of loading (Cousins and Lesko, 2004).

Fatigue durability of FRP bridge decks has also been evaluated at extreme temperatures (Dutta et al., 2007). Deck prototypes were fatigue tested at -30°C and 50°C . Design loads were applied simultaneously at two points. The researchers noted no significant distress after 10,000,000 cycles. However, degradation in stiffness with load cycling was noted, particularly at the high temperature. Reduction in stiffness at low temperatures was not as significant.

2.3.7 Extreme Temperatures

Extreme temperatures are a concern for FRP decks. The "fire resistance limit" of an FRP bridge deck installed on a 60-year-old, 42.7 m long truss bridge over Bentley Creek in New York was studied using fully coupled thermal stress analysis (Alnahhal et al., 2006). The light weight of FRP deck was utilized to improve the load rating of the bridge. Accidental fire may degrade the composite material, which shows lower heat resistance than conventional construction materials. Such a fire might be caused by an oil truck being

(a) Interference fit with cast shear key



(b) T&G connection in pultruded hollow core



(c) Butt joint with shear splice plate strip



Figure 2.11: Types of Panel-to-Panel Connections (Telang, et al., 2006)

involved in an accident and oil spill. This type of fire was simulated in thermal stress analysis on a finite element model that had been verified for static stress analysis with field measurements. A number of fire scenarios were explored, with different locations above and below the bridge. The simulations predicted failure after 440 seconds of a burning truck on the deck. Failure was according to the Tsai-Hill failure index. Clearly, immediate evacuation of a bridge with an FRP deck subjected to fire is required. The type of resin and fiber and effect on fire resistance were not studied here. A study by Dodds et al. (2000) demonstrated that phenolic resin would tend to delaminate in a fire.

Dao and Asaro (1999) studied the structural integrity of E-glass composites subjected to fire, conducting tests according to ASTM E119 and comparing to predictions. Good agreement was found between numerical and experimental simulations. Structural collapse was found for combined thermal and mechanical loading. Only tests on single skin composites were conducted, although plans were in place to test sandwich panels.

Even less extreme temperatures can cause problems for FRP decks. On the Salem Avenue Bridge in Ohio, thermal characteristics of some of the four different panels used on the bridge resulted in “unexpected uplifts and significant thermal gradients,” depending on

the panel details (Reising et al., 2004). In some cases, top or bottom skins of panels delaminated.

2.3.8 Durability

Studies have shown that FRP composites deteriorate with environmental exposure and repeated application of load. It has been suggested that these effects be quantified and incorporated into design. For example, “degrading of Young’s Modulus of Elasticity, E, has been measured experimentally in accelerated durability tests for various FRPs. If the degradation of E is reliably quantified, it can be treated as losses of prestress are currently treated in the design of prestressed concrete girders. FRP composite components can be designed using the degraded E estimated for the end of the design life (Mertz et al., 2003).”

A study by Xi et al. (2004) addressed some gaps in the knowledge base related to durability of FRP. “Although much research has been done on the mechanical properties of FRPs, the overall long-term durability of GFRPs under severe environmental conditions has not been systematically evaluated (Xi et al., 2004).” The study included an in-house experimental study on the durability of the selected GFRPs, and a load test and long-term monitoring of a panel in

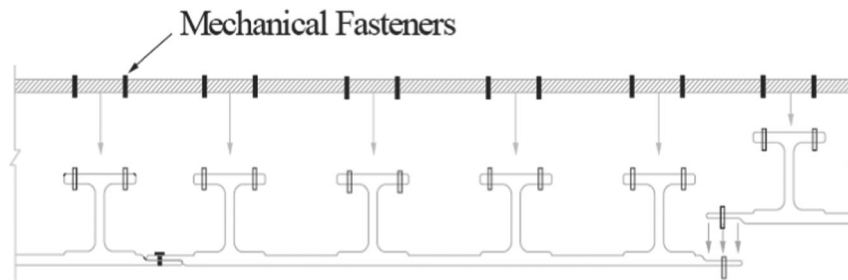


Figure 2.12: Mechanical Fasteners for Panel to Panel Connections and Top Plate Connection (Zhao, 2006)

the field. Factors studied included freeze-thaw cycles, moisture penetration, deicing chemicals, alkali and acid attacks, and ultraviolet light.

Xi et al. (2004) commented that, since FRPs are non-corrosive materials, the deicing chemicals will not corrode the FRP. However, there may be other adverse effects on the fibers, such as degradation of stiffness and strength if the fibers are inappropriately coated and shielded by the resin matrix during the production process. The durability of FRP materials in the alkaline environment is strongly dependent on resin types and the manufacturing processes (Xi et al., 2004). Meanwhile, ultraviolet (UV) light may cause photo-oxidative reactions, causing microcracking in the FRP.

The GFRP laminated plates were cut into rectangular shapes of 0.96 in \times 9.0 in \times 0.14 in. Vinylester was used for matrix material of the specimens. ASTM C666 (Standard Test Methods for Resistance of Concrete to Rapid Freezing Thawing) was used for the freeze-thaw conditioning of GFRP specimens, although the testing procedures specified by ASTM C666 were originally designed for the durability of concrete.

The specimens were subjected to a temperature variation ranging between -20°F (-29°C) to 68°F (20°C), over 8 cycles per day with one hour at -20°F and 20 minutes at 68°F . The specimens were exposed to 300 total freeze-thaw cycles (750 total hours of exposure). In order to investigate the effects of wetting/drying cycles on the durability of the GFRP, two specimens were immersed in a water bath at room temperature for 30 minutes, then pulled out of the bath and hung in the air for 30 minutes. The wetting/drying cycles were repeated 2,160 times over 90 days.

Both long-term ponding tests and long-term cyclic wetting/drying tests with deicing chemicals were conducted. For the ponding test, a total of 15 specimens were immersed in the solutions of three deicing chemicals. The deicer solutions were magnesium chloride ($\text{Mg}(\text{Cl})_2$) of 3%, calcium chloride ($\text{Ca}(\text{Cl})_2$) of 3%, and sodium chloride (NaCl) of 3%. The ponding tests were continued at room temperature for 90 days. For the cyclic wetting/drying test in the chloride solutions, a total of 12 specimens were tested. Alkaline and acid attacks to GFRPs were simulated by using sodium hydroxide solution (1M NaOH) and hypochloric acid (1M HCl). A total of 4 specimens were submerged in the alkali and acid solutions respectively for 90 days at room temperature.

In order to investigate the effects of ultraviolet radiation, a standard ultraviolet (UV) resistance test based on ASTM G53 was used. The test procedure followed the testing cycles specified in ASTM D 5208. Three specimens were exposed to the cyclic fluorescent ultraviolet radiation in an environmental chamber for 90 days. The temperature in the chamber was kept at 50°C .

Every environmental parameter tested in the study resulted in a degradation of GFRPs to a certain extent. From the strength aspect, the worst degradation was a

35% reduction of tensile strength of the GFRP subjected to the ponding of 1M NaOH solution. From the stiffness point of view, the worst degradation was a 32% reduction of Young's modulus of the GFRP subjected to the ponding of the 3% Ca (Cl_2) solution. The researchers suggested that the degradation of FRP should be tested with coupling effects between moisture and elevated temperatures. For example, degradation could be accelerated by high diffusion rates.

Xi et al. (2004) also compared the effect of environmental temperature with the effect of mechanical loading, and they found that temperature dominated. The authors noted that a larger scale cyclic temperature test for the FRP panel is very necessary and important for evaluating the long-term performance of the panel.

Meanwhile, freeze-thaw cycles in cold region environments may change the material properties of the FRP. Microcracks and voids in the polymer matrix can occur in FRP materials during a freeze-thaw cycling due to differences in the coefficients of thermal expansion of fibers and resin. Ma et al. (2007) conducted cyclic tests on FRP sandwich deck panels at very cold temperatures. A 2.134 m \times 0.340 m \times 0.178 m section was cyclically tested under three-point bending at temperatures as low as -55°C . At these very low temperatures, the stiffness of the specimen decreased by 11.5% compared to room temperature. This degradation in stiffness could not be recovered. Acoustic emission testing confirmed matrix hardening, matrix microcracking, and fiber-matrix debonding (Ma et al., 2007). Shao and Darchis (2007) also found reduction in stiffness due to saturation and freeze-thaw cycling, as well as saturation and continuous freezing. Stiffness loss was on the order of 10% in the longitudinal direction and 17% in the transverse direction. Strength reduction also ranged from 10% to about 27%.

Fatigue durability of FRP bridge decks has also been evaluated at extreme temperatures (Dutta et al., 2007). Deck prototypes were fatigue tested at -30°C and 50°C . Design loads were applied simultaneously at two points. The researchers noted no significant distress after 10,000,000 cycles. However, degradation in stiffness with load cycling was noted, particularly at the high temperature. Reduction in stiffness at low temperatures was not as significant.

2.3.9 Wearing Surface

Wearing surface delamination has been observed on many existing GFRP decks. In an effort to address this issue, a number of tests on wearing surfaces bonded to GFRP panels were conducted at Syracuse University (Wattanadechachan et al., 2006). A number of wearing surface materials were used, the FRP surface prepared in some cases, and the 300 mm \times 300 mm (12 in \times 12 in) samples were tested under a variety of environmental conditions. The standard ASTM C884 method was used, as well as two new methods. Freeze-thaw-heat and submerge-freeze cycles were included.

Following ASTM C884, the researchers conducted the first test with five cycles of temperature changes: 25°C (77°F) and -23°C (-10°F). Specimens were kept for 24 hours at every temperature level during each cycle. If the specimens that passed this test, the second test was conducted. The second test, named freeze-thaw-heat nonstandard test, consisted of five cycles of temperature change: -23°C (-10°F), 25°C (77°F), and 60°C (140°F). Successful completion of the second test led to the third test. The third test consisted of five cycles of condition changes. The specimens were submerged in the water for 24 hours at room temperature and then kept in a freezer for 24 hours at -23°C (-10°F). Cracks at the interface were monitored at every cycle. Debonding of the WS from the FRP panel was considered a failure state of the system.

Wattanadechachan et al. (2006) found that, of the wearing surfaces tested, a two-layer hybrid system consisting of a polymer concrete underlayer and a polymer modified concrete top layer performed the best. The polymer concrete has good adhesion to the FRP, but not good skid resistance, which is provided by the polymer modified concrete top layer. These tests did not include any mechanical loading.

For the post-tensioned, concrete filled FRP tube deck studied by Wolfe et al. (2003), studies were conducted on the bridge subjected to normal traffic loads. One portion of the bridge deck was replaced with a conventional reinforced concrete deck. Three weeks after the bridge was opened to the public, the cracking in the overlay was considerably more in the FRP. Furthermore, when the temperature would reach above 66°F, the deck would separate from its haunches. Such gaps were reportedly visible from up to forty feet away.

2.3.10 Guardrails/Barriers

In NCHRP Report 503, Mertz et al. (2003) note the issue of guardrails. “No crash-test-approved guardrail attachment system or fully FRP composite guardrail system exists. Studies have been initiated through ongoing IBRC projects to investigate connections that will enable traditional guardrails to be safely attached to the FRP decks.” A survey of the IBRC website (ibrc.fhwa.dot.gov) and the literature reveals at least one project specifically

related to composite guardrails, but no clear comprehensive, published results leading to progress for approved guardrails or attachments. Attachments for guardrails to date have included connections to the deck, connections directly to the exterior or fascia girder, and attachment both to girder and deck.

Toillion (2001) reported on static tests of a concrete barrier and a steel rail to an FRP bridge deck panel. A concrete F-shaped barrier was bolted to an FRP bridge deck panel by six bolts. The test was successful and then was repeated after removal of two center bolts. A steel rail configuration was reportedly tested the previous summer with a plate connection to the deck. The initial plate was deemed to be too wide and a possible “snagging point” for snowplows. A revised, half-plate with six bolts was tested successfully. Figure 2.13 shows the two tests.

Nystrom et al. (2002) noted that the technique of attaching the guardrail posts to the FRP panels for the St. Francis Street Bridge worked well. The connection was similar to that used for connections to timber bridges (Figure 2.14). The test of the guardrail system was conducted by the manufacturer, as noted by Toillion (2001). A static horizontal load was applied to one of the guardrail posts. Deformation of the guardrail post was achieved without damage to the FRP panel.

2.3.11 Issues for Testing

Loading of FRP bridge deck panels is an issue in experimental evaluation. A number of journal articles report failure by punching shear, not a limit state considered in design. One example is the test of the tube and plate deck by Hayes et al. (2000), in which the out-of-plane shear failure of the composite laminate was observed at the end of the second load cycle. This failure occurred along the long side of the 508 × 305-mm load patch. Camata and Shing (2004) reported similar failures. These failures appear to be directly related to loading by rectangular steel plates or similar elements bearing on the FRP faces, as shown in Figure 2.15. These failures occurred even with the presence of a 3/4-inch rubber pad between the steel plate and deck, as used by Camata and Shing (2004).



Figure 2.13: Test of Concrete Barrier (left) and Steel Rail (right) (Toillion, 2001)



Figure 2.14: Guide rail and Connection to Deck (Nystrom, et al., 2002)

Such failures could have been mitigated by a loading more representative of a true tire patch. In tests conducted at Virginia Tech and now at Purdue University, actual tire elements have been used to protect the FRP faces from the loading plates and provide a more realistic tire patch (Cousins and Lesko, 2004). Cousins and Lesko (2004) tested both with a rectangular steel plate, or load patch, as specified by AASHTO, and a simulated tire patch as shown in Figure 2.16. The failure with the steel plate was punching shear. The failure observed with the simulated tire patch limited to surface cracking, as shown in Figure 2.17. These crack locations coincided with the centers of the tube flanges. Even with the simulated tire patch, the importance of stiffening the deck face against localized failures is highlighted.

2.3.12 Limit State Tests

A number of laboratory and field tests have been conducted to evaluate strength and serviceability of FRP bridge decks. Nystrom et al. (2002) conducted in-situ load tests on a GFRP honeycomb sandwich panel. Three-point bending tests were also conducted in the laboratory on unit width beams. Failure modes

observed included delamination of the face from the core and buckling of the core (Figure 2.18).

Camata and Shing (2004) tested full-scale two-span panels to evaluate load-carrying capacity and fatigue endurance. The GFRP panels tested in the laboratory had the same properties as the O’Fallon Park Bridge in Denver, CO. An initial phase of testing included four GFRP beams were tested for evaluation of strength and stiffness. Compression tests were also conducted for an assessment of crushing capacity. These first tests were intended as confirmation of the deck sections proposed by the manufacturer.

The second phase of testing included static and fatigue testing of the full-size two-span GFRP panel. The panel was roughly 10 ft square (Figure 2.19), representing just a portion of the O’Fallon Park Bridge, for which the deck is 16.25 ft wide and 43.75 ft long and supported on concrete girders at roughly 4 ft spacing. The bridge was intended mostly for pedestrian traffic, but designed and tested at the level of an HS25. Loads were applied with $13 \times 13 \times 1$ -in steel plates, with $\frac{3}{4}$ -inch rubber pads beneath. The panel was loaded with two actuators, one on each span, simulating wheel loads (Figure 2.20).

The influence of load cycles was studied. Three different loading phases were used, one for which the

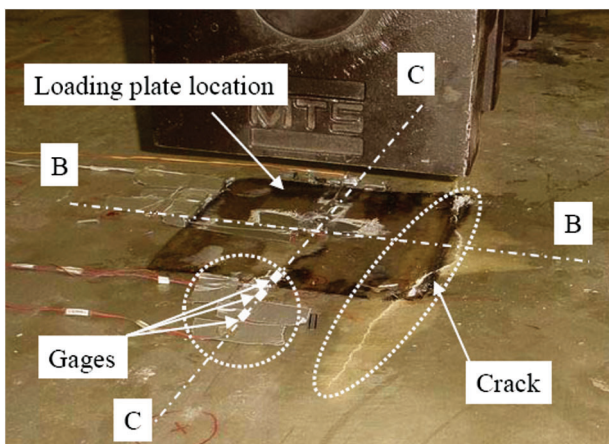


Figure 2.15: Failure of FRP Face at Loading Plate (Camata and Shing, 2004)

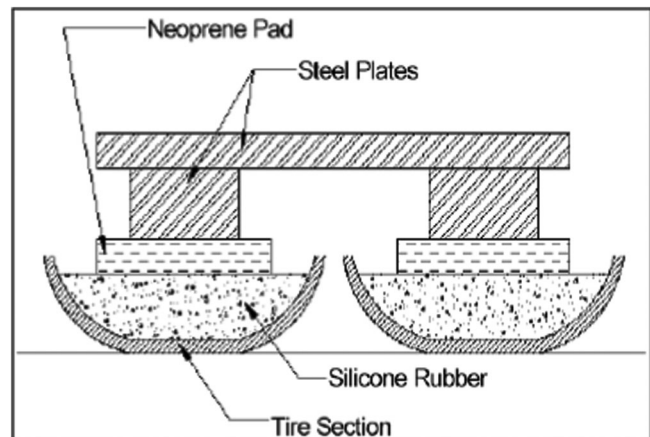


Figure 2.16: Simulated Tire Patch (Cousins and Lesko, 2004)

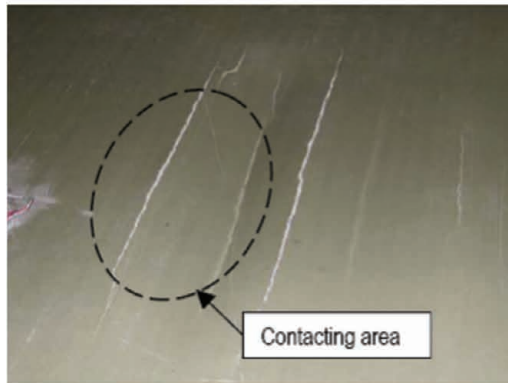


Figure 2.17: Punching Shear due to Steel Plate (left) and Surface Cracking for Simulated Tire Patch (Cousins and Lesko, 2004)

loads in the two actuators were 180 degrees off-phases with a peak load of 40 kips. Another phase had only one actuator with a peak load of 22 kips, and then a final phase with only one actuator with a peak load of 31 kips. In the first phase, the investigators noted possible delamination of the upper face from the core, but no visible damage. No damage was noted in the second phase or third phase up to 1,500,000 cycles, when load-deformation curves and observations indicated delamination. Also, the performance of the anchor bolts to the concrete girders was investigated. Testing revealed that the anchor bolts could fail due to

an HS25 loading. Some of the anchor bolts on the external support slipped. Therefore, for the O'Fallon Park Bridge, an epoxy anchor was used. There were no comments about the behavior of the panel-to-panel connection (Figure 2.19) or any separate tests on these connections. These connections were glued, with a 3 oz. GFRP mat placed on the panel top surface across the joint.

Cousins and Lesko (2004) tested a plate and tube FRP bridge deck. This research examined the use of pultruded, off the shelf components as a lower cost alternative FRP bridge deck system. The FRP deck system is fabricated by adhesively bonding standard pultruded structural square tubes and plates produced by Strongwell Corp. of Bristol, Virginia. Not including wearing surface, the decks tested were 4.65 m (15¼ ft) long, 1.52 m (5 ft) wide, and 17.2cm (6¾ in.) thick. A schematic of the tested FRP deck panel over three supporting steel girders is shown in Figure 2.21.

Through-rods, transverse to the tubes, provide additional connectivity. Stiffness and strength as related to number of through-rods were investigated. The deck was fastened to the supports using a 12.7 mm (½ in.) diameter A325 bolt in twelve locations (four to each support beam). A detail drawing of the connection was shown in Figure 2.8.

Static and fatigue tests were conducted. The panel was loaded with load patches at the middle of each span, simulating a truck axle load. At 245 kN (55 kips) for each load patch, debonding between the face plates and tubes was observed. The ultimate capacity was about 609 kN (137 kips) and corresponded to surface cracking underneath the simulated tire patches. Meanwhile, laboratory tests showed no strength or stiffness degradation after 4,000,000 cycles of loading. Field measurements on the deck installed at a weigh station showed no significant stiffness loss after 7,000,000 cycles of loading (Cousins and Lesko, 2004).

Zhao (2006) conducted static and fatigue tests on the Zellcomp deck. The test set-up was similar to studies discussed previously. The two-span specimen was supported on 3 girders, with loads at the middle of each span for the fatigue tests. Girder spacing was 4 ft; panel width was 5 ft. For the static tests, only one span was loaded at a time. For fatigue, the panel was loaded



Figure 2.18: Delamination (a) and Buckling of Core (b) for honeycomb sandwich panel (Nystrom, et al., 2002)

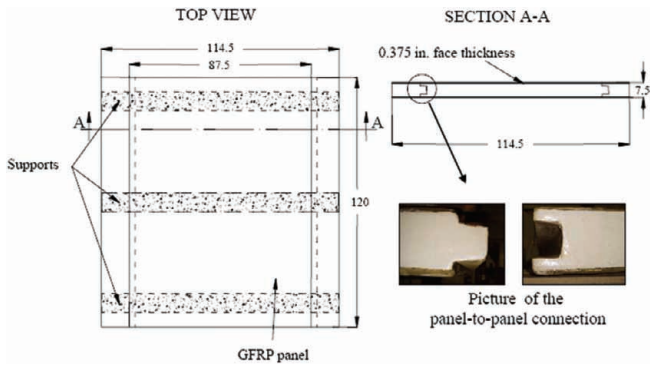


Figure 2.19: Plan View of Test Set-up for O'Fallon Park Bridge (Camata and Shing, 2004)

to 2,000,000 cycles at 18 kips for each load. No damage was observed. For the static tests, debonding and web buckling failure were observed at over 83 kips, over twice the required strength according to the AASHTO Strength I case (Figure 2.22)(Zhao, 2006).

2.3.13 Existing Acceptance Test Criteria for FRP Bridge Decks

GangaRao, et al., (2002) proposed acceptance test criteria for FRP bridge decks and superstructures in an FHWA report which also included specifications for the decks and their installation. The authors state, “prior to designing and constructing FRP decks and superstructures, one needs to fully understand the behavior of an individual component of an FRP bridge deck and their connection to other components. Also FRP deck to beam connection integrity needs to be evaluated accurately. The performance of FRP components and their connections can be evaluated with high degree of accuracy only by adopting standard testing procedures in the laboratory.”

The tests are to be conducted on 2.43 m × 1.8 m (8 ft × 6 ft) panels. These panels are to be supported by two steel girders. Static tests must be conducted to evaluate local, deck, and global deflections and capacity. Fatigue tests must be conducted to evaluate fatigue life. GangaRao et al. (2002) also suggest evaluation of the

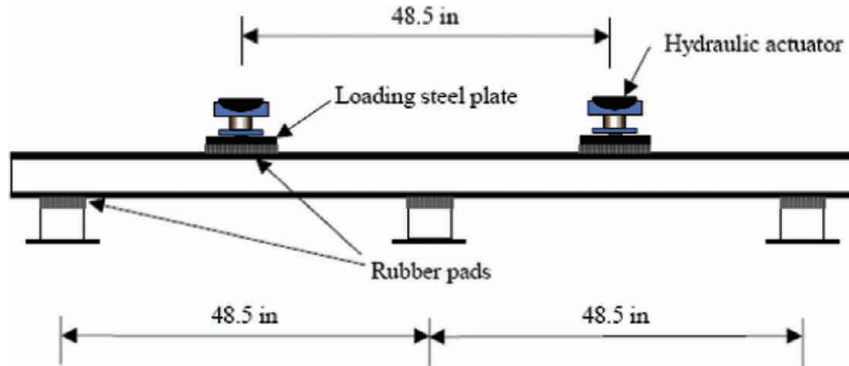


Figure 2.20: Loading for O'Fallon Park Bridge (Camata and Shing, 2004)

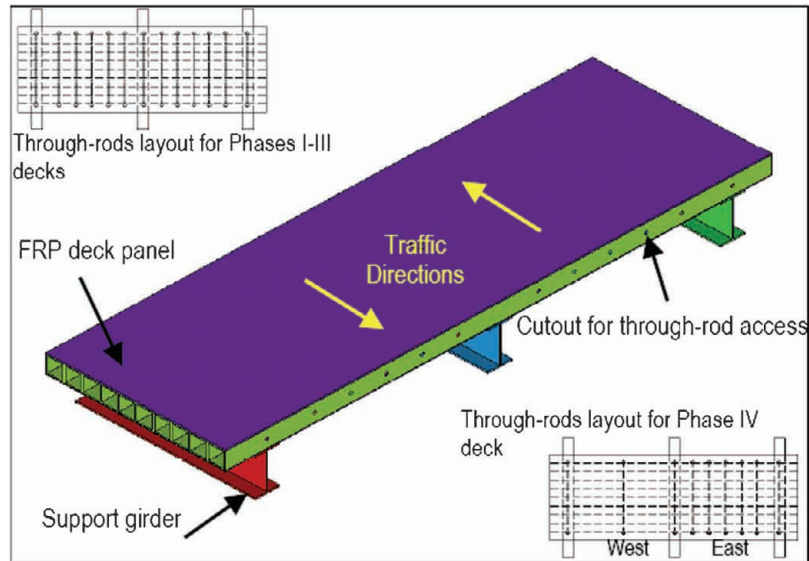


Figure 2.21: Test Specimen for Plate and Tube FRP deck (Cousins and Lesko, 2004)

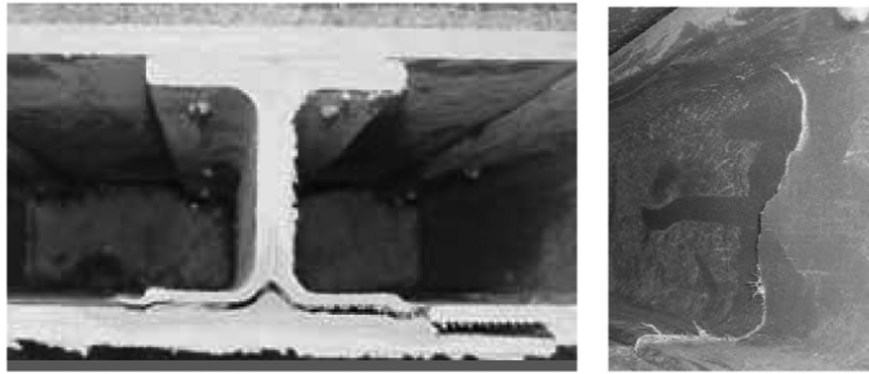


Figure 2.22: Delamination of Bottom Flange (left) and Web Failure (right) for Zellcomp Deck (Zhao, 2006)

integrity of the panel connections subjected to cyclic loading, as well as an evaluation of the fundamental frequency and use of a non-destructive evaluation method. An alternative test panel is 2.43 m × 3.6 m (8 ft × 12 ft), supported by three steel girders. This specimen reportedly can be used to evaluate load distribution and composite action, as well as items mentioned above.

A push-out shear test of the connection of the deck to the girder is regarded as mandatory. Joint strength and stiffness are to be measured in this test. The objectives for this test are to evaluate the initial slip resistance and to evaluate the ductility of the connection at ultimate capacity.

GangaRao et al. (2002) specify that these tests be conducted by the FRP deck manufacturer prior to delivery of the deck to the construction site. Qualification of an FRP deck would be valid only after tests are repeated on three specimens for each test method.

Furthermore, specifications are provided for the wearing surface. Related to testing, there is a particular provision that “wearing surface materials applied to finished FRP deck panels by the FRP deck manufacturer shall be certified to be strain compatible with the fiberglass decking materials by conducting short beam strength tests in tension and compression in accordance with ASTM D 2344 (GangaRao, et al., 2002).”

Meanwhile, a project sponsored by the Federal Highway Administration is focused on accelerated test methods to determine long-term behavior of FRP composites. The primary objective of this work is on development of these test methods. Secondary objectives are to provide researchers with the tools to develop design criteria and to provide the industry with an accepted test method for evaluating composites for highway bridges. “The major thrusts of this plan are to develop tests on four different scales, i.e., material, element, connection and full-structure; to isolate different mechanical and environmental loading conditions; to perform both destructive and nondestructive mechanical testing; to perform chemical analysis of deteriorated FRP materials; and to develop mathematical models that can predict the long term behavior of FRP materials and structures (Zureick, 2007).”

2.3.14 Key Issues and Scope of the Project

Of the key issues summarized above, the topics of serviceability (deflection limits), issues for testing (e.g., load patches), limit states (e.g., delamination and how to inspect for such limit states) took top priority. Other topics, such as wearing surface, panel to panel connections, deck to girder connections, and guardrails were secondary areas of study. Guardrails were not explicitly studied, but recommendations made to the structural engineer for the case-study bridge based on the literature. Issues such as fatigue response and extreme temperatures were outside the scope of this study. Each topic studied and all parameters were related specifically to the case-study bridge.

2.4 FRP Decks in Study

Two different FRP decks were studied during this project; one panel was manufactured by Kansas Structural Composites, Inc. and one was manufactured by ZellComp, Inc. The basic configurations and connections for each panel are described in the following sections.

2.4.1 Kansas Structural Composites, Inc.

The first panels studied were manufactured by Kansas Composites, Inc. This sandwich panel was made using the hand lay-up technique. It consists of top and bottom ½ inch flat face sheets with a honeycomb core, all adhered together with resin to create an 8 inch thick panel. The core consists of sinusoidal and flat pieces all placed one beside the other as seen in Figure 2.23.

KSCI deck panels are shipped to the site in separate pieces. Each piece is 8 feet wide, and its length matches the width of the bridge for which it is manufactured. These panels are joined together longitudinally with a tongue-and-groove connection (Figure 2.24) and are placed one by one, with the sinusoidal core oriented perpendicular to the girders (Figure 2.25). Each panel is attached to the girders using a bent plate and threaded shear studs welded to the steel girders as seen in Figure 2.26 and Figure 2.27. After all the panels are in place, a strip of fiber glass with epoxy seals the joints.

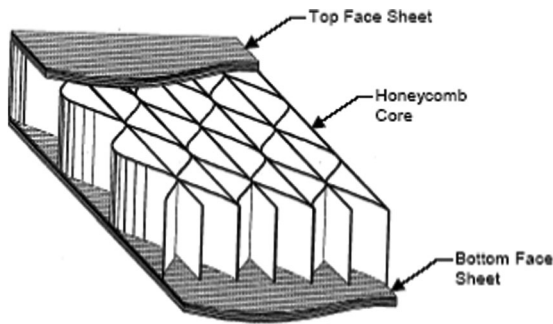


Figure 2.23 KSCI Deck Cross-Section (Righman, 2004)

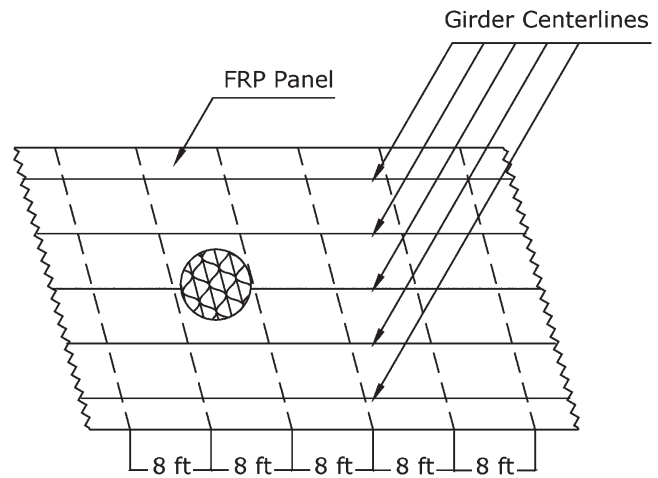


Figure 2.25: Direction of KSCI Panels with Respect to Bridge Girders

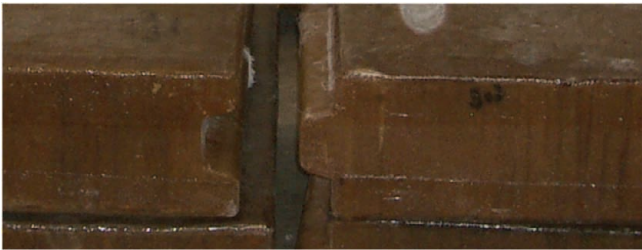


Figure 2.24: Tongue and Groove Connection

The specific setup used during this study will be presented in a future chapter and will depend on the geometry of the case study bridge.

2.4.2 ZellComp, Inc.

The panels manufactured by ZellComp, Inc. incorporate two pultruded parts: a bottom section and a top plate, attached together with resin-infused mechanical fasteners (Figure 2.28), creating a 7 inch deep decking system. A cross section of the deck can be seen in Figure 2.29. The top plates are pultruded 1/2 inch FRP solid sheets, while the bottom part consists of I-shaped sections, spaced approximately 8 inches web to web, all connected together by a 1/2 inch FRP sheet at the bottom. This bottom part is pultruded as one piece, which can be as long as needed and is 33.5 inches wide due to machinery constraints. The bottom pieces are attached together at a lap joint using the same mechanical fasteners that attach the top plate to the bottom section. The I-sections span from girder to girder on the bridge. The panels are connected to the

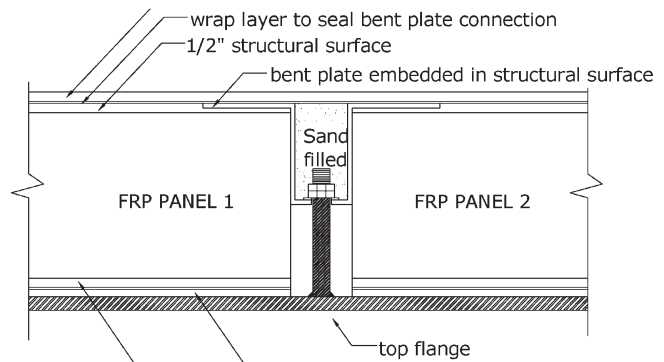


Figure 2.26: Sketch of Panel to Girder Connection

bridge girders with studs that are grouted in place (Figure 2.30). Fiber properties of the ZellComp deck are as summarized in Figure 2.31.

The specific setup used for this study will be described in more detail in a future chapter and will depend on the geometry of the case study bridge.

2.5 Conclusions

There exist a number of FRP decks of varying geometries and properties. However, overall, the key issues are consistent. Of the concerns with FRP decks



Figure 2.27: Picture of Panel to Girder Connection



Figure 2.28: Resin Infused Mechanical Fasteners



Figure 2.30: Grouted-in-Place Stud Connection

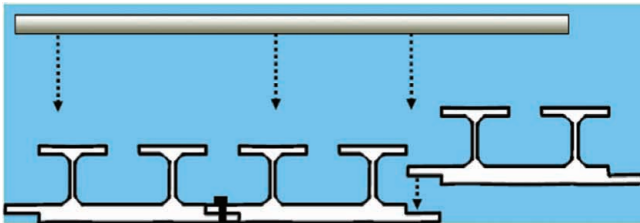


Figure 2.29: ZellComp Deck Cross-Section

observed in the literature, the topics of serviceability (deflection limits), issues for testing (e.g., load patches), limit states (e.g., delamination and how to inspect for

such limit states) were most significant and took top priority in this study. Other topics, such as wearing surface, panel to panel connections, deck to girder connections, and guardrails were secondary areas of study. Guardrails were not explicitly studied, but recommendations made to the structural engineer for the case-study bridge based on the literature. Issues such as fatigue response and extreme temperatures were outside the scope of this study. Two FRP decks and two different case study bridges were chosen at different times over the course of the project. Each topic studied and all parameters were related specifically to each FRP Deck and associated case-study bridge; details are presented in the following chapters.

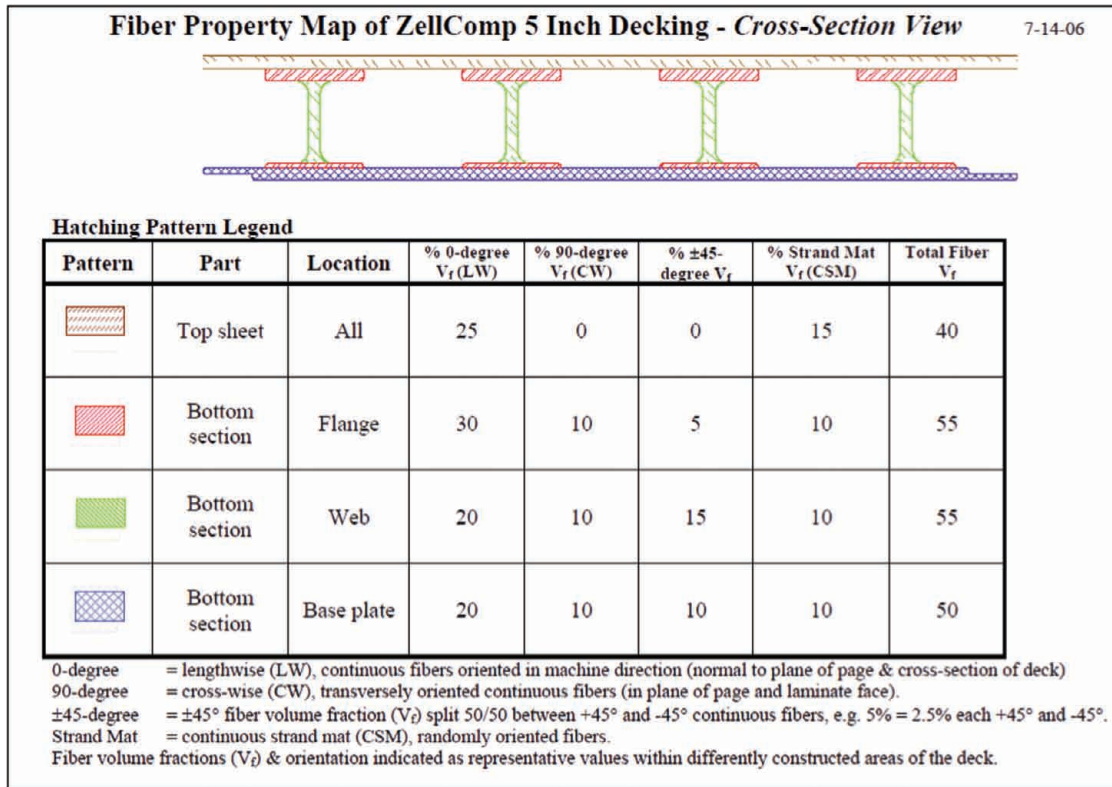


Figure 2.31: Fiber Properties for the ZellComp Deck

CHAPTER 3. SERVICEABILITY CRITERIA FOR FRP BRIDGE DECKS

3.1 Background and Motivation

A number of efforts to implement FRP composite bridge decks as an alternative to bridge rehabilitation have taken place over the past decade or so. However, appropriate design guidelines pertaining to this innovative construction material are still lacking. Current AASHTO serviceability criteria involve span-to-deflection ratios that are based on bridge accelerations tolerable to humans traversing the bridge. These criteria are quick and easy for the designer to use, but supply little knowledge to the engineer as to what these quantities represent, *i.e.* what does the serviceability check actually accomplish in the overall design of the bridge? The current serviceability checks, when applied to conventional bridge materials, should be sufficient for design since in most cases deflections/vibrations do not govern, thus making these checks *guidelines*, not requirements. FRP is known to have a high strength and low stiffness, therefore serviceability limits often control the design of the deck. Present deflection criteria are typically violated well before the ultimate strength of this material is reached, thereby establishing a large factor of safety. Furthermore, it is not clear whether or not the deflection limits established for conventional materials are applicable to relatively lightweight FRP decks.

This chapter provides background information on current serviceability criteria, a summary of a parametric study used to establish the best type of model to use to predict deflections in the bridge deck, information on a numerical study with a moving load analysis and a proposal for new serviceability criteria, an alternative hybrid deck solution to address serviceability issues, and information on the actual criteria used for the case study bridge. Note that the parametric study, moving load analysis, and hybrid deck solution were all based on the KSCI deck, as these investigations were conducted relatively early in the project.

3.2 Current Specifications

The AASHTO LRFD (1998) provision gives an optional guideline that limits bridge deflections. This criterion was imposed with the purpose of controlling

vibrations induced by vehicles passing over the structure and that can be felt by pedestrian users. Deflection limitations can be traced back to 1871. The specifications of the Phoenix Bridge Company limited the passage of a train and locomotive at 30 mph to $L/1200$, where L is the length of the span. In 1905, depth limitations to girders and pony trusses appeared in the American Railway Engineering Association (A.R.E.A) Proceedings. These limitations were modified with time, becoming more flexible for plate girders and rolled beams. While it is clear that their origin was based partly on economics, the origin and cause of the changes have not been clearly documented.

In the early 1930's, reports of unpleasant vibrations in steel highway bridges began to emerge. These reports often involved bridges with continuous spans or cantilevers. The Bureau of Public Roads conducted a study and came to the conclusion that all the bridges that were showing an unpleasant vibration had live-load deflections of more than $L/800$ between spans and $L/400$ in their cantilever arms. The actual design specifications were issued in 1936 and amended in 1939, limiting the deflection under live load plus impact. The present requirements (Figure 3.1) were issued first in the 1941 provisions.

These limitations were derived empirically, and with subjective parameters of human tolerance to vibrations. The specifics of the study, conducted in the attempt to link the live-load deflection to the vibration suffered by the sample bridges, is lost in history, but the study concluded that structures having 'unacceptable' vibrations had deflections that exceeded $L/800$. However, the sample bridges utilized in that study were made of somewhat different materials than the ones utilized in construction today. The live loads employed were also very different to the ones used today.

Further studies have not found an obvious link to excessive deflections and structural problems. The studies concluded that human tolerance to vibration/deflection is the main issue addressed in the deflection criteria. Nevertheless, it is not clear how the slenderness and flexibility limits contribute to the serviceability and/or safety of bridges

A studied conducted by Walker and Wright in 1971 investigated the effect of bridge slenderness and flexibility on human response to vibration. The researchers concluded that live-load deflections did

| |
|---|
| <p>2.5.2.6.2 Criteria for Deflection (AASHTO-LRFD 1998)</p> <p><i>In the absence of other criteria, the following deflection limits may be considered for steel, aluminum, and/or concrete construction:</i></p> <ul style="list-style-type: none">- Vehicular load, general $Span/800$,- Vehicular and/or pedestrian loads $Span/1000$,- Vehicular load on cantilever arms $Span/300$, and- Vehicular and/or pedestrian loads on cantilever arms $Span/375$ |
|---|

Figure 3.1: Serviceability Criterion

not affect significant structural damage to the bridges and that a limit on deflection is not the most appropriate method to control vibrations. It seems that a criterion for the comfort of pedestrians, and not solely deflections, should limit the acceleration in the fundamental mode of vibration at the mid-span region of the bridge. An acceleration criterion will offer comfort and economy in the design.

Many studies have researched the human response to vibration. The important parameters that affect human perception to vibration are the acceleration, deflection, and period of the response (Roeder et al., 2002).

A laboratory test conducted in 1931 by Reiher and Meister produced tolerance ranges based on reaction of adults between different ages. These ranges were classified as imperceptible, slightly perceptible, distinctly perceptible, annoying, disturbing, and injurious. These ranges were shown in a graph of displacement amplitude versus frequency.

In 1957, Oehler referred to a study by Janeway (1948) which used amplitude limits to control vibration. All these different studies try to quantify the human tolerance to vibration and to vertical acceleration, with relation to deflection.

Human tolerance to vibration will always be a subjective matter, but from all these studies one can conclude that deflection does not directly relate to vibration and to human reaction. With the development of new materials (such as FRP) these deflection criteria should be investigated in detail and amended. Attempts to satisfy the existing serviceability criteria with FRP decks would typically result in the requirement that more material and perhaps that a larger number of deck-to-girder connectors be used. This would result in expensive, impractical designs. Moreover, the lack of a reliable and relevant serviceability criterion for these decks may be an additional impediment for their use in practice.

3.2.1 Alternative Live-Load Deflection Serviceability Criteria

There are a few recommended design parameters related to the dynamic properties of a bridge. Janeway (1948) recommended a limit of $af^2 = 2$ for bridges with frequency of 1 to 6 cps, and an $af^2 = 1/3$ for higher bridge frequencies, where a is the amplitude and f is the frequency of vibration. The study made by Oehler (1957) measured the deflection, vibration amplitude, and frequency of vibration in 15 bridges, and compared the results to Janeway's recommended limits. Their results produced vibrations that exceed Janeway's limits, and the researchers performing the tests disagreed with the limits set by Janeway.

Another approach to the problem of the dynamic response of bridges is the one given by the Ontario Highway Bridge Design Code (Ministry 1992). Instead of providing a generic deflection restraint built with a specific material, the code limits the deflection based on the dynamic characteristics of the bridge. The designers

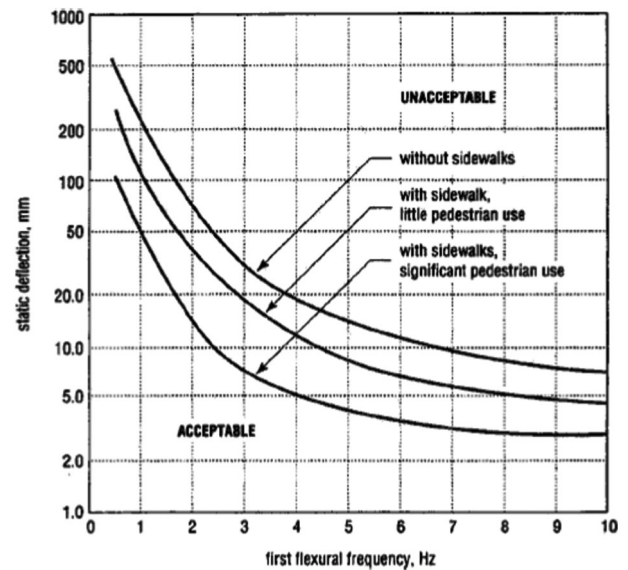


Figure 3.2: Service Deflection criteria per Ontario code (Ministry 1992)

choose the criteria from Figure 3.2, depending on the number of pedestrians using the bridge. Figure 3.3 illustrates the human tolerance criteria to acceleration as a function of frequency as provided in the Ontario Highway Bridge Design Code (Ministry 1995).

In 1971 the American Iron and Steel Institute reviewed AASHTO criteria and recommended design limits based on the vertical acceleration (Roeder, et al., 2004). This criterion uses the natural frequency of the spans, a speed parameter, an impact factor and a dynamic component of acceleration. The acceleration limit must not exceed 100 in/sec^2 . If the dynamic

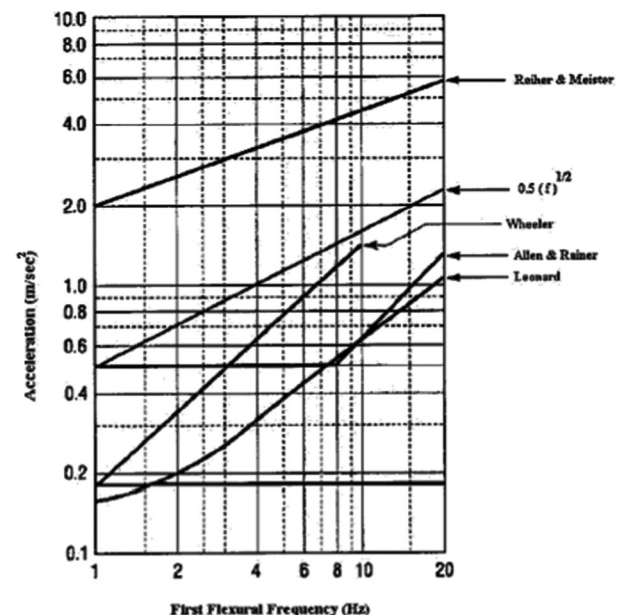


Figure 3.3: Criteria for human response to acceleration (Ministry 1995)

acceleration limit exceeds 100 in/sec^2 a redesign should be made.

There are many different alternatives for serviceability criteria used in specifications on other countries, some are based on deflection, and others on dynamic parameters. However, all have a certain grade of subjectivity related to the human tolerance to vibration. It is apparent that all the criteria mentioned above are meant to control vibration and not for structural reasons.

3.3 Numerical Models for Predicting Deflections

Since static deflections and deflection limits are a standard measure for evaluation of bridge decks, options for modeling the bridge deck and predicting the deflections were investigated. The purpose of the following numerical analyses was to evaluate the relative accuracy of various numerical models. Results from the numerical analyses were compared to test data from the literature. For this part of the study, the geometric characteristics of the KSCI FRP panels and the Wildcat Creek Bridge (described in detail in Chapter 4) were used. Sections of KSCI FRP deck panels were tested as beams by Lopez (2002); these “beams” were also modeled and numerical results compared with the experimental results.

Two models were adopted to simulate the behavior of a transverse strip of entire width of the bridge deck. Each deck model had four continuous 5'-7" spans and 3'-2" overhangs at each end (Figure 3.4). The supports in the model represent the locations of the bridge girders. *Deflection Model #1* considered the FRP panel to be isotropic using the material properties obtained from KSCI ($E=1940 \text{ ksi}$, $\nu=0.30$). These values were derived from prior testing of simply supported “beams” commissioned by KSCI and represent an effective modulus and Poisson’s ratio. *Deflection Model #2* considered the panel to be orthotropic using the material properties given by Davalos et al. (2000) ($E_x=1273 \text{ ksi}$, $E_y=806 \text{ ksi}$, $\nu_{xy}=0.30$). In both cases the section of FRP panel was modeled as a 28 ft – 8 in. long and 20 inch wide beam. Also, in both cases, beam elements in SAP2000 were compared to plate elements used in ANSYS. Furthermore, the KSCI deck is a honeycomb sandwich panel, but the beam and plate models consist of solid cross sections. Therefore, in order to get the same moment of inertia as the real 9

inch deep FRP deck, an equivalent height of 6.73 inches was adopted.

The 20-inch width of the model was based on the patch load for an HS-20 truck wheel. The loading from this truck was represented by 2-point loads of 16 kips each, spaced 6 feet from each other. The first load was placed 1 feet away from the end. Loadings of 0.35 kips were also applied to represent the guardrails. This load was adopted from the New York DOT, which states that a steel guardrail, commonly used in this type of bridges, weighs 0.21 kips/ft. Since the model is 20 inches wide, the total load must be 0.35 kips (Figure 3.4).

Deflection Model #3 simulated a 28'-8" long and 8 foot wide panel. The 8 foot width is the typical width of a panel shipped to the site. This model also considered the same truck loading as for *Deflection Models #1 and #2*, but in this case the load of the guardrails was distributed along the 8 foot edges, and the truck patches placed along the centerline of the model. The same height of 6.73 inches was adopted represent the equivalent section, and the panel was modeled with both the isotropic parameters given by KSCI and the orthotropic parameters given by Davalos et al (2000).

Deflection Model #4 was created by simulating the behavior of the beam tested by Lopez (2002) under 4-point loading. These beams were 32'-2" long, 12 inches wide, and 31 inches deep. An equivalent height of 19.5 inches was used for an equivalent solid section to represent the honeycomb core. These beams were considered to be isotropic with the modulus of elasticity $E = 1556.5 \text{ ksi}$ and Poisson’s ratio $\nu = 0.3$. Two beams were modeled, simulating the beam tested by Lopez. One beam had a total load of 10 kips (*Beam #4.1, #4.3*), while the other had a total load of 70 kips (*Beam #4.2, #4.4*). Each beam was analyzed by using both SAP2000 and ANSYS. The results of these analyses can be seen in Table 3-1.

Based on the comparison of results from these models, it can be observed that:

- a. The results given by SAP2000 and ANSYS using isotropic properties (*Deflection Model #1*) are very similar. This does not occur when orthotropic properties are considered (*Deflection Model #2*). The beam modeled in ANSYS as a panel using plate elements reflects a higher deflection than the beam modeled with SAP2000. This behavior was expected since the beam model in SAP2000 only uses the elastic modulus in the 1-direction, longitudinal to the deck strip, which is higher than the elastic modulus in the 2-direction. On the other hand, the model tested in ANSYS is

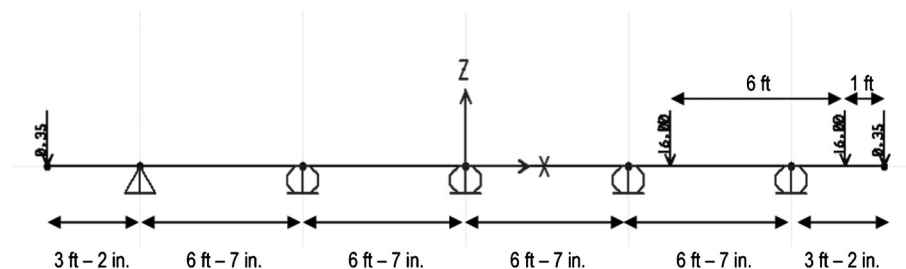


Figure 3.4: Elevation View of Bridge Deck Model + Loading

TABLE 3-1:
Comparisons of Deflection Models

| Model | Beam | Description | Loading | Analysis | Deflection (in) |
|---------------------|------------|---|-----------------|----------|-----------------|
| Deflection Model #1 | Beam #1.1 | 28'-8"x20" Isotropic, E=1940ksi | 1 HS-20 | SAP 2000 | 0.41 |
| | Plate #1.1 | 28'-8"x20" Plate elements, Isotropic, E=1940ksi | 1 HS-20 | ANSYS | 0.21 |
| Deflection Model #2 | Beam #2.1 | 28'-8"x20" Orthotropic, E ₁ =1273ksi E ₂ =806ksi | 1 HS-20 | SAP 2000 | 0.64 |
| | Plate #2.1 | 28'-8"x20" Plate Elements, Orthotropic, E ₁ =1273ksi E ₂ =806ksi | 1 HS-20 | ANSYS | 0.53 |
| Deflection Model #3 | Panel #3.1 | 28'-8"x8'-0" Plate Elements Orthotropic, E ₁ =1273ksi E ₂ =806ksi | 1 HS-20 | ANSYS | 0.43 |
| Deflection Model #4 | Panel #3.2 | 28'-8"x8'-0" Plate elements, Isotropic, E=1940ksi | 1 HS-20 | ANSYS | 0.167 |
| | Beam #4.1 | 32'-2" × 31"x12" Isotropic E=1557 ksi | 4-point loading | SAP 2000 | 0.72 |
| | Beam #4.2 | 32'-2" × 31"x12" Isotropic E=1557 ksi | 4-point loading | SAP 2000 | 5.01 |
| | Beam #4.3 | 32'-2" × 31"x12" Isotropic E=1557 ksi | 4-point loading | ANSYS | 0.72 |
| | Beam #4.4 | 32'-2" × 31"x12" Isotropic E=1557 ksi | 4-point loading | ANSYS | 5.02 |

more flexible, because it takes into account both of the elastic moduli. For beam models, as explained later, this is perhaps not valid, but for panel models, this is perhaps more realistic. If orthotropic properties are used with the panel models (*Deflection Model #3*), the model considers the actual two-way bending of the panel.

- b. From comparisons of the behavior of the panels (isotropic and orthotropic) with the behavior of the different beams, it is observed that the results of the beams are relatively conservative. The isotropic panel (*Deflection Model #3*) resulted in a deflection of 0.167 inch which is significantly smaller than the deflection of the isotropic beam (*Deflection Model #1*) modeled in ANSYS which was 0.41 inch. The orthotropic panel (*Deflection Model #3*) showed the same behavior. In this case, the panel deflected 0.43 inch, which is also smaller than the 0.53 inch observed in the beam modeled in ANSYS (*Deflection Model #2*).
- c. Comparisons with the results given by Lopez (2002) for two different models of a similar beam in ANSYS and SAP2000 show comparable results and suggest that the models are representing the deck fairly well.

As expected, from comparisons among the different models developed to represent an FRP deck bridge, the beam models (*Beam #1.1* and *Beam #2.1*) gave the most conservative results of maximum vertical displacement of an overhang. The orthotropic model of the beam (*Beam #2.1*) gives the highest value – 0.64 inch. However, it should be noted that, from the beam theory, the elastic modulus in the transverse direction and the shear modulus are not used. So, in reality, the orthotropic beam behaves isotropically, which is too conservative considering the fact that the elastic modulus in the longitudinal direction, $E_1 = 1273\text{ksi}$, is much lower than the experimentally derived, equivalent, isotropic elastic modulus, $E = 1940\text{ksi}$.

In order to evaluate the serviceability of a case study bridge (that will be discussed in more detail on the following chapter) with a 38 inch overhang, the conservative value obtained from *Beam #1.1*, 0.41 inches, can be used. If compared with $L/300$, where $L = 38$ inches, the beam does not satisfy the adopted criterion or limit of 0.13 inches.

Deflection Model #4 was created only to certify the validity of the other models, and as expected, both

SAP2000 and ANSYS reproduced the experimental values.

3.4 Alternative Vibration Control Serviceability Criteria

This section presents a proposed acceleration-based serviceability criterion which was based on the results of a numerical parametric study conducted to evaluate the acceleration response of FRP deck-on-steel girder bridges subjected to moving traffic loads. As previously mentioned, the proposed criterion was based on the human tolerance to the bridge acceleration response induced by moving traffic loads. A matrix of bridges representing a wide range of FRP deck-on-steel girder bridge configurations was analyzed. The goal of this study was to determine the acceleration (frequency) response of these bridges when subjected to a moving truck load. Key design parameters such as girder spacing, overhang length, and cross-section geometry were considered. All bridge configurations met relevant strength limits applicable to FRP decks. However, not all bridge configurations satisfied the AASHTO *Length/800* or *Length/300* live-load deflection criterion.

Each bridge configuration was modeled according to the finite element technique presented by Machado et al (2006). Also, each bridge configuration was subjected to a moving traffic loading, according to the dynamic transient analysis described by Machado (2006). Vertical acceleration histories and their correspondent frequency responses were calculated. From these responses, peak accelerations were obtained and compared to the limit of human tolerance presented by Wright and Walker (1971), or 50 in./s^2 .

The presented parametric study also gives information about interaction between various combinations of design variables and peak accelerations. This interaction results in useful recommendations for future designs of FRP-deck-on-steel girder bridges. These recommendations lead to more economical designs than the AASHTO static deflection serviceability criteria. The proposed criterion will enable engineers to more confidently use these decks in real world applications.

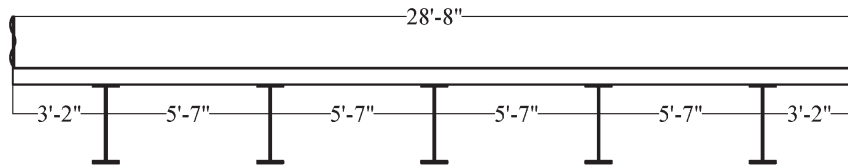


Figure 3.5: FRP deck-on-steel girder bridge cross-sections of models 1,2,3, and 4

3.4.1 Design Parameters

For the parametric study, a preliminary bridge configuration was selected. This preliminary bridge was 50 feet long and 28.675 feet wide. The FRP deck was supported by five W30 × 124 steel girders, spaced at 67 inches and supported by concrete piers at 0 inches and 50 feet. Two 38 inch overhangs completed the width of the bridge. Steel guardrails were used on each side of the bridge. At every 12 feet along the length of the bridge, steel diaphragms, C15 × 33.9, were connected to the girder webs. Four different deck thicknesses were then selected: 6 inches, 8 inches, 10 inches, and 12 inches. After the selection of the preliminary bridge configuration, two other values of girder spacing were also chosen (*i.e.* 6.50 feet and 7.15 feet), keeping the total bridge width constant. The 6.50 feet girder spacing configuration produced two 16 inch overhangs, while the 7.15 feet girder spacing resulted in no overhangs. Figure 3.5, Figure 3.6, and Figure 3.7 show each of the three cross-sections used to investigate the bridge acceleration response induced by moving traffic loadings.

Parameters that described the cross-section of the bridge, *i.e.* the girder spacing (*S*), the deck thickness (*D*) and the overhang length (*O*), were varied throughout the study as illustrated in Table 3-2. From the twelve initially selected bridge configurations, only one configuration, labeled as “Model 1,” was discarded for not meeting minimum strength requirements. The study considered a wide range of ratios varying from 5.58 to 14.33. Also, the study considers two overhang lengths: 16 inches and 38 inches.

3.4.2 Acceleration-Based Serviceability Criterion

Initially the acceleration-based serviceability criteria available in the literature were considered as possible alternatives to the existing AASHTO LRFD static deflection criteria for FRP deck-on-steel girder bridges. However, after thorough investigation, it was concluded that none of these alternative serviceability criteria are suitable for this type of bridge. This is because these criteria were developed for beam-like bridges and, consequently, they only accounted for peak accelerations and/or maximum static deflections that are functions of just the first bending modal frequency of the bridge. Clearly, this ignores the important effect of the first torsional modal frequency when off-centered loads are applied, which typically occurs in bridges under realistic traffic loading. Additionally, according to Oehler (1957), Wright and Green (1959), and Wright and Walker (1971), the peak accelerations were obtained in the travel lane instead of at locations where possible pedestrian or stationary vehicles would likely be located.

Meanwhile, Table 3-3 presents vertical acceleration limits suggested by Oehler (1957) and reported by Wright and Walker (1971). Such limits were based on the reactions of people standing on a bridge to the bridge vertical acceleration response to transient traffic loads. Oehler (1957) concluded that it seems consistent to evaluate human reaction by the amplitudes of sustained acceleration due to the application of a simple harmonic motion with duration of minutes (Goldman 1948), but with a tenfold increase in transient acceleration, due to the application of a

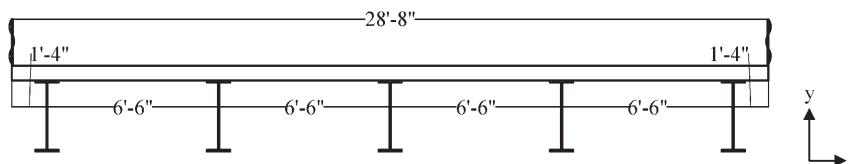


Figure 3.6: FRP deck-on-steel girder bridge cross-sections of models 5,6,7, and 8

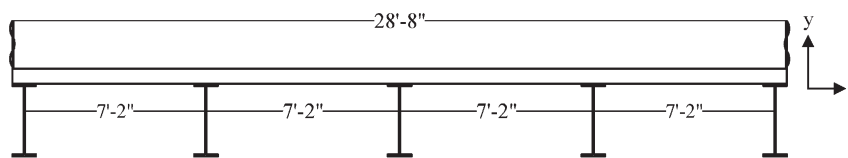


Figure 3.7: FRP deck-on-steel girder bridge cross-sections of models 9,10,11, and 12

TABLE 3-2:
Matrix of Selected Design Parameters

| Parameters | Deck | Girder | Overhang | |
|------------|---------------|-------------|------------|-------|
| Model | thickness (D) | spacing (S) | length (O) | S/D |
| #1 | 6 in. | 5ft-7in. | 3ft-2in. | 11.16 |
| #2 | 8 in. | 5ft-7in. | 3ft-2in. | 8.38 |
| #3 | 10 in. | 5ft-7in. | 3ft-2in. | 6.70 |
| #4 | 12 in. | 5ft-7in. | 3ft-2in. | 5.58 |
| #5 | 6 in. | 6ft-6in. | 1ft-4in. | 13.00 |
| #6 | 8 in. | 6ft-6in. | 1ft-4in. | 9.75 |
| #7 | 10 in. | 6ft-6in. | 1ft-4in. | 7.80 |
| #8 | 12 in. | 6ft-6in. | 1ft-4in. | 6.50 |
| #9 | 6 in. | 7ft-2in. | 0 in. | 14.33 |
| #10 | 8 in. | 7ft-2in. | 0 in. | 10.75 |
| #11 | 10 in. | 7ft-2in. | 0 in. | 8.60 |
| #12 | 12 in. | 7ft-2in. | 0 in. | 7.17 |

motion with duration of seconds. Even though the values presented in Table 3-3 are subjective, they are not a function of the first bending mode of the bridge and can be applied to any type of bridge. Therefore, they were used in this study for direct comparison with peak accelerations obtained for the different bridge configurations used in the parametric study. A maximum peak acceleration of 50 in./s² corresponding to the limit of ‘perceptible’ is used here as a limit for the obtained peak accelerations between girders and at the overhang. Above that limit, accelerations would produce unpleasant reactions, according to the classification given by Oehler (1957). If a bridge presents values greater than the suggested limit, this bridge configuration should be considered to be inadequate and should be redesigned.

3.4.3 Methodology

The selected bridge configurations (“Model 2” to “Model 12” described in Table 3-2) were subjected to the transient dynamic analysis. For that, a thoroughly verified finite element technique, presented by Machado et al. (2006), was used. In this study, the moving AASHTO HS25 truck was represented by a series of point loads traveling at a constant velocity but in discrete steps (Δt), according to the schematic load trend shown in Figure 3.8. From time $t+\Delta t$ to time $t+2\Delta t$, for example, node $i+1$ was loaded by a ramp function

TABLE 3-3:
Peak acceleration limits for human response to vertical vibrations
(Wright and Walker 1971)

| Human Responses | Peak Acceleration (in./s ²) | |
|---------------------|---|-----------|
| | Transient | Sustained |
| Imperceptible | 5 | 0.5 |
| Perceptible to Some | 10 | 1 |
| Perceptible to Most | 20 | 2 |
| Perceptible | 50 | 5 |
| Unpleasant to Few | 100 | 10 |

increasing from 0 to F_m (the magnitude of the truck load) while node i was unloaded by a similar but decreasing ramp force from F_m to 0. A constant number of sub-steps were applied. This had the effect of moving the constant load at a constant velocity but in discrete steps. The magnitude of the AASHTO HS45 truck load was equal to the wheel weight distribution of truck, with two pairs of rear and middle wheel loads of 20 kips spaced 14 feet from each other, and one pair front wheels of 5 kips spaced 14 feet from the middle wheel loads; each pair was spaced 6 feet from the other pair. The truck was positioned in middle of left lane (50 inches from the bridge edge). In the presented parametric study, all bridge configurations had their decks modeled with a constant element length equal to 3 inches throughout the bridge length. Since the adopted truck velocity was equal to 50 mi/hr, the resulting Δt was equal to 0.00341s. Forty sub-steps were used to ensure accuracy of the obtained results. The truck was positioned in the center on the left lane, while peak accelerations were measured at the overhang opposite to the travel lane and between girders at the first deck span inside the same overhang.

From this analysis, acceleration histories and their corresponding frequency responses were obtained at the mid-span and across the width of each bridge configuration, at locations of maximum peak accelerations between girders and at overhang. The acceleration histories were filtered using the procedure described by Machado (2006). From the filtered acceleration histories, peak accelerations were obtained and compared to the limit of 50 in./s². Figure 3.9 shows a typical acceleration history and its respective frequency response of an FRP deck-on-steel girder bridge subjected to a moving load presented in Figure 3.8.

3.4.4 Results

Table 3-4 summarizes the maximum peak accelerations at locations between girders and at the overhang for the different bridge configurations and the comparisons with the acceleration limit of 50 in./s². It should be noted that the obtained peak acceleration for a model of a concrete deck-on-steel girder bridge has a 10% confidence interval when compared with experimental results of peak accelerations measured in the field (Figure 3.10) on the Wildcat Creek bridge on which the finite element model is based (Machado 2006). However, this confidence interval was not incorporated into the results presented in Table 3-4, due to the subjective nature of the 50 in./s² human tolerance limit used for comparison. The results of Figure 3.10 were used to validate the moving loading procedure presented in Figure 3.8. Also, in order to validate the results of peak acceleration presented in Table 3-4, due to lack of experimental values for FRP deck, a modal and a static analysis were conducted using an FRP beam, and the obtained results were compared to available experimental results. Details of these comparisons can be found in Machado et al. (2006) and Machado (2006). The results of the modal and the static analyses showed

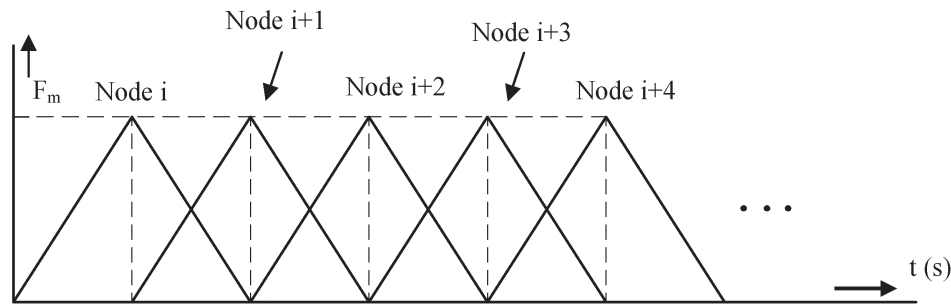


Figure 3.8: Schematic of the applied moving load model

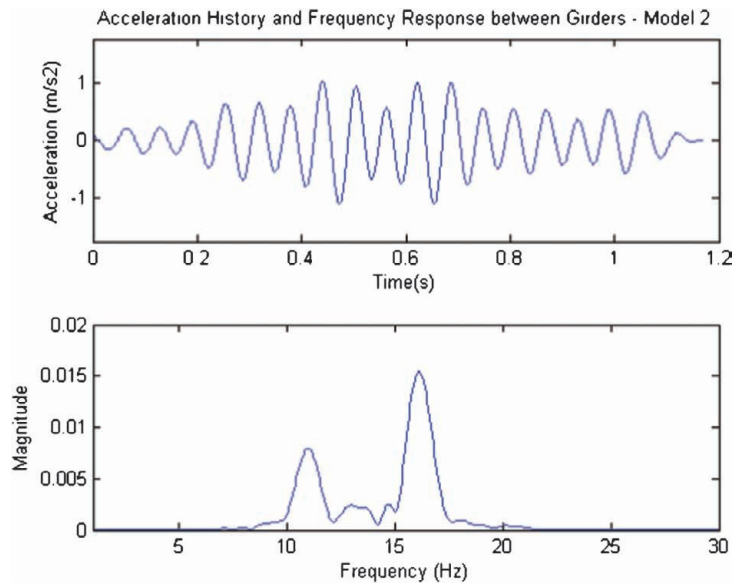


Figure 3.9: Acceleration history and frequency response between girders of model 2

that the numerical model represents well the stiffness and the mass of the FRP panel, main parameters for conducting a dynamic analysis.

“Model 2” (S = 67 inches and D = 8 inches), “Model 5” (S = 6.5 feet and D = 6 inches), and “Model 9” (S = 85.8 feet and D = 6 inches) produced accelerations greater than the limit. “Model 2” and “Model 5” produced peak accelerations equal to 64 in./s² and 61 in./s² at the

overhang, respectively. “Model 5” and “Model 9” produced peak accelerations equal to 55 in./s² and 59 in./s² between girders, respectively. All these values are classified as ‘unpleasant to few,’ according to Table 3-3.

Table 3-4 also shows the comparisons to the AASHTO serviceability criteria. ‘Yes’ or ‘No’ indicates in Table 3-4 whether or not the static deflections satisfy the deflection limits (i.e. the Length/800 limit for the

TABLE 3-4:
Results of parametric study

| Model | Peak acceleration between girders | Satisfy acceleration limit? | Satisfy Length/800? | Peak acceleration at overhang | Satisfy acceleration limit? | Satisfy Length/300? |
|-------|-----------------------------------|-----------------------------|---------------------|-------------------------------|-----------------------------|---------------------|
| #2 | 45 | Yes | Yes | 64 | No | No |
| #3 | 40 | Yes | Yes | 49 | Yes | No |
| #4 | 38 | Yes | Yes | 42 | Yes | No |
| #5 | 55 | No | No | 61 | No | Yes |
| #6 | 46 | Yes | Yes | 48 | Yes | Yes |
| #7 | 41 | Yes | Yes | 36 | Yes | Yes |
| #8 | 38 | Yes | Yes | 29 | Yes | Yes |
| #9 | 59 | No | No | N/A | N/A | N/A |
| #10 | 48 | Yes | No | N/A | N/A | N/A |
| #11 | 43 | Yes | No | N/A | N/A | N/A |
| #12 | 39 | Yes | Yes | N/A | N/A | N/A |

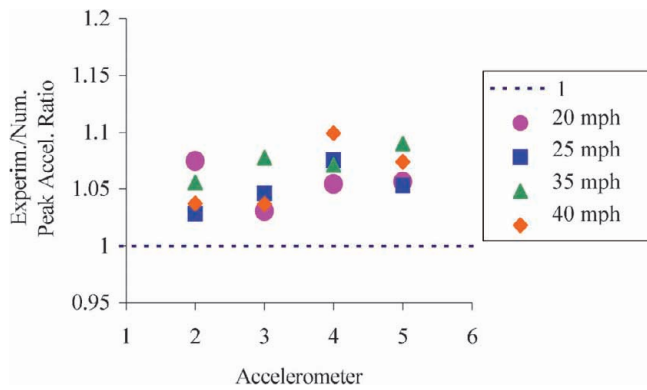


Figure 3.10: Experimental over numerical peak acceleration ratios

girder span and Length/300 for the overhang span). As expected, the application of the AASHTO serviceability criteria to FRP deck-on-steel girder bridges leads to relatively conservative and expensive designs. “Model 2”, “Model 3” ($S = 67$ inches and $D = 10$ inches), and “Model 4” ($S = 67$ inches and $D = 12$ inches) produced static deflections greater than Length/300 at overhang. “Model 5”, “Model 9” ($S = 6.5$ feet and $D = 6$ inches), “Model 10” ($S = 7.15$ ft and $D = 8$ inches), and “Model 11” ($S = 7.15$ feet and $D = 10$ inches) produced static deflections greater than Length/800 between girders. The application of the AASHTO static deflection criteria requires a deck thickness (D) greater than 12 inches, 6 inches, and 10 inches, for bridge configurations with girder spacing (S) equal to 67 inches (with overhang length equal to 38 inches), 78 inches (with overhang length equal to 16 inches), and 7.15 feet, respectively. However, the application of the proposed acceleration-based criterion only requires a deck thickness (D) greater than 8 inches, 6 inches, and 6 inches, respectively, for the same bridge configurations. From Table 3-4, for example, “Model 3” satisfies maximum peak acceleration at overhang, but has a maximum static deflection 69% greater than Length/300 (i.e., a deflection-to-limit ratio of 1.69). Also, from Table 3-4, “Model 10” satisfies maximum peak acceleration between girders, but with a maximum static deflection 27% greater than Length/800, does not satisfy the deflection limit.

3.4.5 Design Recommendations for FRP Deck-on-Steel Girder Bridges

Further analysis of the results of the conducted parametric study revealed trends with respect to deck properties and acceptable accelerations. From these trends, several recommendations were developed for future design of FRP deck-on-steel girder bridges. The recommendations presented below are based upon $\frac{S}{D}$ ratios of the decks and the maximum first bending and first torsional modal frequency ranges of the bridges. The recommendations are:

- A maximum $\frac{S}{D}$ ratio of 11.33.
- A first bending modal frequency no greater than 10.7 Hz.

- For bridges without overhangs, a first bending modal frequency no greater than 11 Hz.
- A first torsional modal frequency no greater than 16 Hz.
- As further verification, the product of the first bending and first torsional modal frequencies should be no greater than 168 Hz².
- For bridges without overhangs, the product of the first bending and first torsional modal frequencies should be no greater than 176 Hz².
- Once D is determined, according to the above recommendations, it is also recommended that the capacity of the bridge deck be checked against strength criteria.
- Additional considerations such as fatigue, cracking of the wearing surface, and failure of the panel-to-panel connection should be addressed per manufacturer recommendations.

It is likely that designers will be faced with bridge configurations different from those used in the presented parametric studies (i.e. bridges with different lengths, number of spans, girder sizes, number of girders, number of lanes, etc.). However, if designers obey the suggested first bending and first torsional modal frequency ranges, all other recommendations can also be applied. Even though the presented parametric study used a relatively narrow number of bridge configurations, the above recommendations can be used to design FRP deck-on-steel girder bridges that are within the same frequency range of the bridges of the parametric study. It is important to notice that the above recommendations are only applicable for bridges with deck-to-girder connection comparable (or with equivalent stiffness and spacing) to the one considered in this study (for the KSCI panel). The characteristics and dimensions of the deck-to-girder connections of the parametric study are described in detail in Machado et al. (2006) and in Chapter 4 of this report. These connections were spaced at every 8 feet along the length of each girder.

Also, by following the above recommendations, designers can rationally select appropriate deck thickness (D) and girder spacing (S) and ensure that the bridge will not have problems with undesirable vibrations, the purpose of any serviceability criterion. By following the above recommendations, designers can also choose a more economical FRP deck than the AASHTO static deflection criteria would allow, making the FRP deck more competitive with respect to traditional materials.

3.4.6 Estimate of First Bending and First Torsional Modal Frequencies

As shown in the previous section, the first bending and the first torsional modal frequencies of FRP deck-on-steel girder bridges are important parameters for the application of the proposed recommendations. Even though a simplified finite element modeling technique was used in this study, the use of such a technique is still too computationally and time intensive for practical designs. Therefore, practical, empirical formulations for determining the first bending and first torsional

frequencies of FRP deck-on-steel girder bridges are presented in this section. Once these two frequencies are determined, the application of the aforementioned recommendations becomes straightforward.

The empirical equations were developed by relating different parameters used in this study with the first bending modal frequency of a simply-supported beam. Wu (2003) showed that the first modal frequency of a bridge is the same as that of a simply-supported beam with equivalent width. In that study, Wu (2003) investigated only composite bridges, so the term $E_G I_G$ was replaced by the term $E_G I_{Tr}$, where I_{Tr} is the transformed moment of inertia of the girder plus the effective width of deck. However, since no composite action is expected in FRP deck-on-steel girder bridges, the stiffness of the deck is ignored.

The empirical first bending modal frequency (f_{bend}) is given by:

$$f_{bend} = \left[S^{(0.0008S+0.024)} \right] \left(\frac{\pi}{2} \right) \sqrt{\frac{E_G I_G}{ML^3}} \quad (3-1)$$

where: S is the girder spacing, E_G is the modulus of elasticity of the girder; I_G is the moment of inertia of the girder alone (no composite action with the deck); M is the total mass of the girder and deck with thickness (D) and equivalent width, according to AASHTO LRFD; and L is the total length of the simply-supported bridge, or the span length of a continuous bridge with equal spans. All parameters should be based on units of kips and inches. The above empirical formulation can be applied for both simply-supported and continuous bridges with equal spans, since the natural frequencies of these two types of bridges are identical. It should be noted that the stiffness of the deck is not taken into account in the $E_G I_G$ term, but included in the $[S^{(0.0008S+0.024)}]$ term. From the above empirical first bending modal frequency, the first torsional modal frequency (f_{tors}), which is also a function of the girder spacing (S), is given by:

$$f_{tors} = \left[S^{(-0.001S+0.17)} \right] f_{bend} \quad (3-2)$$

It should be noted that Eq.(3-1) and Eq.(3-2) are valid only for FRP deck-on-steel girder bridges. For example, a composite RC-deck-on-steel girder bridge has first bending and first torsional modal frequencies equal to 7.14 Hz and 11.3 Hz, respectively. This bridge has same characteristics of the FRP deck-on-steel-girder bridge labeled as “Model 2” in the presented parametric study (*i.e.* a 6 inches long and 344 inches wide bridge, with $D = 8$ inches and $S = 67$ inches). The first bending and torsional modal frequencies have been determined in ANSYS using the eccentric beam model presented by Machado (2006). Eq. (3-1) and Eq.(3-2) would predict first bending and the first torsional modal frequencies equal to 6.15 Hz and 9.53 Hz, respectively. This comparison also reinforced the idea that this type of non-composite FRP deck-on-steel girder bridge has different vibration characteristics than a composite RC deck-on-steel girder bridge of similar

geometry. The same conclusion has been stated by Cai et al. (2006), who studied the difference in vibration response between a self-supported FRP deck bridge and a simply-supported RC deck bridge. On the other hand, for FRP deck “Model 2”, Eq. (3-1) and Eq.(3-2) predicted first bending and the first torsional modal frequencies equal to 10.7 Hz and 16.56 Hz, respectively, with errors of 0.83% and 1.25%, respectively, when compared with 10.61 Hz and 16.36 Hz determined in ANSYS.

3.4.7 Conclusions for Alternative Serviceability Criterion Study

The existing AASHTO static deflection criteria, which are used in the design of bridges with traditional reinforced concrete decks, are not applicable to FRP decks. The proposed alternative serviceability criterion was based on the bridge vertical acceleration response to traffic and human tolerance to vibrations.

This study presents the results of a parametric study with a matrix of FRP deck-on-steel girder bridge configurations. From the filtered acceleration histories, peak accelerations were obtained in places where possible pedestrian or stationary vehicles could be present, *i.e.*, between girders and at the overhang. The obtained peak accelerations are compared to a limit based on human tolerance, a maximum acceptable acceleration equal to 50 in./s^2 . From the comparison with the AASHTO serviceability criterion results, the acceleration-based serviceability criterion produces more economical bridge designs. For example, for a bridge configuration with $S = 67$ inches, following the AASHTO specification, requires a minimum deck thickness (D) of 12 inches, while the acceleration-based criterion requires a minimum D of only 8 inches. This constitutes about 30% savings in deck material costs for this design. Consequently, the application of a more rational serviceability criterion on FRP deck-on-steel girder bridge design makes the use of these decks a more competitive alternative to traditional decks.

From the comparisons among geometric parameters and peak accelerations and natural frequencies, a series of recommendations for the design of FRP deck-on-steel girder bridges were provided. These recommendations provided specific limits for deck thickness (D), girder spacing (S), first bending and first torsional modal frequencies. In order to make the proposed recommendations more practical for implementation, empirical formulations for predicting the first bending and the first torsional modal frequencies of FRP deck-on-steel-girder bridges were also proposed. With these tools, the design engineer would not be required to use three-dimensional finite element models to estimate the frequencies.

It can also be concluded that the proposed design recommendations are appropriate to simply-supported and continuous FRP deck-on-steel girder bridges with equal spans. The only requirement when using the proposed recommendations is that the bridge must

have natural frequencies within the range of those investigated in this work. Even though the parametric study considered only simply-supported bridges, continuous bridges with equal spans have same frequencies and the same maximum response to traffic as simply-supported bridges and can be design following the proposed recommendations.

3.5 Hybrid Beam Concept

Based on the lack of sound technical background literature regarding serviceability criteria for FRP decks, for the case study bridge, the decision was made to follow the AASHTO LRFD 1998 design guidelines (L/300 on cantilever arms and L/800 for spans between girders), as they provide conservative results. From the numerical analyses shown in Section 3.3, it can be concluded that the L/300 criterion for a 3'-2" overhang will not be satisfied under the loading conditions specified by AASHTO. For this reason, there is a need to further study different methods to increase the stiffness of the FRP panel.

As a result of this stiffness problem, the concept of incorporating steel into the cross section of the KSCI FRP bridge deck panels was proposed by the manufacturer. This led to initial studies performed to determine the most effective, economical and practical method of combining steel with FRP. The incorporation of steel in either the face sheets or the honeycomb core was explored to determine the most efficient way to increase the sandwich panel flexural and shear stiffness.

This investigation included numerical parametric and experimental studies. The parametric studies were used for preliminary evaluation of various options before choosing one option for experimental validation. The initial parametric study involved a hybrid concept of embedding steel plates within the KSCI face sheet fiber layup (Hybrid Model 1 in Table 3-5). Also studied was an option including placement of steel tubes at discrete locations within the KSCI honeycomb core (Hybrid

Model 2 in Table 3-5). Based on results from the steel tube parametric studies, additional analyses were needed to assess the independent contributions of the face sheets and honeycomb core to the overall stiffness of the KSCI product (Hybrid Model 3 in Table 3-5). These results led to the development of a steel hexagonal honeycomb core concept. Finite element (FE) parametric studies were then performed to determine the best available hexagonal honeycomb core geometry based on industry provided steel floor and roof deck (Hybrid Model 4 in Table 3-5). The finalized steel deck core concept was then compared with the hybrid face sheet embedded steel plate idea to determine the most practical GFRP-steel end product. The steel deck hexagonal honeycomb core was chosen as the final hybrid concept and was investigated experimentally. The experimentation included a set of small-scale tests, the purpose of which was to determine the orthotropic elastic moduli of the steel hexagonal honeycomb (Lombardi, 2008; Lombardi and Liu, 2009). Large-scale tests (Specimens 5 and 6 in Table 3-5) were also performed. The large-scale tests were used to determine the stiffness contribution of the steel core when incorporated into the KSCI sandwich constructed bridge deck panels and served as a pilot study for the GFRP-steel hybrid concept.

3.5.1 Preliminary Hybrid Parametric Analyses (Hybrid Models 1 and 2)

Hybrid Models 1 and 2 included the alternative of pattern hole-punched steel plates within the face sheets and the alternative of steel tubes at discrete points within the existing reinforced-sinusoidal honeycomb core, respectively. The steel plates were to increase the flexural rigidity (EI) of the face sheets by increasing the moment of inertia of the transformed composite cross section. The tubes were envisioned to provide anchoring points to the supporting bridge beams and also to stiffen the overhang. In parametric studies on both alternatives, the cantilever span lengths were 24 inches,

TABLE 3-5:
Hybrid GFRP-steel study progression matrix

| Hybrid Model/ Specimen | Type | Configuration | Parameters | Numerical/ Experimental | Comments |
|---------------------------|-------------------------------------|--|---|----------------------------|--|
| 1 | Steel plates in face sheet | 2D cantilever (3D FE/ structural analysis/equiv width) | Plate thickness, cantilever span | Numerical | Preliminary parametric study to investigate feasibility of option |
| 2 | Steel tubes in core | 3D cantilever (FE) | Tube thickness, tube spacing, cantilever span | Numerical | Preliminary parametric study to investigate feasibility of option |
| 3 | L-, W-dir KSCI core beam | 3D simply supported beam (FE) | Face sheet modulus and thickness Core wall modulus and thickness | Numerical | Investigate role of face sheet stiffness using isotropic face sheet Investigate role of core stiffness using isotropic face sheet |
| 4 | L-, W-dir steel core beam | 3D simply supported beam (FE) | Steel deck core configuration | Numerical | Preliminary evaluation of steel core concept |
| 5 | Baseline L-, W-dir KSCI beams | Simply supported beam | — | Experimental | Provide baseline for hybrid (steel core) concept |
| 6 | Hybrid (steel core) L-, W-dir beams | Simply supported beam | — | Experimental | Evaluation of hybrid (steel core) concept |

36 inches and 48 inches to capture a range of overhang lengths. Also, in each study, the cantilever was loaded at the free end with a 16 kip load (i.e., AASHTO HS20-44 service wheel load). The model dimensions were typical of KSCI production at the time, with an overall depth of 8 inches, a core depth of 7 inches and a face sheet thickness of 1/2 inches. The reinforced-sinusoidal honeycomb core wall thickness was 0.09 inches.

3.5.1.1 Steel Plate Embedded In Face Sheets (Hybrid Model 1)

The steel plate parametric study was based on simple equivalent beams and therefore involved the assessment of equivalent width. The equivalent width determination for the beam model was based on relating three-dimensional (3D) FE deflection results to two-dimensional (2D) beam deflection calculations. An equivalent width that would allow for use of 2D structural analysis cantilever deflection calculations in the parametric study was determined using Eq. (3-3).

$$\Delta_{FE} = \frac{PL^3}{3E_1I_f} + \frac{6}{5} \frac{PL}{G_{ChSM}A_c} \quad (3-3)$$

In Eq. (3-3), Δ_{FE} is the maximum cantilever deflection using 3D FE. P is the load applied at the cantilever tip, L is overhang span, E_1 is the face sheet modulus in the span direction, $6/5$ is the form factor for shear of rectangular cross sections, and G_{ChSM} is shear modulus of ChSM core walls. I_f is the face sheet moment of inertia written in terms of the equivalent width, b_{equiv} , beam depth, D , and core depth, d_c . A_c is the area of flats (sinusoidal area is neglected) in the KSCI core written in terms of b_{equiv} , d_c , and the flat thickness, t_{flat} . The equivalent width is then the variable that can be solved for in Eq. ((3-3).) (Lombardi, 2008).

The solid steel plates varied in thickness from 22 gauge (0.034 inches) to 11 gauge (1/8 inches). For the initial analyses, holes in the plates were neglected. The resulting, hybrid face sheet moment of inertia was computed based on a transformed section calculated using mechanics of materials principles.

3.5.1.2 Steel Tubes Placed within Honeycomb Core (Hybrid Model 2)

Steel tube parametric studies were conducted using ABAQUS FE software, since the hybrid deck cross section was not uniform across its width. The structure analyzed in FE was a detailed, 3D FRP hybrid (FRPh) cantilever model, representing the overhang of a bridge deck. The detailed model included the geometry of the reinforced-sinusoidal honeycomb core as seen in Figure 3.11. The parameters included cantilever span, tube thickness and center-to-center tube spacing. Steel tubes with dimension 4 inches by 7 inches with varying wall thicknesses of 1/16 inches, 1/8 inches, 1/4 inches, 3/8 inches, 1/2 inches, and 5/8 inches were used. The center-to-center tube spacing along the longitudinal axis of the bridge (i.e., steel tubes running perpendicular to the bridge longitudinal direction) 24 inches or 48 inches.

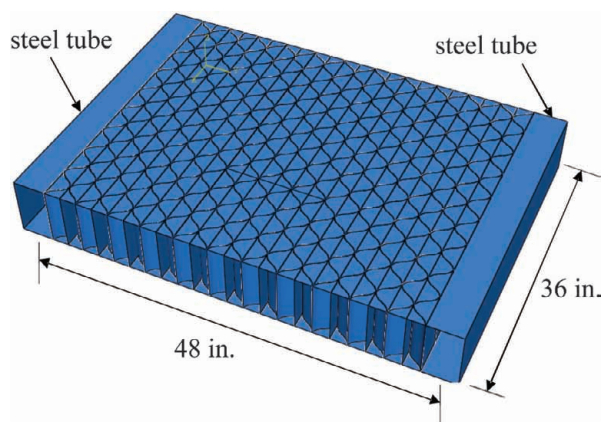


Figure 3.11: Steel tube FE model: 36 inch overhang/48 inch tube spacing

These spacings were considered to be practical based on the KSCI honeycomb core geometry, as the tubes would replace unit cells within the core and would not require cutting of any core elements. For the purpose of the FE parametric analyses, an ideal perfect connection was modeled between the face sheets, steel tubes, and honeycomb core.

Four face sheet layup alternatives were studied to assess the performance of the steel tube hybrid concept. The main focus was to improve the face sheet stiffness in the direction spanning between the steel tubes (E_2). It was desired to increase the stiffness in this direction because the FE model results demonstrated that two-way bending, or dishing, was occurring at the load application point. The initial face sheet was based on KSCI's original layup consisting of two biaxial, nine uniaxial, and one 3 oz/ft² ChSM bonding layer, where the elastic properties were determined experimentally by Kalny et al. (2004). The Kalny face sheet elastic properties are designated as (I). The next face sheet layup was based on strength studies conducted by Chen (2004). Elastic moduli were computed for each stacking sequence specified in Chen. The Chen layup, consisting of seven biaxial plies, produced the highest E_2 modulus and was chosen for the study and will be designated as (II). Face sheet designation (III) is the maximum in-plane 2-direction stiffness, E_2t , which consists of eight biaxial and two uniaxial plies. The final face sheet (IV) was evaluated to produce maximum in-plane shear stiffness, $G_{12}t$. This face sheet layup consisted of five $\pm 45^\circ$ and three biaxial plies.

Figure 3.12 displays an example comparison of steel plate (Hybrid Model 1) and steel tube (Hybrid Model 2) results for a 36 inch overhang. The figure plots maximum overhang deflection as a function of steel area. The labels (I), (II), (III), and (IV) are the four face sheet alternatives described earlier. The AASHTO overhang span-to-deflection limitation of $L/300$ was also plotted for comparison. All steel tube (Hybrid Model 2) alternatives were ineffective compared to the steel plate option (Hybrid Model 1), regardless of face sheet. For all face sheet layups, it was seen that for

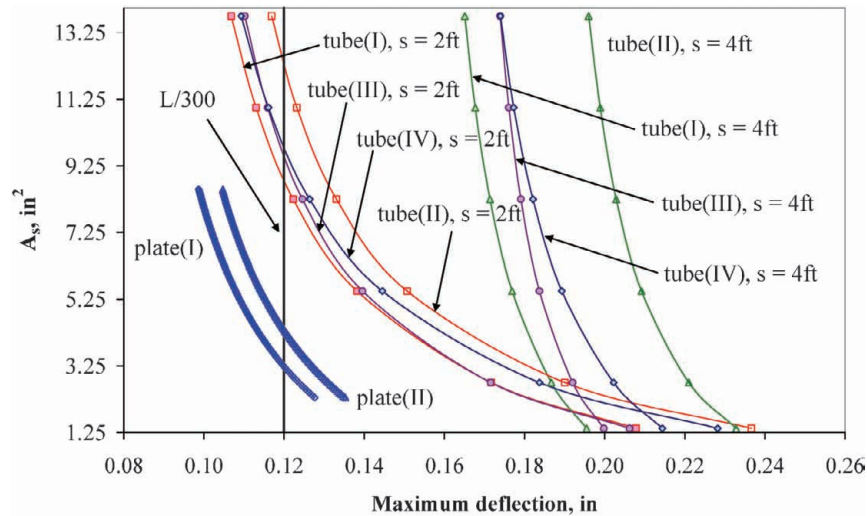


Figure 3.12: Steel plate and steel tube summary: 36 inch overhang

equal areas of steel, the plate option produced less deflection and was capable of satisfying the AASHTO LRFD (2004) span-to-deflection ratio of $L/300$ (Figure 3.12). For all overhang span lengths explored, the steel tube idea demonstrated a higher flexibility than the plate concept. The 24 inch tube spacing was the only option that satisfied the $L/300$ criterion, but required tubes with wall thicknesses of $\frac{1}{2}$ inches and $\frac{5}{8}$ inches to attain the required stiffness. It was decided to eliminate the steel tube hybrid idea as a result of its dependence on thick and/or high modulus face sheets as well as thick-walled, heavy steel tubes, since this would result in an impractical design.

Thus, additional hybrid alternatives were pursued and compared with the steel plate option. The focus of the other options would involve an attempt to create a hybrid FRP-steel concept that combined superior stiffness and less stringent constructability requirements than the steel plate concept. These constructability requirements were related to quality control in the manufacturing of the steel plate hybrid idea. The primary concerns involved the embedment of steel into the fiberglass face sheets and steel contaminants such as

dirt and surface rust which needed to be kept out of the face sheet. These contaminants could result in a poor bonding between the face sheet lamina and the steel thus causing delamination at their interface.

3.5.1.3 KSCI L-Direction and W-Direction Beam Studies (Hybrid Model 3)

In the previous steel tube analyses, deformations were localized to the point of load application, regardless of face sheet stiffness. This suggested that the honeycomb core was the main contributor to the hybrid deck panel deformations. Therefore, the next step was to study the effect of the honeycomb core geometry on these deformations. The assessment of the core stiffness would involve investigation of the core in both the L-direction and W-direction (refer to Figure 3.13, which shows the L and W directions).

3.5.1.3.1 Face Sheet and Honeycomb Core Stiffness Study (Hybrid Model 3) The Hybrid Model 3 study would assess contributions of the honeycomb core in the L and W directions through comparisons of simply supported (three-point bending) beam model results. It was anticipated that later

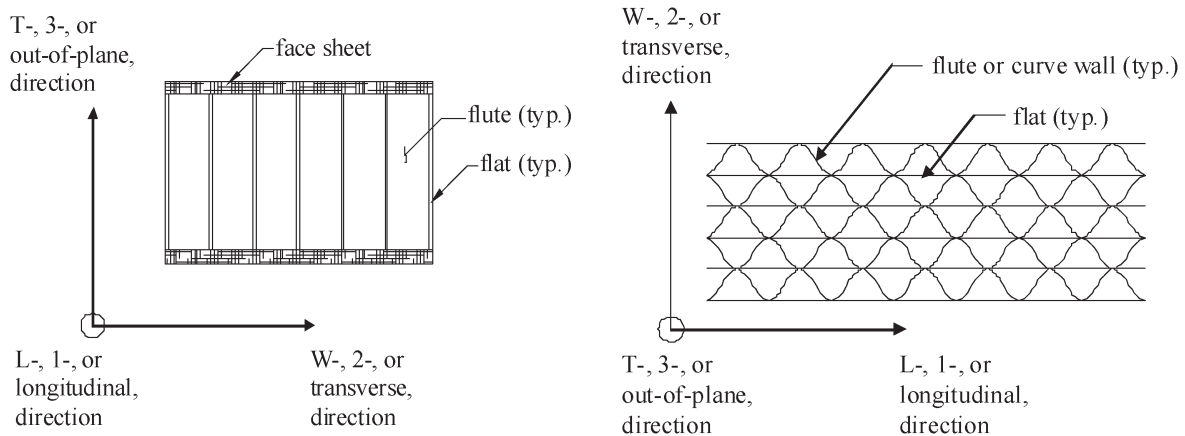


Figure 3.13: KSCI cross section (left) and plan view (right)

experimental tests would be most easily conducted on simply supported beams. The beam cross section was 8.25 inches deep and spanned 8 feet between supports. Isotropic (aluminum) face sheets were modeled to eliminate the directional properties of orthotropic FRP materials thus focusing the study on the directional properties of the honeycomb core. Furthermore, by changing the isotropic face sheet stiffness, the effects of the face sheet could be assessed for both the L and W directions. The main objective was to determine how a beam with longitudinal axis oriented in the W-direction changed stiffness relative to an L-direction beam.

The beams were studied with three scenarios for the face sheets. The first case was the baseline with $E = 10,000$ ksi, $\nu = 0.30$ and face thickness, $t_f = 1/2$ inches. For the second case, the face sheet thickness was increased by 25%, making $t_f = 5/8$ inches, with the material properties remaining the same as the baseline. For the third and final case, the face sheet elastic modulus was increased by 25%, making $E = 12,500$ ksi. Again, the remaining properties were kept the same as the baseline case. The above three face sheet cases were studied for beams with the KSCI honeycomb core spanning in both the L-direction and W-direction.

The beams were then studied with three scenarios for the honeycomb core. The aluminum face sheet properties were the same as the baseline case from before. The first case was the baseline with $E_{ChSM} = 1,150$ ksi, $\nu_{ChSM} = 0.30$ and core wall thickness, $t_{wall} = 0.09$ inches. For the second case, the core wall thickness was increased by 25%, making $t_{wall} = 0.113$ inches, with the material properties remaining the same as the baseline. For the third and final case, the core wall elastic modulus was increased by 25%, making $E_{ChSM} = 1,440$ ksi. Again, the remaining properties were kept the same as the baseline case.

Figure 3.14 summarizes the results of the face sheet and honeycomb core stiffness analyses. The y-axis plots

the beam midspan deflection, normalized to the baseline case, while the x-axis plots the stiffness variables (i.e., elastic modulus, E , and thickness, t) for both the L and W direction core beams. The stiffness variables are for both the face sheet and honeycomb core walls. As can be seen from the figure, the W-direction stiffness is increased (midspan deflection decreased) most significantly when the honeycomb core wall thickness or elastic modulus were increased. This shows that the W-direction is influenced most by the honeycomb core stiffness, not from the face sheet stiffness.

Therefore, it was decided to pursue modifications to the existing KSCI honeycomb core in an attempt to stiffen the existing KSCI sandwich panel.

3.5.1.4 Steel Deck Hexagonal Honeycomb Core Concept (Hybrid Model 4)

It was desirable to increase the overall stiffness of the existing KSCI honeycomb core without drastically changing the current design and fabrication methods or eliminating the high strength-to-weight ratio. Based on previous model results, the main objective for Hybrid Model 4 was to increase the W-direction core stiffness while maintaining or improving the L-direction stiffness. Most important of all, the new core design needed to be easily constructed. With these considerations, it was decided to maintain a honeycomb core, but to construct it out of steel decking. Two steel deck suppliers were considered for their products, United Steel Deck, Inc. and Vulcraft. The steel deck choices from each company were based on keeping the unit cell sizes as close to the current KSCI design as possible, again to try to provide an easily adaptable product while maintaining the identity of the KSCI product.

Simply supported L-direction and W-direction core beam studies were conducted in ABAQUS to assess the effectiveness of each steel deck honeycomb core orientation as compared with the current KSCI

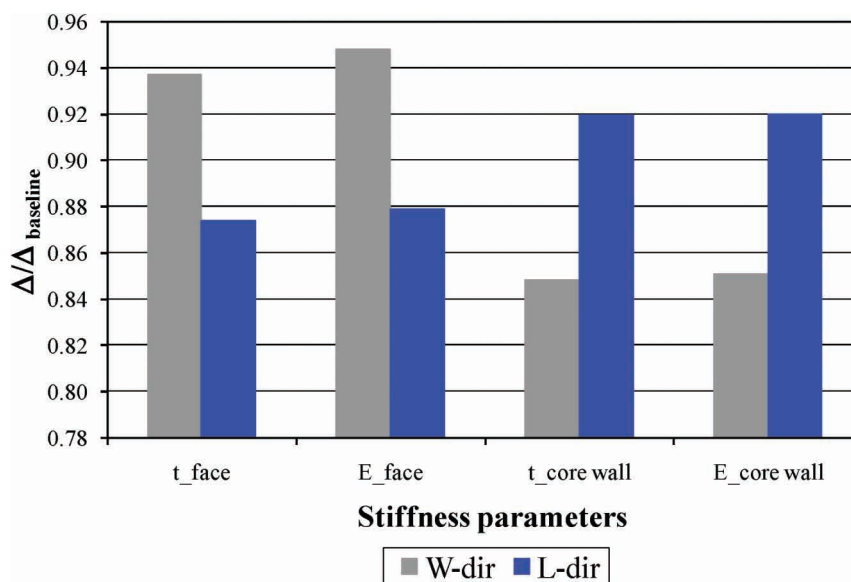


Figure 3.14: Face sheet stiffness/honeycomb core stiffness study results

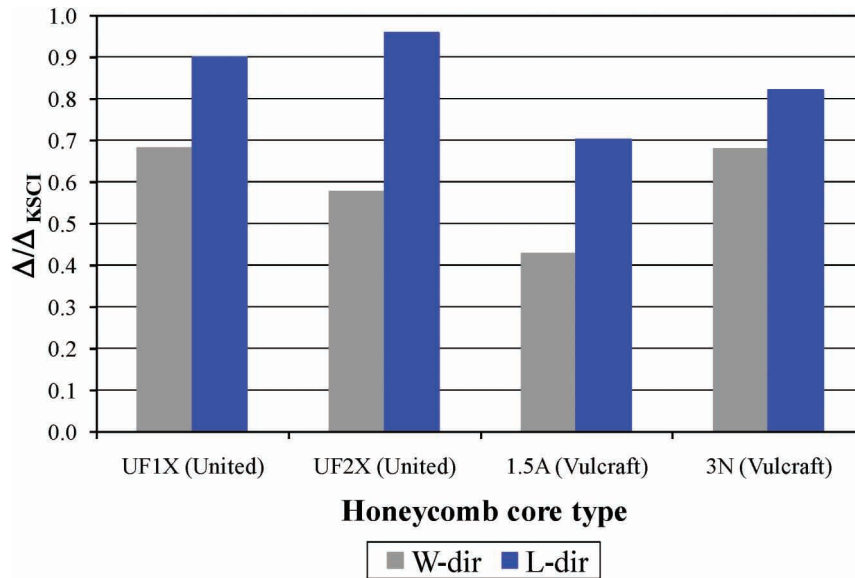


Figure 3.15: Steel deck core FE model comparison

honeycomb core (Figure 3.15). In Figure 3.15, the y-axis plots the hybrid beam midspan deflection, normalized to the KSCI deflection, while the x-axis plots the steel deck type, for both the L and W direction core beams. From the figure, it is clear that the Vulcraft 1.5A roof deck reduces the KSCI deflections the most in both the L and W directions. Therefore it was concluded that the 1.5A steel decking would be used to replace the existing KSCI reinforced-sinusoidal honeycomb core and would be investigated experimentally in further detail. The Vulcraft 1.5A basic unit cell is shown in Figure 3.16 (Lombardi, 2008). As shown in the figure, the unit cell dimensions include wall thickness, $t = 0.048$ inches, $h = 5$ inches, $l = 1.53$ inches, and $\theta = 0.204$ radians.

Note that this steel honeycomb configuration would be used simply to determine the best of the existing floor or roof steel deck options for the honeycomb core, tested at the request of KSCI as a proof of concept. The steel honeycomb core was not optimized for the $L/300$ requirement of the Wildcat Creek Bridge. The steel honeycomb core, while heavier than the GFRP core, would result in a weight equivalent to 12% the weight

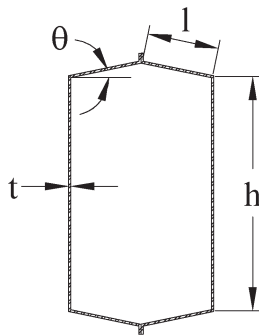


Figure 3.16: Vulcraft 1.5A hexagonal honeycomb core unit cell

of a solid concrete deck. Light weight and corrosion resistant properties, as previously mentioned, are useful in any application where these characteristics are deemed essential.

3.5.2 Experimental Studies (Specimens 5 and 6 in Table 3-5)

The purpose of testing large-scale beams with both the steel hexagonal core and the current KSCI reinforced-sinusoidal core was to compare the improved stiffness of the overall hybrid concept to the current KSCI design in both the L and W directions. It was anticipated, based on the increased shear stiffness of the steel hexagonal honeycomb core, that the hybrid beams would exhibit increased stiffness over the KSCI beams in both the L and W honeycomb core directions.

3.5.2.1 Hybrid and KSCI L and W Direction Beams (Specimens 5 and 6)

L and W direction large-scale hybrid and KSCI beam specimens were tested in three-point bending to obtain and compare load versus displacement data. The face sheet consisted of biaxial and ChSM layers, and therefore had equal elastic moduli in the plane of the face sheet (L and W directions). Since the face sheet layups were the same for the hybrid and KSCI beams, the effect of the honeycomb core could be isolated. The contribution of the steel core to the overall beam stiffness could then be assessed in comparison with the KSCI fiberglass reinforced-sinusoidal core. From the load versus displacement data, equivalent flexure and shear modulus plots would be obtained and used to compare with the KSCI conventional baseline beam specimens.

The hybrid beam experimental investigation included the testing of two L-direction and two W-direction beam samples. The connection between face and steel core was achieved as previously described for the FRP

KSCI honeycomb core. The two L-direction large-scale hybrid beam specimens were 12 inches wide (4 unit cells). This was based on typical KSCI practice. The core was 7 inches thick to represent in-field applications. The simply supported beam span was 7'-6" or 90 inches center-to-center of supports. The two W-direction large-scale hybrid beam specimens were both 18 inches wide (3 unit cells) to allow the formation of two longitudinal stiffeners from the intermediate cells produced when the honeycomb core was assembled (Figure 3.17). The core depth and beam span were the same as that for the L-direction beams.

The KSCI baseline beam experimental investigation included the testing of only one L-direction and one W-direction beam sample. The large-scale KSCI control beam specimens were both approximately 12 inches wide as per typical KSCI practice (2.5 unit cells and 3.5 unit cells for the L-direction and W-direction beams, respectively). The core depth and beam span were the same as for the hybrid beam specimens.

Figure 3.18 displays the components used in all large-scale hybrid and KSCI beam specimen testing series. The supports included W14 × 82 steel beams with plates and rollers welded to the top flanges. Both plates had grooves for the rollers to set in, resulting in pin supports at both ends of the beam. In order to create a roller at one support, Teflon was adhesively attached to the ½ inch thick neoprene pads placed between the beam specimens and the support plates/rollers. The load was introduced from a hydraulic ram onto the plate and roller assembly at midspan of the beam (Figure 3.18). An additional 6 inches wide by 12 inches long by 1 inch thick plate was placed between the larger plate and roller assembly and beam sample to provide the desired bearing area on the specimens. A ½ inch thick piece of neoprene was placed between the load plate and the beam specimen to reduce stress concentrations from the loading plate.

Instrumentation of the large-scale beams consisted of two linear variable differential transducers (LVDTs), one placed on either side of the specimen at midspan (Figure 3.18). Five strain gage rosettes were also placed on the honeycomb core, three on one side and two on the other, located approximately at the quarter span of the simply supported beam. On the three rosette side,

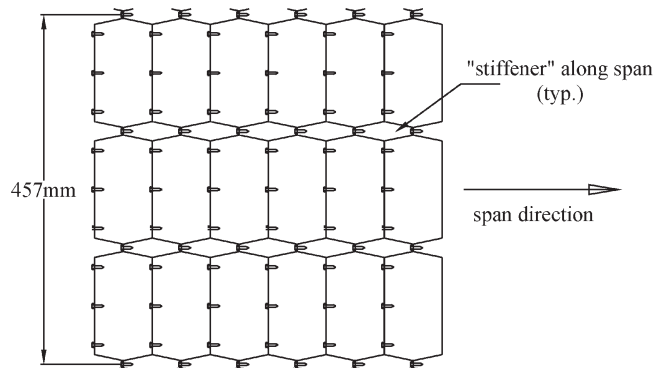


Figure 3.17: W-direction hybrid beam honeycomb core (plan view)

the rosettes were placed through the depth of the core (Figure 3.18, middle left). The first rosette was placed at the neutral axis, or middle of the core, with the other two placed 2.5 inches above and below the neutral axis rosette. The side with two rosettes had the reference rosette at the neutral axis with the other gage placed 2.5 inches below the neutral axis (Figure 3.18, middle right). In addition, two uniaxial strain gages were placed on the core to confirm longitudinal strain readings from the strain rosettes (Figure 3.18, middle left). At the same location of the rosettes along the span, two uniaxial strain gages were placed both on the top and bottom face sheets across the width. Two uniaxial strain gages were also placed at midspan on the bottom face sheet to obtain maximum bending stresses of the beams. Finally, for the hybrid beam samples, two strain gage rosettes were embedded within the top and bottom face sheets across the width at the same longitudinal locations as the core rosettes and face sheet uniaxial strain gages.

3.5.3 Equivalent Flexural Modulus Comparison

The beam specimens tested as part of the experimental program all had slightly different cross sectional dimensions between each set of core direction specimens. The beams all had about the same face sheet thickness and core thickness, but the hybrid beam specimens displayed face sheet widths that varied slightly between sets of specimens. The core widths and face sheet widths were not comparable between hybrid and KSCI control beams, therefore prohibiting direct load versus displacement comparisons. Thus, it was decided to compare both equivalent flexural stress versus average midspan strain gage readings and equivalent shear stress versus average maximum shear strain gage readings from each test. The bending stress was computed in Eq. (3-4) using the flexure formula, whereas the bending moment was that for a simply supported beam with a concentrated load at midspan.

$$\sigma = \frac{Mc}{I_{transf,b}} = \frac{(PL/4) \times (D/2)}{I_{transf,b}} = \frac{PLD}{8I_{transf,b}} \quad (3-4)$$

In Eq. (3-4), σ is the normal stress due to bending and M is the maximum bending moment occurring at the beam midspan, equal to $PL/4$. P is the applied midspan load, and L is the beam span, center-to-center of supports. The variable c is the distance from the neutral axis to the extreme fiber of the beam cross section; or half of the total beam depth, $D/2$. $I_{transf,b}$ is the transformed moment of inertia of the hybrid beam composite cross section. The moment of inertia was transformed with respect to the face sheet because all beam specimens had identical face sheet layups resulting in elastic moduli and face sheet thicknesses that were all the same. The equation defining the transformed moment of inertia is shown in Eq. (3-5), where the modular ratio, n_c , is simply the fraction of the core modulus to the face sheet modulus, or E_{core}/E_{face} . Values b_f and t_f are the width and thickness of the face sheet.

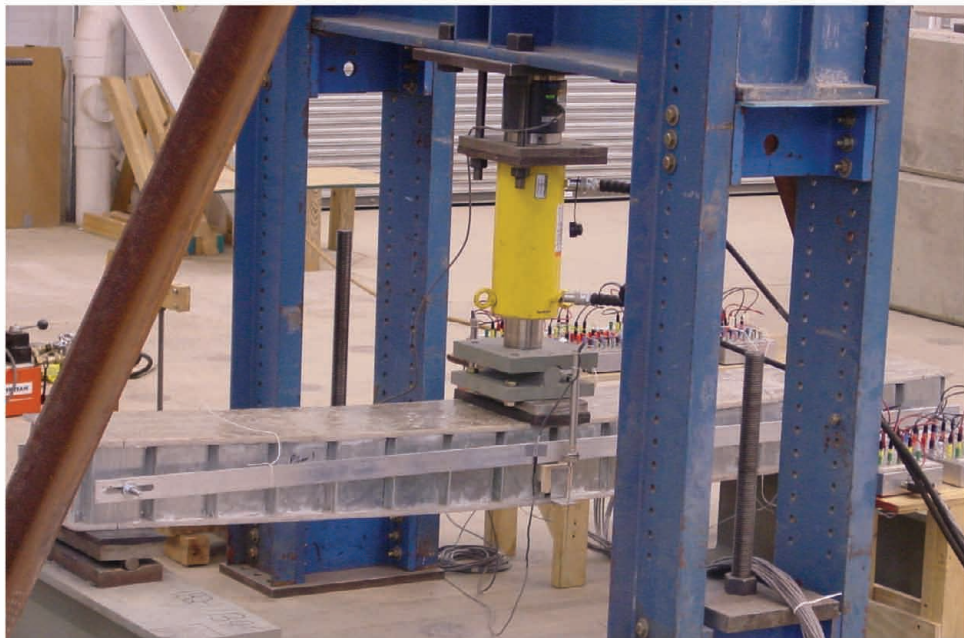
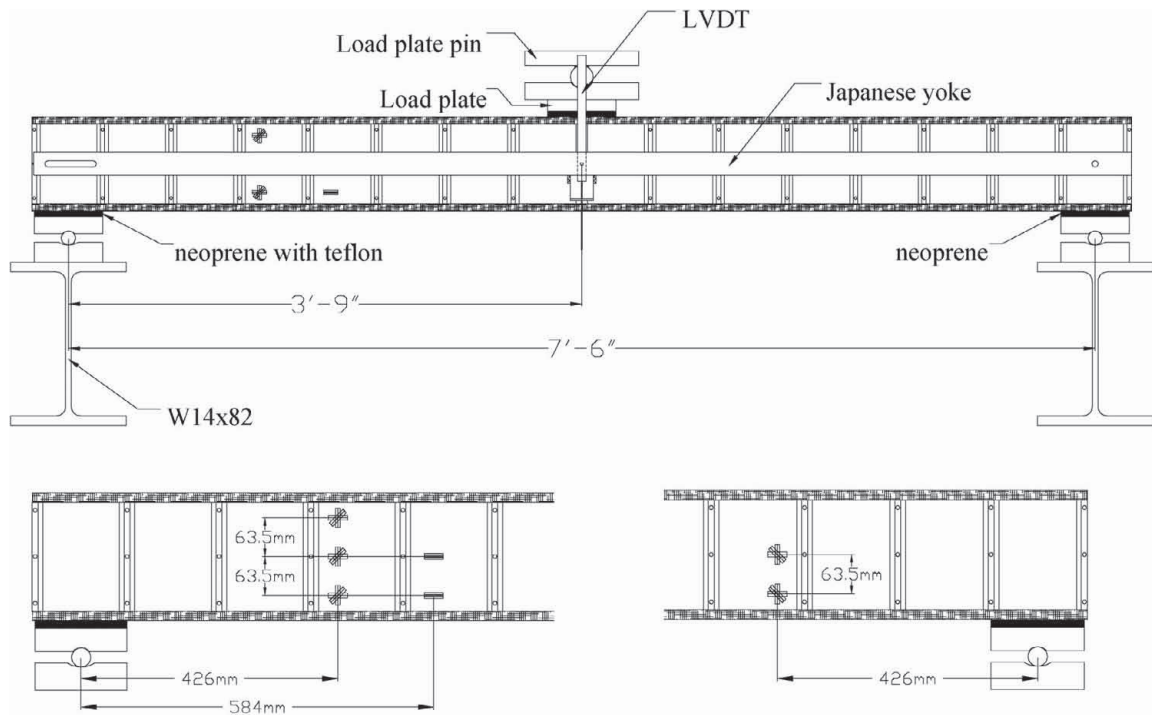


Figure 3.18: Typical beam test setup and components (drawings and photo of specimen being tested)

The honeycomb core was represented by an equivalent core. The equivalent core was a solid section, of the same overall depth, d_c , and width, b_c , of the original core. This equivalent core had an equivalent modulus derived from the small-scale tests conducted prior to the large-scale tests (Lombardi, 2008; Lombardi and Liu, 2009). These small-scale tests included tension and compression tests of unit cells in each orthogonal direction. Shear tests

were also conducted. As such, parameters for modeling a unit cell as a solid section were developed.

$$I_{transf,b} = 2 \left(\frac{b_f t_f^3}{12} + b_f t_f \left(\frac{t_f + d_c}{2} \right)^2 \right) + \frac{n_c b_c d_c^3}{12} \quad (3-5)$$

The resulting equivalent elastic flexural moduli for all L and W direction beam specimens are displayed in

TABLE 3-6:
L and W direction beam equivalent flexural modulus summary

| Specimen | E_L (GPa) | $E_{L,Hybrid}/$ $E_{L,KSCI}$ | E_W (GPa) | $E_{W,Hybrid}/$ $E_{W,KSCI}$ |
|----------|-------------|---------------------------------|-------------|---------------------------------|
| Hybrid-1 | 14.6 | 1.45 | 16.6 | 1.13 |
| Hybrid-2 | 14.1 | 1.41 | 13.6 | 0.92 |
| KSCI | 10.1 | — | 14.7 | — |

Table 3-6. As shown in the table, the hybrid beams are an average of 43% stiffer as compared with the KSCI specimen in the L-direction. Since each beam specimen contained identical face sheet material and thickness, the increase in stiffness can be attributed to the steel expanded hexagonal core geometry and material properties.

From the results shown in Table 3-6 for the W-direction beam specimens, the KSCI beam equivalent stiffness falls between the two hybrid beams. This is a display of inconsistency between two hybrid beam specimens. The inconsistency can manifest itself from such factors as production variability (i.e., the bonding of the face sheet to the steel core). Therefore, it can only be concluded that the existing KSCI W-direction beam is about as stiff as the average of the corresponding experimental hybrid beams, contradicting initial predictions. This could have been due to the changes in the KSCI honeycomb core production methods. The honeycomb core wall thickness was increased from the time the initial analyses were performed. Also, an improved construction technique used by KSCI to assemble their honeycomb core significantly increased the end product quality, and thus the structural performance.

3.5.4 Equivalent Shear Modulus Comparison

It was advantageous to compare the equivalent shear moduli of both the KSCI and hybrid honeycombs since

TABLE 3-7:
L and W direction beam equivalent shear modulus summary

| Specimen | G_{LT} (ksi) | $G_{LT,Hybrid}/$ $G_{LT,KSCI}$ | G_{WT} (ksi) | $G_{WT,Hybrid}/$ $G_{WT,KSCI}$ |
|----------|----------------|-----------------------------------|----------------|-----------------------------------|
| Hybrid-1 | 361 | 2.56 | 335 | 4.28 |
| Hybrid-2 | 482 | 3.41 | 382 | 4.89 |
| KSCI | 141 | — | 78.3 | — |

the honeycomb was the only difference between the two beam specimen types. As per structural sandwich panel theory (Allen, 1969), the shear stiffness was contributed mainly by the honeycomb core. The transverse honeycomb core shear stress was computed in Eq. (3-6), where the shearing force was that for a simply supported beam with a concentrated load at midspan.

$$\tau = \frac{VQ_{transf,v}}{I_{transf,v}b_c} = \frac{(P/2) \times Q_{transf,v}}{I_{transf,v}b_c} = \frac{PQ_{transf,v}}{2I_{transf,v}b_c} \quad (3-6)$$

In Eq. (3-6), τ is the transverse shear stress and V is the maximum shear force, equal to $P/2$. The variable b_c is the width of the honeycomb core. $I_{transf,v}$ is the moment of inertia of the hybrid beam composite cross section, transformed into all honeycomb core material. $Q_{transf,v}$ is the first area moment with respect to the neutral axis of the transformed section. P is the applied midspan load. Similar to the flexural modulus comparison, the transformed moment of inertia was computed by converting the face sheet into equivalent honeycomb core material through the modular ratio.

Figure 3.19 shows a summary shear stress versus strain plot of all L-direction large-scale beams tested. The equivalent elastic shear modulus for each specimen is also displayed in Table 3-7. As shown in the table, the hybrid beams are an average of 298% stiffer as compared with the KSCI specimen. Since the beam comparison was based on equivalent honeycomb core properties, the increase in stiffness is directly related to

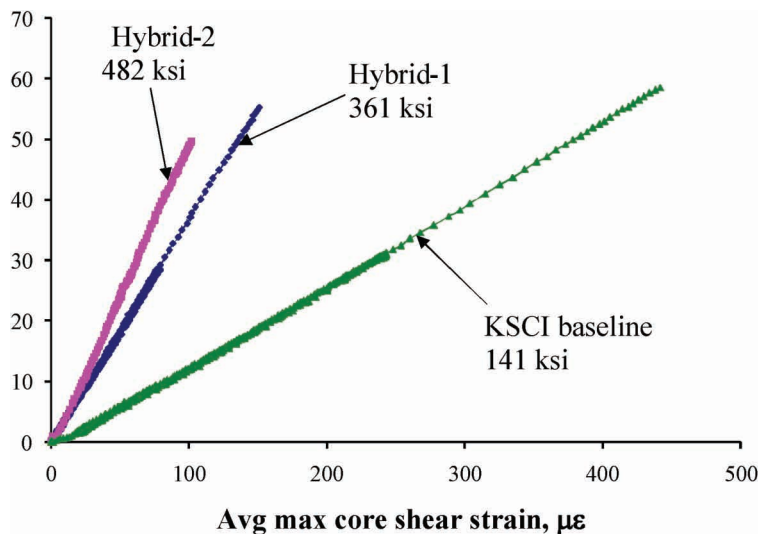


Figure 3.19: L-direction beam core shear stress vs. strain summary

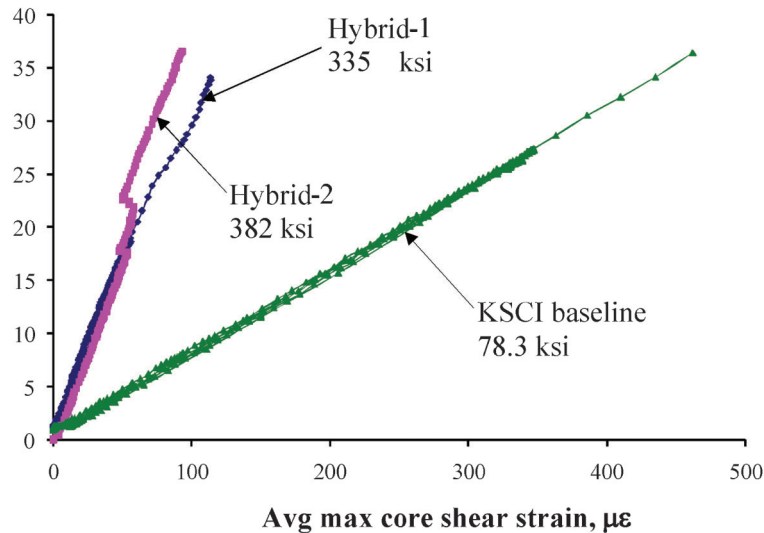


Figure 3.20: W-direction beam core shear stress vs. strain summary

the steel expanded hexagonal core geometry and material properties.

Figure 3.20 displays a summary shear stress versus strain plot of all W-direction large-scale beams tested. The equivalent elastic shear modulus for each specimen is also displayed in Table 4. As shown in the table, the hybrid beams are an average of 458% stiffer as compared with the KSCI specimen. Again, since the beam comparison was based on equivalent honeycomb core properties, the increase in stiffness is directly related to the steel expanded hexagonal core geometry and material properties.

Eq. (3-6) was used to plot the y-axis value for the equivalent shear modulus. Strain gauge rosettes at the quarter span were plotted on the x-axis on the shear modulus plots. The face sheets contribute little to the transverse shear stiffness as they are assumed to be in plane stress. Therefore, the honeycomb core shear modulus (Lombardi and Liu, 2010) can be compared to the equivalent shear modulus results from the stress-strain plots.

3.5.5 Conclusions for Hybrid Deck Study

The most important outcome of the current study, the objective of which was to increase the structural stiffness of the KSCI FRP honeycomb sandwich panel through the incorporation of steel into the cross section, was the innovative modification to the existing KSCI honeycomb core. This modification included the replacement of the existing FRP reinforced-sinusoidal honeycomb core with an over-expanded hexagonal honeycomb constructed with steel roof decking.

After several numerical parametric studies and the development of the steel core concept, large-scale beam tests were performed to compare the relative stiffness of the steel hexagonal core to the existing KSCI FRP reinforced-sinusoidal honeycomb core. From the results, it was concluded that in the L-direction, the

hybrid concept results in a significant increase in both flexural and shear stiffness. In the W-direction beam samples, the hybrid and KSCI flexural stiffness results were about the same, apparently due to some changes in the KSCI baseline beam. Despite only maintaining the flexural stiffness in the W-direction, the steel hexagonal honeycomb core concept proved itself by considerably increasing the equivalent shear stiffness. Thus the steel honeycomb core concept maintained or increased the flexural and shear stiffness in both the core L and W directions.

3.6 Conclusions

Serviceability criteria, or deflection limits, govern the design of FRP decks. However, the limits typically used for bridge decks may not be applicable to FRP decks because of their relative light weight, low stiffness, and resulting difference in vibration response. A couple of side studies were conducted on this issue of deflection limits, as well as a small literature review. One study investigated the development of an alternative criterion based on the dynamic response of the FRP decks. Another investigated a hybrid GFRP-steel solution, providing a deck with much higher shear stiffness in the core. Meanwhile, one suggestion made later in the project for the actual case study bridge was a deflection limit between girders of span/500, based on expected strains in the deck and wearing surface and an attempt to minimize cracking of the wearing surface in the negative moment region over girders (GangaRao et al., 2002).

CHAPTER 4. CASE STUDY BRIDGE: WILDCAT CREEK BRIDGE

4.1 General

WildCat Creek Bridge, located in Tippecanoe County, Indiana, carries CR 900E over the North

Fork of the WildCat Creek and was one of two bridges considered. The proposal was that the existing concrete deck would be replaced with a comparable FRP deck manufactured by Kansas Structural Composites, Inc. (KSCI). However, deflection limits were a primary concern for the potential rehabilitation of this bridge with an FRP deck. This bridge structure would have been widened without repositioning of the steel girders. This would have resulted in a bridge deck overhang of over 3 feet. The FRP overhang would violate the recommended span-to-deflection ratio of 300 for cantilever arms as specified in AASHTO (1998), as well as the span-to-deflection ratio of 500 recommended by GangRao et al. (2002), as has been discussed in Chapter 3.

This chapter describes the numerical analysis as well as experimental work conducted on the KSCI FRP bridge deck panels in order to establish performance specifications and understand the limit states of the panel before the final bridge design. First, a numerical analysis was conducted to determine if it was viable to change the dimensions of the panel in order to comply with the AASHTO serviceability recommendations. After this study, four different experimental tests were conducted. Two tests were conducted on one KSCI panel that included deck panel to girder connections as well as a panel to panel joint. The first test demonstrated the performance of the overhang at service and failure loads, and the second test was used to measure the deflection between girders at service and failure loads. A second KSCI panel with a modified panel to panel joint was tested to observe the performance of the overhang. One last test was conducted to observe the in-plane performance of the deck to girder connections.

Unfortunately, time delays and rising costs for the FRP deck made this case study bridge and KSCI panel cost-prohibitive. However, the results of this portion of the study are still viable in terms of general observations and issues with FRP bridge deck construction.

4.2 Case Study Bridge: WildCat Creek Bridge

The WildCat Creek Bridge consists of 3 continuous spans, 50 ft, 60 ft and 50 ft long respectively, with 28 ft - 8 in long approaches, and a 15 degree skew. The bridge needed to be widened; the proposal was to replace the concrete deck with an FRP deck so as to get the width without increasing the dead load of the bridge. In order to save money during construction, the girders for the proposed bridge would remain at 5 ft - 7 in spacing. Only the 3 middle spans, with non-composite steel girders, would be replaced. Figure 4.1 shows the existing and proposed cross sections of the bridge. Spans A and E in the figure are the approach spans. Spans B,C, and D are the middle spans to be replaced.

The WildCat Creek bridge presented a problem not encountered on previous FRP deck implementations. Due to the width desired, the resulting overhang violated the AASHTO-LRFD deflection criterion of L/300 (Chapter 3). Since the GangaRao et al., criterion

of L/500 (2002) was not part of an actual design specification, there was reluctance by the consulting engineer at this time in the study to utilize other than the AASHTO provisions. The following numerical and experimental study on the KSCI bridge deck specimens was undertaken to try to establish design guidelines in the absence of any FRP performance specifications.

4.3 Simple Overhang Serviceability Parametric Study for KSCI Panels

A simple parametric study was performed in order to determine if practical changes in the geometry of the panel would improve its stiffness sufficiently to satisfy AASHTO recommendations on the overhang deflections. The KSCI FRP deck panel is manufactured by the hand lay-up technique, which allows for some flexibility in dimensions such as depth of the core and thickness of the face sheets. The base configuration for the KSCI deck included an 8 inch core and 0.5 inch thick flanges.

Four different geometric configurations were considered, two in which the depth of the core were increased by an inch from 8 inches to 9 inches, and two in which the thicknesses of the top flanges were increased by $\frac{1}{4}$ inch and an equivalent inertia was calculated for each configuration utilizing a spreadsheet provided by KSCI. The expected deflections for a 3'-2" cantilever with a 16 kip concentrated load at its end were calculated for each geometric configuration and the results can be seen in Table 4-1. 24 inch and 36 inch wide equivalent beams were considered, also based on KSCI recommendations.

As can be expected the 36 inches wide equivalent beam resulted in smaller deflections than the 24 inch wide one, but the truck load was perhaps not expected to distribute through more than 24 inches at most, based on the assumed patch load. As this the case, neither the increase on the depth of the core nor the increase of the thickness of the flanges is not enough to satisfy the AASHTO serviceability criteria.

To increase the depth of the core even more is not feasible as it will not match properly with the depth of the concrete approaches and would require a retrofitting of the concrete approaches. Also, according to the manufacturer, to increase the thickness of the flanges would raise the price of the FRP panel prohibitively.

As discussed in the previous chapter, the AASHTO serviceability criterion was intended for the design of concrete and steel bridge structures and may not be appropriate for FRP design. Furthermore, simplified calculations as shown above were based on numerous assumptions. Therefore, an experimental study was conducted to examine the behavior of the KSCI FRP panel in more detail.

4.4 Experimental Work

Four large scale tests were conducted using the KSCI FRP deck. The general objective of the tests was to

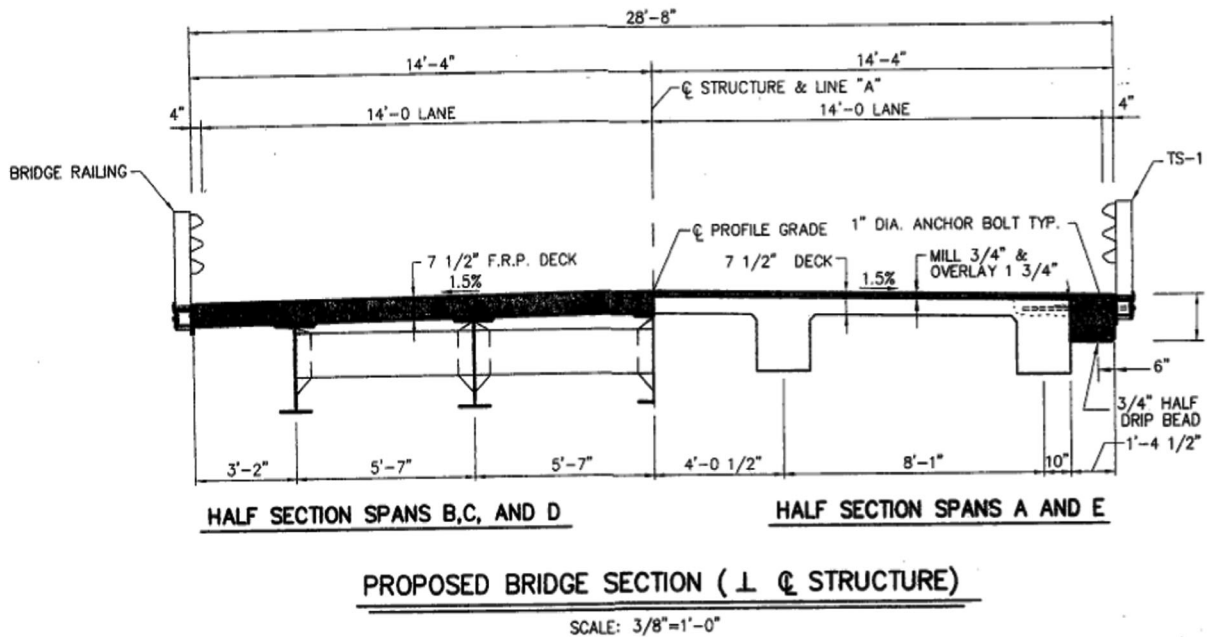
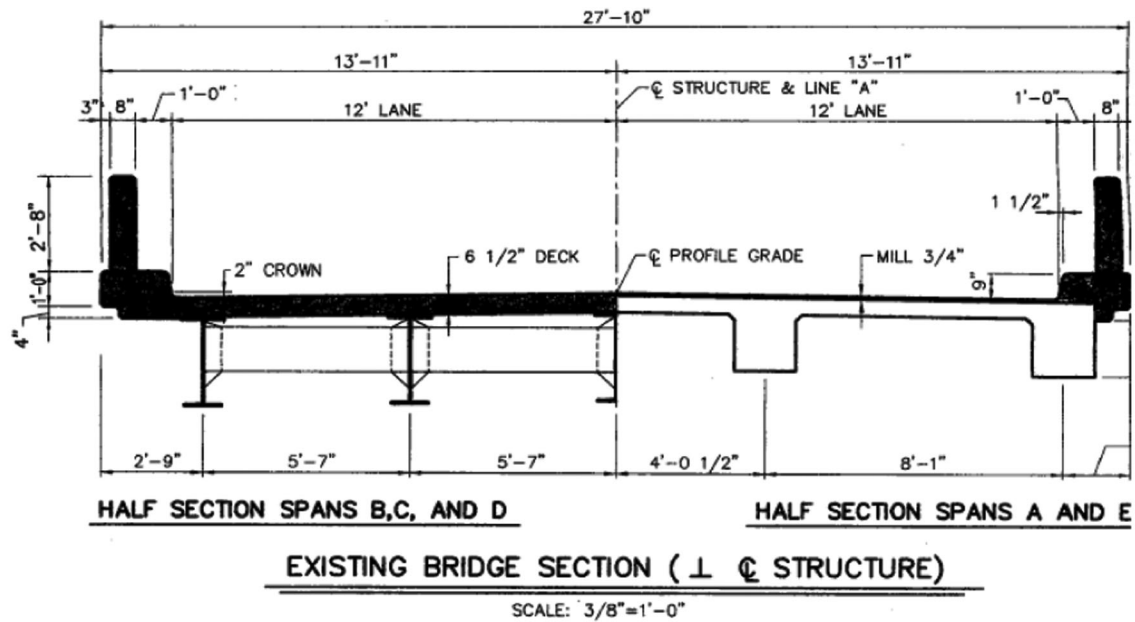


Figure 4.1: Wild Cat Creek Bridge Existing and Proposed Cross-Sections

TABLE 4-1:
Overhang Deflections

| Cross Sectional Dimensions | | | | AASHTO | Deflection, I_{equiv} |
|----------------------------|------------|-------------|-------|-----------|-------------------------|
| $t_{flanges}$ | d_{core} | d_{total} | width | criterion | 16 kips |
| (in.) | (in.) | (in.) | (in.) | (in.) | (in.) |
| 0.5 | 9 | 10 | 24 | 0.13 | 0.16 |
| 0.5 | 9 | 10 | 36 | 0.13 | 0.11 |
| 0.625 | 8 | 9.25 | 24 | 0.13 | 0.16 |
| 0.625 | 8 | 9.25 | 36 | 0.13 | 0.11 |

observe the behavior of the panel during service loads and study its failure mode. The first test was an overhang test (KSCI #P1a) with a concentrated load at the overhang. During this test, the deflections at the overhang caused by service and failure loads were observed. The second test (KSCI #P1b) studied the deflection between girders under a line load across the width of the panel. The third test (KSCI #P2) was an overhang test as well, but for this specimen the panel to panel connection was modified. This test was subjected to the same loads as KSCI #P1a. The last test (KSCI

#P3) observed the behavior of the girder to girder connector.

4.4.1 Test Specimens and Test Set-up

4.4.1.1 KSCI Panel 1 (KSCI #P1a & KSCI #P1b)

The first KSCI FRP panel sample tested was 17 ft long and 4 ft wide. The sample consisted of two 2 feet wide by 16.5 feet long sections joined together with a longitudinal tongue-and-groove joint and was used for two different experiments (KSCI #P1a and KSCI #P1b). The joint consisted of 0.12 inch thick chopped strand mat (ChSM) pieces molded and roughly fitted with honeycomb core pieces to form a tongue and a groove (Figure 2.24).

The FRP panel sample was supported on W14 × 82 steel girders spaced at 5 ft-7 in. to represent one half of the width of the WildCat Creek Bridge. At each of the three steel beams there were deck-to-girder bent plate connectors (Figure 2.26) which allowed for the panel sample to be clamped to the supporting steel girders by 0.75 inch threaded studs and nuts. The FRP-to-steel girder connection consisted of tightening a nut and washer against the bent plate with a specification from KSCI to tighten the nut hand-tight plus a quarter turn.

The W14 × 82 support beams were chosen to most closely resemble the existing W30 × 124 bridge girder flange width and thickness of the case study bridge, to best represent how the FRP panel would interact with the support beams. The test specimen provided was longer than needed for half of the width of the case study bridge. Therefore, the exterior girder was placed at 4 ft- 4 in. from the sample end, which provided a larger overhang than the one on the proposed bridge. This was taken into account in the placement of the instrumentation and the loading locations. The next two support girders were placed at a distance of 5 ft-7 in to replicate the spacing of beams on the WildCat Creek Bridge. Finally, there was 1 ft-8 in overhang to the side of the W-shape representing the centerline girder on the

case study bridge. This short overhang primarily served the purpose of providing a continuity boundary condition when loading the FRP beam sample. Due to the non-uniformity of the FRP beam sample, ½ inch thick neoprene pads were placed on top of the steel support beams. This allowed the FRP beams to be clamped and have full contact with the supports. Figure 4.2 shows KSCI Panel #1 in place.

4.4.1.2 KSCI Panel 2 (KSCI #P2)

The second KSCI FRP panel sample had similar dimensions as the first panel, but this panel had a retrofitted tongue-and-groove connection. This specimen was used for test KSCI #P2. The joint consisted of chopped strand mat (ChSM) pieces molded to form a solid tongue and a groove. The FRP beam sample was supported on the same W14 × 82 steel girders used for the first two tests; the beams were also spaced at 5 ft-7 in. representing one half of the width of the WildCat Creek Case Study Bridge, with a 3ft – 2in overhang on one side and a 1ft – 8in. overhang on the other side of the beam representing the centerline girder; the shorter overhang was tied down to the floor with a pair of rods and channels across the width to provide continuity. The panel-to-girder connections were the same as those used for the first panel, following the KSCI specifications. Figure 4.3 and Figure 4.4 show the second panel and set-up used on test KSCI #P2.

4.4.1.3 KSCI Panel 3 (KSCI #P3)

The fourth test was conducted on a FRP KSCI panel 8 ft long, 4ft.-0 in. wide, and 10 inches thick. This specimen was composed of two 4'-0" long panels connected to an 8'-0" long steel girder by a single deck-to-girder connection located at the center of the specimen. This specimen did not include the neoprene pad that the other specimens had between the FRP panel and the steel girder. A bent plate and a 7/8 inch stud connected the panel with the steel girder as specified by KSCI. The two panels were not jacked

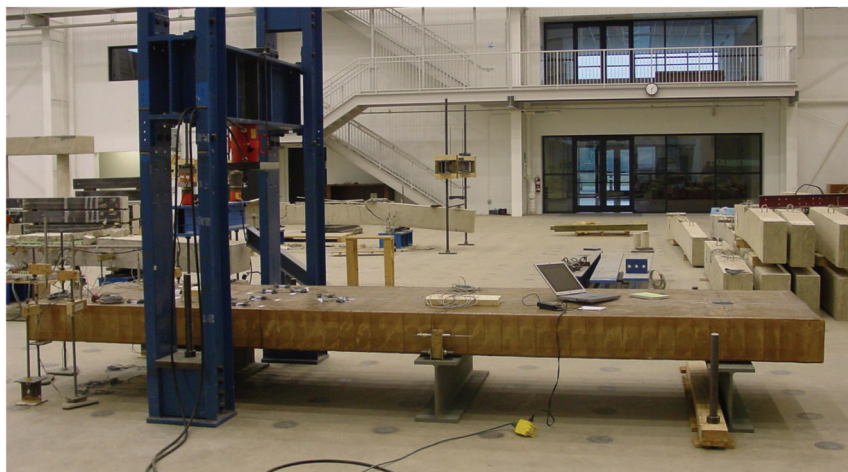


Figure 4.2: KSCI Sample Panel #1



Figure 4.3: KSCI Panel 2 Setup

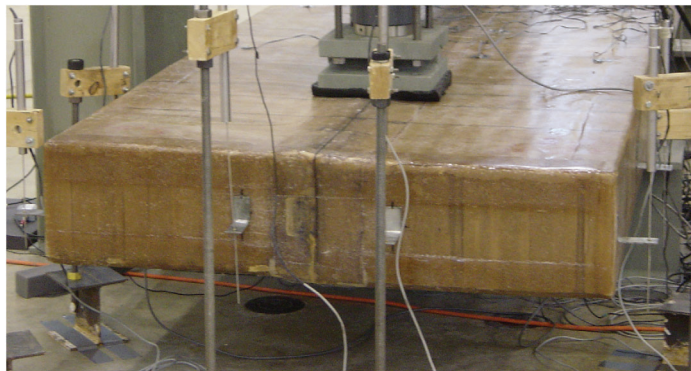


Figure 4.4: Picture of Retrofitted Connection for KSCI #P2

together as they would be in the field. Figure 4.5 shows a schematic of the setup. Two wood frames were placed on top of the specimen to provide support in case uplift occurred during testing.

4.4.2 Loading

4.4.2.1 KSCI Panel 1 (KSCI #P1a: Overhang Test)

For the first test, the FRP KSCI Panel 1 sample was loaded simulating an HS20-44 truck axle with two wheel loads spaced at 6 ft center-to-center. The centerline of the exterior wheel was placed 12 in from the edge of where the guardrail should be located, per AASHTO specifications. Again, the sample was manufactured with an actual overhang of 4 ft-4 in and the Wildcat Creek Bridge overhang, after bridge widening, was 3 ft-2 in. Therefore, the load was placed relative to the bridge overhang, and one wheel load was located at 2ft-2in from the centerline of the support.

The wheel loads were applied to the FRP panel sample through a 7 ft long W16×89 steel spreader beam with plates, rollers, and load cells placed at each

support location (i.e., 6 ft center-to-center). The load cells were strategically placed under the steel spreader beam to monitor the load magnitudes to the FRP panel sample at high loads. It was anticipated that at high loads and large overhang deflections, the load would be redistributed, reducing the overhang load and increasing the wheel load between support beams where the stiffness is greater. The load was applied through 10 in × 10 in steel plates that transferred the force to the FRP sample through tire pads cut to accommodate the 10 in × 10 in steel plates. The steel-reinforced rubber

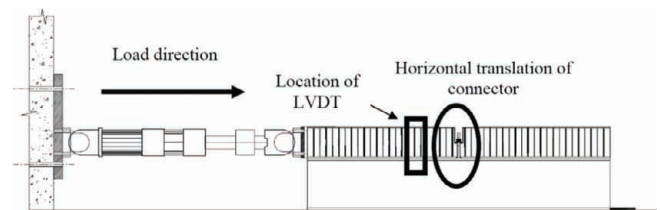


Figure 4.5: Schematic of KSCI #P3 Test Setup

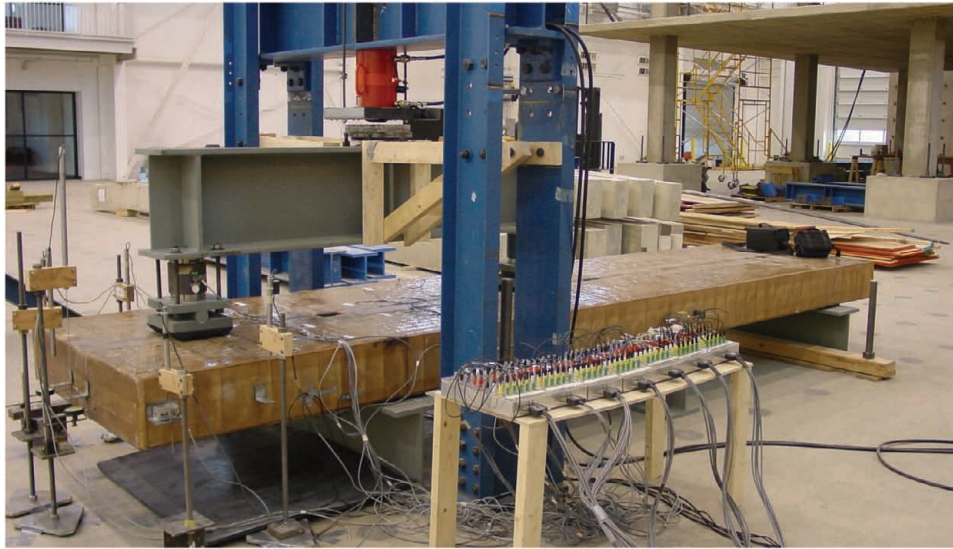


Figure 4.6: Picture of KSCI #P1a Test Setup

tires allowed for little deformation at high loads and prevented local stress concentrations in the FRP deck that could occur from the use of steel plates alone. Figure 4.6 shows a picture of KSCI #P1a test setup.

4.4.2.2 KSCI Panel 1 (KSCI #P1b-Girder Span Test)

The same beam specimen used for the KSCI #P1a test was used for KSCI #P1b. However, for KSCI #P1b test, the load was applied using the W16×89 steel spreader beam as a linear load across the width of the specimen and between the steel girders on the undamaged side of the specimen. The deflection was

measured under the applied load. Figure 4.7 shows a picture of the loaded specimen KSCI #P1b.

4.4.2.3 KSCI Panel 2 (KSCI #P2)

The FRP KSCI Panel 2 sample was loaded simulating an HS20-44 truck axle with two wheel loads spaced at 6 ft center-to-center one foot away from the overhang. The centerline of the exterior wheel was placed 12 in from the edge of guardrail per AASHTO specifications, which was assumed to be the overhang free end. The same W16×89 steel spreader beam with load cells at each support location (i.e., 6 ft center-to-center) that



Figure 4.7: Picture of KSCI #P1b Test Setup During Loading

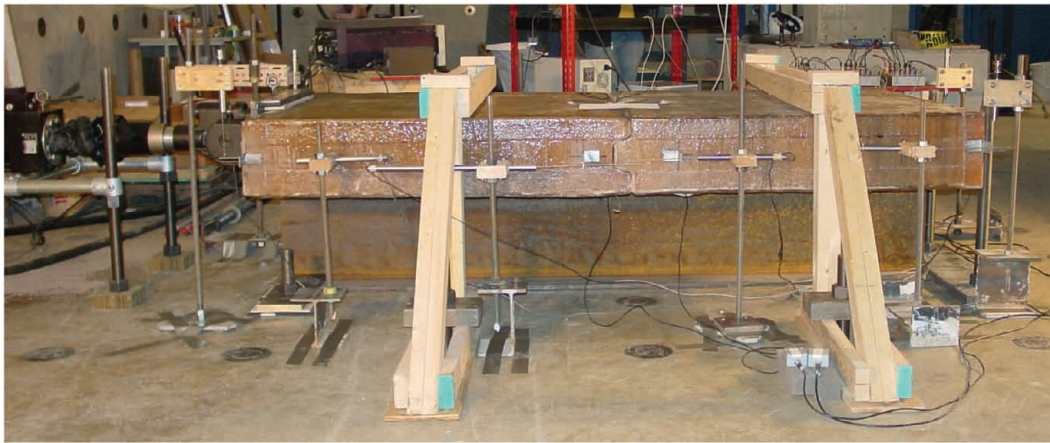


Figure 4.8: Picture of KSCI Panel 3 (KSCI #P3) Test Setup

was used for the previous tests was also used on this test to apply the load. The load was applied using rollers and 10 in \times 10 in steel plates that transferred the force to the FRP sample through tire pads of the same size. Figure 4.3 shows a picture of KSCI #P2 test setup.

4.4.2.4 KSCI Panel 3 (KSCI #P3)

KSCI Panel 3 was loaded in-plane at one of its ends (in the horizontal or X-direction) by a 55-kip actuator, until the failure of the connection was reached. A steel plate placed along the edge of one of its ends transferred the load of the actuator to the FRP panel. The steel support girder was fixed to the floor so that it could not slide during the test once the load was applied. Figure 4.8 shows a picture of the specimen in place ready to be tested.

4.4.3 Instrumentation

4.4.3.1 KSCI Panel 1 (KSCI #P1a)

The FRP panel was instrumented with strain gages and linear variable displacement transducers (LVDTs). The strain gages placed on the top of the panel sample were located at the exterior beam support where maximum negative moment and maximum flexural strains were anticipated. Also, strain gages were placed in the first 5'-7" span closest to the loaded overhang to measure the strain distribution across the width of the 4 ft sample. Finally, two strain gages were placed at each wheel load location in an attempt to measure stress concentrations. The bottom of the panel was instrumented with strain gages at the exterior steel girder support, adjacent to the loaded overhang and within the 5'-7" span closest to the loaded overhang. Two horizontal LVDTs were placed at the exterior support beam closest to the loaded overhang to measure any longitudinal displacement of the FRP panel sample. Also, one LVDT was placed on each side of the beam sample at the location of the overhang wheel load. Four LVDTs were placed at the overhang free end. Two of those LVDTs were positioned adjacent to the panel longitudinal joint while the other two were placed on

the sides of the beam. Finally, two inclinometers were used to measure the rotation of the panel at the free end. Figure 4.9 provides a schematic of the instrumentation for Panel 1 during KSCI #P1a test. Note that the same LVDTs are shown on both the top view and the bottom view.

4.4.3.2 KSCI Panel 1 (KSCI #P1b)

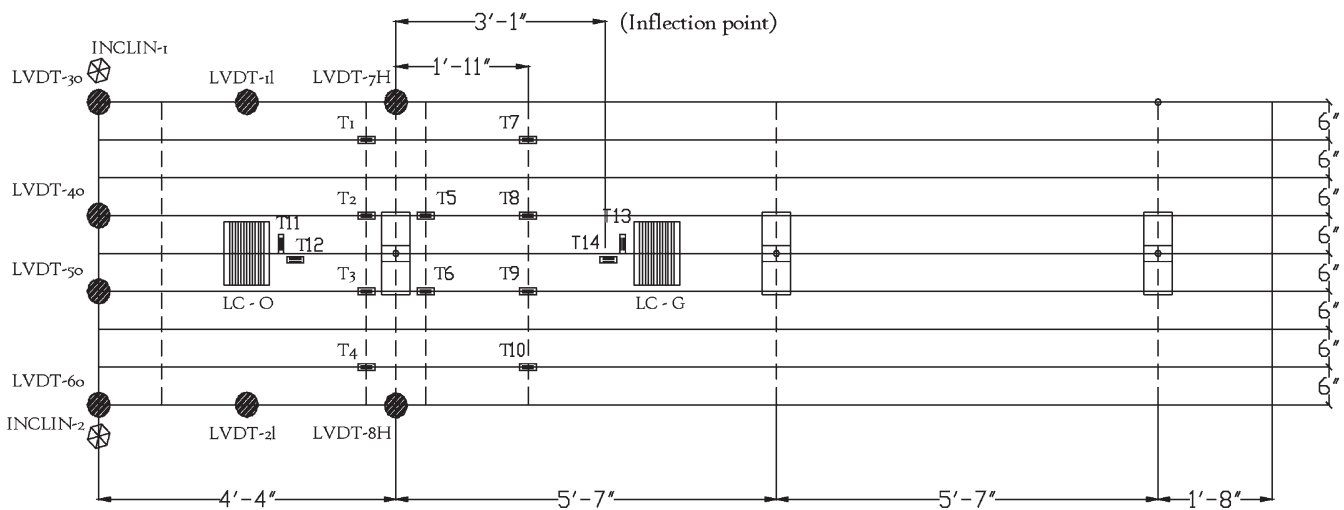
Even though KSCI Panel 1 was reused for KSCI #P1b test, this test used a different instrumentation layout. For the KSCI #P1b test, eight strain gages and two LVDTs were used. Four strain gauges on the top of the panel at the center line of the adjacent steel girder, and four on the bottom of the panel, right underneath the applied load. The LVDTs were placed at each side of the panel, at the center line of the applied load. Figure 4.10 shows the exact location of each sensor for KSCI #P1b test. In the 'Top View' in Figure 4.10, the rectangle at the left side with the honeycomb hatching denotes the damaged part of the specimen, which was opened so that the core could be inspected for damage.

4.4.3.3 KSCI Panel 2 (KSCI #P2)

FRP Panel 2 was instrumented with strain gages and LVDTs. The strain gages placed on the top of the panel sample were located at the exterior beam support where maximum flexural strains were anticipated. Also, strain gages were placed in the first 5'-7" span closest to the loaded overhang to measure the strain distribution across the width of the 4 ft sample.

The bottom of the panel was instrumented with strain gages at the exterior steel girder support, adjacent to the loaded overhang and within the 5'-7" span closest to the loaded overhang. One LVDT was placed on each side of the beam sample at the location of the overhang wheel load. Finally, four LVDTs were placed at the overhang free end. Two LVDTs were positioned adjacent to the beam longitudinal joint while the other two were placed on the sides of the beam. Figure 4.11 provides a schematic of the instrumentation for Panel 2 during KSCI #P2 Test.

TOP VIEW



BOTTOM VIEW

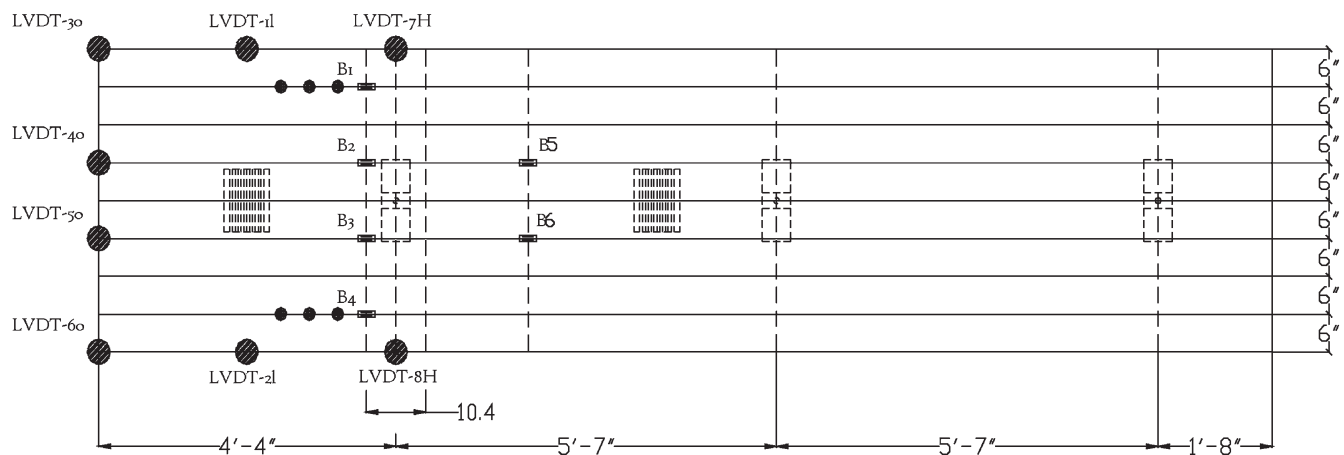


Figure 4.9: Schematic of Instrumentation for KSCI Panel 1 – KSCI #P1a Test

4.4.3.4 KSCI Panel 3 (KSCI #P3)

Panel 3 for the KSCI #P3 test was instrumented with a number of LVDTs, but the primary instrumentation was essentially two LVDTs. Each LVDT was placed along each side of the specimen to monitor the horizontal translation of the FRP panels with respect to the steel girder. Figure 4.5 and Figure 4.8 show the locations of these two main sensors. Other LVDTs were used to measure any potential, unintended uplift of the specimen, any differential translation of the different panel sections, or unintended slip of the steel girder support.

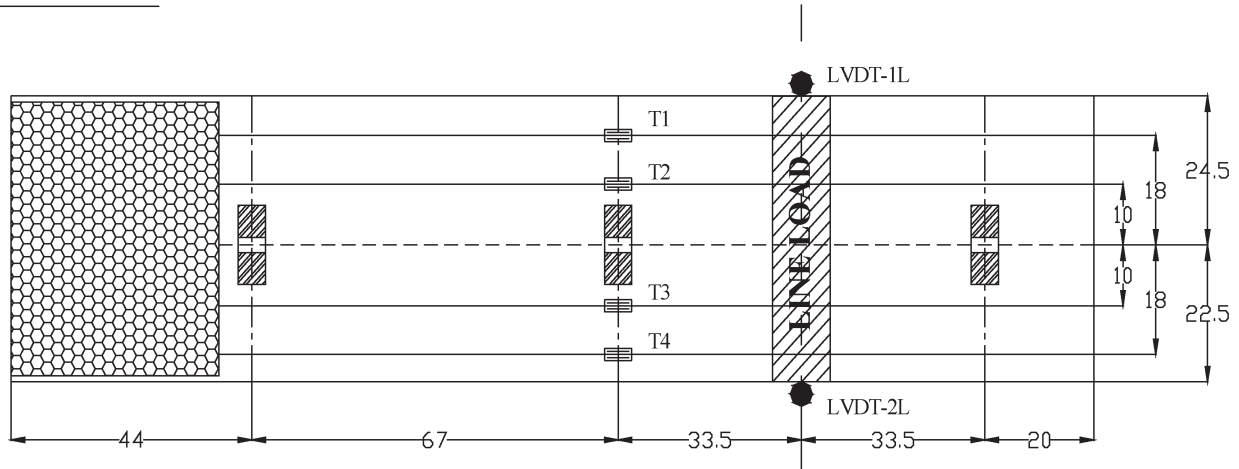
4.4.4 Test Results

4.4.4.1 KSCI Panel 1 (KSCI #P1a)

Until failure, the response of the panel was linear, as expected, even as additional load cycles were applied.

The specimen was loaded and unloaded to zero and loaded again to increasing levels for six different cycles for the purposes of acoustic emission measurements (Chapter 6). Load cycles were as follows: Cycle 1 – 0 to 10 kips, Cycle 2 – 0 to 32 kips, Cycle 3 – 0 to 35 kips, Cycle 4 – 0 to 41 kips, Cycle 5 – 0 to 56.5 kips, and Cycle 6 – 0 to 51.6 kips. Cycle 2 corresponded to the service axle load. Cycle 4 corresponded roughly to service axle load including impact. As shown in Figure 4.12, stiffness of the panel decreased with some of the progressive cycles. This was due to damage to the longitudinal panel joint at the overhang, as well as possible damage to the core and the core-top-plate interface. With Cycle 5, the damage was significant enough that the same maximum load could not be obtained with Cycle 6. However, as shown in Figure 4.13, the response of the panel in terms of longitudinal strains on the top of the panel remained

TOP VIEW



BOTTOM VIEW

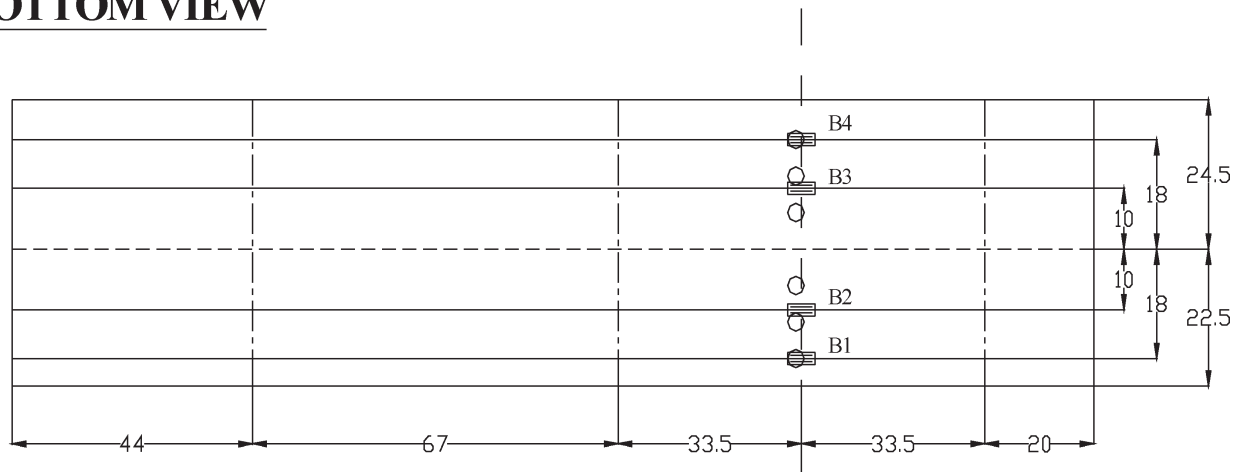


Figure 0.60: Schematic of Instrumentation for KSCI Panel 1 – KSCI #P1b Test

Figure 4.10: Schematic of Instrumentation for KSCI Panel 1 – KSCI #P1b Test

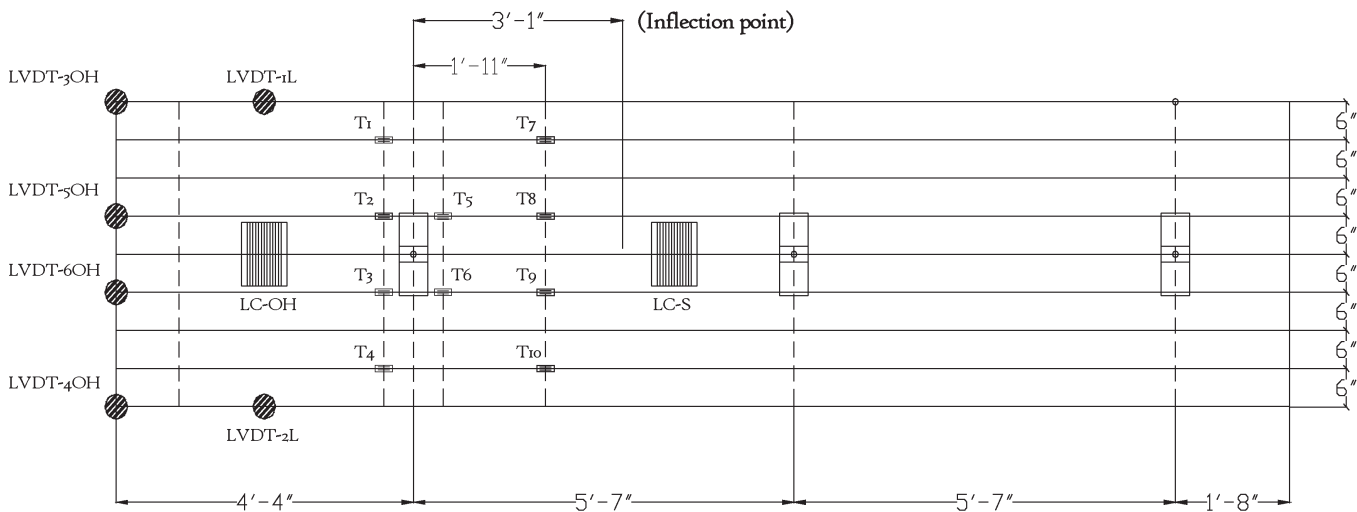
largely linear; any irregularities in the graph occurred near or at the load corresponding to panel joint failure. Similar results were observed for strains at the bottom of the panel as well.

Figure 4.12 also shows that the $L/300$ deflection criterion for the overhang, or 0.13 inches, would not be satisfied at a service wheel load of 16 kips, with or without impact. This deflection limit was already exceeded at a total (axle) load of about 10 kips.

Damage to the longitudinal joint can be seen by the whitening of local areas of stress in Figure 4.14 and Figure 4.15. After the test, the top and sides of the deck panel were removed so that the honeycomb core and joint could be examined. A top view (Figure 4.16) revealed more about the core than the joint; the sinusoidal pieces of the core were not always alternating direction, as intended, such that the peaks of the sinusoidal waves met to form strong joints. Even if the

sinusoidal pieces were alternating direction, the peaks of the sinusoidal curves did not line up with the valleys of the adjacent sinusoids. The result would be out of plane deformation of the vertical flat pieces, which do not have much out-of-plane stiffness. Furthermore, Figure 4.16 shows some locations with no fibers sticking up after removal of the top plate. This indicates that there were some regions where the top plate was not adequately bonded to the core. These issues were believed to have resulted in a reduction in stiffness of the panel even without longitudinal joint damage. The end view (Figure 4.17) revealed that there were significant voids in the tongue and groove joint. The visible weakness of this joint appeared to be one of the major causes of the observed damage. The problems with the sinusoidal pieces and the longitudinal joint were noted, and an improved panel and strengthened joint were then provided for Panel 2.

TOP VIEW



BOTTOM VIEW

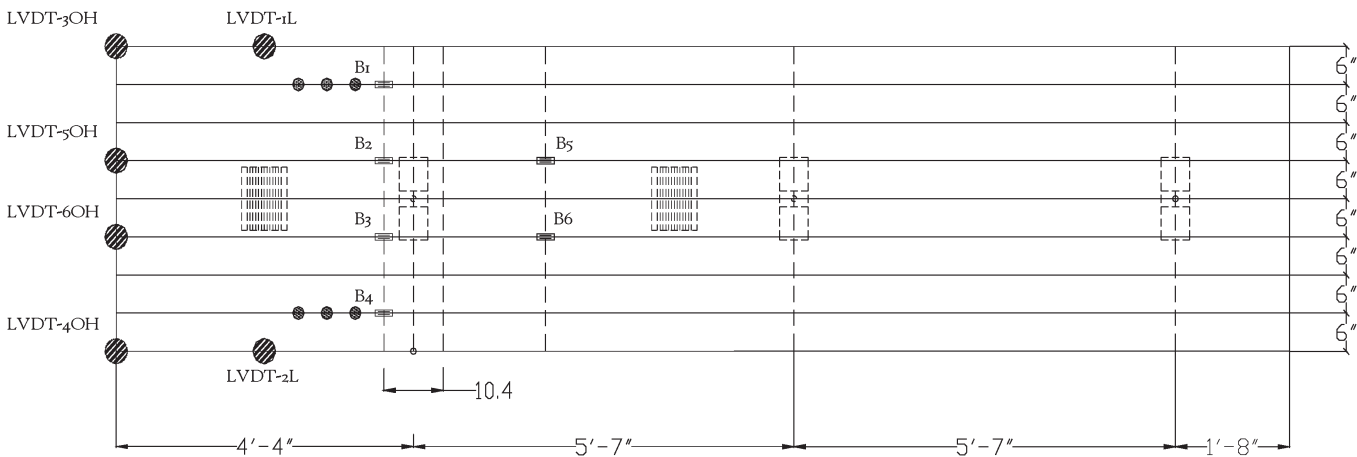


Figure 4.11: Schematic of Instrumentation for KSCI Panel 2 – KSCI #P2 Test

4.4.4.2 KSCI Panel 1 (KSCI #P1b)

Until failure, the response of the panel loaded between supports was essentially linear, as expected, even as additional load cycles were applied. The specimen was loaded and unloaded to zero and loaded again to increasing levels for three different cycles for the purposes of acoustic emission measurements (Chapter 6). Load cycles were as follows: Cycle 1 – 0 to 16 kips, Cycle 2 – 0 to 21 kips, and Cycle 3 – 0 to 85 kips.

A noise was observed at about 25 kips, suggesting some damage to the panel. A small change in slope was also observed in the load-deflection plot. Between 30 and 35 kips of load, there was some shifting of the load frame; this was reflected in the deflection and strain data, as seen in Figure 4.18. Also, at 30 kips, some whitening of the longitudinal joint was observed at the

location of the loading beam (Figure 4.19). This correlated to damage at the joint. Loud noises were heard at about 40 kips, also, but no other damage of this joint was observed externally, even at the maximum load (Figure 4.20). The specimen was loaded to 85 kips, at which point there was some rotation of the loading jack. The test was stopped because of concerns with the stability of the loading apparatus. The specimen did not appear to have reached its ultimate capacity. However, the specimen was also relatively flexible and did not satisfy the deck panel deflection limits for spans between girders.

4.4.4.3 KSCI Panel 2 (KSCI #P2)

The load-deflection plot for Specimen #P2 is shown in Figure 4.21. The initial slope observed in the plot is

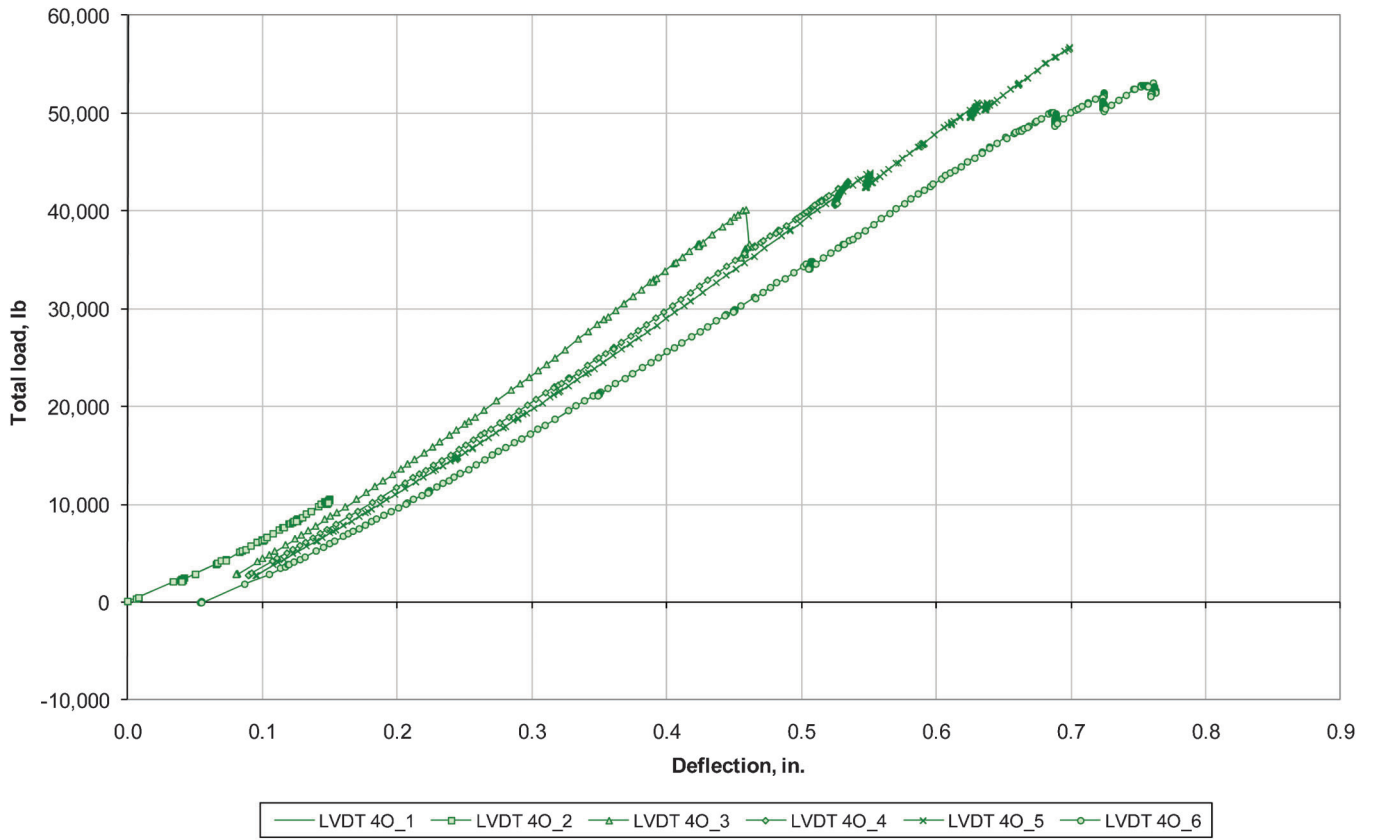


Figure 4.12: Total Load vs. Overhang Deflection near Joint (LVDT 4O) – KSCI #P1a Test

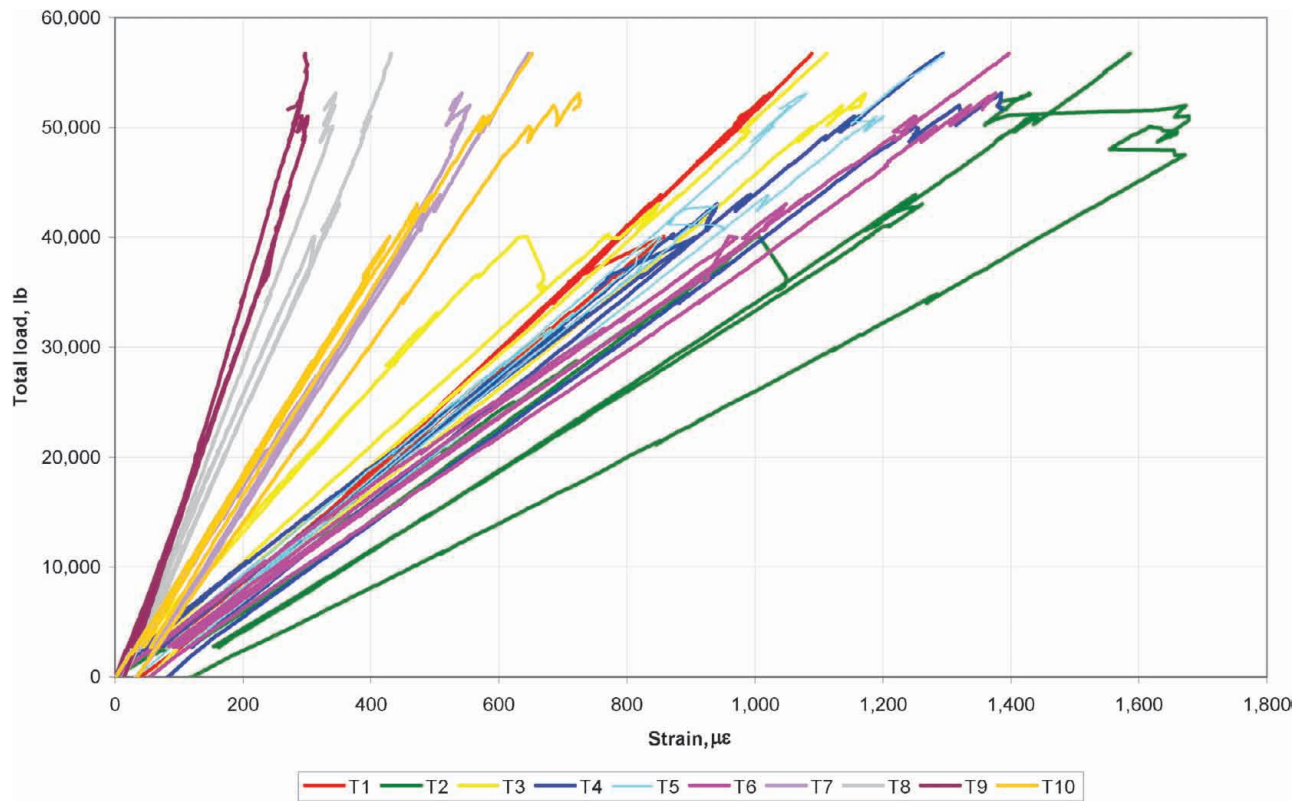


Figure 4.13: Total Load vs. Top Panel Longitudinal Strains – KSCI #P1a Test



Figure 4.14: Longitudinal Joint Damage at Overhang at 50-kips Total Load – KSCI #P1a Test

the closing of a gap at the girder farthest away from the overhang. Despite the use of a tie-down at that girder to represent continuity of the bridge deck at the centerline girder, there was an initial deformation to the deck panel that prevented contact of the deck with that

girder, as shown in Figure 4.22 and Figure 4.23. Otherwise, the response of the panel after closing of that gap was similar to that of the other specimens. The response was generally linear, with some noises and some slight ‘jumps’ in the data. No damage was visually



Figure 4.15: View of Longitudinal Joint Damage at Overhang – KSCI #P1a Test

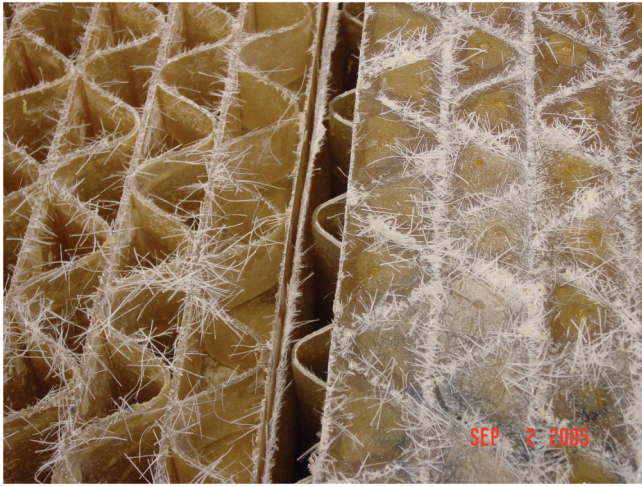


Figure 4.16: View of Longitudinal Joint; Top Plate Removed – KSCI #P1a Test

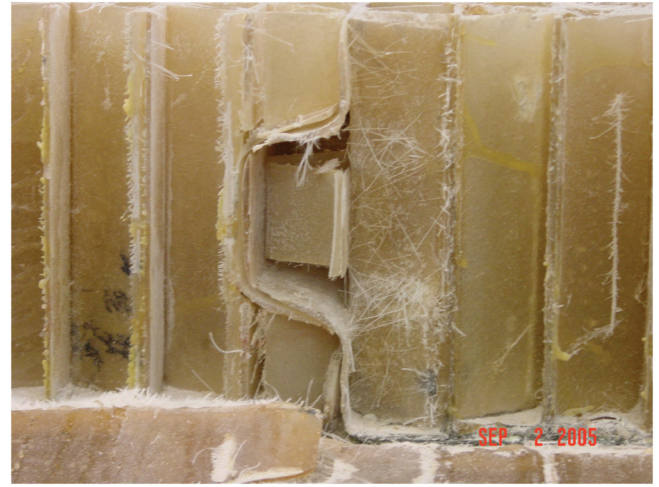


Figure 4.17: View of Longitudinal Joint; Side Removed, Showing Voids – KSCI #P1a Test

observed. The noises were believed to have been associated with damage to the core. Deflection limits for the overhang were not satisfied with this specimen.

4.4.4.4 KSCI Panel 3 (KSCI #P3)

Figure 4.24 shows the load-horizontal translation curve of a LVDT located next to the deck-to-girder connection of KSCI #P3. This curve indicates that no slip occurred in the initial loading stage, until approximately 500 lbs load. The initial portion of the curve

indicates that the connection had infinite stiffness until it started taking the load. Then, the shear stud started bending elastically, indicating that both FRP specimen and connector were working together. After this stage, the stud started yielding, followed by the bearing of the stud and possibly the clamp plate, causing tearing of FRP fibers, possible rupture of the base weld, and deformation of clamp plate. This last stage indicated failure of the deck-to-girder connection, although the specimen continued to take load. Figure 4.25 shows a

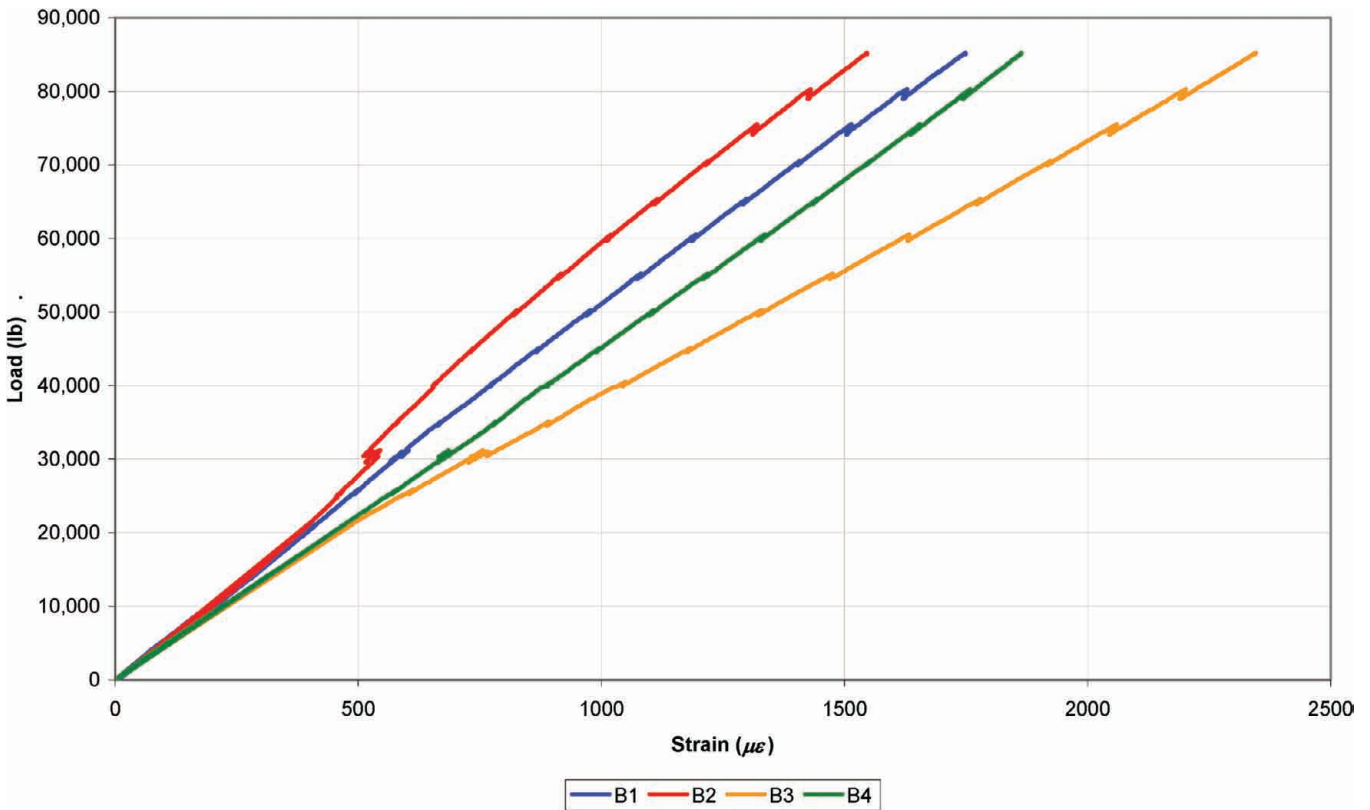


Figure 4.18: Bottom Panel Longitudinal Strains – KSCI #P1b Test



Figure 4.19: KSCI #P1b Test Specimen Damage at Longitudinal Joint Under Loading Beam

detail of the stud connector after the test, once the panel was unassembled. This picture shows that the stud connector yielded causing tearing of the FRP fibers, finally failing at its base where it is welded to the steel girder.

Figure 4.26 shows a zoomed-in view of the initial portion of the load-horizontal translation curve. From this zoomed-in view of the curve, a very small initial slip can be seen before elastic bending of the stud. This initial slip is attributed not to the overall translation of the entire 8'-0" specimen, but to the translation of the 4'-0" specimen located next to the actuator. This initial slip is due to the fact that both panels were not jacked

together as they would be at the field. The results of this test indicate that the deck-to-girder in-plane stiffness (K_x) is essentially infinite stiffness, and consequently no initial slip.

4.5 Conclusions

The KSCI specimens exhibited generally linear response to failure, except for issues with a weak longitudinal joint or gap in the test set-up. Even with a reinforced longitudinal joint, however, noises indicated damage to the core of the specimen; the specimen also did not satisfy deflection limits. It was believed that



Figure 4.20: KSCI #P1b Test Specimen at Maximum Applied Load

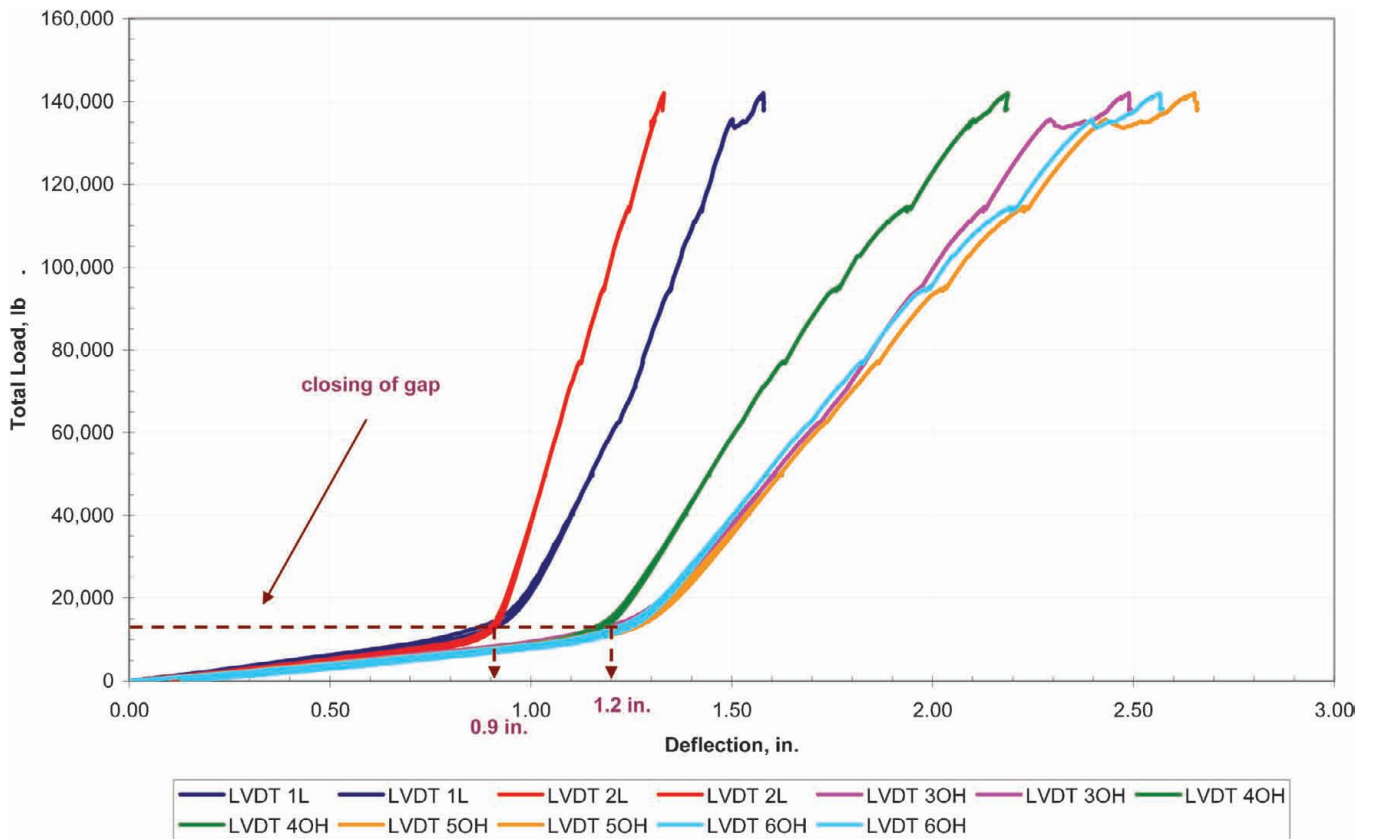


Figure 4.21: KSCI #P2 Test Specimen Total Load-Deflection Plot



Figure 4.22: East side of the panel: $1 \frac{3}{8}''$ (total gap) – $\frac{1}{2}''$ (neoprene thickness) = $\frac{7}{8}''$



Figure 4.23: Opening at West Side of FRP Panel: $1\ 1/4''$ (total gap) – $1/2''$ (neoprene thickness) = $3/4''$

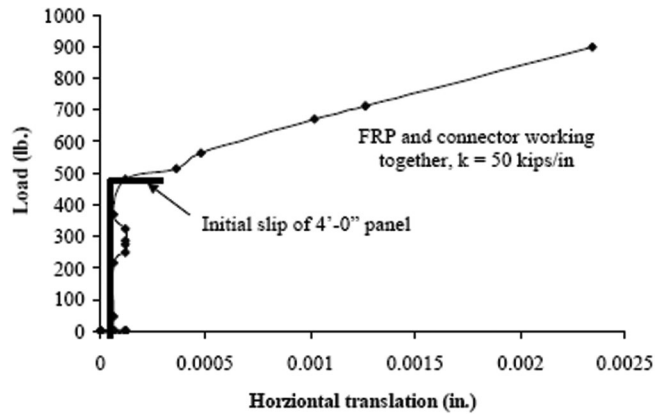


Figure 4.26: Initial Portion of Experimental Load-Horizontal Translation Deck-to-Girder Connection (Machado, 2006)

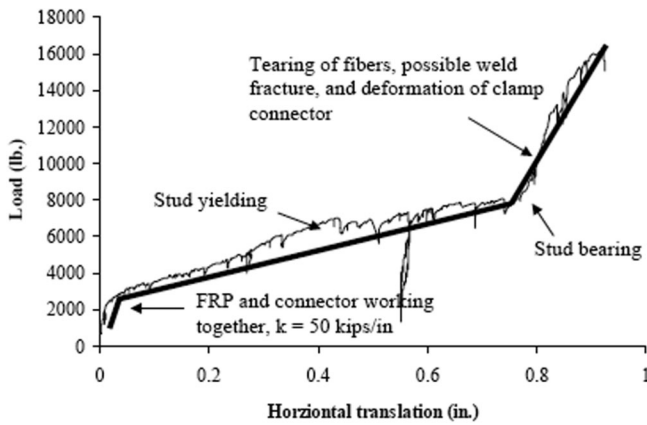


Figure 4.24: Experimental Load-Horizontal Translation

damage to the core and the shear deformations in the core contributed to the larger than acceptable deflections. Meanwhile, a deck-to-girder connection test showed essentially infinite initial stiffness to the connection and failure of the stud at ultimate load.



Figure 4.25: Detail of the Stud Connector After Test

CHAPTER 5. CASE STUDY BRIDGE: SUGAR CREEK BRIDGE

5.1 General

The case study bridge, CR 900 E. over Sugar Creek, was the second bridge studied for use of a fiber reinforced polymer (FRP) deck for bridge rehabilitation and deck widening. The 2% cross slope on the deck was to be built into the FRP deck installation; the crown connection was one of a number of concerns that were studied experimentally. The composite deck system manufactured by ZellComp, Inc. was the one used for this specific rehabilitation project. The ZellComp deck was installed on the Sugar Creek Bridge in November 2009.

5.2 Case Study Bridge: Sugar Creek Bridge

The case study bridge, CR 900 E. over Sugar Creek, is the first bridge in the State of Indiana to use an FRP deck. County Road 900E bridge consisted of a 60 feet simple span, 24 feet wide. It had 5 girders spaced at 5'-10" with a 2'-2" overhang (Figure 5.1). The rehabilitation consisted of replacing the concrete slab with an FRP deck that increased its clear roadway from 24 feet to 28 feet. To do so, and not confront the serviceability issues presented in the past chapters, the design proposed to move the steel girders and spaced them at 6'-3", which resulted in a 1'-9" overhang (Figure 5.2). The ZellComp deck panels, typically 33" wide, were to be placed transverse to the bridge girders. The panel lengths corresponded to half the width of the bridge deck.

The deck rehabilitation maintained the existing 2% cross-slope. This cross-slope presented a unique challenge in that the structure required a crown connection in the ZellComp deck that had never been used before. This cross-slope was achieved with grouted haunches at each of the girders (Figure 5.3). The FRP deck panels were to be laid across those haunches; shear studs in grouted pockets secured the panels to the girders

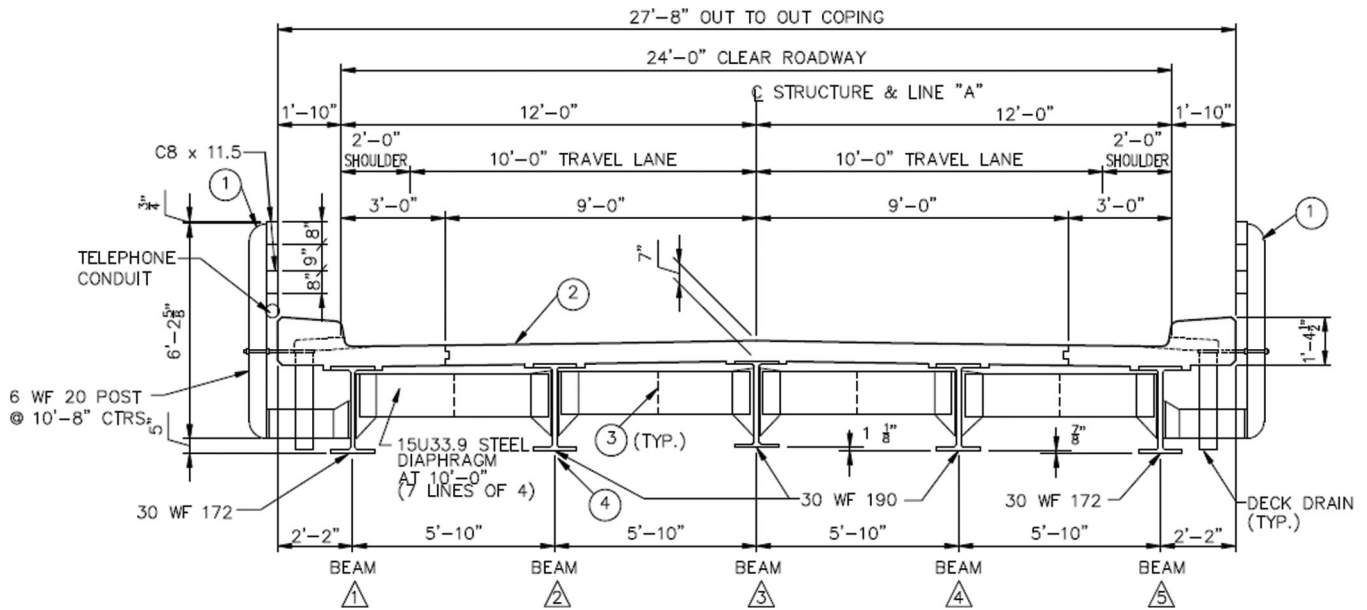


Figure 5.1: Existing Sugar Creek Bridge Cross Section

(Figure 5.4). Foam dams that were custom-manufactured to fit to the ZellComp deck were used to form the grout pockets. The FRP deck panels met at an angle at the crown connection, requiring a splice plate and a special overlay at the top of the deck to address concerns of moisture ingress (Figure 5.5).

5.3 Experimental Work

A series of tests were used to evaluate the performance of this new deck and details introduced for this case study bridge prior to installation in the

field. Quasi-static tests were used to evaluate the capacity of this deck and its response at service loads. The tests were also used to assess the performance of the panel-to-panel connection, the deck-to-girder connectors, the crown connection, and the wearing surface.

5.3.1 Test Setup

The main test setup consisted of a steel frame, post tensioned to the strong floor, a load cell, and a hydraulic ram.

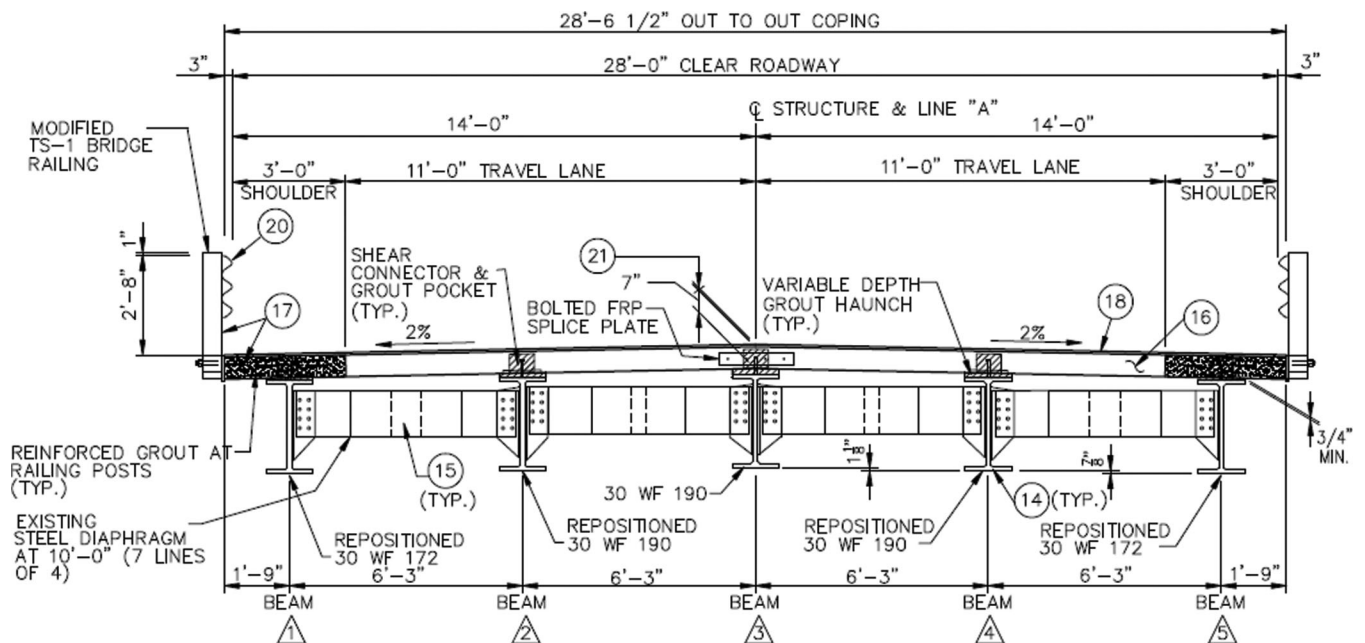


Figure 5.2: Rehabilitated Sugar Creek Bridge Cross Section

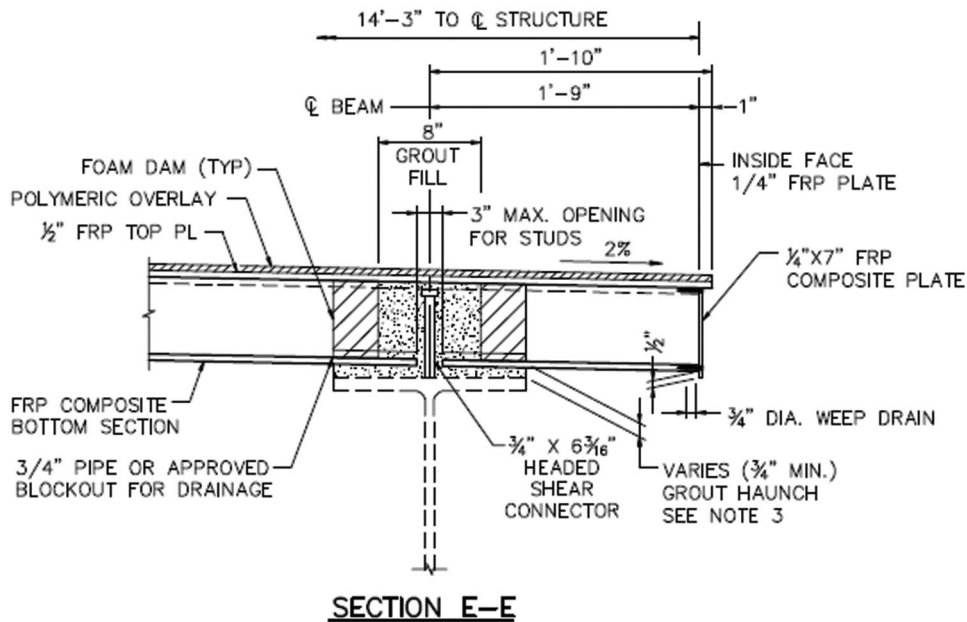


Figure 5.3: Section View at Grouted Haunch

The test specimens consisted of three girders spaced at 6'-3", with a crown at the center girder, resembling the case study bridge. Figure 5.6 shows the bridge cross section, with the test specimen defined by a dashed line. Each girder had the appropriate step and haunch needed to create the desired 2% cross-slope. The initial design for the bridge utilized a continuous FRP deck panel for the entire width of the bridge. Therefore, the bottom section was cut partly through its depth at the crown connection to provide some flexibility and allow

it to deform to accommodate the cross-slope. Figure 5.7 shows how these cuts were made. The center top plate for the first test was also cut partially through its thickness to provide flexibility (Figure 5.8); however, for the second test, two individual center plates were provided (Figure 5.11).

For the first test specimen, each panel section was 22.5 in. wide, connected longitudinally by a lap joint connection as seen in Figure 5.9. Self drilling epoxy-infused screws (Figure 5.9(c) and Figure 5.10) were used

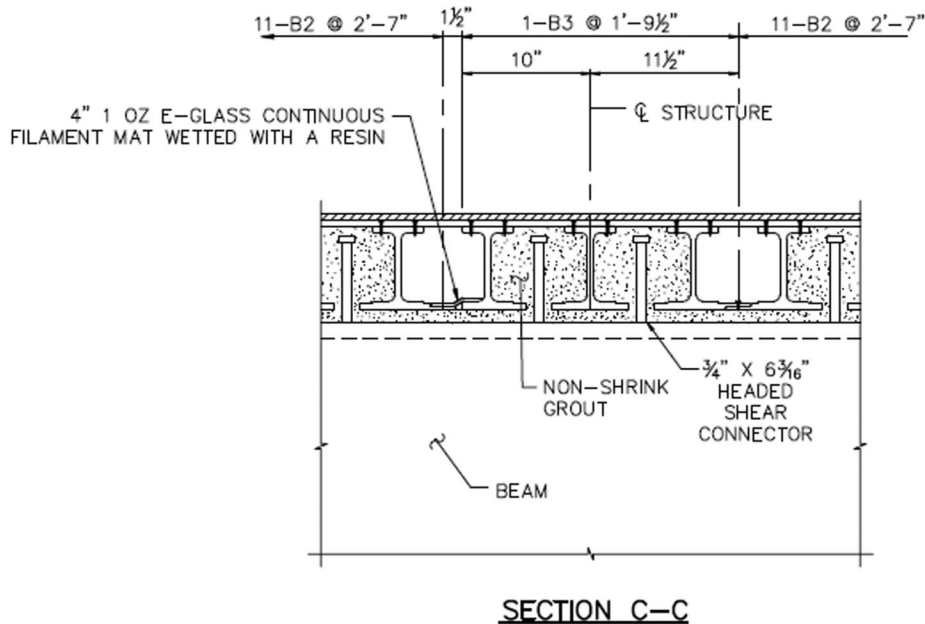
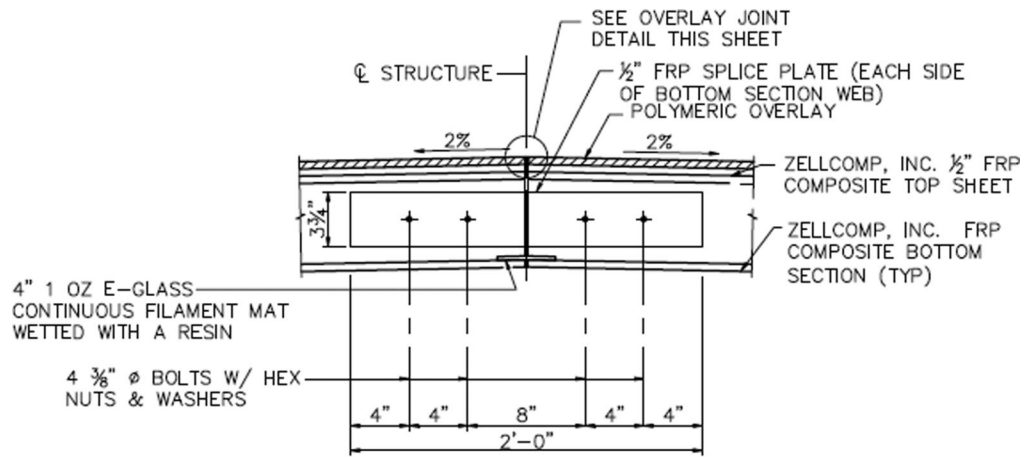


Figure 5.4: Section View Showing Shear Studs in Grout Pockets



SECTION A-A
(TYPICAL BOTTOM SECTION LONGITUDINAL SPLICE DETAIL)

Figure 5.5: Section View at Crown Connection

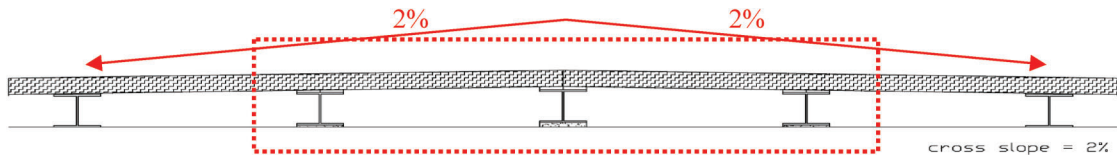


Figure 5.6: Bridge Cross Section



Figure 5.7: Cut at Center of Bottom Section

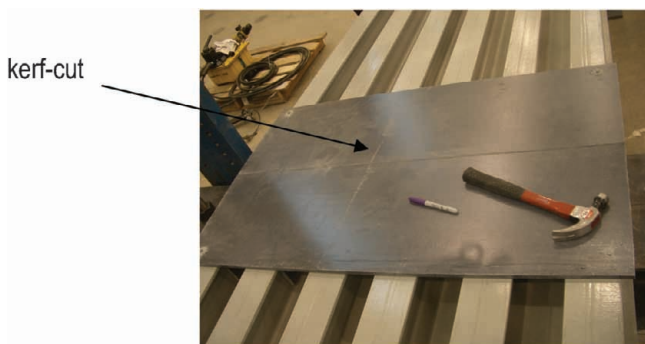


Figure 5.8: Kerf-cut at Center Top Plate (Test #1)

to connect the top plate with the bottom section, as well as the lap joint of the panel-to-panel connection. The top plates, each of a different length, were laid out on top of the bottom section, covering both panels as seen in Figure 5.11. Two headed shear studs at each girder, embedded in non-shrink epoxy grout, were used for the deck-to-girder connectors (Figure 5.12). Top plates were attached to the bottom sections with epoxy-infused screws (Figure 5.13).

A spreader beam, braced laterally, was used to apply two patch loads spaced at 6 ft on center onto the specimen (Figure 5.14). This load represents a truck axle. Each patch load was applied at either side of the

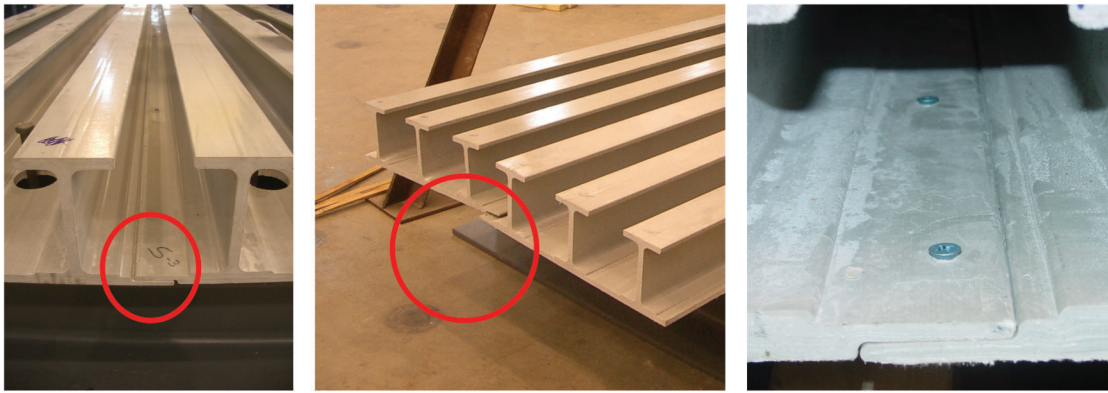


Figure 5.9: (a) & (b) Views of the Panel to Panel Connection; (c) Panel to Panel Connection with Screws



Figure 5.10: Epoxy-infused Screws

5.3.2 Instrumentation

Nineteen uniaxial strain gages and four displacement potentiometers were used to acquire the desired data. The two potentiometers were placed under each load, one on each side of the lap joint connection. The strain gages were located at the top plates as well as at the bottom section of the panel. Figure 5.15 shows the placement for the potentiometers and the strain gages; the rectangles represent strain gages, and the circles represent the potentiometers.

Seven gages were attached to the top plates of the panel. Three gages (T-CL 1, T-CL 2, and T-CL 3) were placed an inch away from the top centerline. Two gages (TS-CL and TN-CL) were located at each side of the center plate, one at the South and another at the North, respectively. The purpose of the position of these gages was to learn how the strains are transmitted from the center top plate to the adjacent plates, and determine what influence, if any, damage at the center plate would have on these other plates. Two more strain gages were placed close to the south load, 12 in. away from the longitudinal centerline.

crown, providing the maximum negative moment at the crown connection. This moment was expected to reveal any potential problems with the crown connection.

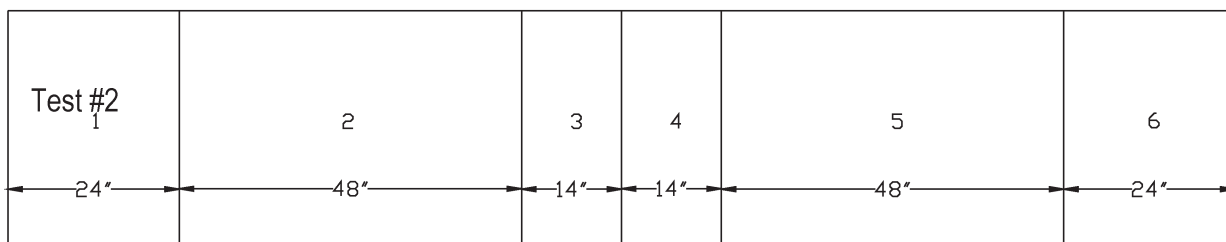
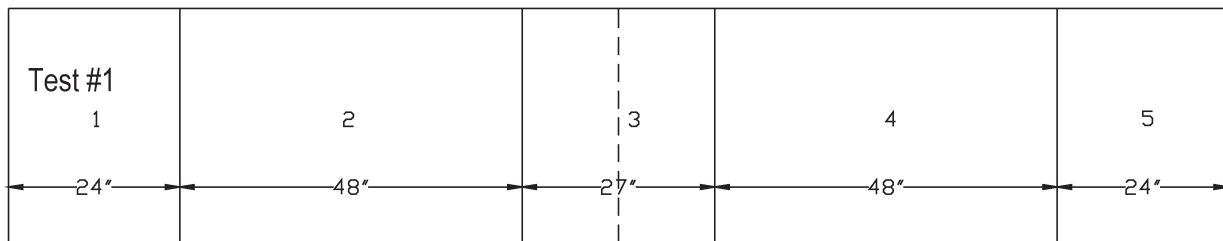


Figure 5.11: Layout of Top Plates



Figure 5.12: Deck to Girder Connectors (embedded in non-shrink epoxy grout)

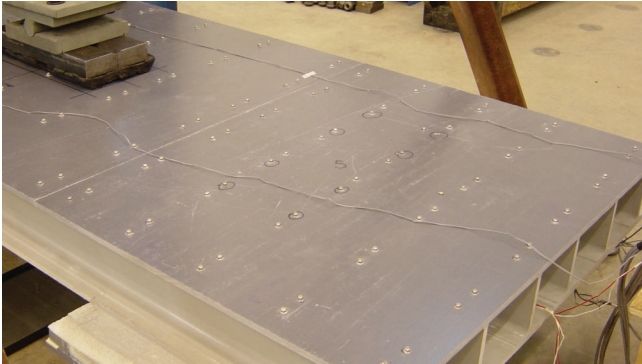


Figure 5.13: Epoxy-infused Screws Connecting Top Plate to Bottom Section

Twelve strain gages were attached to the bottom section of the panel. Gages BS-CL 1 and BS-CL 2 were located 3 in. away from the longitudinal centerline, one to the west side and the other at the east side; just an

inch away from the center girder on its south side. Gages BN-CL 1 and BN-CL 2 were placed in the same way, but they were located to the north side of the girder. Four gages were located under each load (North and South) to acquire the local strains at this area. Strain gages BS Load 1 and BS Load 2 were placed exactly underneath the gages TS Load 1 and TS Load 2, respectively. Strain gages BN Load 1 and BN Load 2 were placed exactly underneath the strain gages TN Load 1 and TN Load 2.

Four potentiometers were attached underneath the panel, right under the loads. Each potentiometer was 3 in. away from the center lap joint connection, one to the West and another to the East. The reason for placing two potentiometers under each load was to determine if the panel to panel connection was deflecting symmetrically, which would imply that the load had been transmitted proportionally.

Also, two rulers were glued underneath the panel (Figure 5.16) and inspected during the test by way of a mirror on the floor to see if there was any visible opening at the lap joint connection. The rulers were right underneath the loads where the maximum deflections were expected.

5.3.3 Loading

For Test #1, five different load cycles were applied. The first cycle had a maximum total load of 10 kips. During this loading the instrumentation was checked and revised to make sure that all the sensors were responding as expected and that the data was recording properly. The maximum total load applied on the second cycle was 32 kips, which represents the axle of an HS-20 truck. During the third cycle, a maximum total load of 42 kips was applied. This load represents

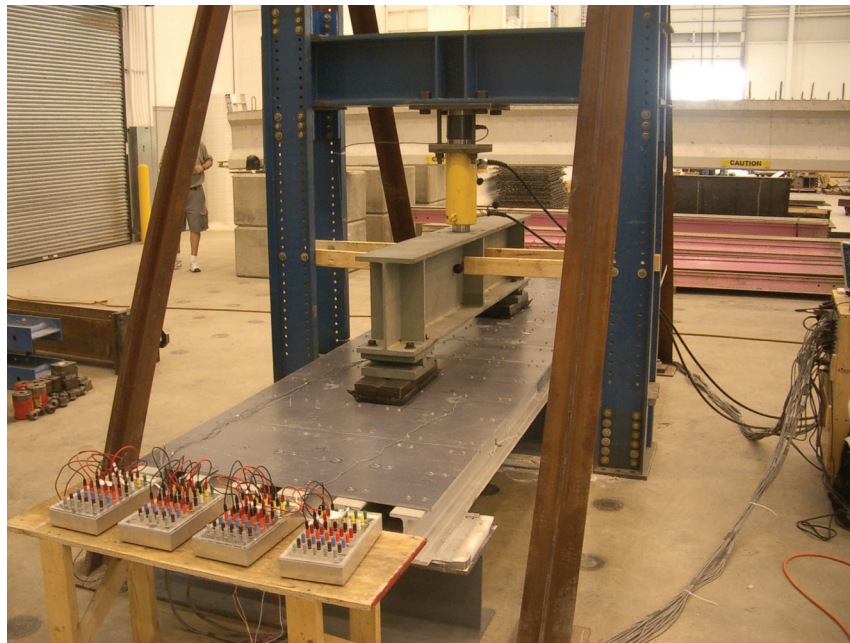


Figure 5.14: ZellComp Specimen with Braced Spreader Beam

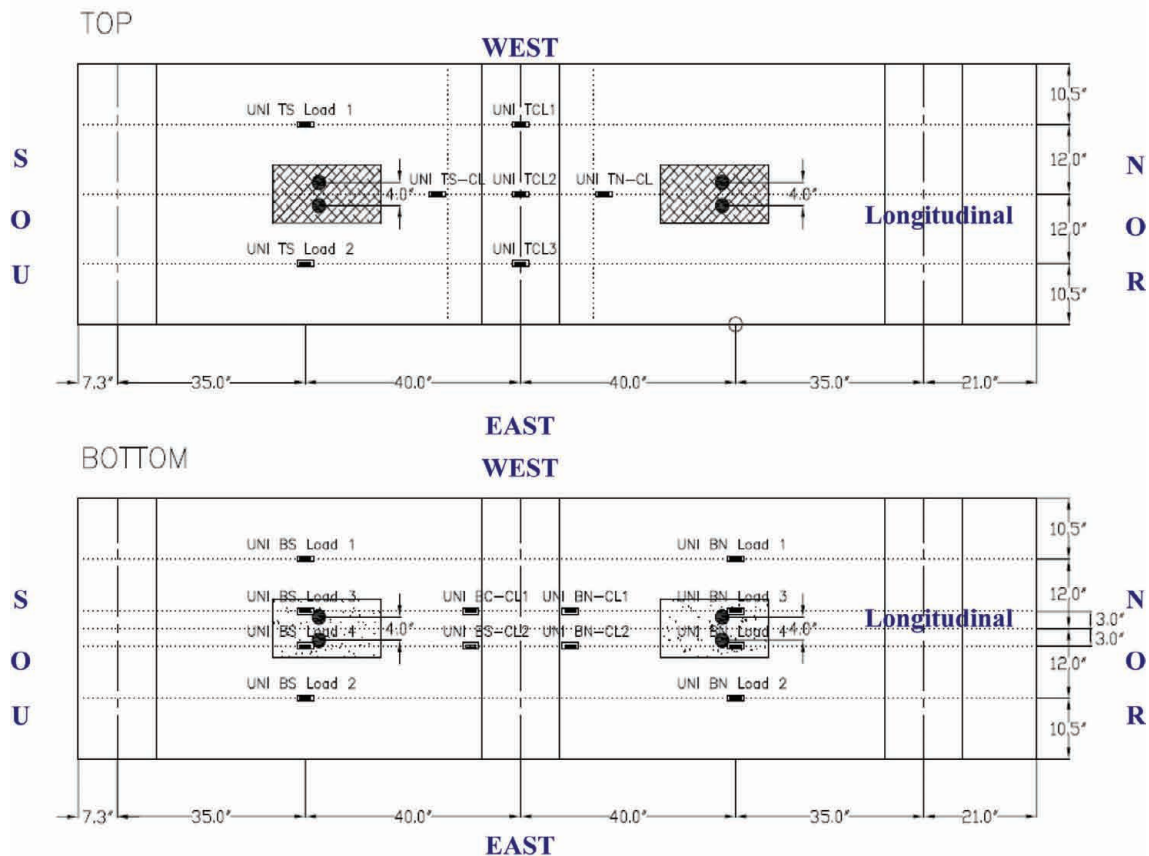


Figure 5.15: Instrumentation Plan

an HS-20 truck axle plus impact as specified by AASHTO (1998). The fourth load cycle was intended to test the ultimate capacity of the specimen and had a maximum total load of approximately 125 kips. The plan was that this would be the last load cycle, but there were some problems with the hydraulic pump, which needed to be replaced. The fifth and last cycle went up to 150 kips, the maximum capacity of the load cell.

For Test #2, the load cell was exchanged for one with a higher capacity. Five individual load cycles were applied during Test #2. The first cycle had a maximum

total load of 42 kips, which represents the axle of an HS-20 truck plus impact. The second cycle went from 0 to 102 kips, the third cycle went from 0 to 140 kips; and the fourth cycle went from 0 to failure at 183 kips. At 183 kips the load dropped approximately 40 kips, which indicated failure, but the specimen was able to sustain the load so a series of “mini cycles” were started. In these “mini cycles,” increasing load was applied to the panel even though in some instances it dropped. One last cycle of load was applied to the specimen; the panel was unloaded all the way to zero and then loaded back up to 165 kips before it was unloaded.

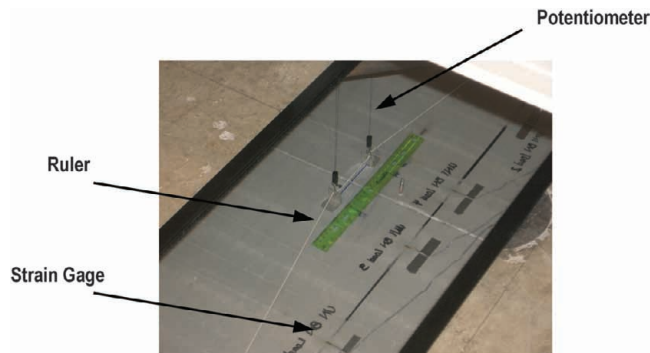


Figure 5.16: Instrumentation (view in the mirror placed on the floor)

5.3.4 Test #1 Results

No damage was observed in the specimen at service loads. At a total load of approximately 130 kips the kerf-cut top plate at the crown cracked completely through its center. This damage is not considered to be structural, but could be detrimental for the wearing surface for the bridge deck in service.

5.3.4.1 Strain Gage Results

Strain gages TS Load 1 and TS Load 2 were attached to the top plate of the panel, near the South load. Each gage was at a different side of the lap joint connection, one to the East and the other to the West. They showed

similar responses. Strain gage TS Load 1 had a maximum compressive strain of 943 $\mu\epsilon$. Strain gage TS Load 2 read a maximum compressive strain of 946 $\mu\epsilon$ (Figure 5.17).

Strain gages TS-CL and TN-CL were attached to the top plates adjacent to the center plate. TS-CL was at the South plate and TN-CL was located at the North plate. Both gages measured compressive strain. An increase of 496 $\mu\epsilon$ was observed at a load of 137 kips for strain gage TS-CL. This drastic change in strain may have been caused by the crack at the center kerf-cut plate. This showed that there was good connection between those top plates and that the stresses were being transferred from one plate to the other effectively. The maximum compression strain observed at 150 kips for strain gage TS-CL was 732 $\mu\epsilon$ and for TN-CL was 309 $\mu\epsilon$ (Figure 5.18).

Strain gages T-CL 1, T-CL 2, and T-CL 3 were attached to the center top plate of the specimen an inch away from the kerf-cut. Strain gage T-CL 2 was located at the center of the panel, then T-CL 1 was 12 in. away towards the West, T-CL 3 was 12 in. towards the East. Strain gage T-CL 3 became off-scale during the test and its data is not valid. Gages T-CL 1 and T-CL 2 showed a significant increase in their strain measurements. Strain gage T-CL 1 observed an increment of 655 $\mu\epsilon$ at 130 kips, and for T-CL 2 an increment of 1013 $\mu\epsilon$ was

observed at 120 kips (Figure 5.19). These increments on strains, without much change in the applied load, could have been due to a crack at the kerf-cut plate.

Also, is noticeable that the strain goes into compression in a zone of the panel where tension strain was expected. A possible reason for this trend is that the strains were not recorded when the center plate was screwed down to the specimen, which would have given a residual strain. It would seem that the specimen, at this negative moment zone, would always be in tension until the crack occurs, perhaps causing the two spans to then act more like simply supported spans. This is supported by the initial tensile strain in T-CL 1 followed by compressive strain after cracking in the top plate. However, other data suggests that, due to presence of the splice plates, continuity was maintained. Furthermore, as explained later in this section, the top plates do not appear to be acting completely compositely with the bottom sections; therefore, assumptions about strains based on beam theory are not entirely valid.

Strain gages BN Load 1, 2, 3 & 4, as well as strain gages BS Load 1, 2, 3 & 4, were all located under the load points, at the North and South sides of the specimen. Figure 5.20 shows that the tensile strains measured on both sides of the panel, at each load point, were symmetric and, as expected, strain gages right

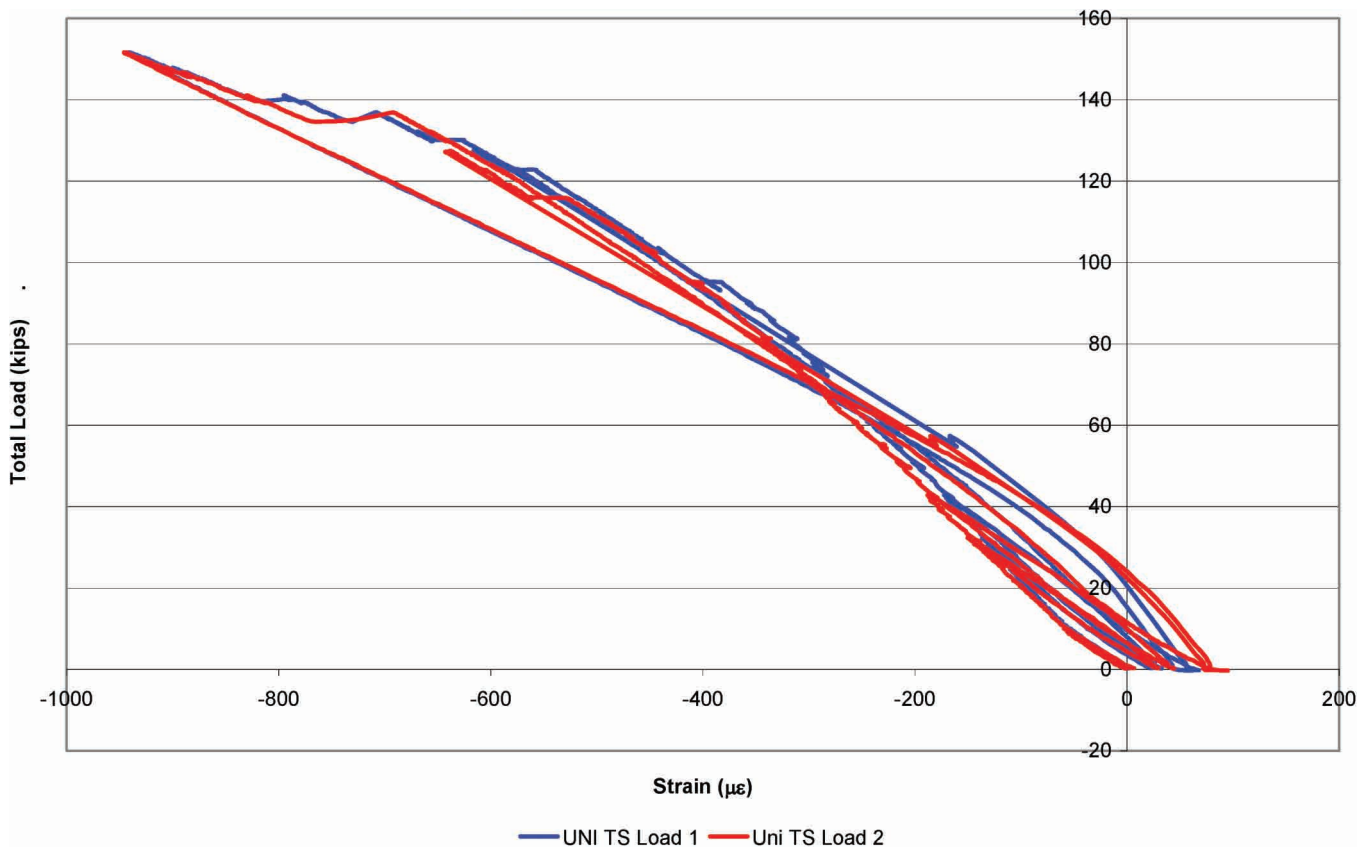


Figure 5.17: TS Load 1 & TS Load 2 vs Total Load

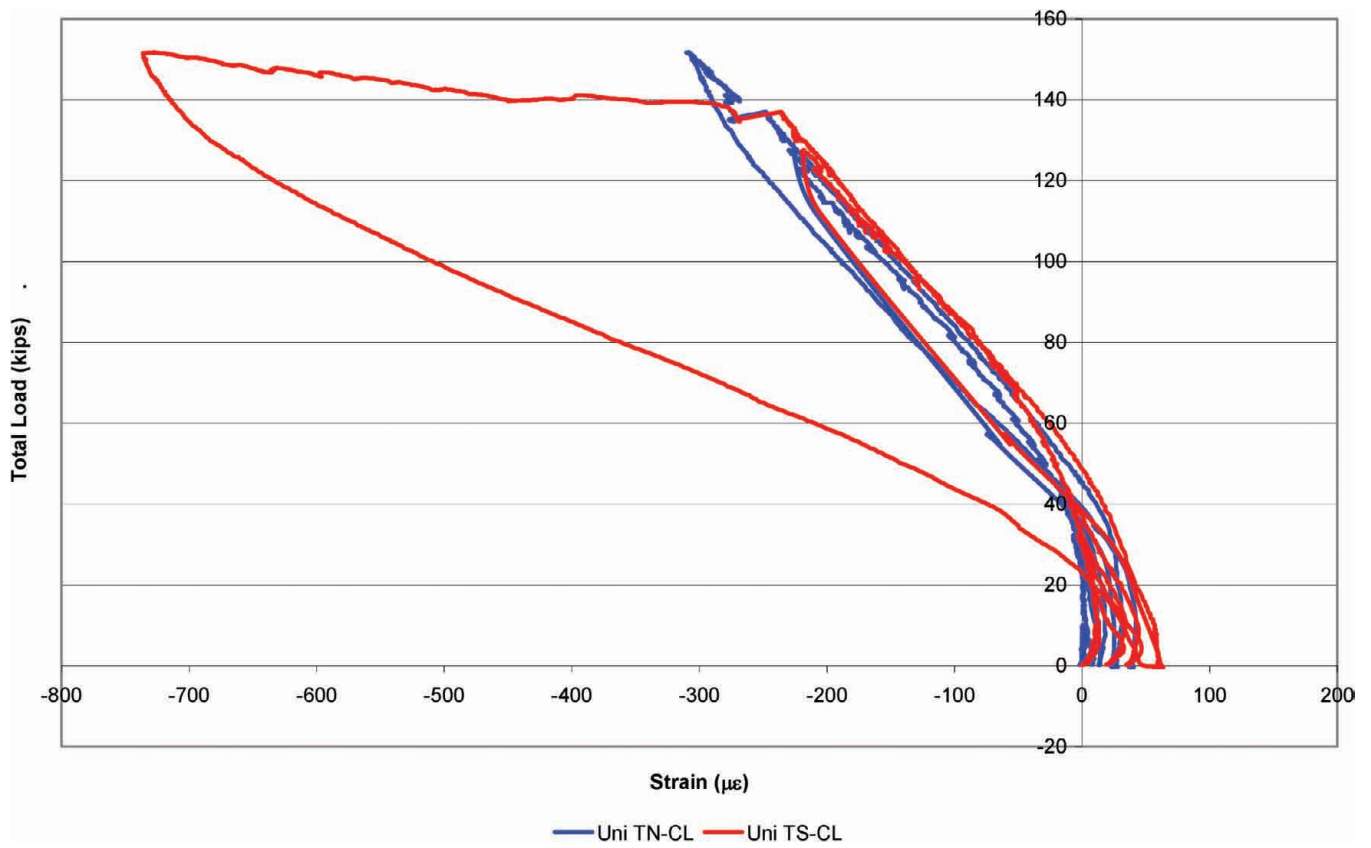


Figure 5.18: TS-CL & TN-CL vs Total Load

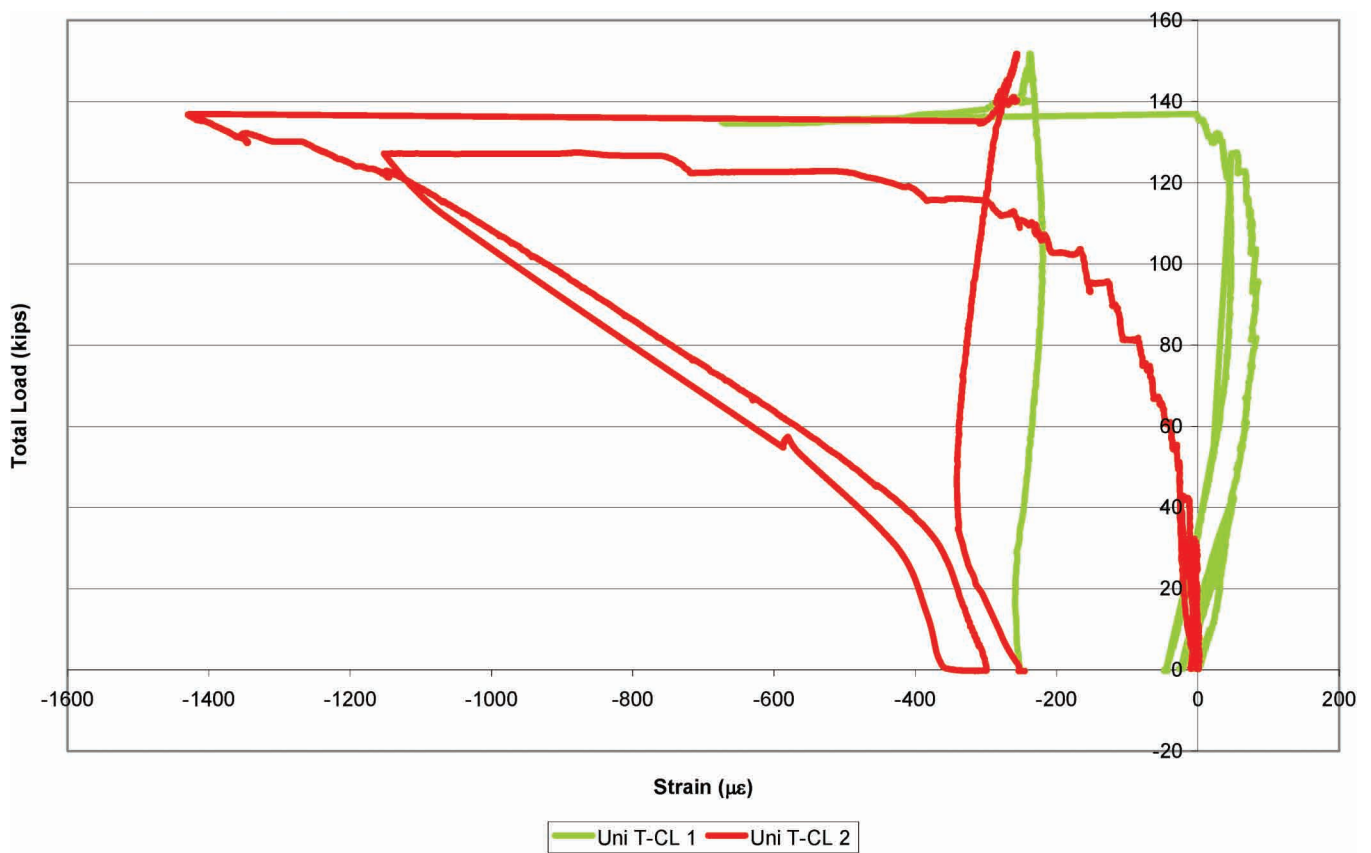


Figure 5.19: T-CL 1 & T-CL 2 vs Total Load

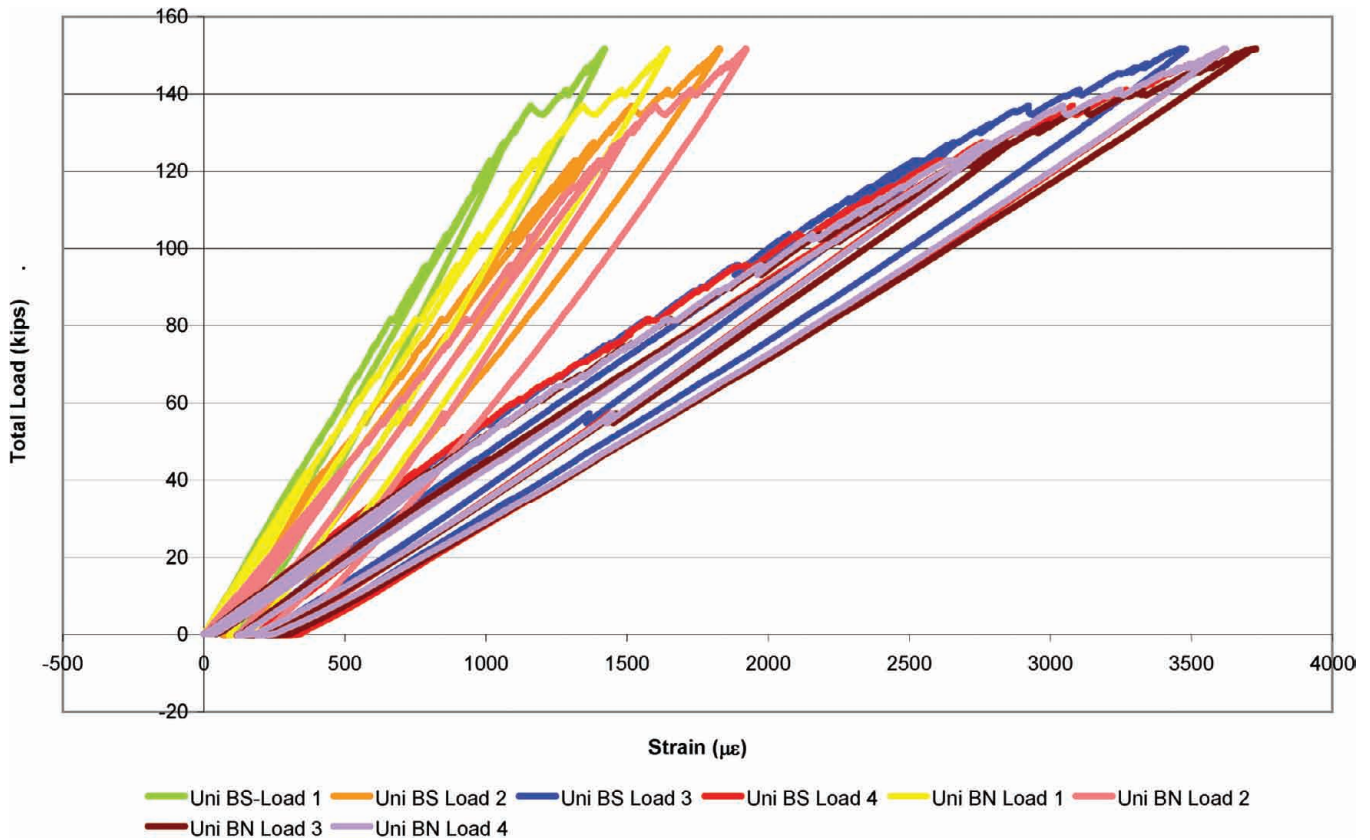


Figure 5.20: BN Load 1,2,3,4 & BS Load 1,2,3,4 vs Total Load

underneath the load (BN Load 3 & 4 and BS Load 3 & 4) measured higher strains than those that were 12 in. offset from the centerline to the West and East.

Figure 5.21 shows a comparison between strain gages BS Load 1, BS Load 2, TS Load 1 and TS Load 2. Strain gage BS Load 1 was right underneath TS Load 1; BS Load 2 was underneath TS Load 2 as well. The slopes on all the data sets were fairly similar, but the strain gages on the bottom of the panel withstand higher tensile strains than the compressive strains experienced by the top gages. The maximum compressive strain observed by TS Load 1 was 942 $\mu\epsilon$ and the maximum tensile strain of BS Load 1 was 1421 $\mu\epsilon$. TS Load 1 experienced 66 % of the strain experienced by the gage underneath it. The maximum compressive strain observed by TS Load 2 was 945 $\mu\epsilon$ and the maximum tensile strain of BS Load 2 was 1829 $\mu\epsilon$. TS Load 2 experienced 52 % of the strain experienced by the gage underneath it. Further discussion on this is in the following section.

5.3.4.2 Inflection Point

In order to check how much the splice plates at the crown connection contribute to the continuity of the specimen, as well as to see how much the crack at the top kerf-cut plate affected the panel, the inflection point was determined using SAP 2000 analysis package and

the data collected from the strain gages. Simple structural analysis using SAP 2000 determined that, for a fully continuous beam with dimensions of the test specimen, the inflection point for the loading applied during the test was located 20 in. away from the centerline, as seen in Figure 5.22.

Figure 5.23 shows the different zones from which data was taken to calculate the inflection point and how the inflection point changed during the test as higher loads were applied, as well as after the top plate cracked.

Figure 5.24 through Figure 5.27 show the plots that detail the measured strain vs. length (or locations along the deck) for each of the sections described above. Four different lines represent the strain measured at each load cycle, and their intercept in y-axis is the location of the inflection point at the respective load cycle. In other words, where all gages measure close to zero strain corresponds to the location of zero moment. Line #1 represents the load cycle with a total load of 42 kips, line #2 the one with a total load of 100 kips, line #3 the cycle with a maximum total load of 125 kips, and line #4 is the one that represents the strains during the cycle that had a maximum total load of 150 kips. All plots showed that the inflection point did not change much as higher loads were applied, and that it did not move after the top plate cracked. The average inflection point

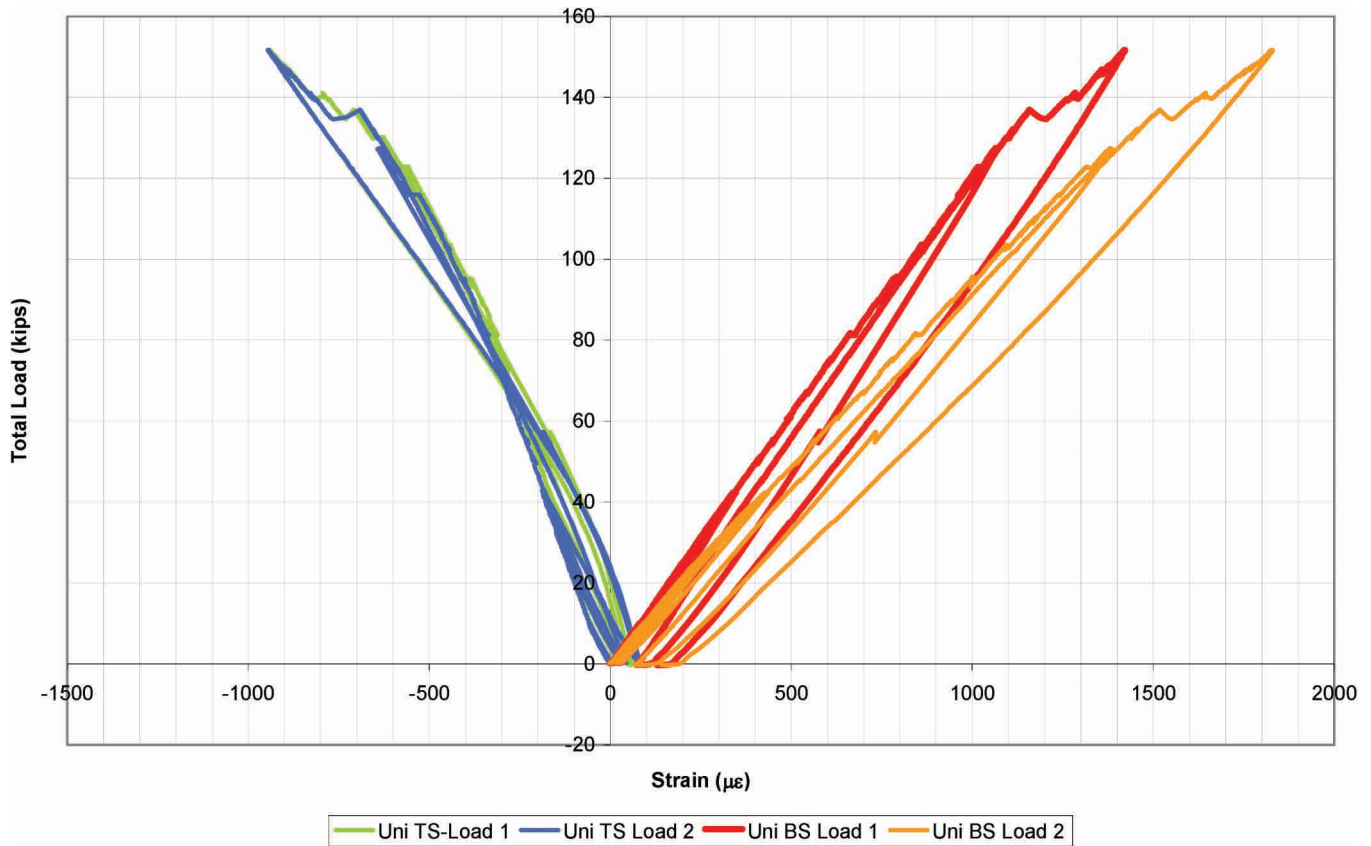


Figure 5.21: TS Load 1,2 & BS Load 1,2 vs Total Load

calculated from the acquired test data was at 18.75 in. from the center, which correlates well with the point determined using SAP 2000 (20 in.).

5.3.4.3 Displacement Data

Four potentiometers were used during the test. Two potentiometers were placed under each load, at each side of the lap joint connection. Figure 5.28 illustrates the deflection measured by each of the potentiometers

up to service load (42 kips) and up to 150 kips. The average deflection measured at 42 kips was 0.13 in. and the average maximum deflection recorded was 0.66 in. All deflection curves show similar slopes, which demonstrate symmetric loading and good behavior of the lap joint connection. A ruler was also placed under each load to monitor the lap joint connection during the test. No visible opening of the joint was observed during the test.

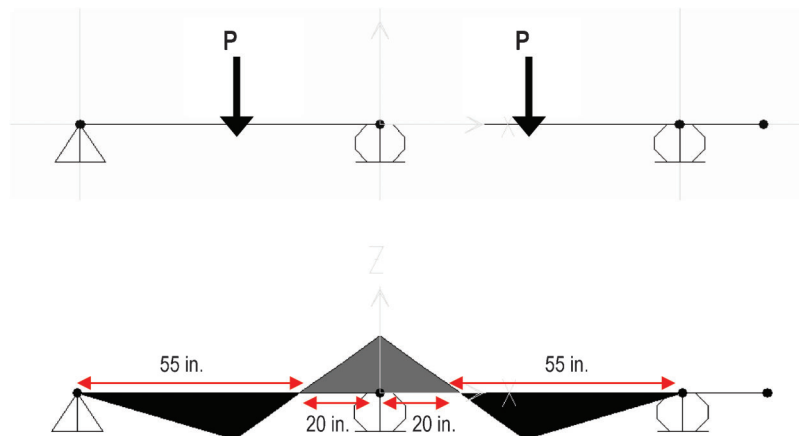


Figure 5.22: SAP 2000 Inflection Point Analysis

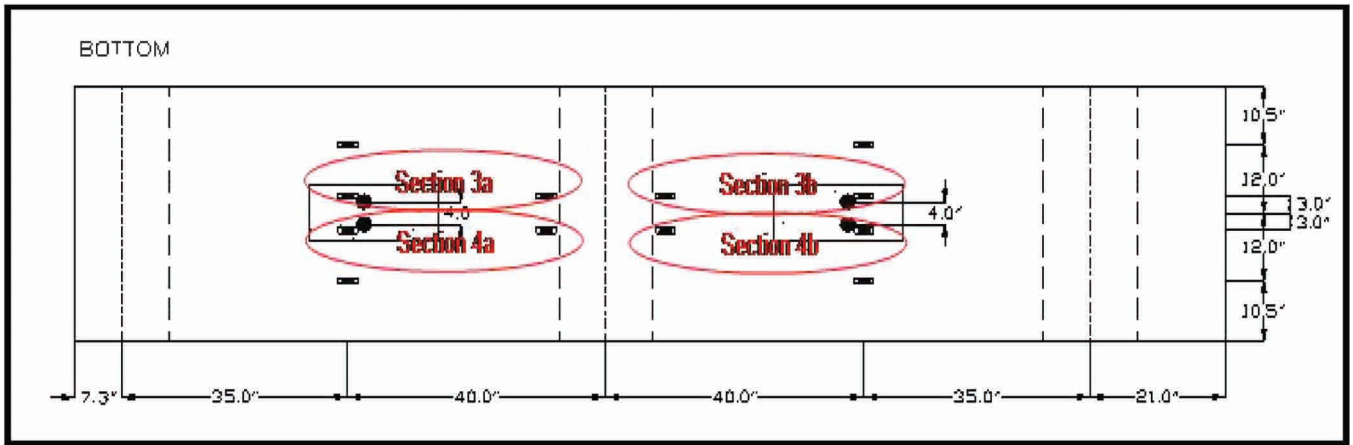


Figure 5.23: Zones Utilized to Calculate the Inflection Point

5.3.5 Test #2 Results

For Test #2, the center top plate was replaced with two individual plates.

5.3.5.1 Strain Gage Results

Strain gages TS Load 1 and TS Load 2 were attached to the top plate of the panel, near the south load. Each gage was at a different side of the lap joint connection, one to the East and the other to the West. Strain gage TS Load 1 had a maximum compressive strain of 350 $\mu\epsilon$. Strain gage TS Load 2 read a maximum compressive strain of 580 $\mu\epsilon$ (Figure 5.29).

Strain gages T-CL 1, T-CL 2, and T-CL 3 were attached to the center top plate of the specimen an inch away from the transverse center line. Strain gage T-CL 2 was located at the center of the panel, then T-CL 1 was 12 in. away towards the West, T-CL 3 was 12 in. towards the East. Gages T-CL 1 and T-CL 3 showed a similar behavior. Strain gage T-CL 2 observed larger strain measurements, with a maximum of 108 $\mu\epsilon$. The maximum strain observed at strain gage T-CL 1 and T-CL 3 was 16 $\mu\epsilon$ and 22 $\mu\epsilon$ respectively (Figure 5.30). The strains observed in this test were considerably smaller than the strains at the center plate on Test #1.

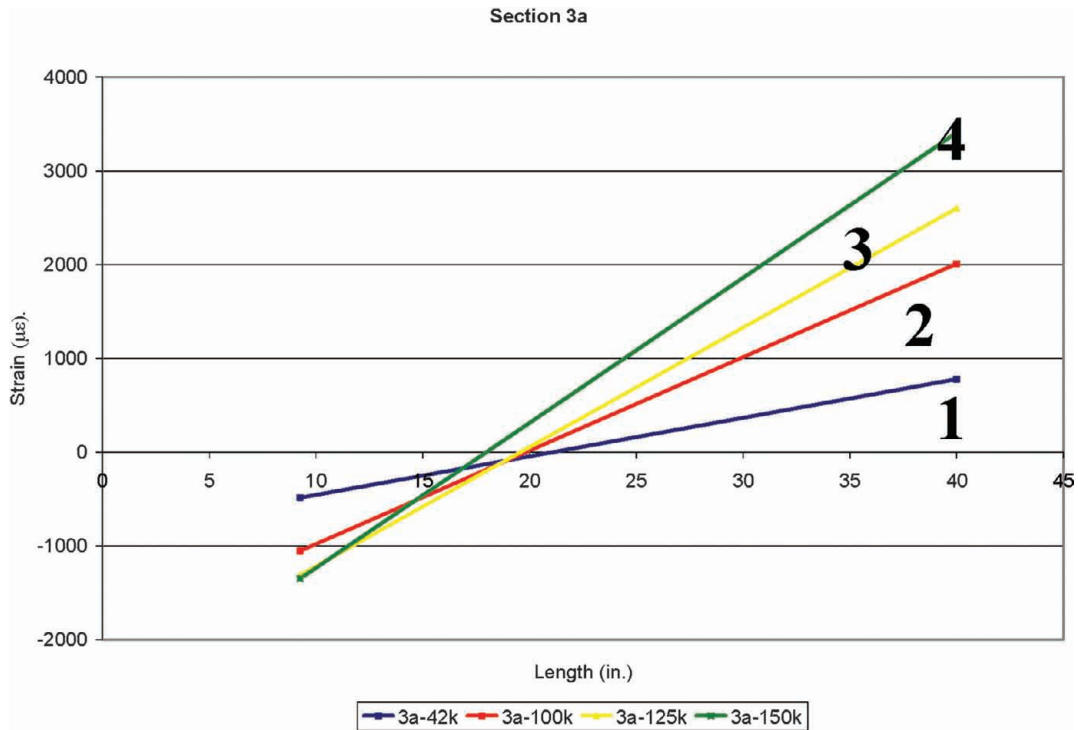


Figure 5.24: Strain vs. Length (Section 3a)

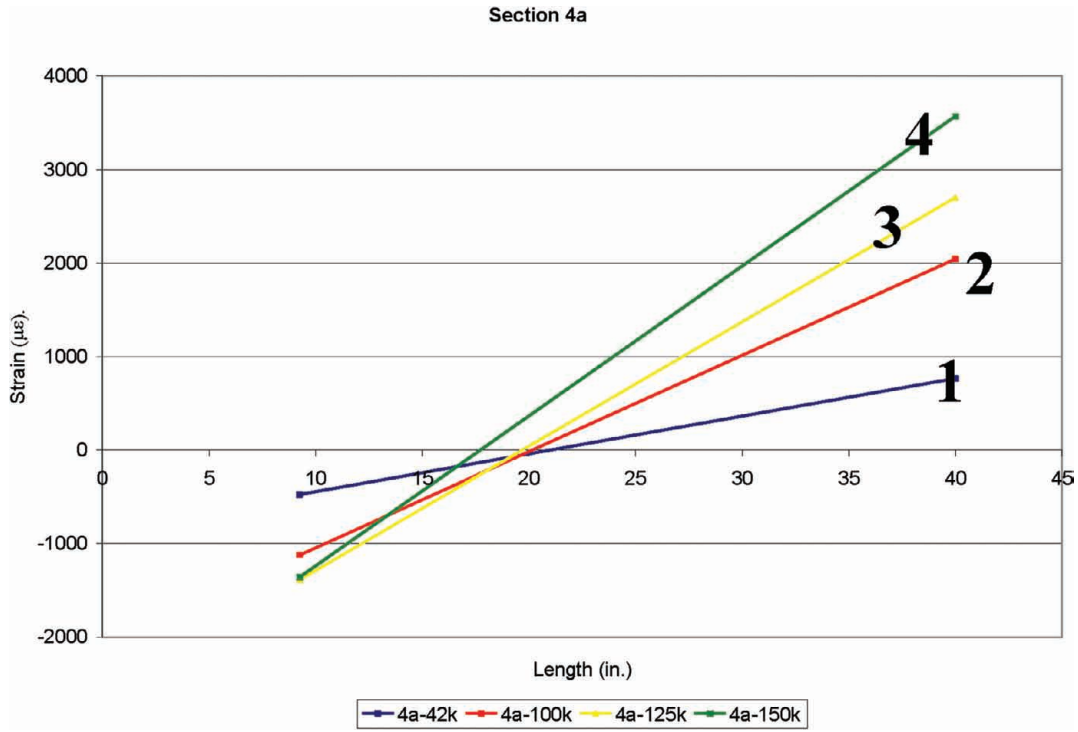


Figure 5.25: Strain vs. Length (Section 4a)

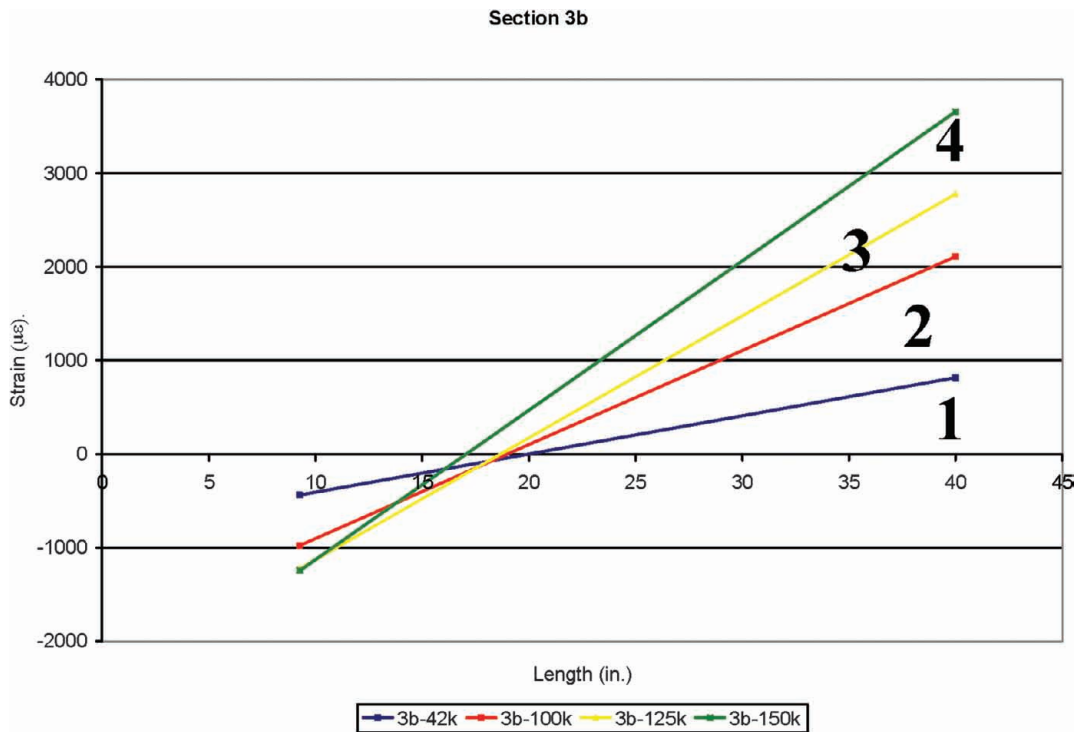


Figure 5.26: Strain vs. Length (Section 3b)

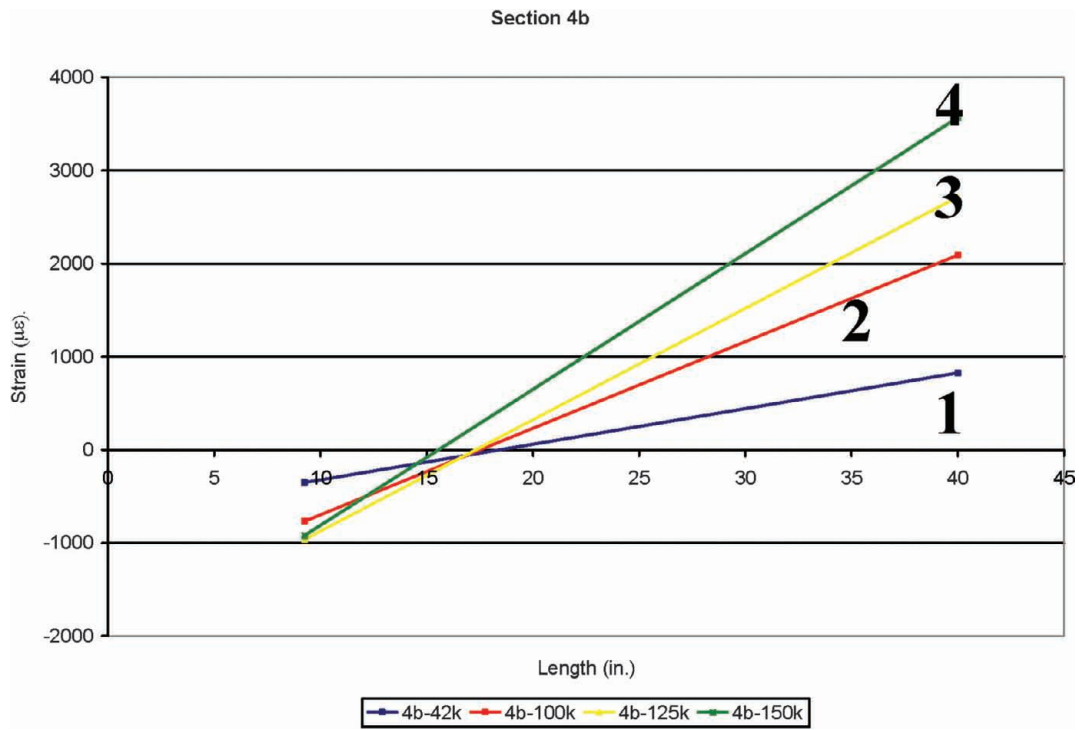


Figure 5.27: Strain vs. Distance (Section 4b)

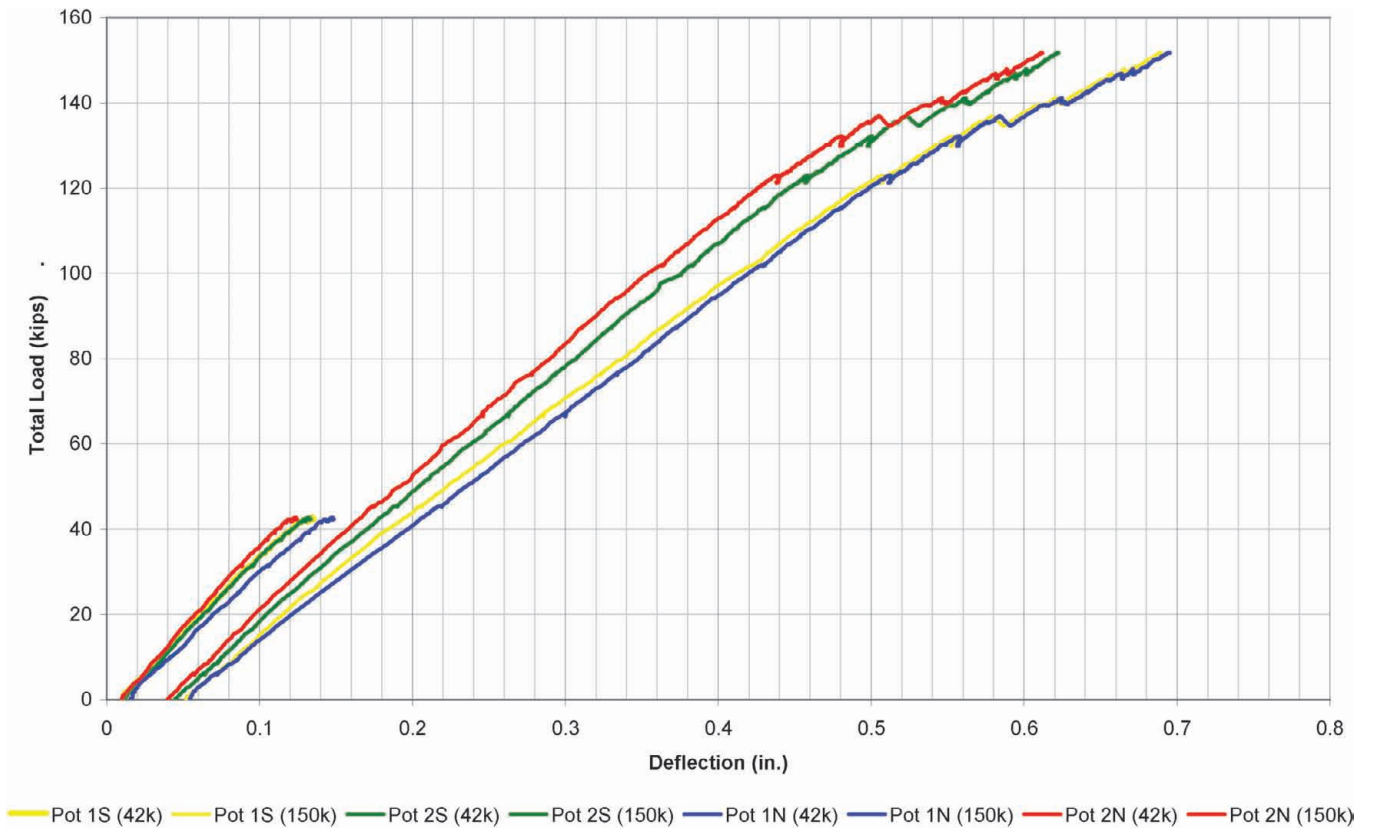


Figure 5.28: Deflection vs. Total Load

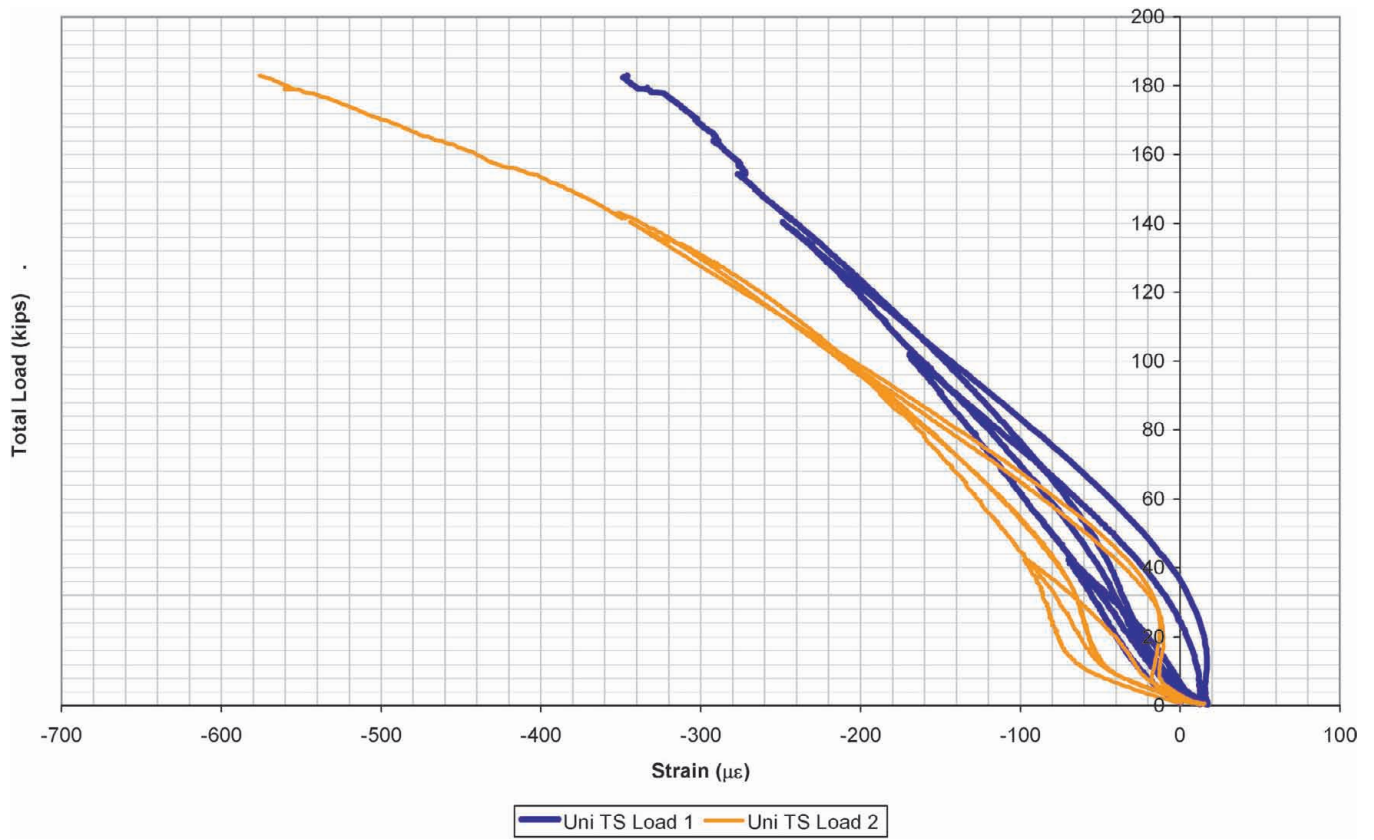


Figure 5.29: TS Load 1 & TS Load 2 vs Total Load

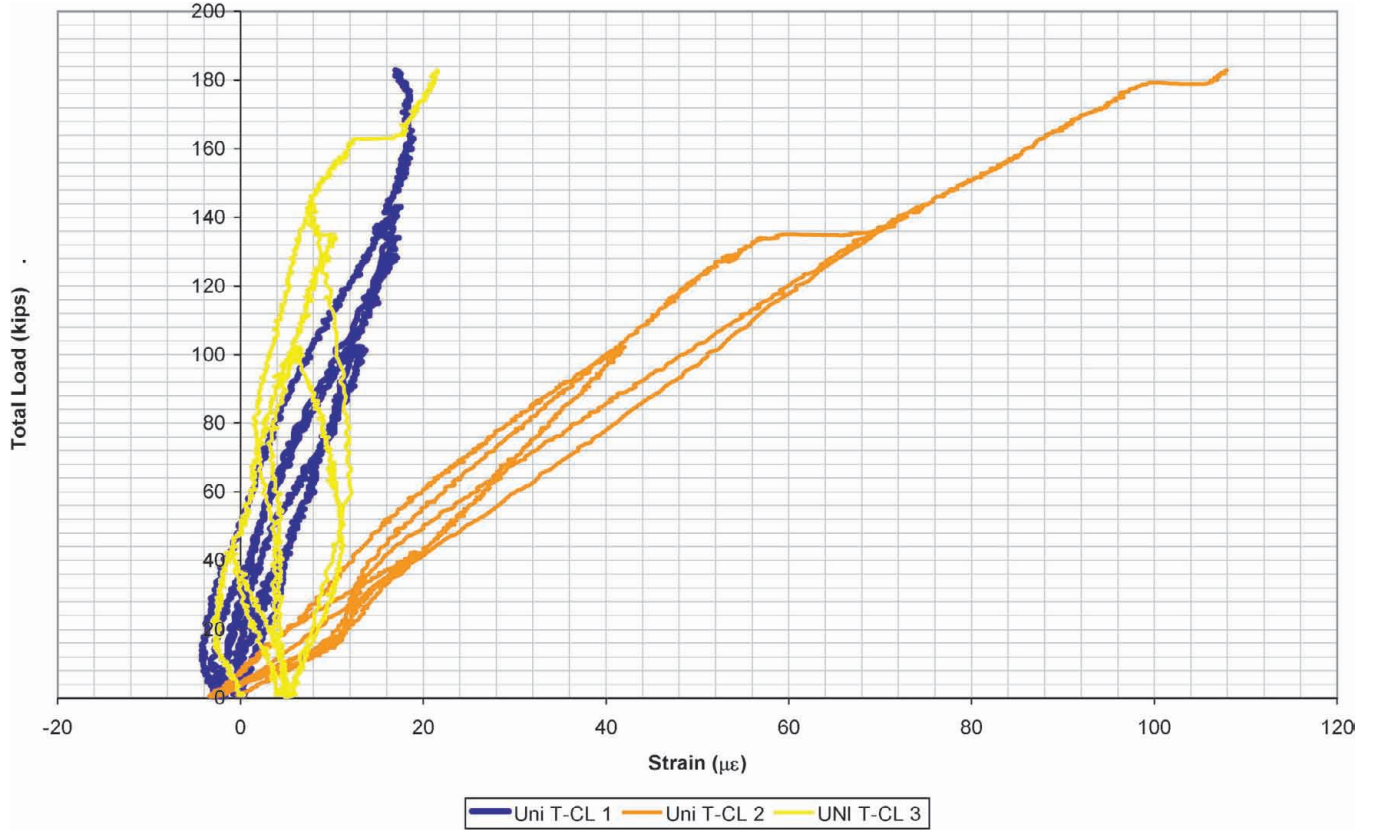


Figure 5.30: T-CL 1, T-CL 2 & T-CL 3 vs Total Load

Strain gages TS-CL and TN-CL were attached to the top plates adjacent to the center plate. TS-CL was at the South plate and TN-CL was located at the North plate. Both gages measured compressive strain. The maximum compression strain observed a total load of 180 kips for strain gage TS-CL was 132 $\mu\epsilon$; strain gage TN-CL appeared to have detached during the test and therefore is not plotted (Figure 5.31). The strains at these locations for the Test #2 were smaller than during Test #1; this seems reasonable because the specimen had already been loaded and seen some damage, and the strains at the center top plates are also smaller as seen in Figure 5.30.

Strain gages BN Load 1, 2, 3 & 4, as well as strain gages BS Load 1, 2, 3 & 4, were all located under the load points, at the North and South sides of the specimen. Figure 5.32 shows that the tensile strains measured on both sides of the panel, at each load point, were symmetric and, as expected, strain gages right underneath the load (BN Load 3 & 4 and BS Load 3 & 4) measured higher strains than those that were 12 in. offset from the centerline to the West and East.

Figure 5.33 shows a comparison between strain gages BS Load 1, BS Load 2, TS Load 1 and TS Load 2. Strain gage BS Load 1 was right underneath TS Load 1; BS Load 2 was underneath TS Load 2 as well. The slopes on all the data sets were fairly similar, but the strain gages on the bottom of the panel withstand

higher tensile strains than the compressive strains experienced by the top gages. The maximum compressive strain observed by TS Load 1 was approximately 360 $\mu\epsilon$ and the maximum tensile strain of BS Load 1 was 800 $\mu\epsilon$. TS Load 1 experienced 45 % of the strain experienced by the gage underneath it. The maximum compressive strain observed by TS Load 2 was 580 $\mu\epsilon$ and the maximum tensile strain of BS Load 2 was 800 $\mu\epsilon$. TS Load 2 experienced 73 % of the strain experienced by the gage underneath it.

Figure 5.34 shows the maximum strains observed at the principal direction on the East web under the South load. The East side of the panel was the one that suffered the most damage during Test #2 due to the South load. The maximum strain recorded at principal direction ϵ_1 was approximately 100 $\mu\epsilon$ and 1150 $\mu\epsilon$ at ϵ_2 . The shear strain observed was approximately 1250 $\mu\epsilon$. These results support the conclusion that the failure was a buckling failure.

Figure 5.35 shows the maximum strains observed at the principal direction on the West web under the North load. The West side of the panel was the one that suffered the most damage caused by the North load during Test #2. The maximum strain recorded at principal direction ϵ_1 was approximately 150 $\mu\epsilon$ and 1600 $\mu\epsilon$ at ϵ_2 . The shear strain observed was approximately 1800 $\mu\epsilon$. These results support the conclusion that the failure was a buckling failure.

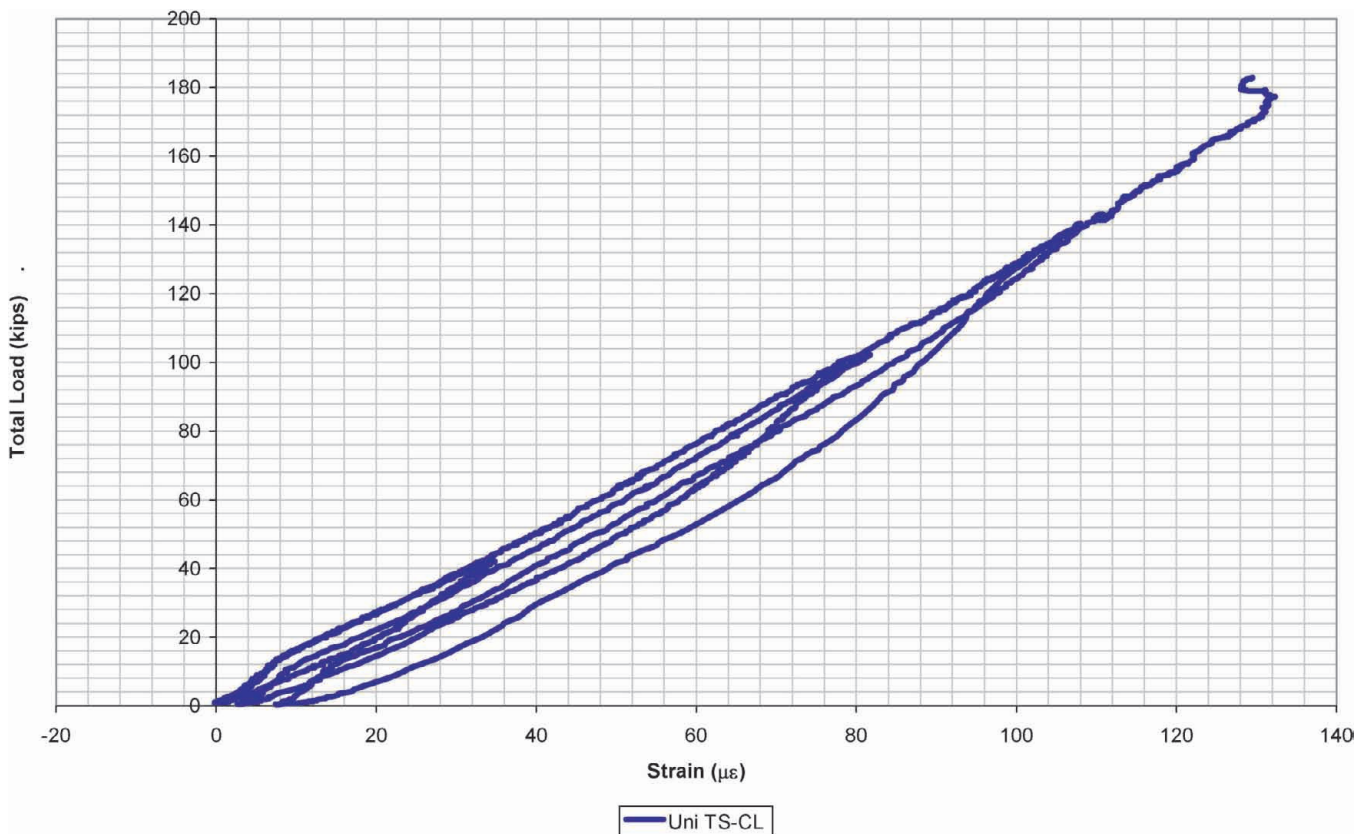


Figure 5.31: TS-CL & TN-CL vs Total Load

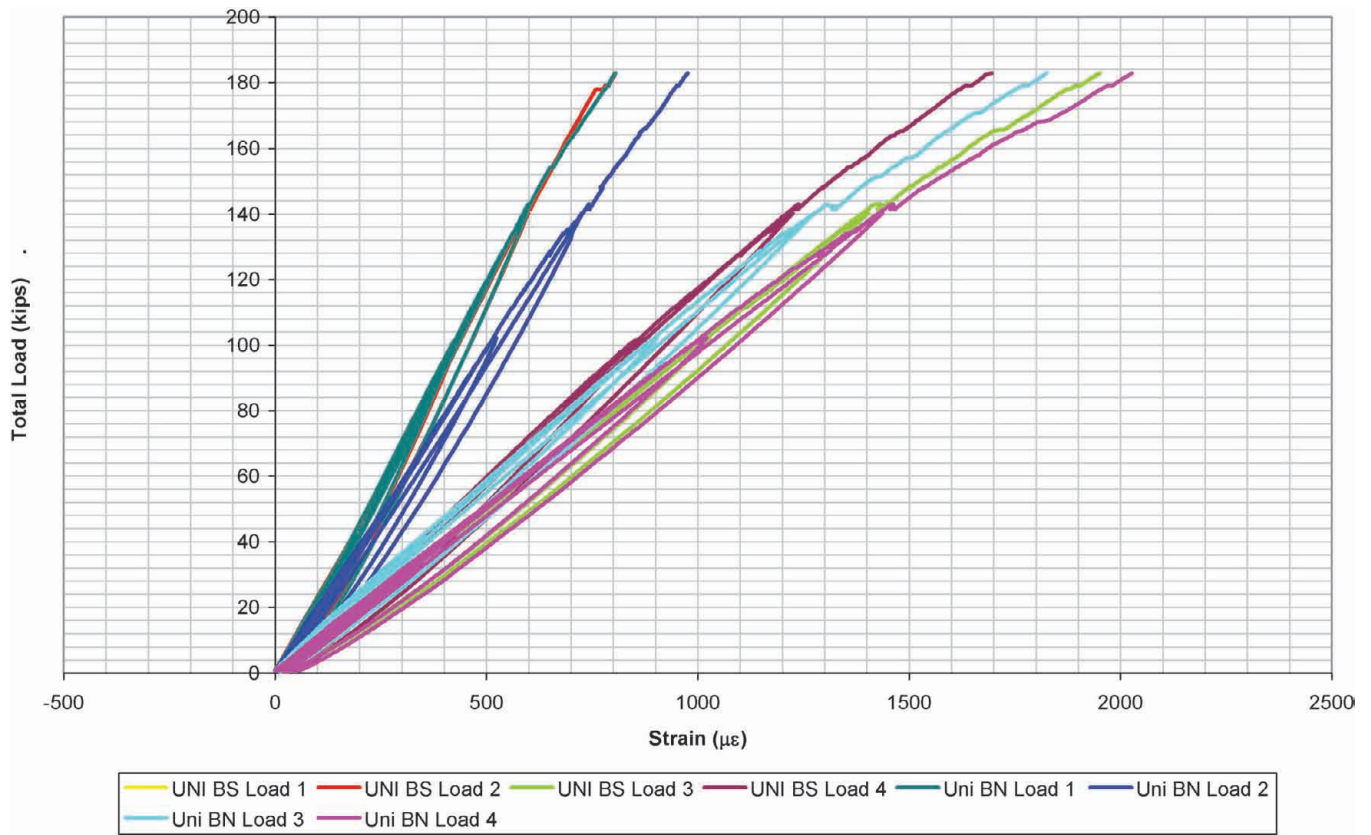


Figure 5.32: BN Load 1,2,3,4 & BS Load 1,2,3,4 vs Total Load

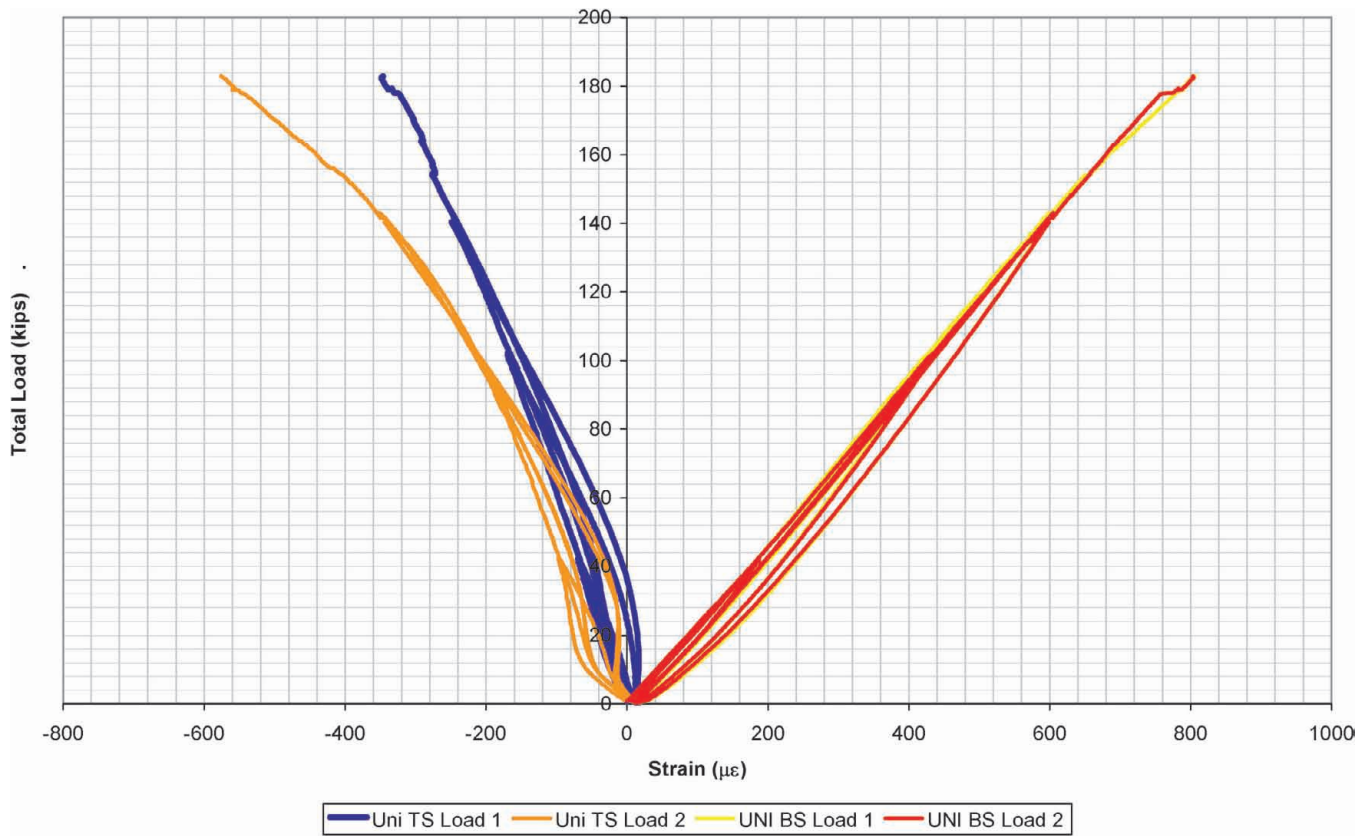


Figure 5.33: TS Load 1, 2 & BS Load 1, 2 vs Total Load

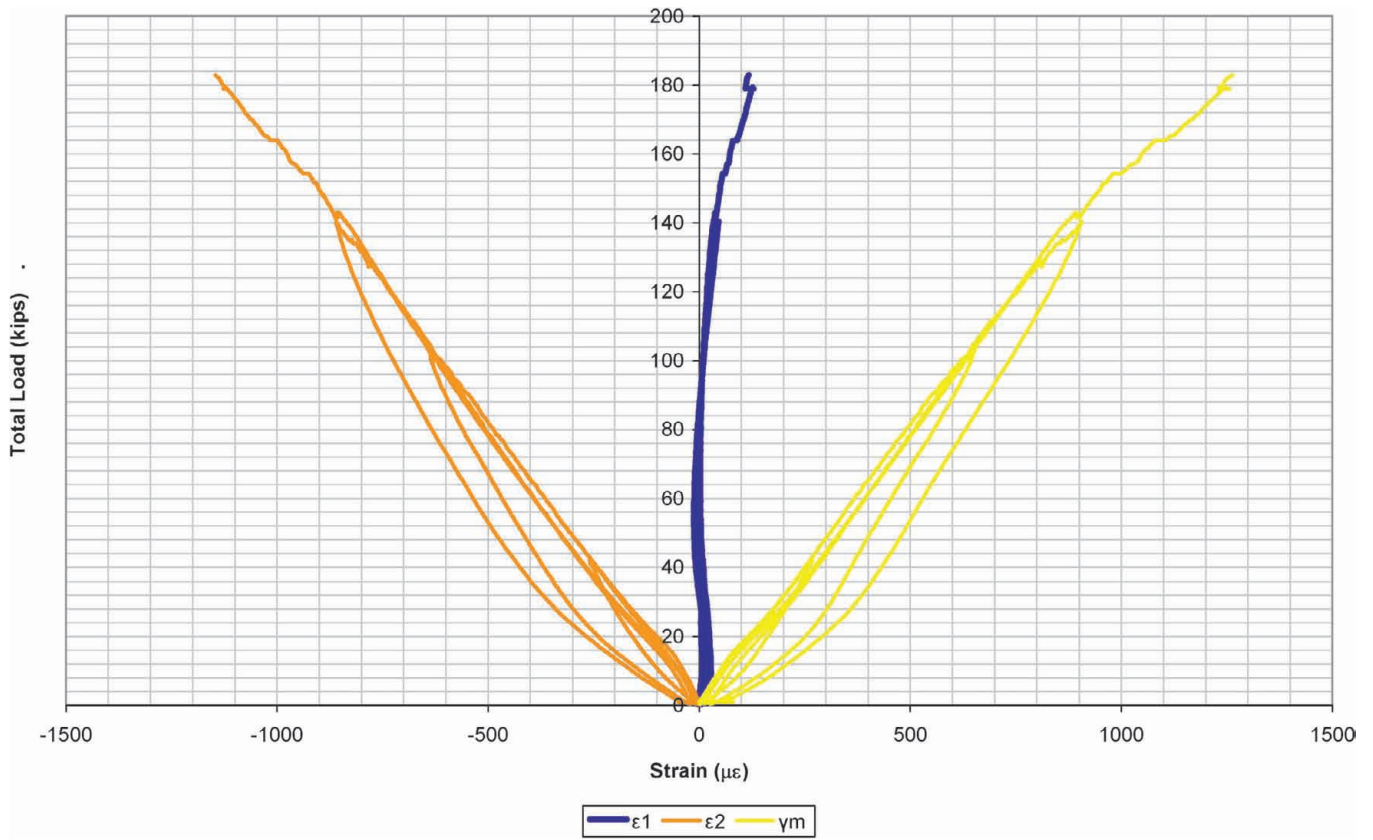


Figure 5.34: Rosette S. Load - E. Web vs Total Load

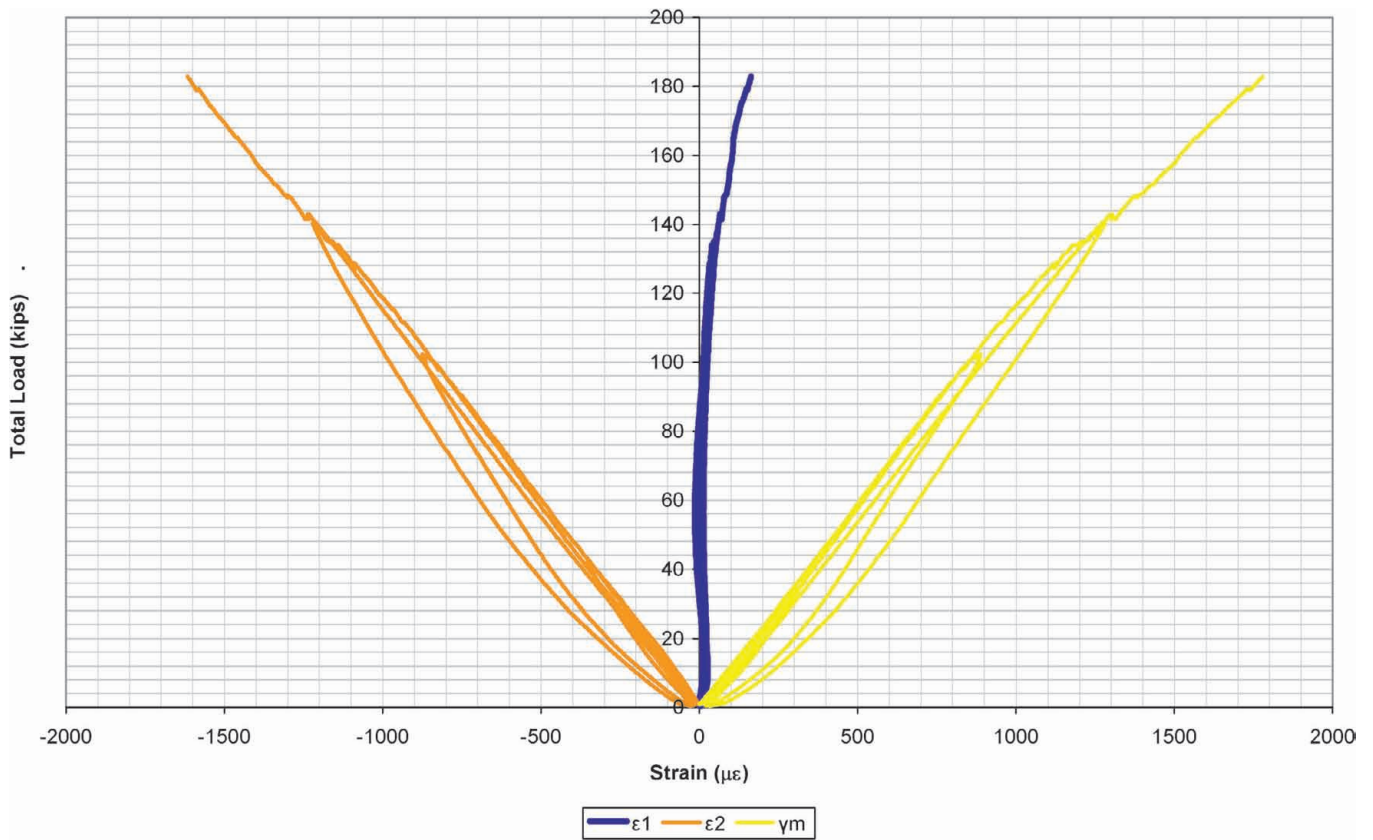


Figure 5.35: N. Load - W. Web vs Total Load

5.3.5.2 Displacement Data

Four potentiometers were used during the test. Two potentiometers were placed under each load, at each side of the lap joint connection. Figure 5.36 illustrates the deflection measured by each of the potentiometers up to service load (42 kips) and up to 180 kips during Test #2. The average deflection measured at 42 kips was 0.17 in. and the average maximum deflection recorded was 0.86 in. All deflection curves show similar slopes, which demonstrate symmetric loading and good behavior of the lap joint connection. A ruler was placed under each load to monitor the lap joint connection during the test. As for Test #1, no visible opening of the joint was noticed during the second test.

5.3.6 Discussion of Results for Test #1 and Test #2

No major damage was observed in Test #1. This test was stopped due to the limit of the load cell used. Buckling failure was observed at the webs right under the applied load at 180 kips, during Test #2; more load was applied until failure of the top plates was noticed. The factor of safety between the maximum load applied during Test #2 and the service load plus impact is 4.3.

The center top plate showed some damage after Test #1. It cracked through its thickness. The crack did not affect the structural integrity of the panel, but such behavior may affect the wearing surface for the deck in

service. For Test #2, this plate was replaced with two individual plates that performed satisfactorily. Only a small opening was observed between the plates during the test.

The splice plates performed well, without visible bearing deformation at the bolt holes. The deck showed no visible damage after Test #1, but showed buckling failure and top plate cracks during Test #2. No cracks in the grout pockets at the deck-to-girder connections and no loosening of the top screws was observed during either of the tests.

The splice plates at the crown connection helped with the continuity of the deck. The inflection point analysis shows the inflection point at around 20 in. away from the center of the specimen; the calculations made with the strain gage data, from Test #1, showed the inflection point at approximately the same place as predicted by the analysis. This inflection point did not move when the crack at the top plate occurred, which also implies that the top plates do not contribute much to the stiffness of the panel. If the top plates were a big factor on the stiffness of the panel, at the moment at which the top plate cracked, the inflection point would have shifted, and this did not occur.

Also, comparisons between the strains at the top and bottom of the panel showed that the strains at the bottom section were higher than those at the top plates, which brings us to the conclusion that the top plates

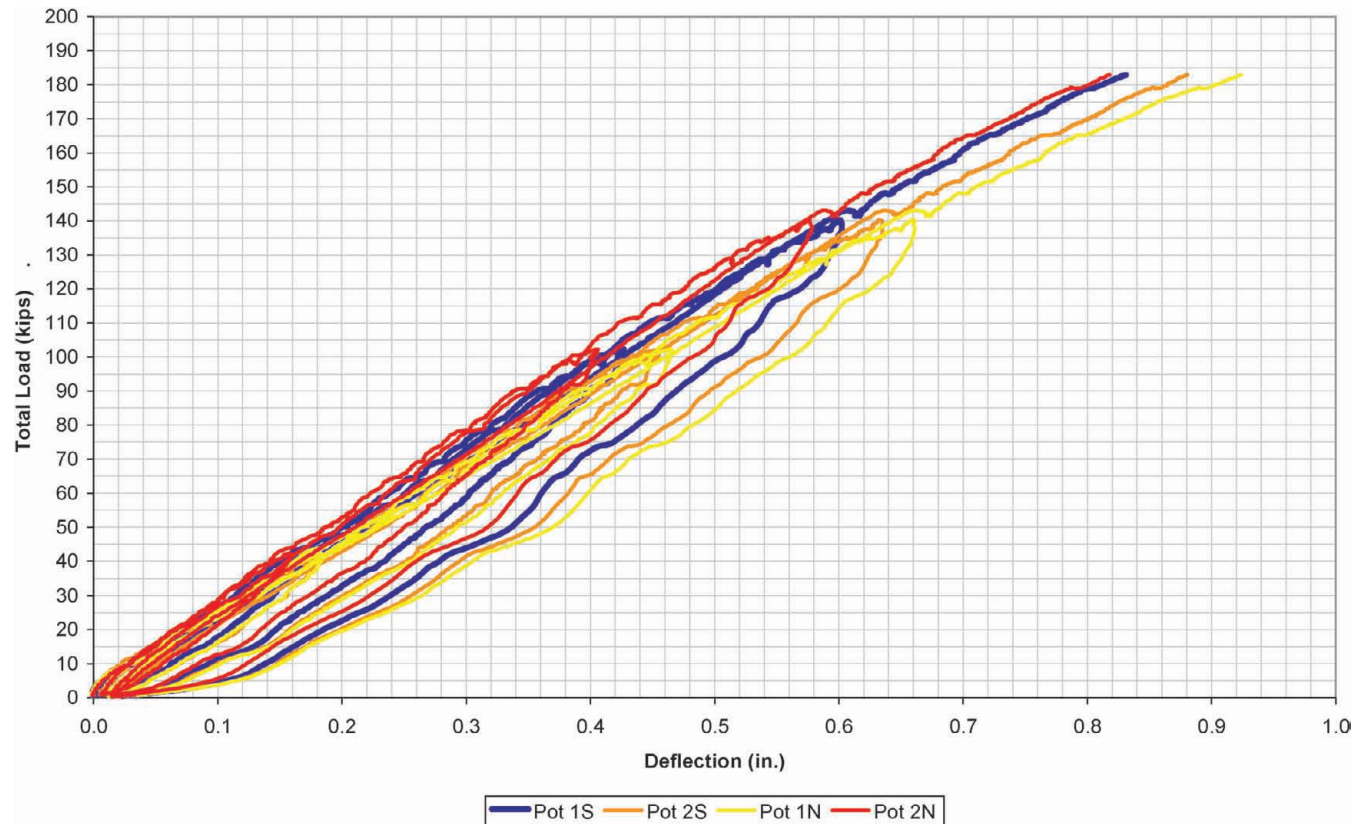


Figure 5.36: Deflection vs. Total Load

were not contributing fully to the stiffness of the panel. If the top plates were fully composite with the bottom section, the strains would have been similar at the extreme fibers on the top and the bottom sections. It can be assumed that the splice plates provided the required continuity to the crown connection. It can be concluded that if the bottom section is in one piece, the top plates do not need to be continuous.

The panel to panel joint worked well; no opening or slip was observed. In addition, the strain gage data showed that both sides of the specimen resisted approximately the same load. For this reason it can be concluded that the joint provided good continuity; if good continuity was not present, it would be expected that the side that had the overlap on the bottom of the lap joint connection may have taken most of the load.

The deflection criterion recommended by GangaRao et al. (2002) was satisfied. GangaRao suggests that the maximum deflection accepted for FRP bridge decks between girders at service loads should be $L/500$, L being the distance between girders. This implies that the maximum deflection between girders accepted for the Sugar Creek Bridge is 0.15 in. During Test #1, the deflection at service load plus impact was 0.13 in. During Test #2, the deflection at service load plus impact was 0.17 in.

5.3.7 Test of Deck with Wearing Surface

A similar test was conducted on a deck panel with two different wearing surfaces applied to the top plate. The main objective of this test was to try to evaluate whether or not deformations of the deck, particularly at

the crown connection, would cause problems with cracking in the wearing surface. A secondary objective was to try to determine if there was a preferable wearing surface for this deck in terms of performance.

5.3.7.1 Wearing Surfaces

Various wearing surfaces were compared to specifications provided by INDOT. These comparisons are shown in Table 5.1, Table 5.2, Table 5.3 and Table 5.4. All but the T-48 appeared to satisfy the requirements. The T-48 wearing surface did not meet the tensile strength requirement. The wearing surfaces for the test were then chosen from the remaining three products; the choice was based partly on INDOT preference.

5.3.7.2 Wearing Surface Crown Connection Test Specimen and Test Set-up

The test set-up for the wearing surface test was identical to that used previously. Again, three supports representing three girder lines were used. A spreader beam was used to apply equal forces, 6 feet apart, at patches representing the wheel loads. The specimen was 28 inches wide with one longitudinal joint (Figure 5.37). The crown connection configuration was essentially the same as on the previous test; at the crown, two separate plates were used, one on either side (Figure 5.38). Four more top plates were used, making six total, separate top plates on this specimen.

Each wearing surface covered half of the specimen longitudinally as shown in Figure 5.37. One wearing surface was called Flexolith, manufactured by Tamms Industries; the other was called Flexogrid and was manufactured by Poly-Carb. Figure 5.39 shows the

TABLE 5-1:
Flexogrid / PolyCarb Specification Comparison

| Test | INDOT Specifications | | Flexogrid / PolyCarb | |
|--|---|--|--|-------------------------------------|
| | Test Method | Value | Test Method | Value |
| Epoxide equivalent | ASTM D 1652 | 270 max | | |
| Pot life | ASTM C 881 (50 ml sample in paper cup) | 15 to 45 min at 75 °F (23.9 °C) | | |
| Tensile strength | ASTM D 638 | 2,500 psi min (13.79 MPa) at 7 days | ASTM D 638-82 | > 2,500 psi (>17.2 MPa) |
| Tensile elongation | ASTM D 638 | 30 to 70 percent at 7 days | ASTM D 638-82 | 35 ± 5 |
| Water absorption | ASTM D 570 | 0.2% max | ASTM D 570 | 0.2% max |
| Viscosity | ASTM D 2393 (Model RVF Brookfield, Spindle No. 3 at 20 rpm) | 7 to 25 poises | ASTM D 2393 (Model RVF Brookfield, Spindle | |
| Shore D Hardness | ASTM D 2240 | 60 min at 77 °F (25 °C) | ASTM D 2240-75 | 65 ± 5 |
| Minimum compressive strength at 3 hrs | ASTM C 109 (Use plastic inserts) | 1,000 psi (6.89 MPa) at 75 °F (23.9 °C) | ASTM C 109 | 7,000 - 9,000 psi (48.3 - 62.1 MPa) |
| Minimum compressive strength at 24 hrs | ASTM C 109 | 5,000 psi min (34.47 MPa) at 75 °F (23.9 °C) | | |
| Minimum adhesion strength at 24 hrs | ASTM C 1583 | 250 psi (1.72 MPa) at 75 °F (23.9 °C) | ASTM C 1583 | |
| Volatile content | ASTM D 1259 Method B for mix system | 3% max | ASTM D 1259 Method B for mix | |

Note: a blank space indicates no information provided by the manufacturer

TABLE 5-2:
Flexolith / TAMMS Specification Comparison

| Test | INDOT Specifications | | Flexolith / TAMMS | |
|--|---|--|--|--------------------|
| | Test Method | Value | Test Method | Value |
| Epoxide equivalent | ASTM D 1652 | 270 max | ASTM D 1652 | |
| Pot life | ASTM C 881 (50 ml sample in paper cup) | 15 to 45 min at 75 °F (23.9 °C) | AASHTO T 237 | 15-30 min. |
| Tensile strength | ASTM D 638 | 2,500 psi min (13.79 MPa) at 7 days | ASTM D 638 | 2,700 psi (18MPa) |
| Tensile elongation | ASTM D 638 | 30 to 70 percent at 7 days | ASTM D 638 | 40% |
| Water absorption | ASTM D 570 | 0.2% max | ASTM D 570 | <0.5% (at 24 hr) |
| Viscosity | ASTM D 2393 (Model RVF Brookfield, Spindle No. 3 at 20 rpm) | 7 to 25 poises | ASTM D 2393 (Model RVF Brookfield, Spindle | |
| Shore D Hardness | ASTM D 2240 | 60 min at 77 °F (25 °C) | ASTM D 2240 | |
| Minimum compressive strength at 3 hrs | ASTM C 109 (Use plastic inserts) | 1,000 psi (6.89 MPa) at 75 °F (23.9 °C) | ASTM C 109 | 5,000 psi (35 MPa) |
| Minimum compressive strength at 24 hrs | ASTM C 109 | 5,000 psi min (34.47 MPa) at 75 °F (23.9 °C) | | |
| Minimum adhesion strength at 24 hrs | ASTM C 1583 | 250 psi (1.72 MPa) at 75 °F (23.9 °C) | ASTM C 1583 | |
| Volatile content | ASTM D 1259 Method B for mix system | 3% max | — | 0.50% |

Note: a blank space indicates no information provided by the manufacturer

specimen in the test set-up with the spreader beam in place.

5.3.7.3 Instrumentation

Instrumentation was somewhat reduced for the wearing surface test based on experience from the previous tests (Figure 5.40). Vertical deflections were

measured with potentiometers placed directly underneath each load patch. Seven strain gages were placed at the top with three near the crown connection and two at each load patch; eight gages were placed on the bottom side of the deck, with three near each load patch and two on either side of the supporting W-shape (Figure 5.40). Rosettes were placed on the FRP deck

TABLE 5-3:
T-48 / Transpo Specification Comparison

| Test | INDOT Specifications | | T-48 / Transpo | |
|--|---|--|------------------------------|-------------------------------------|
| | Test Method | Value | Test Method | Value |
| Epoxide equivalent | ASTM D 1652 | 270 max | ASTM D 1652 | |
| Pot life | ASTM C 881 (50 ml sample in paper cup) | 15 to 45 min at 75 °F (23.9 °C) | AASHTO T 237 | 15 - 30 min. at 70 °F |
| Tensile strength | ASTM D 638 | 2,500 psi min (13.79 MPa) at 7 days | ASTM D 638 | 1800 psi (12 MPa) min |
| Tensile elongation | ASTM D 638 | 30 to 70 percent at 7 days | ASTM D 638 | 45% min |
| Water absorption | ASTM D 570 | 0.2% max | ASTM D 570 | |
| Viscosity | ASTM D 2393 (Model RVF Brookfield, Spindle No. 3 at 20 rpm) | 7 to 25 poises | Brookfield | 1,200 - 1,600 cps (MPa - sec) |
| Shore D Hardness | ASTM D 2240 | 60 min at 77 °F (25 °C) | ASTM D 2240 | 60 min. |
| Minimum compressive strength at 3 hrs | ASTM C 109 (Use plastic inserts) | 1,000 psi (6.89 MPa) at 75 °F (23.9 °C) | ASTM D 695 | 5,000 psi (34MPa) min. |
| Minimum compressive strength at 24 hrs | ASTM C 109 | 5,000 psi min (34.47 MPa) at 75 °F (23.9 °C) | | |
| Minimum adhesion strength at 24 hrs | ASTM C 1583 | 250 psi (1.72 MPa) at 75 °F (23.9 °C) | ACI 503R | 250 psi (1.7MPa) min. (to concrete) |
| Volatile content | ASTM D 1259 Method B for mix system | 3% max | ASTM D 1259 Method B for mix | |

Note: a blank space indicates no information provided by the manufacturer

TABLE 5-4:
Flexogrid Specification Comparison

| Test | INDOT Specifications | | PPC 1121 / KwikBond | |
|--|---|--|--|-------------------------|
| | Test Method | Value | Test Method | Value |
| Epoxide equivalent | ASTM D 1652 | 270 max | ASTM D 1652 | |
| Pot life | ASTM C 881 (50 ml sample in paper cup) | 15 to 45 min at 75 °F (23.9 °C) | ASTM C 881 (50 ml sample in paper cup) | |
| Tensile strength | ASTM D 638 | 2,500 psi min (13.79 MPa) at 7 days | ASTM D-638 (5.5-7.5mm) | > 2,540 psi (>17.5 MPa) |
| Tensile elongation | ASTM D 638 | 30 to 70 percent at 7 days | ASTM D-638 (5.5-7.5mm) | 35% min |
| Water absorption | ASTM D 570 | 0.2% max | ASTM D 570 | |
| Viscosity | ASTM D 2393 (Model RVF Brookfield, Spindle No. 3 at 20 rpm) | 7 to 25 poises | ASTM D 2196 | 0.075 - 0.2 Pa-s |
| Shore D Hardness | ASTM D 2240 | 60 min at 77 °F (25 °C) | ASTM D 2240 | |
| Minimum compressive strength at 3 hrs | ASTM C 109 (Use plastic inserts) | 1,000 psi (6.89 MPa) at 75 °F (23.9 °C) | ASTM C 109 (Use plastic inserts) | |
| Minimum compressive strength at 24 hrs | ASTM C 109 | 5,000 psi min (34.47 MPa) at 75 °F (23.9 °C) | ASTM C 109 | |
| Minimum adhesion strength at 24 hrs | ASTM C 1583 | 250 psi (1.72 MPa) at 75 °F (23.9 °C) | Cal Trans Test Method 551 | >3.5 MPa |
| Volatile content | ASTM D 1259 Method B for mix system | 3% max | ASTM D 1259 Method B for mix system | |

Note: a blank space indicates no information provided by the manufacturer

webs; two at each load patch, one at mid-depth on each of two webs directly under the load. Video cameras were placed within the longitudinal cells at either end of the deck, so that any web buckling could be captured.

Also, string lines were attached to each side of the deck, following the 2% cross-slope, so that any vertical ‘dishing’ deformations of the deck would be more easily identified and compared to the original,

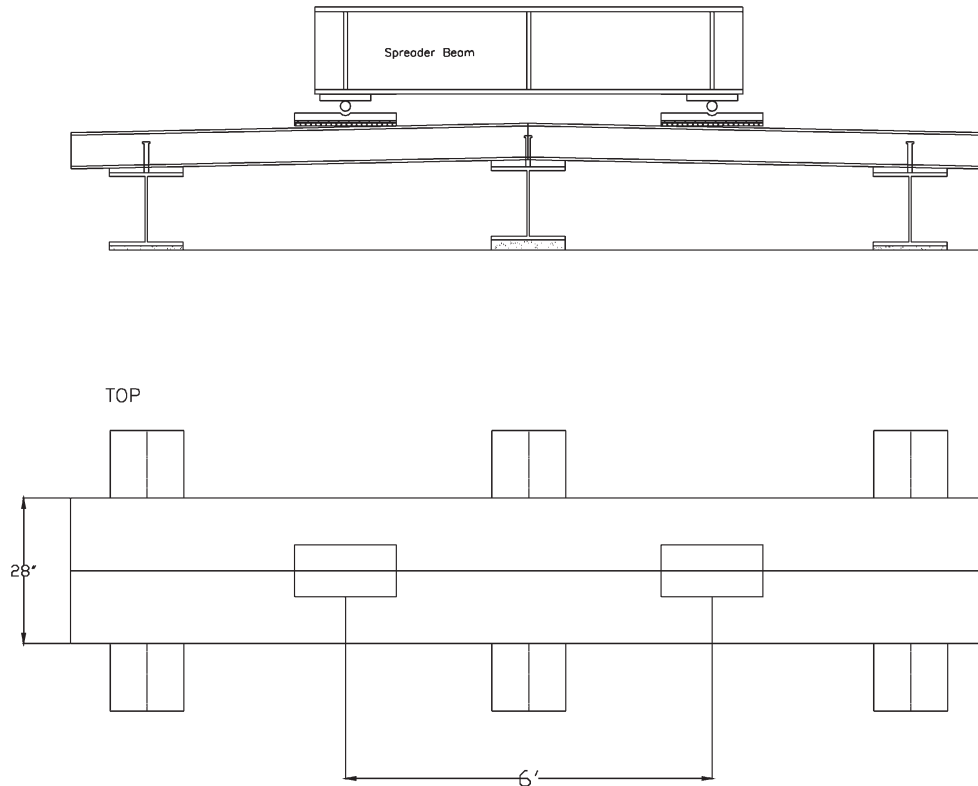


Figure 5.37: Loading for Wearing Surface Test

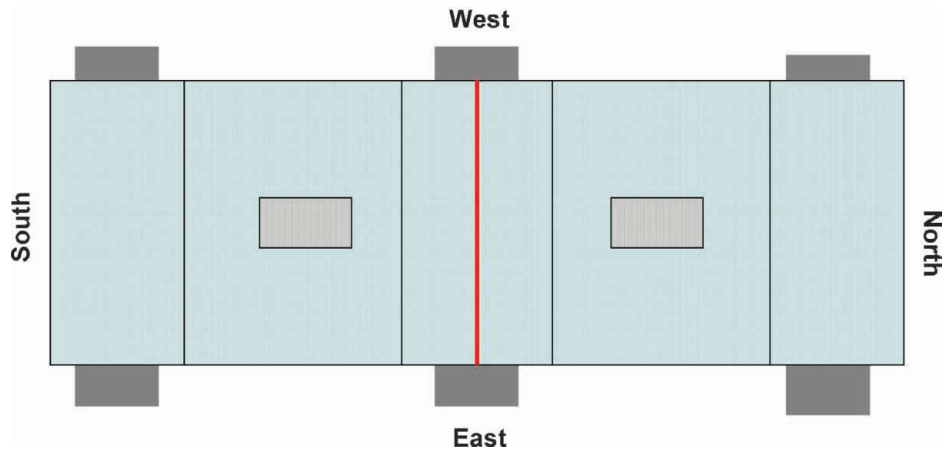


Figure 5.38: Placement of Top Plates in Wearing Surface Specimen



Figure 5.39: Wearing Surface Specimen in Loading Frame

undeformed deck. These reference string lines are shown with the arrows in Figure 5.41; the string lines are pink in color.

5.3.7.4 Wearing Surface Test Results

The overall load-deformation response of the wearing surface test specimen was comparable to what was observed in previous tests. The maximum load for this test was 209 kips total, or roughly 104 kips at each load patch. This translates into a factor of safety of about 5 with respect to the service load plus impact. Furthermore, the measured deflection corresponding to the service load plus impact satisfied the L/500 deflection criterion. Strain gage data produced similar results to those observed in previous tests.

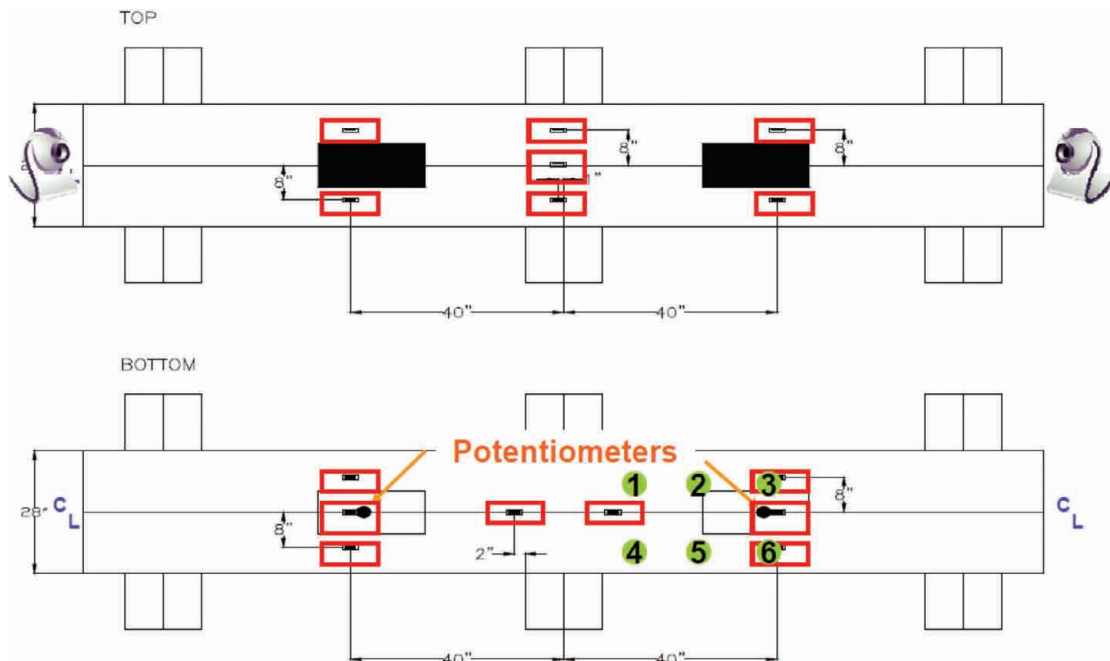


Figure 5.40: Instrumentation of Wearing Surface Specimen

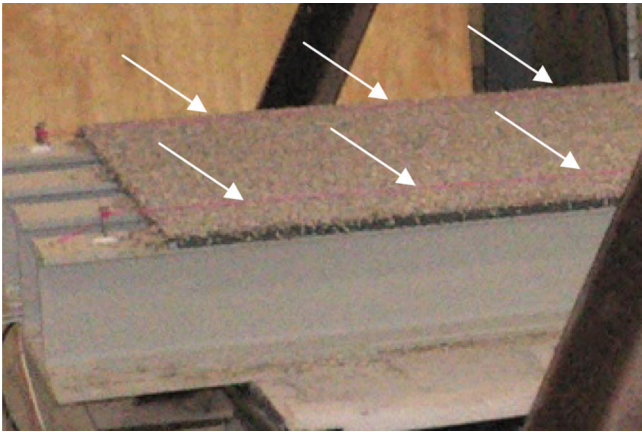


Figure 5.41: Reference String Lines on Both Sides of Wearing Surface Specimen

At the crown connection, both wearing surfaces cracked fairly early in the test; unfortunately, there is no record of exactly when this crack, which extended completely across the width of the deck specimen, formed (Figure 5.42). However, this crack was observed at a service-level load. Based on this result, recommendations were made to the consulting engineers by INDOT personnel. One possibility was to place a backer rod or water stop in the joint and then seal the joint. If using silicone, this might need to be replaced every 7 years. The deck installation would include an FRP overlay at the crown connection.

Meanwhile, despite severe deformations and dishing of the wearing surface at the load patches and top plates, the deck top plates performed well, and no cracks were observed at any other locations in the wearing surface. An example of the severe dishing at the load patches is shown in Figure 5.43; the dishing was so severe that an upwards deformation was observed at the edge of the deck specimen. The upwards deformation of the top plate at the edge was believed to be a result of the boundary conditions for this specimen,

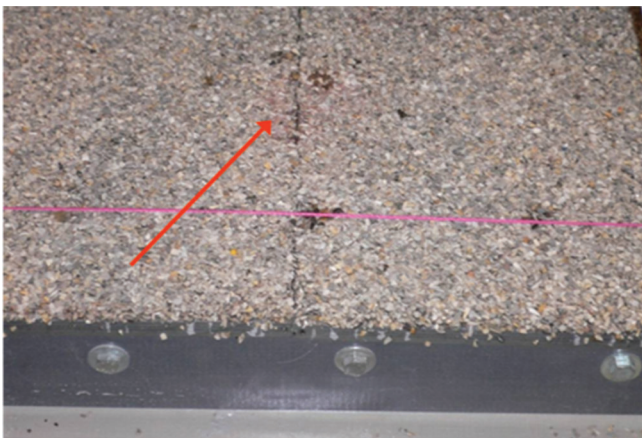


Figure 5.42: Crown Connection Crack in Wearing Surface

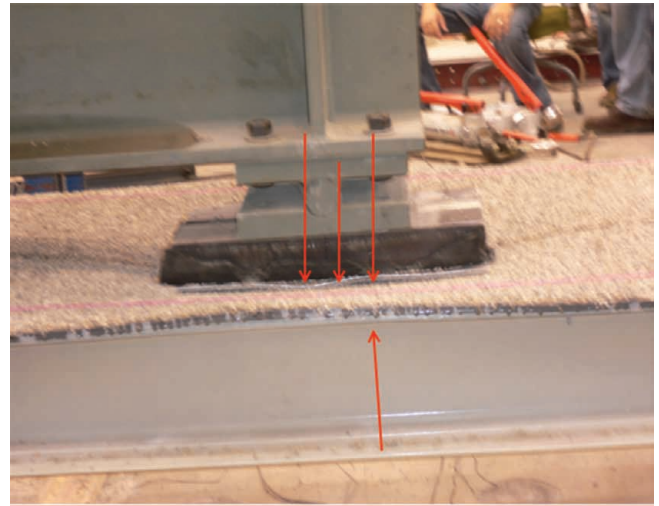


Figure 5.43: Dishing Deformation at the Load Patch

which was relatively narrow (28 inches). Therefore, the upwards deformation was not believed to be an issue for the in-service FRP bridge deck.

The ultimate failure mode for this specimen was primarily web buckling, precipitated by failure of the flange-web joint (Figure 5.44). This is the same as in the previous test. Web buckling essentially led to fracture of fibers in the web surfaces as shown in Figure 5.45. This failure mode was not observed until the ultimate load of the test specimen. Therefore, it is not considered to be a common issue for in-service performance of the FRP deck.

5.3.7.5 Wearing Surface Pull-Off Tests

Pull-off tests were also conducted on the two wearing surfaces used on the test specimen following ASTM C1583. These tests were used to evaluate the bond strength of the wearing surface. Unfortunately, issues with the adhesion of the steel disk to the wearing surface prevented proper evaluation of the wearing surface. A variety of adhesives (glues) were tried; however, failure consistently occurred at the steel disk and wearing surface interface, rather than the wearing surface and FRP plate interface as intended. For tests #4, #5, and #6, the failure did occur at a stress level higher than the 250 psi required, however, suggesting

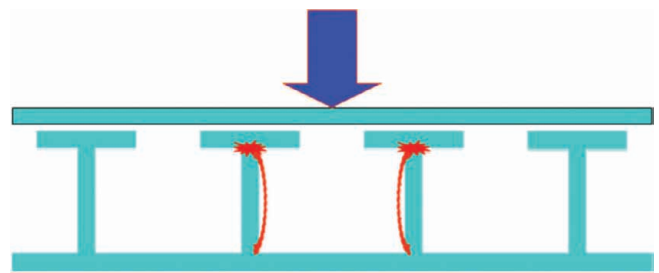


Figure 5.44: Schematic of Web Buckling



Figure 5.45: Damage to Deck Webs Under Load Patch

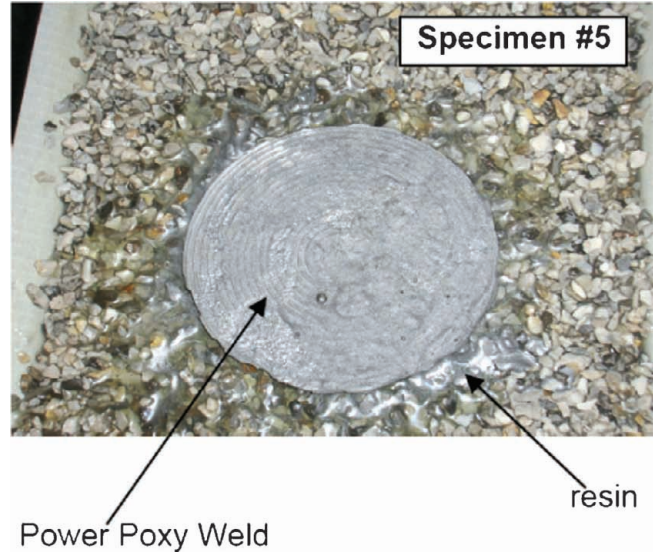


Figure 5.47: Failure of Steel Disk to Wearing Surface in Test Specimen #5

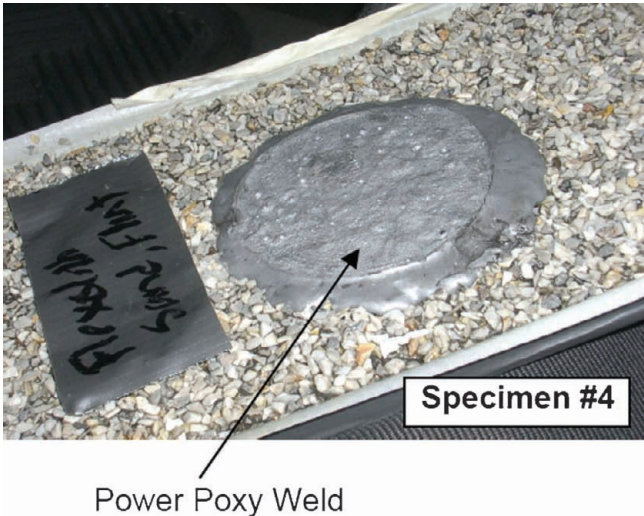


Figure 5.46: Failure of Steel Disk to Wearing Surface in Test Specimen #4

5.4 Sugar Creek Bridge Deck Installation

Installation of the FRP deck on the Sugar Creek Bridge began mid-November 2009. As described in Section 5.2, the Sugar Creek Bridge is a 60 feet simple span, 24 feet wide. It had 5 girders spaced at 5'-10" with a 2'-2" overhang (Figure 5.1). The rehabilitation consisted of replacing the concrete slab with an FRP deck that increased its clear roadway from 24 feet to 28 feet. The girders were moved and spaced at 6'-3", which resulted in a 1'-9" overhang (Figure 5.2). The ZellComp deck panels, typically 33" wide, were placed transverse to the bridge girders. The panel lengths corresponded to half the width of the bridge deck, meeting at the centerline of the bridge at the crown connection. Figure 5.49 shows the FRP deck layout on the bridge. Shaded sections on Figure 5.49 indicate grouted sections. These grouted sections include the crown connection (at bridge centerline), at the abutments where impact from vehicles entering the bridge is expected, and on each side of the bridge where steel reinforcement and attachments for guardrails were to be located.

that the wearing surface – FRP plate interface was adequate (Table 5.5). Images of these test specimens after each test are shown in Figure 5.46, Figure 5.47, and Figure 5.48.

TABLE 5.5:
Pull-off Test Results

| Test Specimen | Manufacturer | Aggregate | Prep. Of Surface | Glue | Failure Load (lbs) | Failure Stress* (psi) |
|---------------|--------------|-----------|------------------|--------------------------------|--------------------|-----------------------|
| #1 | PolyCarb | Flint | no sanding | Lord High-Performance Adhesive | 1000 | 141 |
| #2 | PolyCarb | Flint | sanding | JB Weld | 300 | 42 |
| #3 | Flexolith | Flint | sanding | ... epoxy | 200 | 28 |
| #4 | Flexolith | Flint | sanding | Power Poxo Weld | 2000 | 283 |
| #5 | Flexolith | Flint | sanding | PolyCarb #163+Power Poxo Weld | 1800 | 255 |
| #6 | Flexolith | Flint | sanding | PolyCarb #163 | 3600 | 509 |

*Considering only the area of the steel disk (3" diameter)
*Required Adhesive Strength by Spec = 250psi

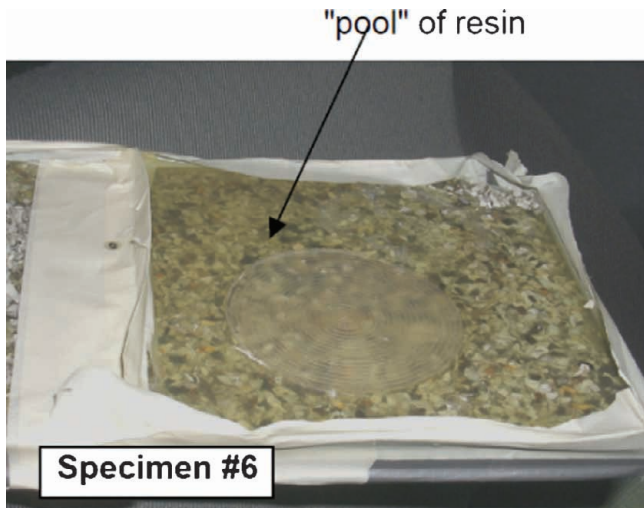


Figure 5.48: Failure of Steel Disk to Wearing Surface in Test Specimen #6

The deck rehabilitation maintained the existing 2% cross-slope. This cross-slope was achieved with grouted haunches at each of the girders (Figure 5.3). The FRP deck panels were laid across those haunches; shear studs in grouted pockets secured the panels to the girders (Figure 5.4). Foam dams that were custom-manufactured to fit to the ZellComp deck were used to

form the grout pockets. The FRP deck panels met at an angle at the crown connection, requiring a splice plate and a special overlay at the top of the deck to address concerns of moisture ingress based on the test results (Figure 5.5).

Figure 5.50 shows the crew, crane, and a stack of bottom FRP deck sections ready for construction. Angles welded into place onto the girder flanges created formwork for the grouted haunches for the cross-slope of the bridge deck (Figure 5.51). Figure 5.52 and Figure 5.53 show placement of the bottom FRP deck section on the girders.

Figure 5.54 shows the holes for the shear studs at the crown connection. It also shows that two different panels, each traversing half of the width of the bridge, met at the crown connection. Figure 5.55 shows the bolted splice plates at the crown connection. The holes in the splice plates were drilled on-site along with the holes in the FRP bottom deck sections. This was done to ensure that the holes in the splice plates and deck sections would match. Also shown in Figure 5.55 is reinforcement for the bridge abutment.

Figure 5.56 shows the shear studs at the exterior girder line and the reinforcement at the guardrail detail. The guardrails were attached to the outside edge of the deck by the long rods anchored into the deck at this location. Foam dams in the foreground of Figure 5.56

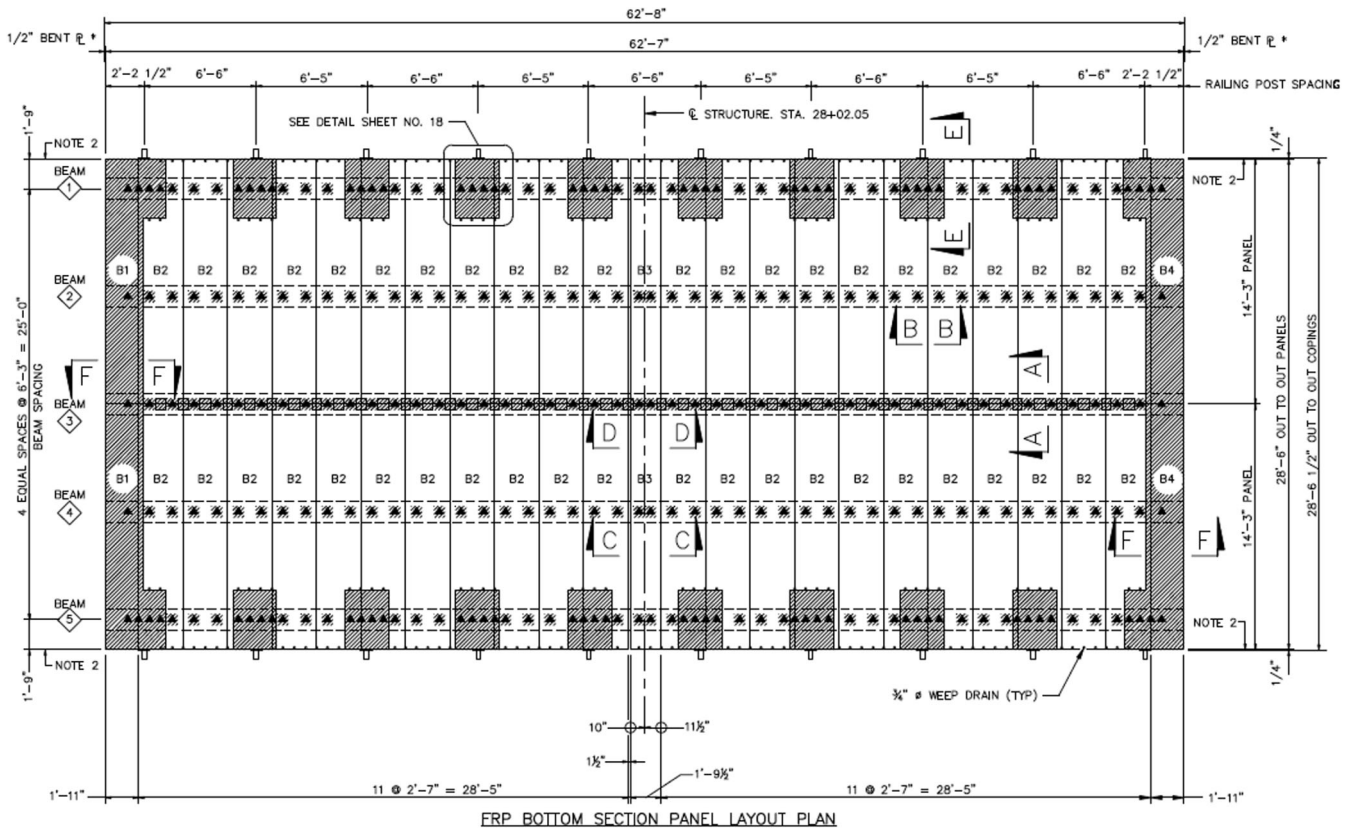


Figure 5.49: Plan View of FRP Deck Layout



Figure 5.50: View of Bottom Deck Sections



Figure 5.53: Placement of an FRP Deck Panel on Girders



Figure 5.51: View of Girders Prepared with Angles for Grouted Haunches



Figure 5.54: Bottom FRP Deck Sections at Crown Connection with Holes for Shear Studs

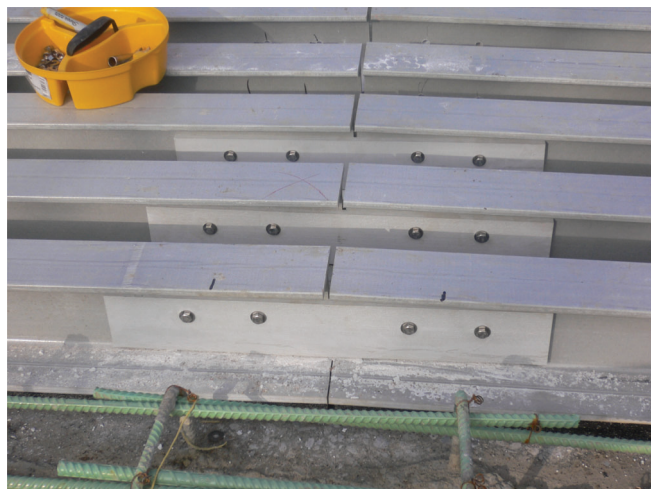


Figure 5.55: Splice Plates at the Crown Connection (Abutment Reinforcement in Foreground)



Figure 5.52: Placement of an FRP Deck Panel on Girders

show the end of the grouted section used to develop the bars for the guardrail connection.

Figure 5.57 shows the shear studs and the foam dams used to form the grout pockets for the shear studs. A

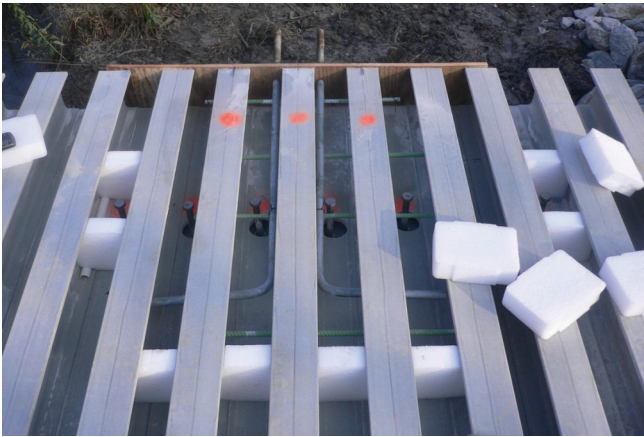


Figure 5.56: Reinforcement and Shear Studs at Guardrail Location

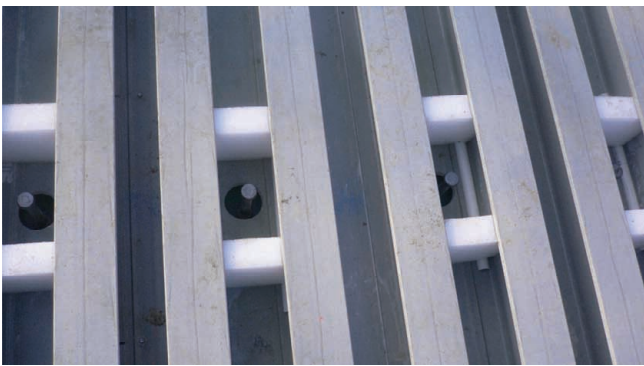


Figure 5.57: Shear Studs and Foam Dams for Grout Pockets

half section of small, PVC tube was run through a bottom corner of each pair of foam dams (Figure 5.58); this would form a path through which water can travel after the grout has been placed and prevent water from being trapped between grouted sections of deck. Figure 5.59 shows the bridge with all foam dams in place at



Figure 5.58: Tube to Allow Water to Flow Through Pocket After Grouted



Figure 5.59: Foam Dams in Place at Girder Lines and Guardrail Connection Locations

shear stud grout pockets and at guardrail attachment locations. Figure 5.60 and Figure 5.61 show placement of grout in a pocket and several completed grout pockets.

Figure 5.62 shows placement of the FRP top plates. Figure 5.63 shows a completed deck but without wearing surface or guardrails. Work had begun on



Figure 5.60: Placement of Grout in Shear Stud Grout Pocket



Figure 5.61: Grout Pockets After Grout Placed



Figure 5.62: Placement of FRP Top Plate

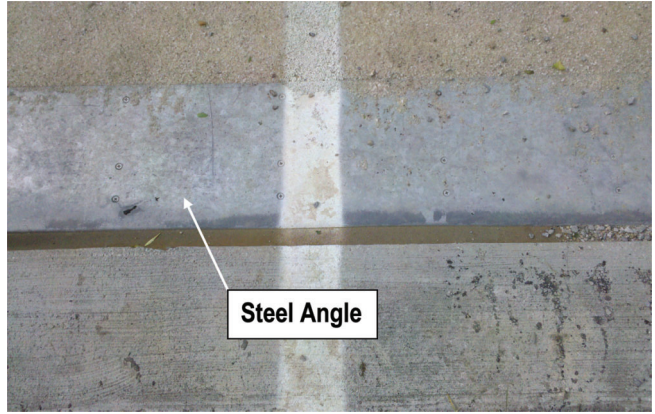


Figure 5.65: Steel Angle Protecting End of Deck from Vehicle Impact Off of Approach Span

the approach spans, so a protective tarp was being placed so as to protect the top deck surface.

Installation of the FRP deck and guardrails took a matter of days, although with a number of weather

delays. The temperature was then too low for application of the wearing surface, and so the bridge remain closed until the wearing surface was applied in late March 2010. Figure 5.64 shows the completed bridge with wearing surface. Figure 5.65 shows a steel angle embedded into the wearing surface at the each end of the deck to help protect the FRP from vehicle impact as vehicles enter the bridge off of the approach span. Figure 5.66 shows the guardrail connection and a view of Sugar Creek.



Figure 5.63: Protective Tarp on Deck Without Wearing Surface; Work on Approach Spans



Figure 5.64: Finished Bridge with Wearing Surface and Guardrails



Figure 5.66: Guardrail and Sugar Creek

5.5 Conclusions

The ZellComp deck was subjected to a number of tests, primarily to evaluate any issues with the crown connection. Test results demonstrated that a special joint would be needed at the crown to prevent moisture ingress. Results also demonstrated that the deck design was adequate. The ultimate failure mode, at a factor of safety of approximately 5, was web buckling. The ZellComp deck was installed on the Sugar Creek Bridge in November 2009.

CHAPTER 6. NON DESTRUCTIVE EVALUATION

6.1 Introduction

Failure for FRP tensile coupons is generally brittle fracture. The response of FRP until failure is also generally linear, so there tends not to be any warning before failure. Response of FRP components or subassemblies may be more non-linear, however, failure modes tend to be concealed within the core of the deck. This behavior, therefore, necessitated the study of non-destructive evaluation methods to find a viable option for in-service FRP bridge decks.

6.2 Non Destructive Evaluation Techniques

A number of non-destructive evaluation (NDE) techniques are currently used to monitor conventional bridges, and these techniques could be adapted to monitor FRP bridge decks. Each method has its advantages and disadvantages.

Deflection measurements can be used to account for imperfections and/or damage on a bridge or bridge deck. Loaded trucks may be parked on the bridge and the resulting deflections measured. This method may be good for measurement of global response, but may not be adequate for detection of the location of the damage. For these FRP panels, it would be very advantageous to be able to determine the exact cause and location of damage and to replace the defective panel.

Strain gages can be used in conjunction with other loading methods to detect large strains in the FRP deck. This method could be good for detecting potential damage in the outside layers of the panel where the strain gage is attached or in a particular region or cross section. However, the most common failures, which occur inside the core, or at the interface between the core and the top or bottom plates, would be difficult to discern.

Fiber-optic strain sensor system is another technology for measurement of strains. These fibers can be embedded inside the panels at the critical locations and can be monitored wirelessly. However the fiber optic sensors require careful attention when they are being embedded in the structure. Another concern in the use of these sensors is their durability. Furthermore, if they slip inside the composite deck, the measurements will

not be accurate. These fiber strain sensors have been used on KSCI panels in a study conducted by Peterman (2005) and embedded in composites on studies conducted by NASA (2001). Both studies experienced hardware problems. The entry and exit of the optical fibers into the specimen are very delicate; sometimes they can cause major problems in the manufacturing of the specimen.

Acoustic emission is another non destructive evaluation technique that recently has been used in the evaluation of in-service FRP bridge decks. The main advantage of this method is that it can be use to detect and localize damage inside the panel at its core, surface and interfaces, even though sensors are typically located on the surface of the panel. This NDE method is relatively new for Civil Engineering applications; however, it has been used successfully in the past in Mechanical and Aerospace Engineering. Many of the parameters studied in these fields for FRP components could be modified and adjusted for use in the Civil Engineering field.

Of the methods surveyed, acoustic emission (AE) appeared to be the most promising; for that reason AE would be the primary focus for the non-destructive evaluation study. Other related and supplemental methods will be studied as well; these include acousto-ultrasonics, thermography, and conventional deflection measurements, but just for deflections of the top plate of the ZellComp deck in service.

6.3 Acoustic Emission

Acoustic emissions are sound waves produced by abrupt releases of energy caused by damage or changes in the integrity of a material. The acoustic emission technique captures those waves or events on piezoelectric devices that transform the waves into small voltages that can be processed.

AE seems to be the most viable method for monitoring FRP decks, due to its capacity to detect damage inside a specimen and its proven track record in Aerospace Engineering. However, as mentioned previously, there is no perfect NDE method to monitor any structure, and the acoustic emission technique has its disadvantages as well. Acoustic emission could be used as a continuous monitoring technique; however, this could be a problematic in terms of installation of the sensors and protection of sensors from the environment. Another disadvantage of this NDE method is that there is not much experience in the Civil Engineering field with regards to implementation on civil structures. Specific problems may occur due to the nature of hand lay-up of sandwich FRP panels, how they are installed, and the bridge application itself. For instance, depending on the size of the bridge to be monitored, a large amount of sensors may be needed. Gaps in panel connections (i.e., longitudinal joint of the ZellComp deck) at installation may cause some of the acoustic signals to be lost on their way to

the sensor. Also, variability inherent in hand lay-up panels can make it difficult to establish parameters and to recognize the different types of failure.

6.4 Previous Studies – Literature Review

Some researchers have been studying the idea of using acoustic emission techniques in the evaluation of FRP sandwich panels. Shafiq et al. (2004) studied carbon fiber sandwich composites used in naval applications. The specimens were fabricated using the VARTM technique. Tests were performed under static and fatigue loadings. Under static loading, cracks initiated at the core and propagated to the external face sheets. During fatigue experiments, there were many initiation cracks at different locations in the core and the interface of the core and the external face sheets. Based on their AE results, Shafiq et al. classified damage using the corresponding amplitudes and energy ranges. Their results showed that AE generated accurate information about the location and extent of the damage.

Gostautas et al. (2005) utilized acoustic emission to monitor and analyze failure on FRP bridge deck panels. They utilized two different approaches to analyze the data; the comparison analysis and the intensity analysis. With the use of these two analyses and visual inspection they detected failure and the location where it initiated. In the comparison analysis, they observed the Kaiser Effect until it was valid. Then, when the Kaiser Effect was no longer valid, the Felicity ratio was calculated. The Kaiser Effect indicates the previous load applied to the specimen; the effect is that there should not be any acoustic emissions on a specimen until the last maximum load applied is surpassed. As long as the Kaiser Effect is valid, there is no damage in the specimen. Right after the Kaiser Effect is nulled, the Felicity ratio can be calculated as shown below in Equation 6.1. A Felicity ratio of larger than or equal to 1 indicates no damage to the specimen, but a decrease in this ratio means that more damage has been induced into the structure. Gostautas et al. calculated Felicity ratios ranging from 0.94 to 0.54.

Felicity Ratio =

$$\frac{\text{load at which AE events occur upon reloading}}{\text{previously applied maximum load}} \quad (6.1)$$

The intensity analysis uses the historic and severity indexes to measure the beginning of damage mechanisms and their extent. The historic index aids in the identification of a damage mechanism. It is calculated as shown in Equation 6.2 (Gostautas 2005). The severity index is calculated as shown in Equation 6.3 (Gostautas 2005). An increase in the severity index indicates that the damage is intensifying.



Figure 6.1: Acoustic Emission Sensors on FRP Sandwich Beam for Pencil Test

$$\text{Historic index} = \frac{N}{N - K} \times \left(\frac{\sum_{j=K+1}^N S_{oi}}{\sum_{j=1}^N S_{oi}} \right) \quad (6.2)$$

| No. of Hits (N) | K |
|-----------------|----------------|
| ≤ 100 | Not applicable |
| 101 to 500 | 0.8 * N |
| > 500 | N - 100 |

N = Number of hits up to and including time (t)

S_{oi} = Signal strength of the i^{th} event

K = empirically derived constant based on material type (composites) and number of hits

The use of intensity analysis aids in the potential identification of the beginning of failure and its dimension. There are certain empirically derived constants, like “K” and “J”, which can be borrowed from early studies in Aerospace Engineering, to facilitate use of the intensity analysis. However, in order to do so, a large amount of tests are needed to be able to identify intensity zones which would denote the structural significance of the emissions.

These above mentioned tests demonstrate the capacity of AE techniques for monitoring of FRP decks, but neither of them really apply the technique to true in-service applications. For instance, Gostautas et al. (2005) installed AE sensors all around the beam specimen; in the case of a real bridge, it is not feasible to install sensors on the top (driving surface) or the side of the panel (panel-to-panel joints).

Related to this issue, a series of tests were conducted at Purdue University to determine the response of the acoustic emission sensors to a repeatable acoustic wave. The so-called “pencil test” experiment was conducted. This test consists of attaching the AE sensors to the specimen (Figure 6.1) and breaking a pencil lead at known positions. The test provided information necessary for determining the optimal positioning of the sensors on the FRP deck studied, gave a sense of how



Figure 6.2: Top Plate and Longitudinal Joint on ZellComp Deck Specimen

the waves travel on this deck, and aided in determining the loss in velocity and distance over which a wave can propagate through the deck. From this simple test, the location from which the signal was emitted could be localized. This experiment gave more confidence in the AE technique for monitoring of FRP bridges and was the basis for this study.

$$Severity\ index = \frac{1}{J} \times \left(\sum_{i=1}^{i=j} S_{om} \right) \quad (6.3)$$

| # of Hits (N) | J |
|---------------|----------------|
| < 20 | Not applicable |
| ≥ 20 | 20 |

S_{om} = is the signal strength of the m^{th} hit, where the ordering of m is based on magnitude of signal strength.

J = empirically derived constant based on material type (composites) and number of hits

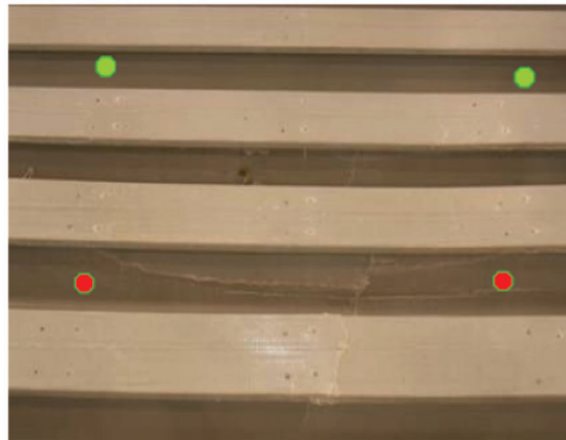
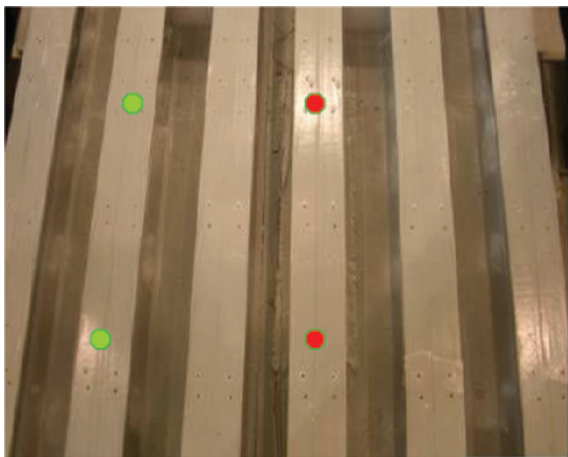


Figure 6.3: Acoustic Emission Sensor Positions for Passive Tests on Damaged Zellcomp Deck

Although these studies in Civil and Aerospace Engineering give us confidence in the reliability of AE for NDE of FRP composites, there are some problems directly related to the manufacturing process of these panels and the environment in which they are installed. These problems must be addressed in the development of a consistent monitoring technique. In the field, there is the need to isolate the sensors from exterior noises that could affect the data. Also, as mentioned before, these sensors would have to be installed at the bottom of the deck; one would have to find a secure and effective method of attachment that

will not affect their readings. Also, for hand lay-up panels, there may be many inconsistencies in geometry, as observed in Chapter 4. The technique created for inspection would have to take into account such variability. Finally, these panels, pultruded or hand lay-up, are connected to each other with some mechanical connection, often with a small gap between panels, creating a challenge for AE monitoring. For all these reasons, one objective of this study will be to determine the best locations in the deck for installation of sensors on an in-service bridge deck, taking into account its size, use, and variability.

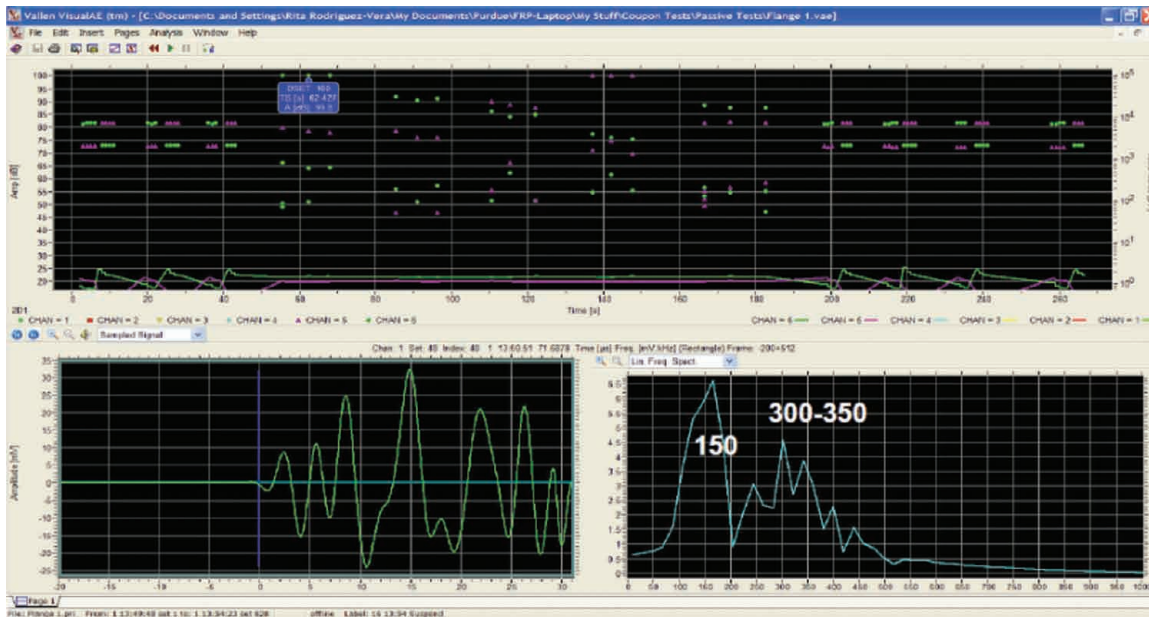


Figure 6.4: Acoustic Emission Data for Passive Tests on Damaged Zellcomp Deck, Flanges

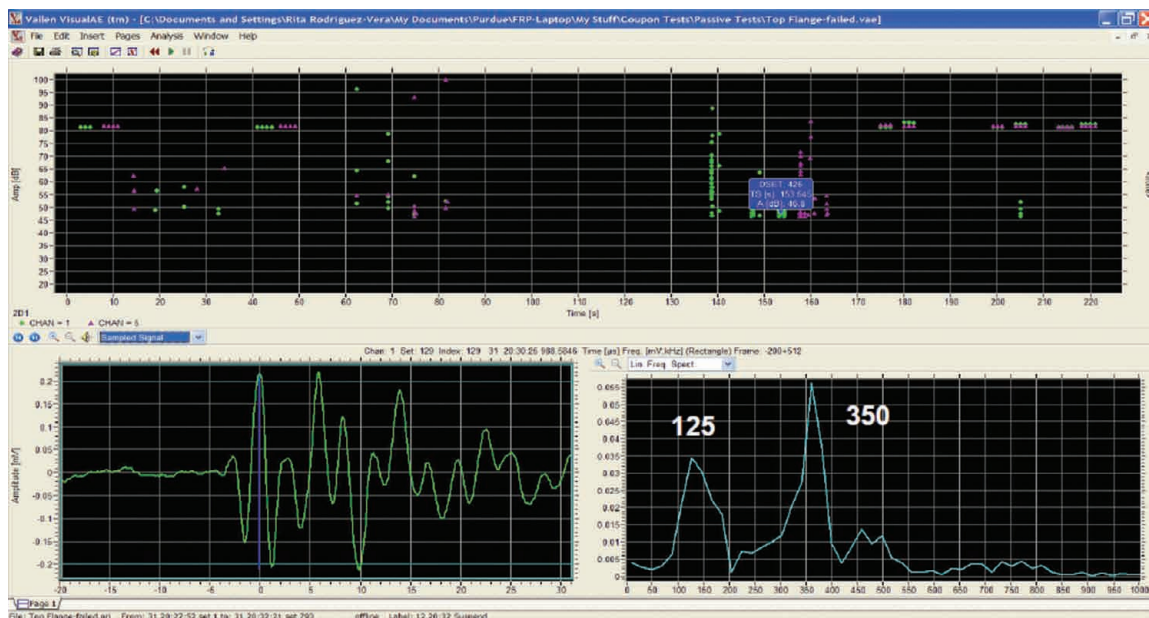


Figure 6.5: Acoustic Emission Data for Passive Tests on Damaged Zellcomp Deck, Webs

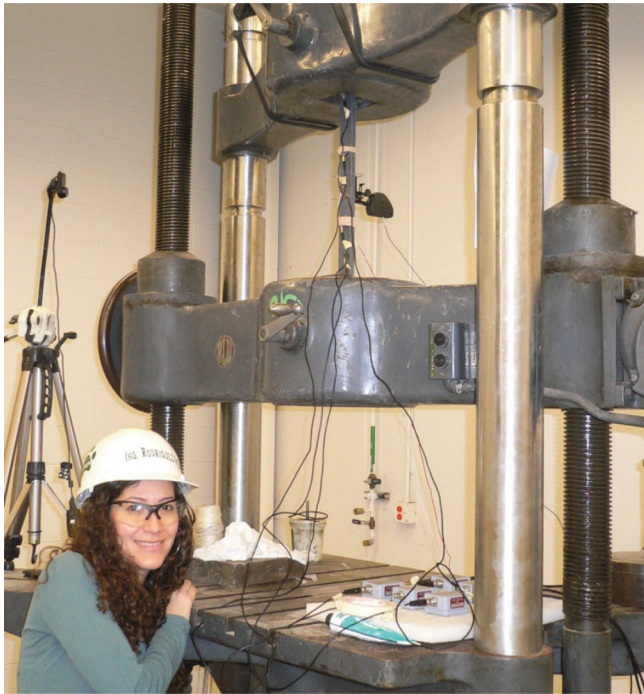


Figure 6.6: Acoustic Emission Test on Tension Coupon

6.5 Acoustic Emission Experimental Results

A number of tests were conducted with the acoustic emission sensors. Sensors were placed on the KSCI panel specimens (Chapter 4) and the ZellComp panel specimens (Chapter 5). Some small FRP plate and wearing surface specimens were also tested with the acoustic emission sensors, as were simple FRP coupons loaded in tension.

6.5.1 Notes from the KSCI Tests

In the KSCI tests, acoustic emission measurements mirrored the observations of the noises and damage to the joint, core, and so on. For example, in the KSCI #P1b test, there were changes in the AE data at around 25 kips, corresponding to the noises heard and the slight change in slope in the load-deflection plots. The AE sensors were placed as shown by the small circles on Figure 4.10. Channel 3, on one side of the longitudinal joint, started to diverge from Channel 4, on the other side of the joint, in the AE measurements. Again, between 30 to 35 kips, with more loud noises, there was also an increase in AE energy. Channel 6 appeared to be measuring more energy than the other channels. This may imply that local damage was occurring on that side of the panel. Similar results were observed for other tests with the AE measurements. It was noted that measurements from one side of the longitudinal joint appeared to be completely separate from the measurements on the other side of the joint. In other words, sensors on one side of the joint did not register any energy from damage on the other side of the joint.

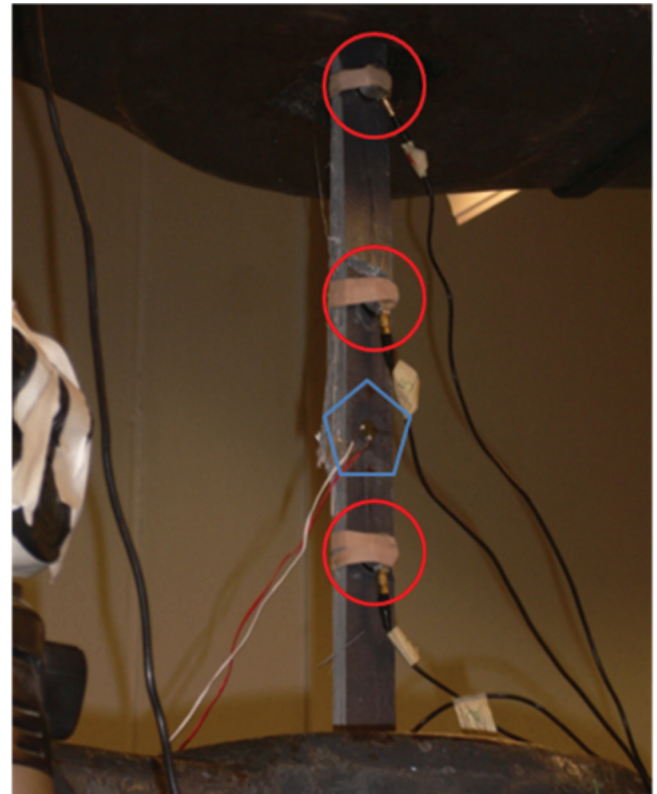


Figure 6.7: Acoustic Emission Sensor Locations (Circles) on Tension Coupon

6.5.2 Notes from the ZellComp Tests

Similar results were observed in the ZellComp Tests. The AE sensors were placed on the wearing surface specimen as shown in Figure 5.40, with 3 sensors on each side of the longitudinal joint. It was again observed that readings from one side of the joint did not appear to be affected by any response from the other side of the joint. This was due to the physical gap at the longitudinal joint. Even though the components overlap at the joint and are in physical contact, as shown in Figure 2.29 and Figure 6.2, this construction provides enough of a barrier that prevents the AE waves from traveling from one side to the other. Furthermore, the top plates are separate pieces that are connected with mechanical fasteners. Therefore, any

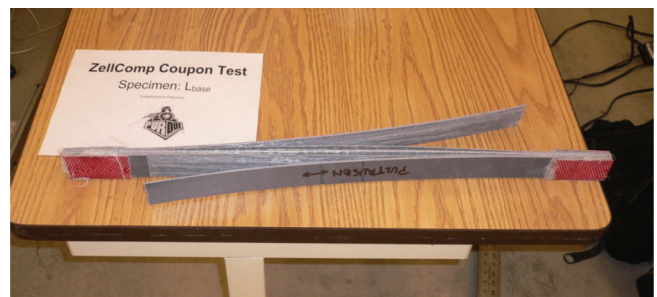


Figure 6.8: Tension Coupon (Fibers Longitudinal) After Test



Figure 6.9: Tension Coupon (Fibers Transverse) After Test

TABLE 6.1:
Tension Coupon Test Results

| Specimen | Failure Load (kips) | Maximum Stress (ksi) |
|----------|---------------------|----------------------|
| Tbase | 9.6 | 12.8 |
| Lbase | 28.1 | 37.5 |
| L1 | 26.0 | 34.7 |
| L2 | 26.5 | 35.3 |

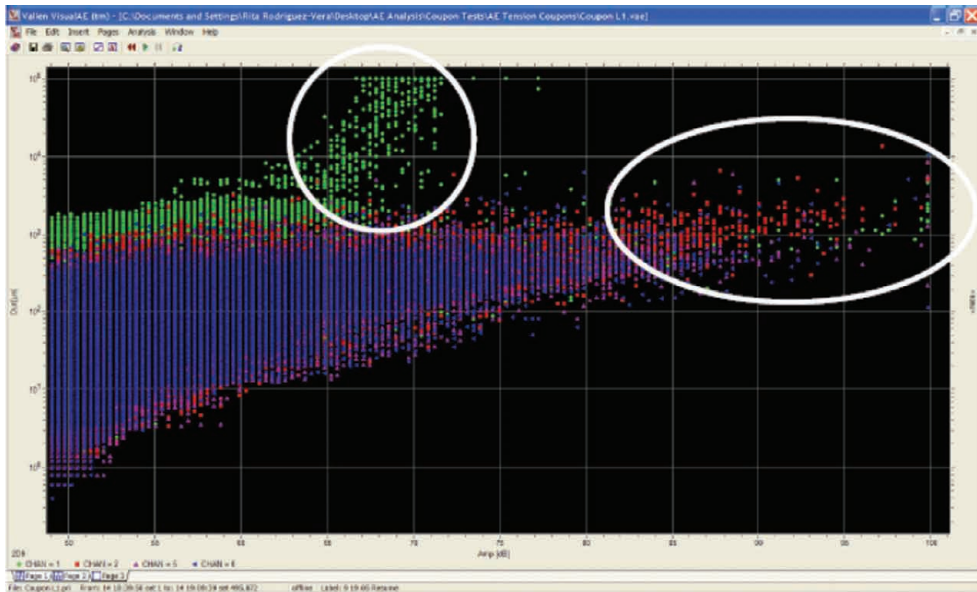


Figure 6.10: Acoustic Emission Duration vs. Amplitude Results for Tension Coupon

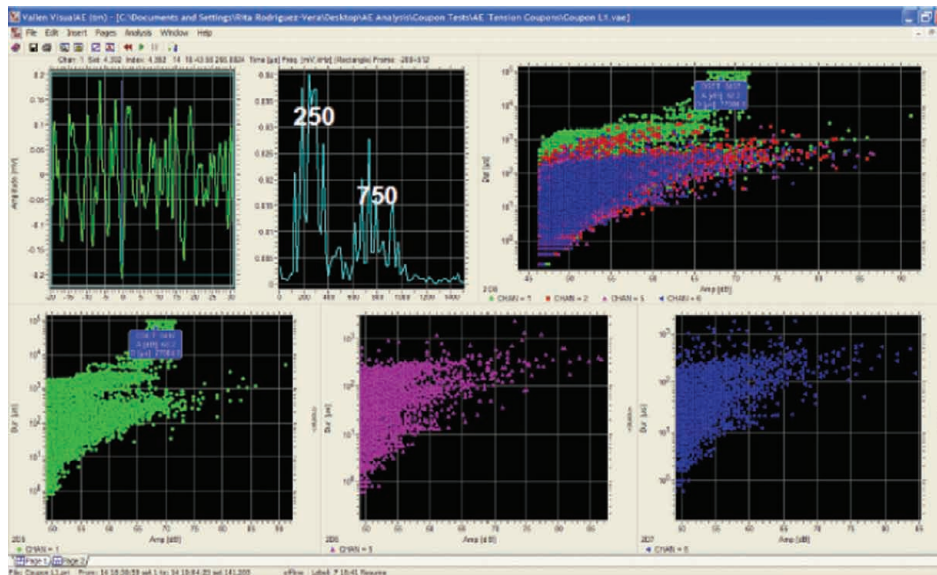


Figure 6.11: Acoustic Emission Output for Tension Coupon

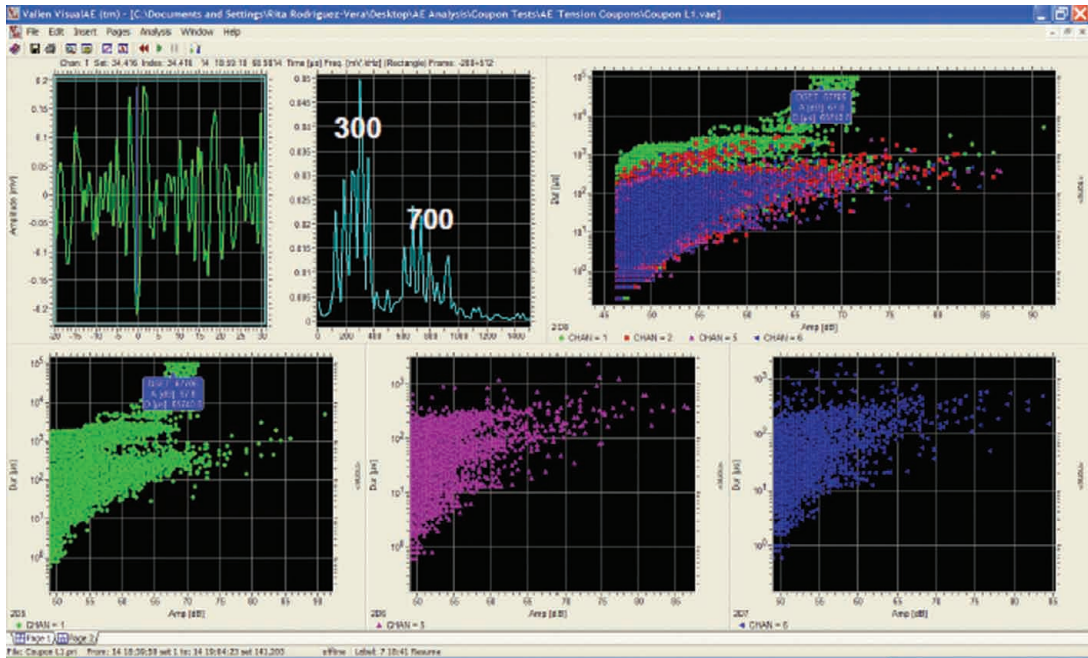


Figure 6.12: Acoustic Emission Output for Tension Coupon

damage in the top plate cannot be measured by AE sensors at the bottom of the panel. Acoustic Emission waves require a clear path.

Some passive acoustic emission tests were also conducted on the already tested and damaged ZellComp deck specimens. One sensor was used to emit a signal; another was used for measurements. Locations of pairs of sensors were as shown in Figure

6.3, with the colored circles. One trial included sensors on the flanges, with one pair location close to a damaged web. A second trial included sensors on the webs, with one pair location on either end of the buckled web section. Figure 6.4 and Figure 6.5 show output from the acoustic emission software. The lower right on each figure is a frequency plot. The higher frequency peaks shown were observed when the sensors

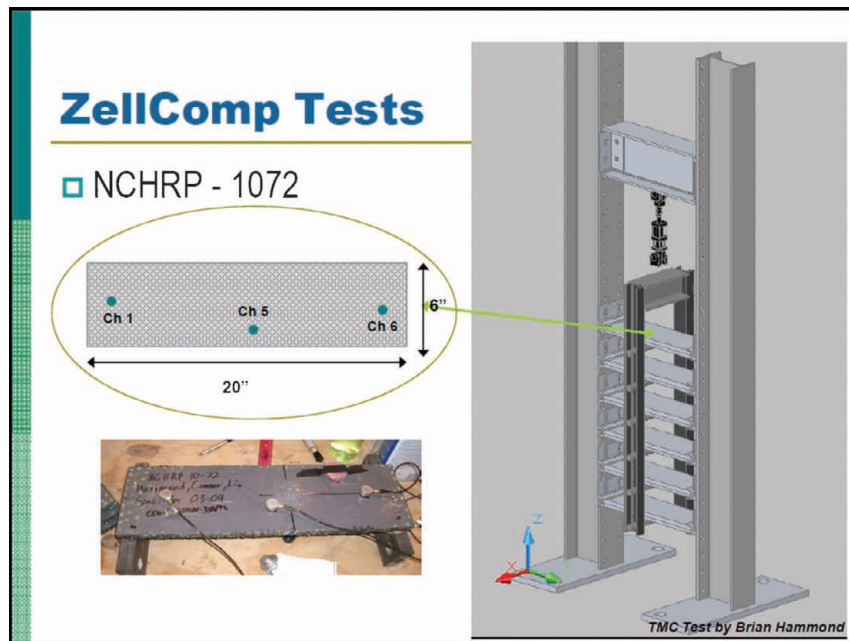


Figure 6.13: Acoustic Emission Sensors on NCHRP Wearing Surface Specimens

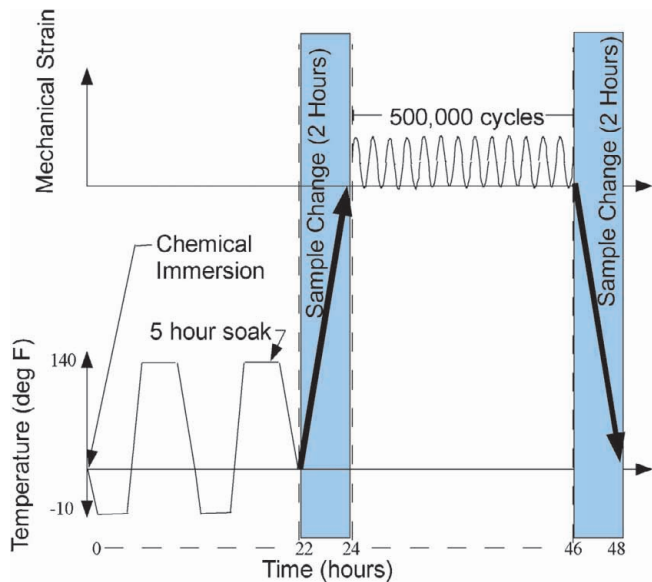


Figure 6.14: NCHRP Wearing Surface Specimen Load Cycle

were close to a damaged location. These passive acoustic emission tests demonstrated that these sensors could perhaps be used to confirm suspected damage.

6.5.3 ZellComp Tension Coupon Acoustic Emission Tests

Additional acoustic emission tests were conducted on simple tension coupon samples. The acoustic emission sensors were used to record data as the tension coupons were loaded to failure. Figure 6.6 shows the test set-up. Figure 6.7 shows the locations of the acoustic emission sensors as circles; a conventional strain gage was also placed (as shown by the pentagon) in the center of the specimen to confirm strain levels.

Five specimens were tested. One coupon was fabricated of pure resin; the resin was the same resin used in the ZellComp FRP deck. The purpose of the resin coupon was to evaluate and identify acoustic



Figure 6.15: NCHRP Wearing Surface Specimen With Acoustic Emission Sensors

emissions resulting from failure of the resin. Unfortunately, the resin coupons shattered immediately and did not produce any useful data.

The other four specimens were three tension coupons with fibers, or the pultruded direction, oriented longitudinally (denoted with an “L”) and one coupon with fibers primarily transverse (denoted as “Tbase”) to the longitudinal axis of the specimen. The longitudinal coupons failed by splitting longitudinally as shown in Figure 6.8. The transverse specimen failed across the width, near the gripped end of the specimen, as shown in Figure 6.9. Failure loads and stresses are shown in Table 6.1.

Acoustic emission results showed that fiber breakage across the width (transverse specimen) exhibited different information than delamination (longitudinal specimens). A plot of the duration versus amplitude showed lower amplitude and longer duration for one failure mode, and higher amplitude and shorter duration for the other (Figure 6.10). Figure 6.11 and Figure 6.12 show different frequencies for the different failure modes, also. Results included 250–300 versus 700–750

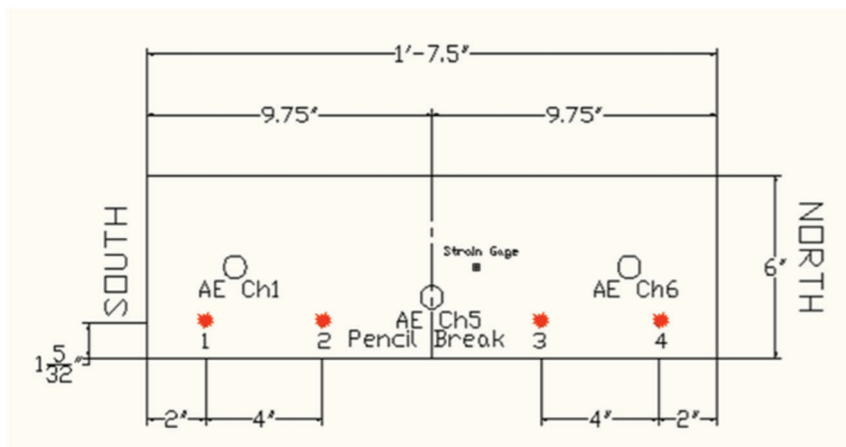


Figure 6.16: NCHRP Wearing Surface Specimen With Acoustic Emission Sensor Locations and Pencil Break Locations

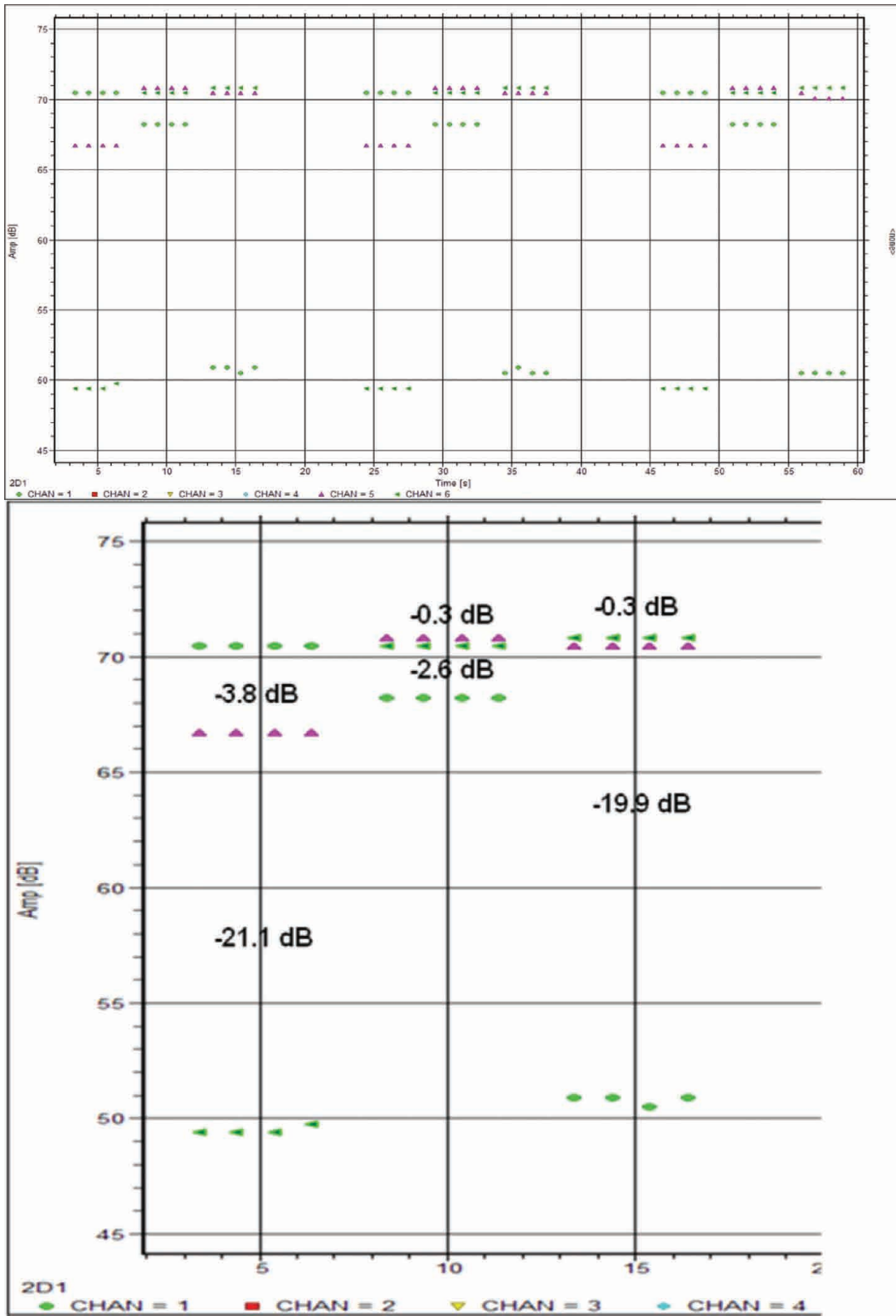


Figure 6.17: NCHRP Wearing Surface Specimen Acoustic Emission Amplitudes After 12 Load Cycles

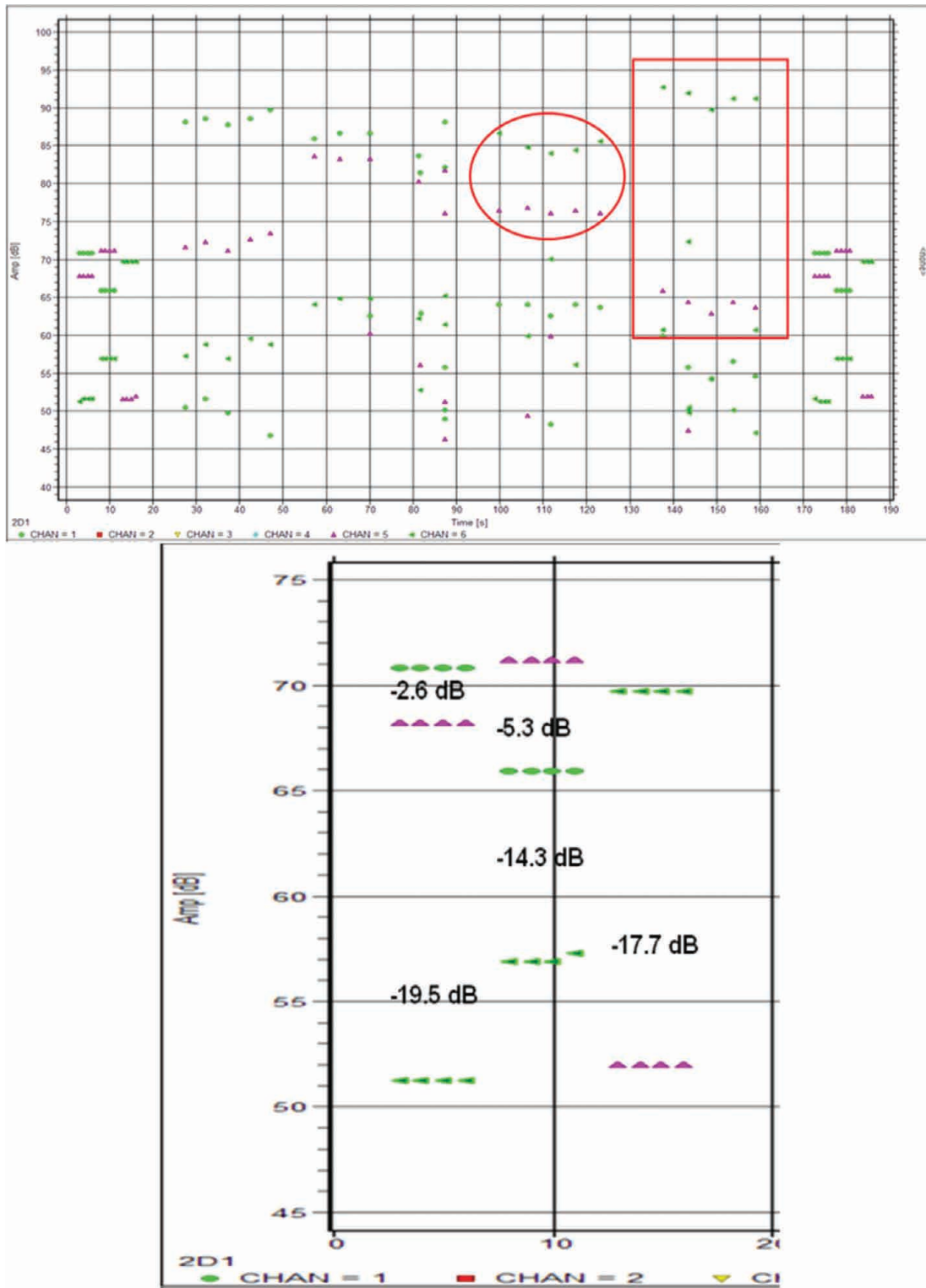


Figure 6.18: NCHRP Wearing Surface Specimen Acoustic Emission Amplitudes After 23 Load Cycles

for the different responses. These distinct responses suggested promise for use of acoustic emission for detecting damage in-situ.

6.5.4 NCHRP ZellComp Acoustic Emission Tests

Pencil tests were also conducted on small FRP plate – wearing surface specimens subjected to fatigue loading. The fatigue tests were part of a National Cooperative Highway Research Program (NCHRP) study at Purdue University. The roughly 6 in. × 20 in. specimens were placed in a loading apparatus as shown in Figure 6.13, and tested six at a time. At various intervals in the cyclic loading, they were removed from the test frame, immersed in a deicing chemical mixture for 2 minutes, then subjected to a temperature cycle (to -10°F , then to 140°F with each temperature held for a minimum of five hours). A typical load cycle is as shown in Figure 6.14. The maximum strain levels for the mechanical loading were comparable to those calculated for the ZellComp deck in service, based on a finite element model of the deck (Hammond, 2009).

Figure 6.15 shows a specimen with the acoustic emission sensors placed on it. Figure 6.16 shows the sensor locations as well as the locations of the pencil lead breaks. Figure 6.17 is a plot (and close-up of that plot) of the measured amplitudes for the different sensors after 12 load cycles. Figure 6.18 shows the amplitude results after 23 load cycles. By 23 load cycles, it was apparent that there had been delamination of the wearing surface. This was confirmed by the larger gaps between the amplitude measurements, as shown in Figure 6.18. This pencil test suggested that this type of measurement might be used to verify a delamination failure.

6.6 NCHRP ZellComp Specimen Thermographic Imaging

Thermographic imaging was also explored as potential in-situ method for identifying delaminations between the wearing surface and the FRP deck. The same NCHRP specimens described in the previous section were used. Figure 6.19 shows heating of the specimen with a heat gun and then taking the thermographic image. Sample images are shown in Figure 6.20. Areas of delamination present as “hot spots” in the thermographic images. Figure 6.21 shows a side view of a specimen with delamination, which can be visually confirmed as a separation of the wearing surface from the FRP plate at the edge.

Use of the thermographic camera presented some practical problems. The quality of the images varied greatly with the duration of time between heating the specimen and taking the thermographic image. The specimen cooled rather quickly; one needed to be immediately ready with the camera upon removal of the heat gun. It was felt that this method would therefore be impractical for trying to locate areas of delamination on a bridge deck, which is many times larger than one of these 6 in. × 20 in. specimens. Even if a good, consistent system of heating and imaging were developed, this method would be labor intensive, requiring heating and imaging of small areas at a time.

6.7 Acousto-Ultrasonics and Airborne UT Sensor

Acousto-Ultrasonics and an Airborne UT sensor were also explored potential in-situ methods of locating damage. Acousto-Ultrasonics is a combination of acoustic emission with ultrasonic scanning. This



Figure 6.19: Heating Specimen (Left) and Taking Image with Thermographic Camera (Right)

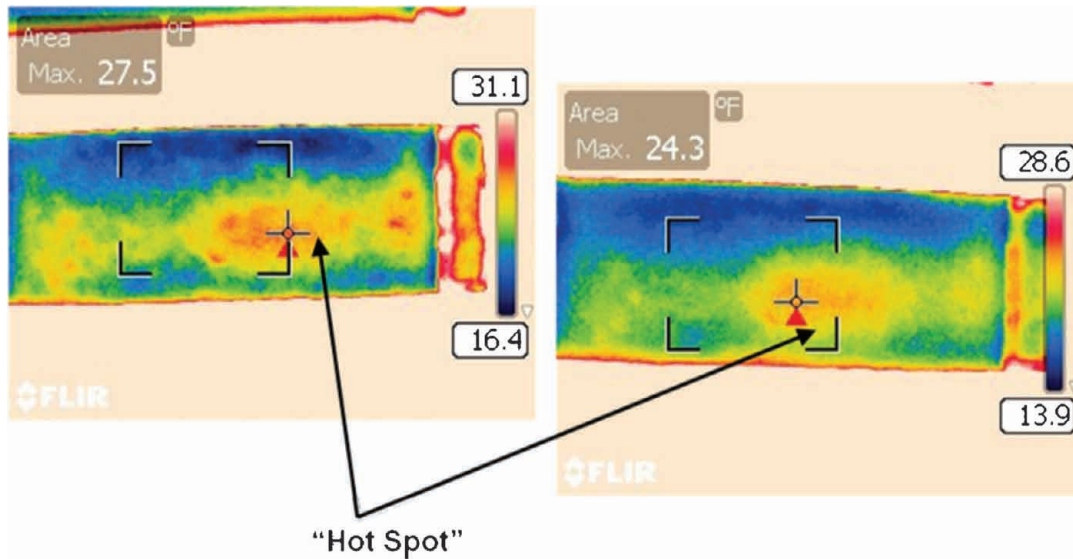


Figure 6.20: “Hot Spot” at Delamination Captured by Thermographic Camera

method was presented as being viable for locating defects in composite, multi-layer materials. A proposed benefit of this method was also the ability to use this equipment from a single side of the material to detect damage. The controller and output device was also produced in a pocket version, as shown in Figure 6.22. A demonstration of this technology was offered to the Purdue research team by a company that was also selling acoustic emission equipment. A member of the research team went to the company’s laboratory with some small, damaged samples of the ZellComp deck for the demonstration. Sample output from an acousto-ultrasonic device for an unknown sample is shown in Figure 6.23; the graphs (a) and (b) in Figure 6.23 are markedly different for the undamaged (a) and damaged (b) areas. Figure 6.24 shows a schematic of acoustic-ultrasonic waves being reflected in a composite

material. Unfortunately, the acousto-ultrasonic device was unable to consistently locate the damage.

Airborne UT was tested in damage detection of a hole in the top of the flange of the ZellComp deck section, as well as a hole gouged into the cross section of the deck to simulate delamination within the flange. A pulser was passed over the deck as a receiver was also rolled across top of the deck. Figure 6.25, Figure 6.26, and Figure 6.27 show the test set-ups and damaged locations for these trials. Unfortunately, the device was unable to consistently locate the damage and presented a number of false positives; in some cases, the sensor



Figure 6.21: Delamination Between Wearing Surface and FRP Plate



Figure 6.22: Pocket Acousto-Ultrasonic Device

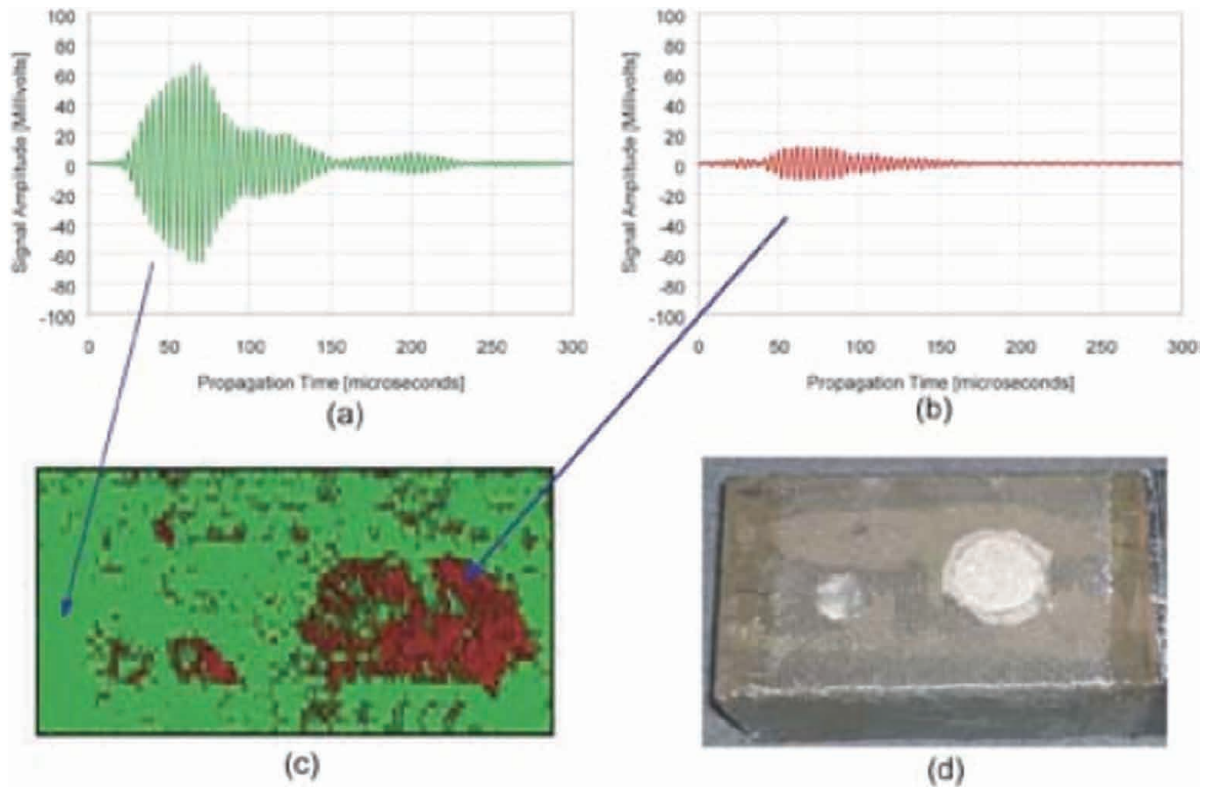


Figure 6.23: Sample Acousto-Ultrasonic Output (a) and (b)

would show a drop in amplitude where no damage was present. Furthermore, the student testing the device found it difficult to continually apply pressure to the receiver as rolling it across the deck; this pressure was necessary to obtain proper measurements. As a result, the Airbone UT and the acousto-ultrasonics device were not pursued further as in-situ damage detection methods.

6.8 Traveling Truck Deflection Measurements

The load tests on the ZellComp deck revealed buckling and fracture in the webs of the deck as the

primary failure mode. Preceding and after failure of the web, the top plate of the FRP deck exhibited severe dishing deformations at the patch load, when loaded. Deformations of the top plate would be more accessible than any sensor data inside the FRP deck section at the webs. Furthermore, any sensors located inside the FRP deck would need to be placed at the time of construction, and it is highly unlikely that the instrumented webs would correspond perfectly with any damaged webs. Therefore, a traveling truck deflection measurement method was developed.

ABAQUS models of the FRP deck were analyzed for deflections due to an assume service wheel load of 16

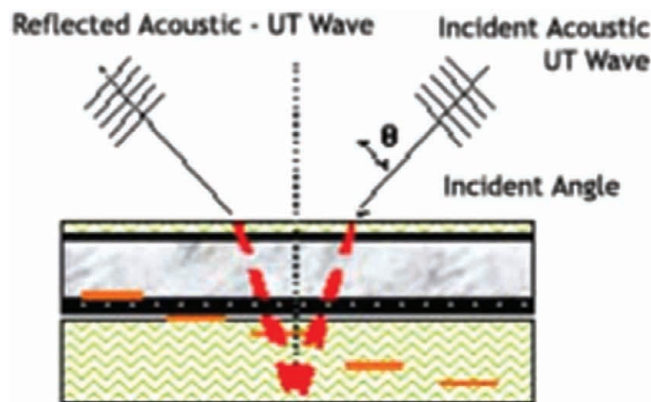


Figure 6.24: Graphic of Acoustic-Ultrasonic Wave Reflected in a Composite

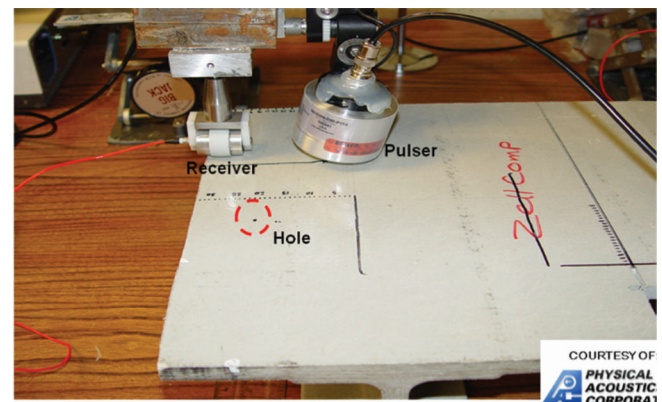


Figure 6.25: Acoustic-Ultrasonic Pulser and Receiver Set-Up To Test Detection of Hole in Top of Flange of ZellComp Deck Section

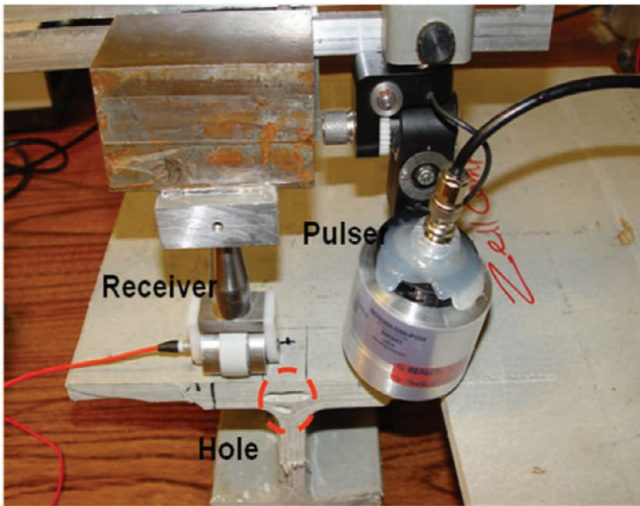


Figure 6.26: Acoustic-Ultrasonic Pulsar and Receiver Set-Up To Test Detection of Simulated Delamination in Flange of ZellComp Deck Section

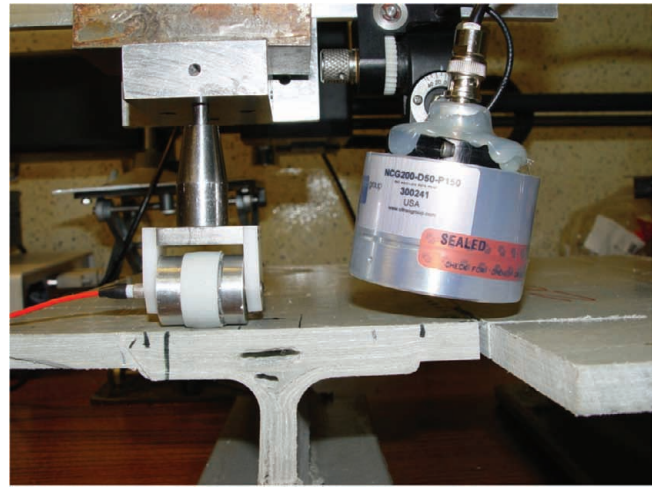


Figure 6.27: Acoustic-Ultrasonic Pulsar and Receiver Set-Up To Test Detection of Simulated Delamination in Flange of ZellComp Deck Section

rips. Figure 6.28 shows the dishing deformations longitudinal and transverse to the truck travel direction for stationary wheel loads. Figure 6.29 shows a plot of deformations longitudinal to the truck travel direction for a stationary wheel load and for decreasing values of web stiffness, simulating damage to the web. “10R” indicates a web with 10 percent of its original stiffness. Note that a positive deflection on Figure 6.29 represents a downwards, or dishing, deformation. Figure 6.30 summarizes deformations longitudinal and transverse to a stationary wheel load and for decreasing web stiffnesses. The ABAQUS models suggested that wheel load and measurements of deformations immediately adjacent to that wheel would show marked increases in dishing at any locations with damage to the web. Therefore, a traveling truck deflection apparatus was developed.

The traveling truck deflection measurement system was built on a truck and data acquisition system borrowed from the INDOT Research facility in West Lafayette. The data acquisition system was configured such that location of the truck relative to its starting position was automatically recorded. The truck was loaded with heavy concrete blocks. The goal was to get a wheel load of 16 kips. Unfortunately, there was not enough weight with the blocks; also, unfortunately, data on the actual, final wheel load has been lost. Figure 6.31 shows the truck with the concrete blocks and part of the deflection frame attached at the rear wheel.

The deflection frame was designed to capture the dishing deformations observed in the ABAQUS model, and in the experiments, at the wheel load. Therefore, an array of fifteen vertical measurement points was

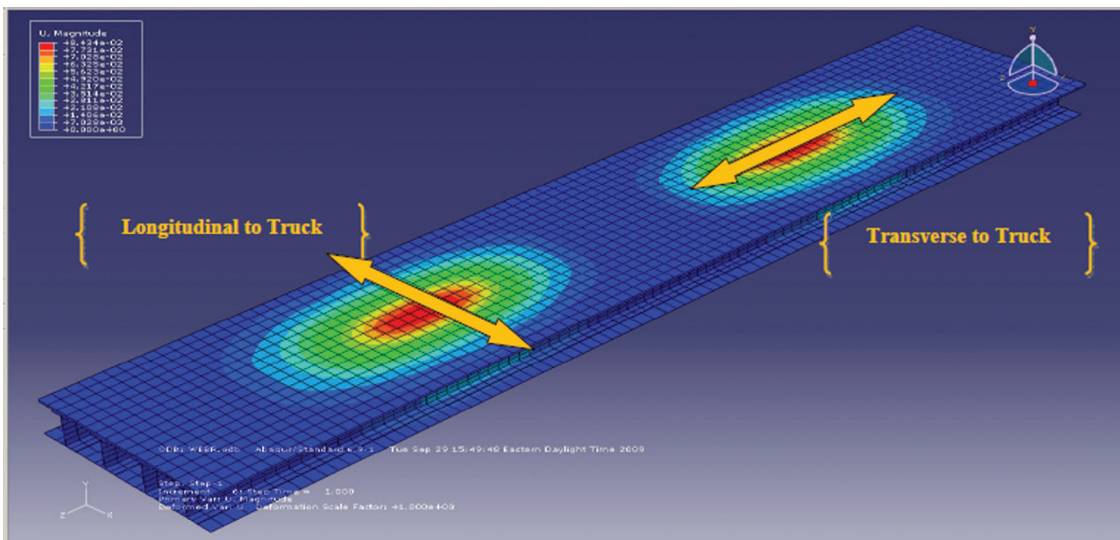


Figure 6.28: ABAQUS Analysis of FRP Top Plate Deflections Longitudinal and Transverse to Truck Travel Direction

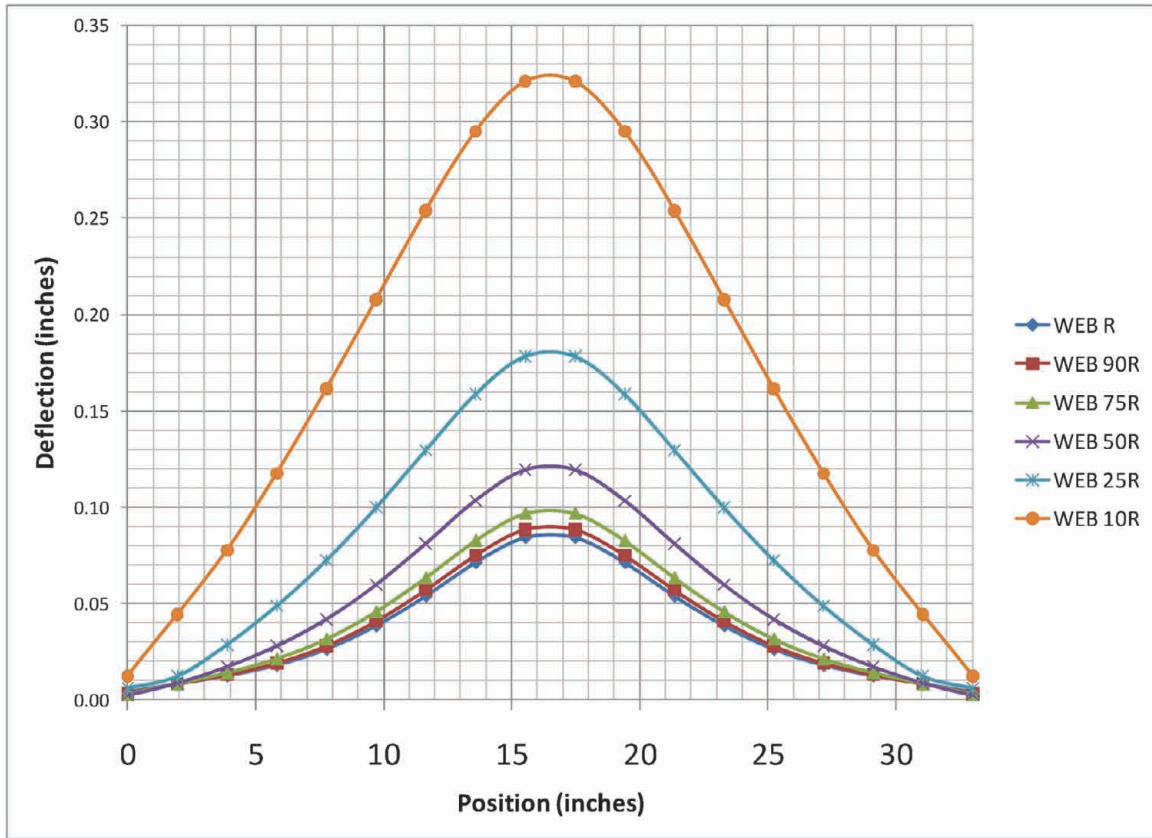


Figure 6.29: ABAQUS Results of FRP Top Plate Deflections Longitudinal to Truck Travel Direction for Reductions in Web Stiffness

constructed. Each measurement point had a caster wheel attached to allow easy movement along the bridge and to maintain contact with the bridge deck. The diameter of the caster wheel was chosen so as to minimize disturbances or chatter due to roughness (i.e., aggregate) in the wearing surface. Each caster wheel was attached to a post that was inserted into a vertical

tube. The post was free to move up and down in within the tube. A displacement potentiometers was then attached at each of the fifteen points, ready to capture vertical movement between the caster wheel and the deflection frame. A bicycle wheel was added to help stabilize the frame as the truck moved across the bridge (Figure 6.32, Figure 6.33).

| □ Longitudinal to Truck | | | | | | |
|-------------------------|--------|---------|---------|---------|---------|---------|
| | WEB R | WEB 90R | WEB 75R | WEB 50R | WEB 25R | WEB 10R |
| MAX U (in) | 0.0843 | 0.0886 | 0.0967 | 0.1193 | 0.1783 | 0.3210 |
| DIFF (in) | | 0.0042 | 0.0124 | 0.0350 | 0.0940 | 0.2367 |
| Percentage of Change | | 5.0% | 14.7% | 41.4% | 111.4% | 280.6% |

| □ Transverse to Truck | | | | | | |
|-----------------------|--------|---------|---------|---------|---------|---------|
| | WEB R | WEB 90R | WEB 75R | WEB 50R | WEB 25R | WEB 10R |
| MAX U (in) | 0.0843 | 0.0886 | 0.0967 | 0.1193 | 0.1783 | 0.3210 |
| DIFF (in) | | 0.0042 | 0.0124 | 0.0350 | 0.0940 | 0.2367 |
| Percentage of Change | | 5.0% | 14.7% | 41.4% | 111.4% | 280.6% |

Figure 6.30: Summary of ABAQUS Results of FRP Top Plate Deflections Longitudinal and Transverse to Truck Travel Direction for Reductions in Web Stiffness



Figure 6.31: Truck with Part of Frame Attached at Rear Wheel

Figure 6.34 shows a dimensioned layout (plan view) for the displacement potentiometers. Potentiometers at 4 inches away from the truck tire were identified as Pots 1–5. Pots 6–10 were then 10 inches away from the first row, and Pots 11–15 were at another 10 inch spacing. Meanwhile, Figure 6.35 shows a plan view of the bridge with grouted sections at the shear studs (girders) and at the edges for the guardrail attachments shaded on the drawing. Less deformation was expected at the grouted sections, so most passes across the bridge were planned for paths along non-grouted sections. The intent was that several passes across the bridge soon after construction would provide baseline deformation measurements. Then, periodically, these measurements should be repeated in order to capture any excessive deformations, indicating damage.

Unfortunately, at the time of the test of the traveling truck measurement frame, the wearing surface had not yet been applied to the deck because of cold weather



Figure 6.32: Truck with Deflection Frame Attached at Rear Wheel, Stopped at End of Bridge

delays. Therefore, the mechanical fasteners (screws) attaching the FRP deck top plate to the bottom section of the deck were all exposed (Figure 6.32). In some cases, these screws would adversely affect the measurements.

Figure 6.36 and Figure 6.37 show results from Pass 2 across the bridge. These figures are representative of the other passes across the bridge. Again, positive deflections values on these plots represent a downwards deformation of the top plate. Therefore, the largest, most positive values indicate the largest downwards deformations. As expected, the potentiometers closest to the truck tire (Pot 1 and Pot 4) measure the largest vertical deformations.

Figure 6.36 exhibits somewhat promising results. Pots 1, 6, and 11 are all in the same longitudinal position relative to the truck, and are 4 inches, 14 inches, and 24 inches, respectively, away from the truck tire. As expected, Pot 1 consistently shows the largest



Figure 6.33: Truck with Deflection Frame Attached at Rear Wheel, at End of Path

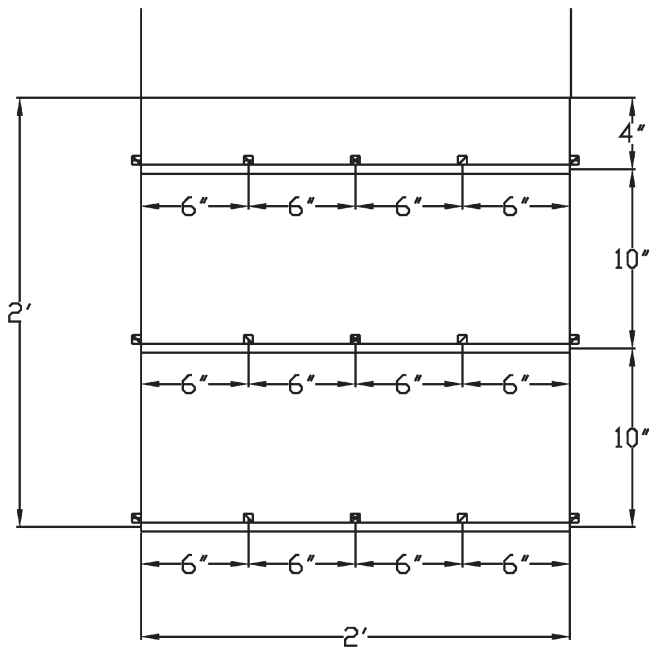


Figure 6.34: Layout of LVDTs for Deflection Frame

deflections due to the wheel load. However, Pot 11, the farthest from the tire, shows the second largest deflections, consistently, followed by Pot 6. One would expect this trend to be reversed between Pot 6 and Pot 11. The reason for this result is unclear.

Meanwhile, Figure 6.37 highlights an apparent weakness in the method. Pots 4, 9 and 14 are also all in one line relative to the truck, with Pot 4 as the one closest to the truck tire, and Pot 14 the one farthest away. Pot 14 shows a number of spikes and measurements that exceed those of Pot 9 and, in some cases, are almost as high as those of Pot 4. Reportedly, the caster wheels on the frame would occasionally pass over

screws protruding up from the surface of the FRP plate, resulting in spikes. However, the relatively high values for Pot 14 between 3 ft and 30 ft along the bridge seem to be because of some other unevenness in the deck construction.

The traveling truck measurement method shows some promise. However, issues related to local spikes in measurements and other uneven results must be examined further and resolved before this method can be a viable method for in-service monitoring of the FRP deck.

6.9 Conclusions

A number of non-destructive evaluation methods were considered for monitoring of the FRP deck in service. Some were evaluated and discarded based on observations in the literature and unsuitability for damage detection in FRP or field conditions, or both. Others, such as the acousto-ultrasonic method, were physically tested on FRP deck samples and demonstrated to be unsuitable.

Of the various technologies, acoustic emission appeared to be the most promising. Passive tests on damaged specimens, acoustic emission tests on FRP deck specimens as they were loaded, and acoustic emission tests on FRP coupons as they were loaded showed different frequencies, amplitudes and durations for different failure modes and proximity to damaged locations. As such, it would seem that acoustic emission methods could be used to locate and identify type of damage. However, some limitations to acoustic emission include the inability of the acoustic waves to traverse joints between FRP deck panel sections, as well as the connection between the top plate and bottom section of the ZellComp deck. Therefore, use of acoustic emission would be labor intensive, requiring

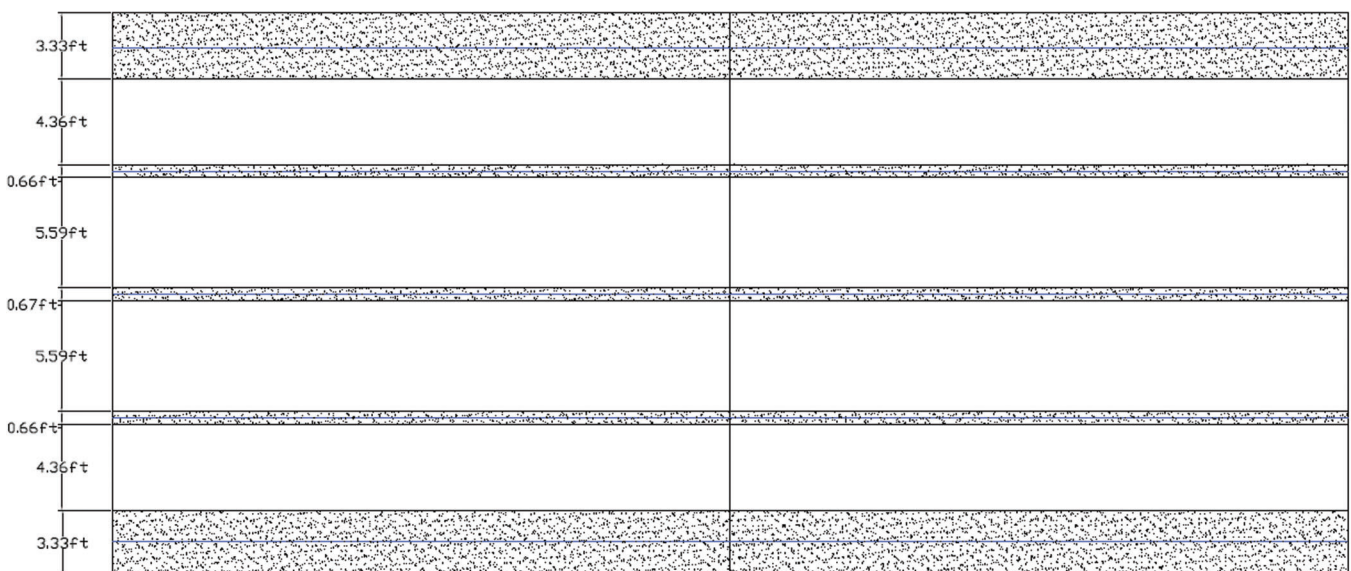


Figure 6.35: Plan View of Bridge Deck with Grouted Sections Shaded

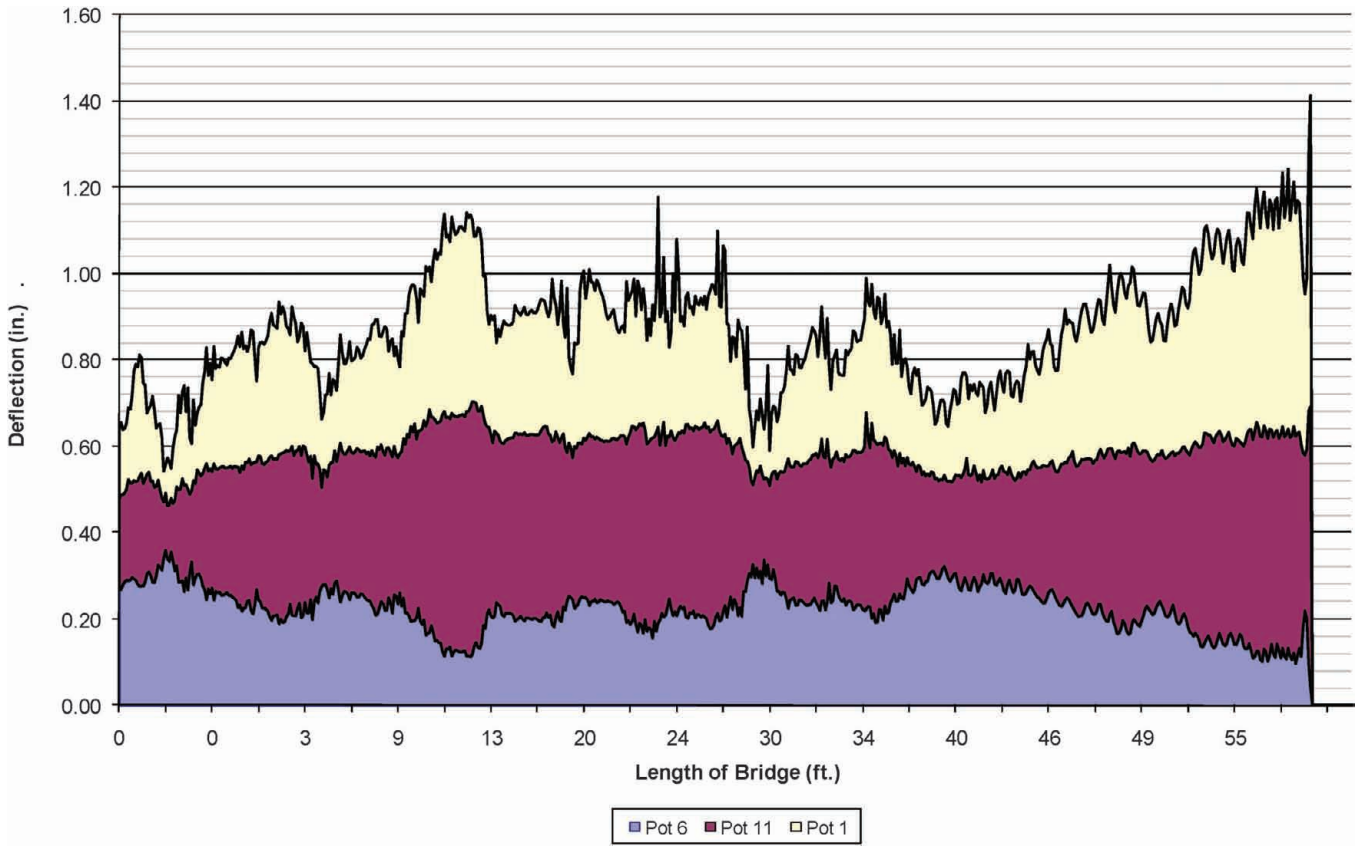


Figure 6.36: Deflection vs. Position on Bridge, Pots 1,6 and 11

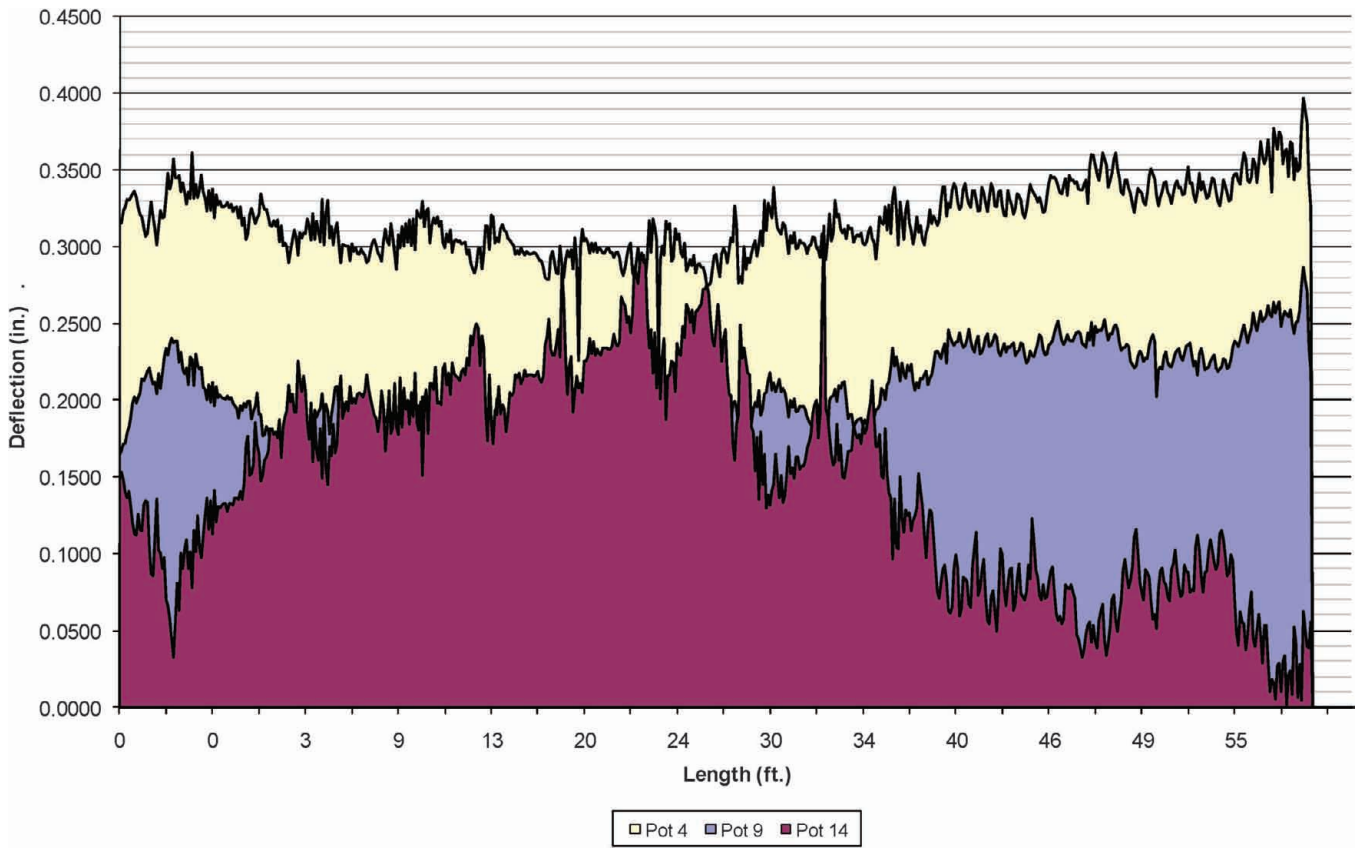


Figure 6.37: Deflection vs. Position on Bridge, Pots 4,9 and 14

measurements at regular and frequent intervals along the deck, between joints.

Infrared thermography also appeared to be promising for identifying delamination between the wearing surface and the FRP top plate. Delaminations were successfully identified. However, use of the infrared thermographic camera would also be labor intensive, requiring heating of small sections of deck at a time and then quickly taking the thermographic image. Furthermore, results would show variability with amount of heating as well as amount of cooling before the image is acquired.

Meanwhile, a traveling truck deflection measurement method was developed based on observations of the severe dishing of the FRP deck top plate under the patch loads when failure, or buckling of the webs, occurred. This procedure was tested on the FRP deck after installed on the Sugar Creek Bridge. This method showed some promise, but also showed variability and sensitivity to small variations in the surface of the deck. It is believed that this method would be successful at locating severe damage of the webs, as deflection measurements would show marked increases local to the damage. However, further validation and baseline measurements of on the FRP bridge deck with the wearing surface are required if this method is to be pursued.

CHAPTER 7. CONCLUSIONS AND FUTURE WORK

7.1 General

This project followed the study of design and monitoring methods for FRP bridge decks, specifically for rehabilitation of an existing bridge in Tippecanoe County with an FRP deck. Tasks included load tests of the bridge deck overhangs and crown connections, development of alternative serviceability criterion, development of a hybrid GFRP-steel deck solution, and evaluation of non-destructive evaluation methods for in-situ monitoring of the FRP bridge deck.

7.2 FRP Bridge Decks

There exist a number of FRP decks of varying geometries and properties. However, overall, the key issues are consistent. Of the concerns with FRP decks observed in the literature, the topics of serviceability (deflection limits), issues for testing (e.g., load patches), limit states (e.g., delamination and how to inspect for such limit states) were most significant and took top priority in this study. Other topics, such as wearing surface, panel to panel connections, deck to girder connections, and guardrails were secondary areas of study. Guardrails were not explicitly studied, but recommendations made to the structural engineer for the case-study bridge based on the literature. Issues such as fatigue response and extreme temperatures were outside the scope of this study. Two FRP decks and two different case study bridges were chosen at different times over the course of the project. Each topic studied

and all parameters were related specifically to each FRP deck and associated case-study bridge.

7.3 Serviceability Criteria

Serviceability criteria, or deflection limits, govern the design of FRP decks. However, the limits typically used for bridge decks may not be applicable to FRP decks because of their relative light weight, low stiffness, and resulting difference in vibration response. A couple of side studies were conducted on this issue of deflection limits, as well as a small literature review. One side study investigated the development of an alternative criterion based on the dynamic response of the FRP decks. Another investigated a hybrid GFRP-steel solution, providing a deck with much higher shear stiffness in the core. Meanwhile, one suggestion made later in the project for the actual case study bridge was a deflection limit between girders of span/500, based on expected strains in the deck and wearing surface and an attempt to minimize cracking of the wearing surface in the negative moment region over girders.

7.4 Wildcat Creek Bridge and KSCI Deck

The KSCI deck was initially studied together with the Wildcat Creek Bridge as the case-study bridge. The KSCI specimens exhibited generally linear response to failure, except for issues with a weak longitudinal joint or gap in the test set-up. Even with a reinforced longitudinal joint, however, noises indicated damage to the core of the specimen; the specimen also did not satisfy deflection limits. It was believed that damage to the core and the shear deformations in the core contributed to the larger than acceptable deflections. Meanwhile, a deck-to-girder connection test showed essentially infinite initial stiffness to the connection and failure of the stud at ultimate load.

Unfortunately, time delays and rising costs for the FRP deck made this case study bridge and KSCI panel cost-prohibitive. However, the results of this portion of the study are still viable in terms of general observations and issues with FRP bridge deck construction.

7.5 Sugar Creek Bridge and ZellComp Deck

The case study bridge, CR 900 E. over Sugar Creek, was the second bridge studied for use of a fiber reinforced polymer (FRP) deck for bridge rehabilitation and deck widening. The 2% cross slope on the deck was to be built into the FRP deck installation; the crown connection was one of a number of concerns that were studied experimentally. The composite deck system manufactured by ZellComp, Inc. was the one used for this specific rehabilitation project. The ZellComp deck was installed on the Sugar Creek Bridge in November 2009.

The ZellComp deck was subjected to a number of tests, primarily to evaluate any issues with the crown connection. Test results demonstrated that a special

joint would be needed at the crown to prevent moisture ingress. Results also demonstrated that the deck design was adequate. The ultimate failure mode, at a factor of safety of approximately 5, was web buckling.

7.6 Non-destructive Evaluation Methods

A number of non-destructive evaluation methods were considered for monitoring of the FRP deck in service. Of the various technologies, acoustic emission appeared to be the most promising. Passive tests on damaged specimens, acoustic emission tests on FRP deck specimens as they were loaded, and acoustic emission tests on FRP coupons as they were loaded showed different frequencies, amplitudes and durations for different failure modes and proximity to damaged locations. However, some limitations to acoustic emission include the inability of the acoustic waves to traverse joints between FRP deck panel sections, as well as the connection between the top plate and bottom section of the ZellComp deck. Therefore, use of acoustic emission would be labor intensive, requiring measurements at regular and frequent intervals along the deck, between deck joints.

Infrared thermography also appeared to be promising for identifying delamination between the wearing surface and the FRP top plate. However, use of the infrared thermographic camera would also be labor intensive, requiring heating of small sections of deck at a time and then quickly taking the thermographic image. Furthermore, results would show variability with amount of heating and cooling before the image is acquired.

Meanwhile, a traveling truck deflection measurement method was developed. This procedure was tested on the FRP deck after installed on the Sugar Creek Bridge. This method showed some promise, but also showed variability and sensitivity to small variations in the surface of the deck. It is believed that this method would be successful at locating severe damage of the webs, as deflection measurements would show marked increases local to the damage. However, further validation and baseline measurements of on the FRP bridge deck with the wearing surface are required if this method is to be pursued.

7.7 Implementation Plan

Items to be implemented include design procedures as related to deflection limits, crown connection details, and guardrail details. Inspection and monitoring procedures may also be implemented. INDOT design and inspection personnel are recommended to be involved in the implementation of the findings of this study.

7.8 Conclusions

In November 2009, Sugar Creek Bridge became the first bridge in Indiana to be rehabilitated with an FRP

bridge deck. An extensive study, including literature review, analysis, and load tests, suggest that the installed deck should perform well, with web buckling as the ultimate failure mode at a factor of safety of 5. Deflection limits, generally an issue with FRP decks, are satisfied with the installed deck. Meanwhile, some combination of acoustic emission methods, infrared thermography and a newly developed traveling truck deflection method shows promise for non-destructive evaluation of the deck in-situ and identification of damage such as delamination of the wearing surface or web buckling. However, such methods have shown variability and could be prohibitively labor-intensive. Therefore, further evaluation is needed if such methods are to be pursued.

REFERENCES

- AASHTO (1998). AASHTO LRFD Bridge Specifications. 2nd Edition, American Association of State Highway and Transportation Officials, Washington, D.C.
- AASHTO (1996). AASHTO Standard Specifications for Highway Bridges. 16th Edition, American Association of State Highway and Transportation Officials, Washington, D.C.
- ABAQUS (2001). Standard User's Manual. Version 6.2. Hibbit, Karlsson & Sorensen, Inc.
- ABAQUS (2007). CAE User's Manual. Version 6.7-1. ABAQUS, Inc., Providence, RI.
- Advanced Fiber Products (2010). <http://www.afpfiberglass.com/images/pultrusionProcess.jpg>
- Allen, H.G. (1969). *Analysis and Design of Structural Sandwich Panels*. Oxford: Pergamon Press.
- AASHTO (2004). *LRFD Bridge Design Specifications*. 3rd Ed. Washington, D.C., 2004.
- ASCE Structures Division (1958). "Deflection Limitations of Bridges: Progress Report of the Committee on Deflection Limitations of Bridges of the Structural Division." *ASCE Journal of the Structural Division*: 1633-1 – 1633-20.
- Cai, C. S.; Zhang, Y.; and Shi, X. (2006). "Vehicle-Induced Dynamic Performance of FRP Slab Bridges." Proceedings of the 17th A&C Specialty Conference, St. Louis, Missouri, May 18–20.
- Camata, G., and Shing, P. B. (2004). "Evaluation of GFRP Deck Panel for the O'Fallon Park Bridge," Report No. CDOT-DTD-R-2004-2, Colorado Department of Transportation.
- Camata, G. and Shing, B. (2005). "Evaluation of GFRP Honeycomb Beams for the O'Fallon Park Bridge." *ASCE Journal of Composites for Construction* 9(6), 545–555.
- Cassidy, P.A. (2000). "Fiber-Reinforced Polymer Bridge Decks," J. Muller International, Chicago, IL. <http://www.nabro.unl.edu/articles/20000805/index.asp>
- Chen, A. (2004). "Strength Evaluation of Honeycomb FRP Sandwich Panels with Sinusoidal Core Geometry." Ph.D. Dissertation, West Virginia University, Morgantown, WV.
- Cole, T., Lopez, M., and Ziehl, P. (2006.) "Fatigue Behavior and Nondestructive Evaluation of Full-Scale FRP Honeycomb Bridge Specimen." *ASCE Journal of Bridge Engineering* 11(4), 420–429.
- Cousins, T. E., and Lesko, J.J. (2004). "Plate and Tube Bridge Deck Evaluation in the Deck Test Bed of the Troutville, Virginia, Weight Station." Final Report to the Virginia Transportation Research Council, VTRC 04-CR12.

- Dao, M., and Asaro, R.J., (1999). "A study on failure prediction and design criteria for fiber composites under fire degradation." *Composites Part A*, 30(2), 123–131.
- Davalos, J. F., Qiao, P., Xu, X. F., Robinson, J., and Barth, K. E. (2001). "Modeling and Characterization of Fiber-reinforced Plastic Honeycomb Sandwich Panels for Highway Bridge Applications." *Composite Structures* 52(3-4), 441–452.
- Demitz, J. R., Mertz, D.R., and Gillespie, J. W. (2003). "Deflection Requirements for Bridges Constructed with Advanced Composite Materials." *ASCE Journal of Bridge Engineering* 8(2) 73–83.
- Dodds, N., Gibson, A. G., Dewhurst, D. and Davies, J. M. (2000). "Fire behaviour of composite laminates." *Composites Part A: Applied Science and Manufacturing* (UK). Vol. 31A, no. 7, pp. 689–702.
- Dutta, P. K., Lopez-Anido, R., and Kwon, S. C. (2007). "Fatigue Durability of FRP Composite Bridge Decks at Extreme Temperatures." *International Journal of Materials and Product Technology* 28(1/2), 198–216.
- Hayes, M. D., Ohanehi, D., Lesko, J. J., Cousins, T. E., and Witcher, D. (2000). "Performance of Tube and Plate Fiberglass Composite Bridge Deck." *J. Composites for Construction* 4, 48.
- Janeway, R. N. (1948). "Vehicle Vibration Limits to Fit the Passenger." *Automotive Industries*, April 1948.
- Kalny, O., and Peterman, R. J. (2005). "Performance Investigation of a Fiber Reinforced Composite Honeycomb Deck for Bridge Applications." FHWA-KS-04-1, Kansas Dept. of Transportation.
- Kalny, O., Peterman, R. J., Ramirez, G., Cai, C. S., and Meggers, D.(2003). "Structural Performance of Fiber-Reinforced Polymer Honeycomb Sandwich Panels - Evaluation of Size Effect and Wrap Strengthening." *Transportation Research Record* 1845, No. 03-3459: 191–199.
- Kalny, O., Peterman, R. J., and Ramirez, G. (2004). "Performance Evaluation of Repair Technique for Damaged Fiber-Reinforced Polymer Honeycomb Bridge Deck Panels." *ASCE Journal of Bridge Engineering* 9(1), 75–86.
- Lombardi, N. J. (2008). "Glass Fiber-Reinforced Polymer/Steel Hybrid Honeycomb Sandwich Concept for Bridge Deck Applications." Ph.D. Dissertation, Purdue University, West Lafayette, IN.
- Lombardi, N. J., and Liu, J. (2010). "Steel Hexagonal Honeycomb Core Equivalent Elastic Moduli for Bridge Deck Sandwich Panels." *ASCE Journal of Aerospace Engineering* 23(1), 62–69.
- Ma, Z., Choppali, U., and Li, L. (2007). "Cycling Tests of a Fibre-Reinforced Polymer Honeycomb Sandwich Deck Panel at Very Cold Temperatures." *International Journal of Materials and Product Technology*, 28(1/2), 178–197.
- Machado, M., Sotelino, E., and Liu, J., (2006). "Modeling Technique for Honeycomb FRP Deck Bridges via Finite Elements," 17th Analysis and Computation Specialty Conference, May, 2006.
- Machado, M. A. S. (2006). Alternative Acceleration-Based Serviceability Criterion for Fiber Reinforced Polymer Deck-on-Steel Girder Bridges. Ph.D. Dissertation, Department of Civil Engineering, Purdue University.
- Nystrom, H., Watkins, S., Stone, D., and Nanni, A. (2002). "Laboratory and Field Testing of FRP Composite Bridge Decks and FRP-Reinforced Concrete Bridge for City of St. James, Phelps County, MO." University of Missouri-Rolla, Report No. RDT02-012, October 2002.
- Precisioneering (2010). http://www.precisioneering.com/images/laminating_methods/vartm.jpg
- Reising, R. M. W., Shahrooz, B. M., Hunt, V. J., Neumann, A. R., Helmicki, A. J., and Hastak, M. (2004). "Close Look at Construction Issues and Performance of Four Fiber-Reinforced Polymer Composite Bridge Decks." *J. Compos. for Constr.* 8, 33.
- Righman, J., Barth, K. and Davalos, J. (2004). "Development of an Efficient Connector System for Fiber Reinforced Polymer Bridge Decks to Steel Girders," *ASCE Journal of Composites for Construction*, 8(4), 279–288.
- Roeder, C., Barth, K., and Bergman, A. (2002). "Improved Live Load Deflection Criteria for Steel Bridges." National Cooperative Highway Research Program Transportation Research Board of the National Academies.
- Roeder, C., Barth, K., and Bergman, A. (2004). "Effect of Live-Load Deflections on Steel Bridge Performance." *Journal of Bridge Engineering*, ASCE 8.2, 259–267.
- Shao, Y. and Darchis, F. (2007). "Low Temperature Response of Pultruded Composites at Saturation," *International Journal of Materials and Product Technology*, 28(1/2), 46–65.
- Stone, D., Nanni, A., and Myers, J. J.(2001). "Field and Laboratory Performance of FRP Bridge Panels." *Composites in Construction*, Proc., CCC, 701–706.
- Strongwell (2006) "Bridge Components: Fiber Reinforced Polymer Composites." Bristol, VA.
- Telang, N. M., Chris Dumlao, C., Mehrabi, A. B., Adrian T. Ciolko, A. T., and Gutierrez, J.(2006). "Field Inspection of In-Service FRP Bridge Decks." NCHRP Report 564, Transportation Research Board, Washington D.C.
- United Steel Deck, Inc (2003). *Steel Decks for Floors and Roofs: Design Manual and Catalog of Products*.
- Vulcraft. *Steel Roof and Floor Deck*. 2001.
- Wattanadechachan, P., Aboutaha, R., Hag-Elsafi, O., and Alampalli, S. (2006). "Thermal Compatibility and Durability of Wearing Surfaces on GFRP Bridge Decks." *J. Bridge Engrg.* 11, 465.
- Wolfe, W. E., Busby, H. R., and Taliaferro, S. (2003). "Performance Evaluation of Bridges with Fiber Reinforced Composite Decks." Final Report, FHWA/OH-2003/016, Columbus, OH.
- Wright, R. N. and Walker, W. H. (1971). "Criteria for Deflection of Steel Bridges." American Iron and Steel Institute. Final report.
- Wu, H., Mu, B., and Warnemuende, K. (2003). "Failure Analysis of FRP Sandwich Bus Panels by Finite Element Method." *Composites Part B: Engineering*, 34(1), 51–58.
- Xi, Y., Chang, S., Asiz, A., and Li, Y. (2004). "Long-Term Durability of Fiber Reinforced Polymers (FRPs) and In-Situ Monitoring of FRP Bridge Decks in O'Fallon Park Bridge." Report CDOT-DTD-R-2004-03, Denver, CO.
- Zellcomp, Inc. (2006) "Fiber-Reinforced Composite High-Load Structural Decking System for highway bridges, parking decks, and other structural applications." Durham, NC.
- Zhang, Y., Cai, C. S., Shi, X., and Wang, C. (2006). "Vehicle-Induced Dynamic Performance of FRP versus Concrete Slab Bridge." *Journal of Bridge Engineering*, 11(4), 410–419.
- Zhao, L. (2006). "Testing of a FRP Bridge deck," Presentation at the FICE/FDOT Design Conference." University of Central Florida, Orlando, FL.
- Zureick, A. (2007). "Accelerated Test Methods to Determine Long-term Behavior of FRP Composites," Georgia Institute of Technology. <http://www.ce.gatech.edu/~az4/Accelerated~20Test~20Methods.htm>